ON THE CONNECTION BETWEEN AGN FEEDBACK AND THE MASSIVE BLACK HOLE SPIN

PhD Thesis - Università degli Studi dell'Insubria

Francesco Bollati

On the connection between AGN feedback and the Massive Black Hole spin

Francesco Bollati

Supervisor: Francesco Haardt
Co-Supervisors: Alessandro Lupi, Massimo Dotti, Marta Volonteri

Dipartimento di Scienza e Alta Tecnologia
Università degli Studi dell'Insubria
Como - Italy

Acknowledgements

Un ringraziamento al mio supervisor F. Haardt, per avermi guidato in questo appassionante progetto, ai Prof. M. Dotti e A. Lupi per i loro preziosi consigli, alla Prof.ssa M. Volonteri, per la nostra breve ma felice collaborazione. Grazie ai miei genitori, che mi hanno insegnato a coltivare le mie passioni, a mio nonno, che mi ha insegnato che non si smette mai di essere curiosi, a mio fratello, per la sua tenace maieutica. Infine un ringraziamento alla mia ragazza Ilaria e ai miei amici, compagni di sogni e avventure.

CERTIFICATE

Date: 31 / 03 / 2024

This is to certify that the thesis entitled **On the connection between AGN feedback and the massive black hole spin** submitted by **Francesco Bollati** to **Università degli Studi dell'Insubria**, is a record of bonafide research work carried out by him under my supervision and is worthy of consideration for the award of the degree of **Doctor of Philosophy** of the Institute.

Francesco Haardt
Professor
DiSAT
Università degli Studi dell'Insubria
Via Valleggio 11, 22100 Como, Italy

DECLARATION

I declare that

(a) the work contained in the thesis is original and has been done by me under the guidance of my supervisors;

(b) the work has not been submitted to any other institute for any degree or diploma;

(c) I have followed the guidelines provided by the Institute in preparing the thesis;

(d) I have conformed to ethical norms and guidelines while writing the thesis;

(e) whenever I have used materials (data, models, figures, and text) from other sources, I have given due credit to them by citing them in the text of the thesis, giving their details in the references, and taking permission from the copyright owners of the sources, if necessary;

(f) whenever I have quoted written materials from other sources, I have put them under quotation marks and given due credit to the sources by citing them and providing required details in the references.

Place: Como

Date: 31 / 03 / 2024

Francesco Bollati

Contents

List of Figures

List of Tables

Abstract

Active-galactic-nucleus (AGN) feedback has nowadays become an imperative ingredient in modern theories of galaxy formation to reproduce key observables of galaxy populations and it is routinely incorporated both in semi-analytic and hydrodynamical simulation models. In this doctoral thesis, I present a new model for AGN feedback in numerical simulations, which takes into account the spin-dependence of feedback anisotropy. Then, I explore some applications of it aimed at advancing our understanding of massive black holes (MBHs) growth, dynamics and their interaction with the host galaxy. In § 1.1, I begin the discussion by introducing relevant concepts about AGNs from both an observational and theoretical perspective. In § 1.2 I outline the fundamentals of AGN feedback, explaining the processes through which AGNs release energy and influence the evolution of their the host galaxies. Section § 1.3 provides insights into the dynamic evolution of pairs and binaries of MBHs and shows how feedback is involved in these processes. In § 2 discuss the development of novel numerical recipe for AGN feedback that accounts for the angular dependence of radiative feedback upon black hole spin. I then show tests of this model and an initial application in the context of co-evolution between an AGN and its host isolated disc galaxy. The results of this work have been presented in [20]. Chapter § 3, which is based on [21], explores the dynamical friction driven inspiral of MBH pairs at tens of pc scale in circum-nuclear-discs, specifically considering the influence of spin-dependent anisotropic feedback. In § 4 I study the implication of this phenomenon on the migration of bound pc-scale MBHs in circum-binary-discs. The main results and limitations of this thesis are summarized in § 5, concluding with a discussion of potential future developments for this project.

Chapter 1

Introduction

1.1 Active Galactic Nuclei and Massive Black Holes

A first indirect evidence for the existence of MBHs at the centre of galaxies comes from the fact that a small fraction of them reveal a much broader spectrum than one would expect from the emission from dust, gas and stars in the galaxy. For such galaxies, in fact, the spectrum extends from the radio band to the X-band, and the UV is often characterised by strong, broad emission lines. In addition, these spectra show a rapid variability (of the order of weeks), which suggests that the radiation originates from a small region, only a few parsecs in size, which is called the Active Galactic Nucleus (AGN). Despite their extremely small size, the AGNs luminosity can exceed that of the host galaxy, sometimes by as much as a factor of a thousand. As discussed below (1.1.3), it is believed that AGNs are powered by matter accreting onto a MBH. Before discussing more in detail the AGNs phenomenology and their theoretical understanding in the framework of accretion disc physics, I briefly recall some fundamentals of astrophysical black holes. I recommend the reviews [1, 2, 22] for a more extensive introduction.

1.1.1 Astrophysical black holes

While from a theoretical point of view BHs can have any mass, provided there is an adequate formation mechanism, observational measurements reveal that the distribution of astrophysical BH masses in the universe is bimodal, characterized by stellar mass and supermassive BHs (see Fig. 1.1):

- Stellar-mass BHs have masses in the range $\sim 3-100\mathrm{M}_{\odot}$, and are thought

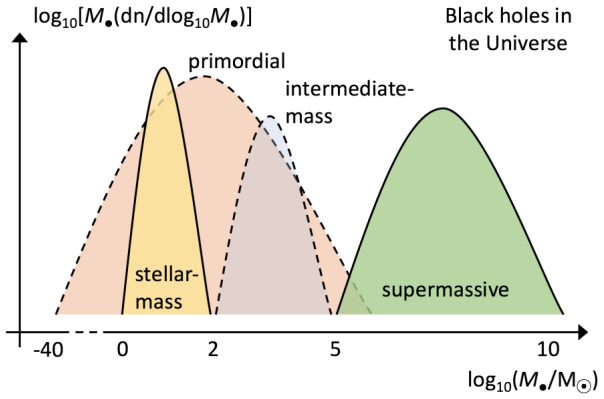

Figure 1.1: Sketched number density of BHs in the Universe. Credit: [1]. In order, are shown primordial BHs, stellar-mass BHs, intermediate-mass BHs and super-massive BHs. The shapes of the dashed distributions are arbitrary, as primordial BHs are speculative and for intermediate mass BHs only few candidates exist.

to originate from the core collapse of massive stars at the end of their lives. Such BHs are often observed in X-ray binary systems, i.e. binary systems consisting of a BH and a star, whose gas accretes on the compact object and as it heats up it emits X-rays. Cygnus X-1 was the first such object to be discovered [23]. The BH masses in these systems can be estimated from binary orbital parameters and/or X-ray luminosity. If stellar mass BHs are not accreting, their mass can be measured from gravitational waves signals (GW) once they coalesce with another compact object [24].

- MBHs are found in practically all observed galaxies with a significant bulge [8, 25], and have masses in the range $\sim 10^5 - 10^{10}\mathrm{M}_\odot$. Estimates of these masses are made using different techniques depending on whether the black hole accretes gas (and shines as an AGN) and whether its sphere of influence, defined as

$$r_{\rm inf} \equiv \frac{GM_\bullet}{\sigma^2} \simeq 10 \left(\frac{M_\bullet}{10^8 \mathrm{M}_\odot} \right) \left(\frac{200 \mathrm{km/s}}{\sigma} \right)^2 \mathrm{pc}, \tag{1.1}$$

is resolved, where G is the gravitational constant, $M_\bullet$ the MBH mass and σ the stellar velocity dispersion of the central part of the galaxy. In particular, if the MBH is accreting, its mass can be estimated via reverberation

(or echo) mapping or simple Eddington-luminosity arguments (see 1.1.4), and if the $r_{\rm inf}$ is resolved BH mass can be measured directly from the dynamics of stars, e.g. (e.g. SgrA$\star$ [26, 27]), and gas. See Sec. 3 of [2] for a review on MBH mass measurements. Differently from stellar mass BHs, whose formation mechanisms are well known, the formation of MBHs progenitors at high redshift and their subsequent growth over cosmic time still represents an intriguing challenge in modern astrophysics.

1.1.2 Black holes in General Relativity

The existence of objects compact enough to retain the light emitted from their surface was hypothesised by [28], simply by applying the Newtonian concept of escape velocity to light particles. Such hypothetical objects, initially named "dark stars", must have a radius smaller than

$$r_{\rm s} = \frac{2GM_\bullet}{c^2} = 2.95\left(\frac{M_\bullet}{\mathrm{M}_\odot}\right)\mathrm{km}, \tag{1.2}$$

where $M_\bullet$ is the mass of the compact object and c the speed of light. [28] also noted that the presence of such invisible dark stars could be inferred indirectly from the motion of proper stars orbiting them.
More than a century later, this intuition was confirmed in Einstein's general relativity and the radius (1.2) is nowadays referred to "Schwarzschild radius", in honour of the physicist who found the first solution of Einstein's field equations in the case of spherical symmetry and in the presence of a static, uncharged, non-rotating point-like massive object [29]. The Schwarzschild space-time metric takes the form

$$ds^2 = -\Big(1-r_{\rm s}/r\Big)c^2dt^2 + \Big(1-r_{\rm s}/r\Big)^{-1}dr^2 + r^2\Big(d\theta^2 + d\varphi^2\sin\varphi^2\Big). \tag{1.3}$$

This solution is characterised by two singularities: at $r=0$ and at $r=r_{\rm s}$. While the first is a physical singularity, i.e. the Riemann curvature tensor diverges, the latter is a coordinate singularity, that is inherent to the chosen coordinates system and not physical. Such singularity demarcates the location of the so called "event horizon", from which neither light nor massive particles can escape from, hence the name "black hole".
In later years, this result was extended, and the most general solution to the stationary metric of a BH is described by the Kerr-Newman metric [30], where

the MBH is characterized by three parameters: its mass, angular momentum $J_\bullet$ and charge $Q_\bullet$. It was later shown that BHs can in fact be described at most by these three parameters (see, e.g. [31]), a result known as "no hair" theorem. Special cases are the Kerr metric [32] ($Q_\bullet = 0$), the Reissner-Nordstrom metric [33] ($J_\bullet = 0$) and the Schwarzschild metric discussed above ($Q_\bullet = 0$, $J_\bullet = 0$). In addition, in typical astrophysical environments, it is usually true that a charged astrophysical object would be rapidly neutralized by surrounding plasma, i.e. it is usually assumed that $Q_\bullet = 0$. In general, we also expect BHs to rotate, either because they are formed by the collapse of a rotating object or because they have accreted surrounding material with non-zero angular momentum. For this reason, the most complete description for an astrophysical BH is the Kerr metric [34]. Using the Boyer-Lindquist coordinates, the Kerr metric reads

$$ds^2 = -\left(1 - r r_\mathrm{s}/\rho^2\right)c^2dt^2 - 2r r_\mathrm{s} a \sin^2\theta \rho^{-2} c dt d\varphi + \rho^2/\Delta dr^2 + \\ + \rho^2 d\theta^2 + \left(r^2 + a^2 + r_\mathrm{s} r a^2 \sin^2\theta \rho^{-2}\right)\sin^2\theta d\varphi^2, \tag{1.4}$$

where $\rho^2 = r^2 + a^2\cos^2\theta$, $\Delta = r^2 - r_\mathrm{s} r + a^2$ and

$$a = \frac{J_\bullet c}{G M_\bullet^2}, \tag{1.5}$$

is the BH spin parameter. Note that, setting $a = 0$ in Eq. (1.4) gives the Schwarzschild metric. It is believed that a cannot exceed the value 1, as it would give a gravitational field with a "naked" singularity, which is believed to be forbidden from the gravitational collapse of well behaved initial conditions. A BH with $a = 1$ is called maximally spinning and negative spin values are used to indicate BH spins w.r.t. counter-rotating particle orbits. Differently from the Schwarzschild metric, the $t\varphi$ component of the Kerr metric is non-vanishing. This implies that a particle with zero angular momentum released from rest far from the Kerr BH acquires a non-zero angular velocity as it spirals toward the BH, a phenomenon known as frame-dragging. In a Kerr BH, the radial coordinate of the horizon can be written as [1]

$$r_\mathrm{k} = \frac{r_\mathrm{s}}{2}\left(1 + \sqrt{1 - a^2}\right). \tag{1.6}$$

[1] In the Kerr metric, there are actually two event horizons (internal and external). However, the external event horizon described here is proper the event horizon of the BH in the sense that it is the first one-way surface an external particle crosses.

Since the Kerr metric varies with the spin parameter, the orbits of massive particles around Kerr BHs also change depending on the value of a. When $a = -1, 0$, and 1, the innermost stable circular orbit (ISCO) of a massive particle[2] is at $r_{\rm isco} = 9, 6$, and $1 \times r_{\rm g}$, respectively, where $r_{\rm g} \equiv r_{\rm s}/2$ denotes the so-called gravitational radius. If $r < r_{\rm isco}$, a particle can only spiral inwards (or outwards, if it has enough velocity to do so) and cannot maintain a stable circular orbit, differently from Newtonian mechanics, which allows stable circular orbits around a point-like object at any radii. More in general, the location of the ISCO as a function of the BH spin reads

$$r_{\rm isco}(a) = \xi(a) r_{\rm g}, \tag{1.7}$$

where

$$\xi(a) = 3 + z_2 \mp \sqrt{(3 - z_1)(3 + z_1 + 2z_2)}, \tag{1.8}$$

and

$$\begin{aligned} z_1(a) &= 1 + (1-a^2)^{1/3}\left[(1+a)^{1/3} + (1-a)^{1/3}\right], \\ z_2(a) &= \sqrt{3a^2 + z_1^2(a)}. \end{aligned} \tag{1.9}$$

The function (1.7) is shown in Fig. 1.2 (*right*) for both the prograde and retrograde case. Astrophysical accreting BHs are believed to be normally surrounded by accretion discs. The ISCO then roughly coincides with their inner edge (see Fig. 1.2, *left*).

We conclude this paragraph briefly introducing the Lense thirring precession [36]. This phenomenon concerns the precession of particles orbits which are misaligned with respect to the BH angular momentum. More specifically, in the weak field limit the acceleration of a particle in motion around a spinning BH can be written as

$$\mathbf{a} = -\nabla\Phi + \mathbf{v} \times \mathbf{\Omega}_{\rm LT}, \tag{1.10}$$

where Φ is the gravitational potential of the BH, $\mathbf{v}$ the particle velocity and $\mathbf{\Omega}_{\rm LT}$ is the Lense-Thirring frequency. The second term in Eq. (1.10) is a correction

[2]The massive particle here is to be understood as a test particle. The moment this approximation ceases to be valid, and the contribution of such a particle to the metric is no longer negligible, then the values of the ISCO given above also change, see e.g. [35].

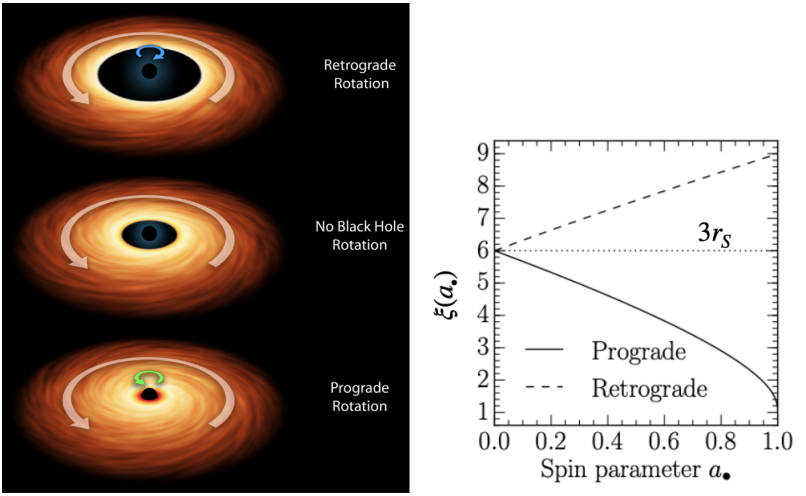

Figure 1.2: (*left*) Illustration of the ISCO as the inner edge of accretion discs, credit [2]; (*right*) the location of the ISCO in units of $r_{\rm g}$ as a function of the spin parameter, credit [3].

of the acceleration due to the BH rotation. The Lense-Thirring frequency reads

$$\mathbf{\Omega_{LT}} = \frac{2G}{cr^3}\left[\mathbf{J}_\bullet - \frac{3(\mathbf{J}_\bullet\cdot\mathbf{r})\mathbf{r}}{r^2}\right], \tag{1.11}$$

and represents the frequency of rotation of the particle orbit around the BH angular momentum direction. In the BH equatorial plane ($\mathbf{J}_\bullet\cdot\mathbf{r}=0$), the precession frequency is given by

$$\mathbf{\Omega}_{\rm LT} = \frac{2G\mathbf{J}_\bullet}{cr^3}. \tag{1.12}$$

I will discuss the implication of this effect in § 1.1.5, in the context of warped accretion discs.

1.1.3 AGN observations

As mentioned at the beginning of this chapter, the existence of MBHs is revealed to us indirectly by the radiation emitted by the gas accreting on them. The first such object to be discovered was the quasar 3c 273 in 1963 [37] (see Fig. 1.3, *left*), which only a few years later would be interpreted as an accreting MBH [38]. To

Figure 1.3: HST images of 3c 273 quasar (*left*) and NCG 4151 Seyfert galaxy (*right*).

date, many other similar objects have been observed, all catalogued under the name AGN. In general, an object is classified as AGN if it has one or more of the following characteristics: i) a compact nuclear region much brighter than a region of the same size in a normal galaxy; ii) non-stellar (non-thermal) continuum emission; iii) strong emission lines; iv) variability in continuum emission and/or in emission lines on relatively short time scales. The observed AGN population is classified into subgroups according to their observational properties. In the following, I give a brief overview of the different classes of AGNs:

- **(a) Seyfert Galaxies**: active galaxies with spiral-like morphologies and bright nuclei (see e.g. Fig. 1.3, *right*). Seyfert galaxies are characterised by continuous non-thermal spectra with strong emission lines and often show variability over a time span of less than one year. Seyfert galaxies are divided into type 1 and type 2 according to the width of the emission lines. Type 1 Seyferts show both broad lines, as for H_α and H_β, with full widths at half maxima (FWHM) corresponding to velocities in the range 1000-5000 km s^{-1}, and narrow lines, as for [OIII], with FWHM corresponding to velocities of a few hundred km s^{-1} (see Fig. 1.4). In contrast, Seyfert 2 galaxies show only narrow lines, typically of a few hundred km s^{-1}. A different width of the lines is interpreted as a consequence of a different region from which they are emitted. In particular, lines with FWHM corresponding to a velocity of about 10^3 km s^{-1}, are said to come from the Broad Line Region (BLR), which extends no further than ~ 1 pc from

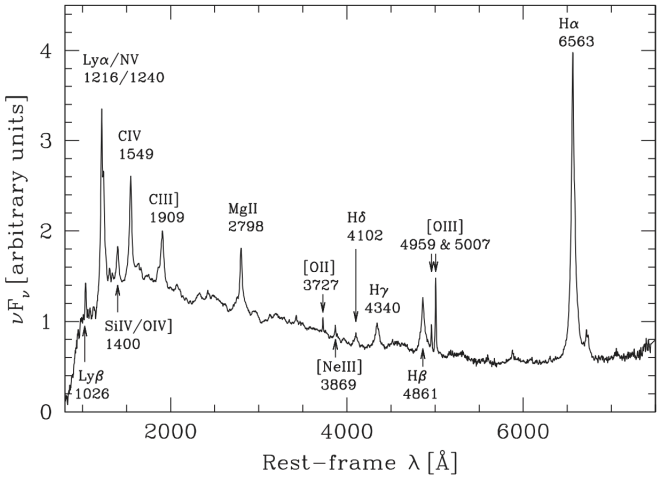

Figure 1.4: A composite spectrum of AGN revealing the typical non-thermal continuum and various emission lines. Credit [4].

the MBH, while narrower lines are said to come from the Narrow Line Region (NRL), which can extend up to 100 pc from the central MBH. See Fig. 1.6 for a schematic representation of the BLR and NLR. I remark that the lack of broad emission lines in Seyfert 2 does not necessarily imply the absence of a BLR, it may merely reflect that this region is blocked from our view.

- **(b) Radio Galaxies**: a class of active galaxies characterized by relatively strong radio emission. Almost all host galaxies of radio AGN are ellipticals, although radio jets have been observed in Seyfert galaxies as well [39]. Radio galaxies can be classified according to the width of the emission lines in the continuum, similar to Syefert galaxies, but also according to the properties of their radio emission, e.g. its morphology and its spectrum. Radio galaxies usually display a double-lobed structure extending to several hundred kiloparsecs or even megaparsecs from the central nucleus (Fig. 1.5).

- **(c) Quasars and QSOs**: objects typically found at high redshift (e.g. $z \sim 2-3$, but also at $z \sim 7$), and initially recognized as stellar objects but with anomalous spectrum and strong radio emission, hence first called "quasi-

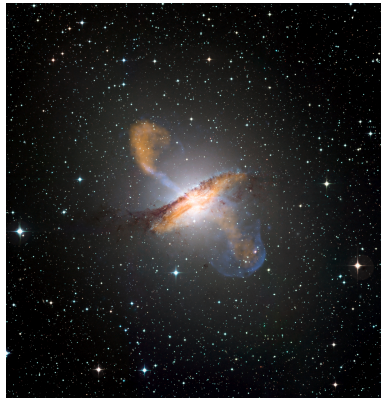

Figure 1.5: Colour composite image of Centaurus A, revealing the lobes and jets emanating from the active galaxys central black hole. The 870-micron sub-millimetre data are obtained from LABOCA on APEX, X-ray data from the Chandra X-ray Observatory, visible light data from the Wide Field Imager (WFI) on the MPG/ESO 2.2 m telescope.

stellar radio sources", or "quasar". The optical spectrum of quasars is very similar to that of Seyfert 1 galaxies, but they are brighter, characterized by luminoisites $L \sim 10^{45} - 10^{47}$ erg/s. Thanks to the spatial resolution of HST, it has been possible to observe the host galaxy of several low redshift quasars and this has revealed that quasars can be found in galaxies that manifest very different morphological properties; while some quasar hosts appear to be normal spirals and ellipticals, others are strongly disturbed or interacting systems [40].

- **(d) Blazars and BL Lac**: objects very luminous at almost all wavelengths, from radio to gamma rays, that display spectra mostly lacking of spectral lines. Their emission is dominated by the emission of a relativistic jet.

The plethora of AGN phenomenologies is often interpreted on the basis of a "unified model of AGNs" [41, 42, 43], as illustrated in Fig. 1.6, initially proposed for the unification of the two Seyfert types of galaxies. The idea is that in the nucleus there is the so-called "central engine", that is an accreting MBH ([44], [38]). Indeed, the small size of the emission region of an AGN, as inferred from time variability of the order of weeks, and the large amount of energy output, suggest that the central engine must be compact and have relatively large mass.

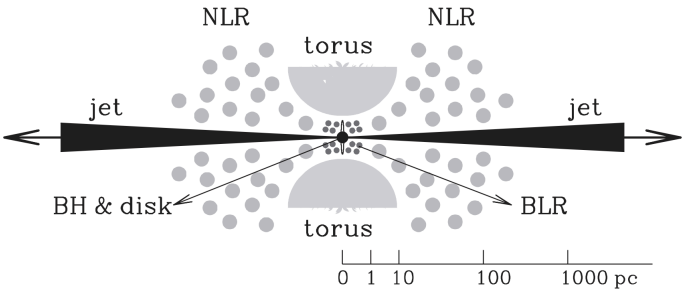

Figure 1.6: Different components of an AGN in the standard paradigm: a central MBH surrounded by an accretion disc at sub-pc scale, the BLR at $\sim$ 1 pc, the dusty torus at $\sim$ 1-10 pc, the NLR at tens of pc and a jet emerging from the inner disc propagating up to kpc scales. Credit [4].

Of all known astrophysical compact objects, black holes are the only ones with such a deep potential wall such that they can convert gravitational energy into radiation in the observed amount, so as to explain AGN luminosities. In the AGN model, the accreting MBH is surrounded by gas moving in the two zones BLR and NRL (one inner and one outer). Also surrounding the MBH is a structure dominated by dust and with a toroidal shape. The various types of AGN listed above are thus distinguished according to i) their high or low luminosity; ii) the presence or absence of a radio jet; iii) the angle of inclination with respect to which we observe them. Indeed, different classes of AGN are not intrinsically different but but only appear different because we observe them at different angles.

1.1.4 Black hole accretion

In the MBH paradigm, an AGN is assumed to be powered by a MBH accreting gas, and the energy source is the gravitational potential of the central black hole.

1.1.4.1 Eddington luminosity

To comprehend the energy scale involved with MBH accretion, we consider the luminosity such that its radiation pressure on a ionized medium due to Thompson scattering equals the gravitational force due to the MBH. This calculation

gives the Eddington luminosity

$$L_{\rm Edd} = \frac{4\pi G c m_{\rm p}}{\sigma_{\rm T}} M_\bullet \simeq 1.28 \cdot 10^{46} M_{\bullet,8}\,{\rm erg/s}, \tag{1.13}$$

where $m_{\rm p}$ is the proton mass, $\sigma_{\rm T}$ the Thompson cross section and $M_{\bullet,8} = M_\bullet/10^8 {\rm M}_\odot$. The Eddington luminosity is the largest possible luminosity that can be achieved under the approximation of spherical accretion and radiation-gas interaction occurring via Thompson scattering. From these simple considerations, we see that a bright quasar with a luminosity $L \sim 10^{46}$ erg/s may be powered by a black hole with a mass $M_\bullet \sim 10^9 {\rm M}_\odot (\lambda_{\rm Edd}/0.1)^{-1}$, where $\lambda_{\rm Edd} \equiv L/L_{\rm Edd}$.

1.1.4.2 Spherical accretion

Early studies of gas accretion on a gravitating object focused on accretion of gas by stars moving through an infinite non-self gravitating gas cloud at steady supersonic speeds. This problem was first studied by [45] and later improved by [46]. Then, [47] studied the spherically symmetric accretion onto a gravitating object at rest in a gaseous medium and found that the accretion rate is given by

$$\dot{M}_{\rm B} = \frac{16\pi\rho G^2 M_\bullet^2}{c_{\rm s}^3} \simeq 3 \cdot 10^{-2} M_{\bullet,6}^2 \Big(\frac{T}{10^4{\rm K}}\Big)^{-3/2} \Big(\frac{\rho}{{\rm M}_\odot/{\rm pc}^3}\Big) {\rm M}_\odot/{\rm yr}. \tag{1.14}$$

where $M_\bullet$ is the mass of the object and $c_{\rm s}$, T and ρ are the gas sound speed, temperature[3] and density of the medium at large distance from the object, i.e. at a distance much larger then

$$r_{\rm B} = \frac{2GM_\bullet}{c_{\rm s}^2} \simeq 30 M_{\bullet,6} \Big(\frac{T}{10^4{\rm K}}\Big)^{-1} {\rm pc}, \tag{1.15}$$

which is known as the Bondi radius. At distances larger than $r_{\rm B}$ the gas internal energy dominates over gravity, while inside the Bondi radius gas dynamics is dominated by the massive object, rather than by its thermal state. In addition, [47] proposed an extension of this formula also valid for objects in motion relative to the medium, which, after being corrected by [48] with an extra factor of two,

[3] In Eq. (1.14) an adiabatic equation of state has been assumed to express the sound speed in terms of temperature.

reads

$$\dot{M}_{\rm B} = \frac{4\pi\rho G^2 M_\bullet^2}{(c_{\rm s}^2 + v_{\rm gas})^{3/2}}, \tag{1.16}$$

where $v_{\rm gas}$ it the object velocity relative to the gaseous medium. I stress that in the derivation of Eqs. (1.14) and (1.16) it is assumed that there is no feedback from the accreting object on surrounding inflowing gas. I recommend [49] for an extended review on Bondi accretion.

1.1.4.3 Accretion discs

In real astrophysical environments, gas always retains a certain amount of angular momentum with respect to the MBH and accretion unlikely occurs in a purely spherical fashion. As gas flows towards the central object, conservation of angular momentum makes it circularize and settle into a Keplerian disc structure and accretion occurs only in the presence of a mechanism that transports gas angular momentum outward and makes the gas flow inward, reach the ISCO and then plunge into the event horizon. During this path, a gas parcel of mass m in the disc, falls onto the MBH following a series of shrinking circular orbits. Due to virial theorem, at each circular orbit of radius r, the gas element mechanical energy is given by $-GM_\bullet m/2r$. If the gas element takes a time Δt to reach the ISCO, starting from distance r_0, then the energy lost per unit time reads

$$\frac{1}{\Delta t}\left(-\frac{GM_\bullet m}{2r}\right)\Bigg|_{r_0}^{r_{\rm isco}} \simeq -\frac{GM_\bullet \dot{M}_{\rm acc}}{2r_{\rm isco}}, \tag{1.17}$$

where we have defined $\dot{M}_{\rm acc} = m/\Delta t$ and used $r_0 \gg r_{\rm isco}$. As the gas element inspirals inwards, its dissipated mechanical energy is converted into heat and then radiated away, yielding a luminosity

$$L = \frac{GM_\bullet \dot{M}_{\rm acc}}{2r_{\rm isco}} = \frac{1}{2\xi}\dot{M}_{\rm acc}c^2 = \eta \dot{M}_{\rm acc}c^2, \tag{1.18}$$

where we have used Eq. (1.7) and we have defined the disc radiative efficiency as

$$\eta(a) = \frac{1}{2\xi(a)}. \tag{1.19}$$

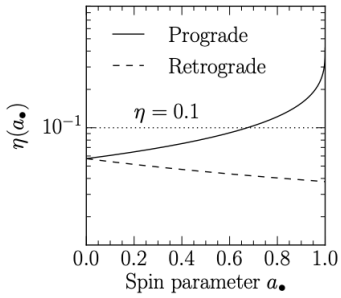

Figure 1.7: Radiative efficiency as a function of the spin parameter. Credit [3].

More precisely, a full GR computation [50] yields

$$\eta(a) = 1 - \sqrt{1 - \frac{2}{3}\frac{1}{\xi(a)}}. \tag{1.20}$$

The function (1.20) is shown in Figure 1.7 for both the prograde and retrograde case. For example, $\eta \sim 0.057$ at $a = 0$ and $\eta = 0.324$ for $a = 0.9982$ (the maximum spin value allowed once the capture of the disc radiation by the BH is taken into account [51]). By contrast, the efficiency with which hydrogen is burned into helium in stars nuclear reaction is only ~ 0.007, almost a factor of one hundred times less efficient than accretion onto a highly spinning MBH, which is then the most efficient process in nature for producing energy.
From Eq. (1.18), in particular, the Eddington luminosity defined in Eq. (1.13) corresponds to a mass accretion rate

$$\dot{M}_{\rm Edd} = \frac{L_{\rm Edd}}{\eta c^2} \simeq 2.8 M_{\bullet,8} \Big(\frac{\eta}{0.1}\Big)^{-1} {\rm M}_\odot/{\rm yr}, \tag{1.21}$$

which is the highest possible accretion rate in the simple spherical model.

Viscosity So far I have simply assumed that gas accretion onto the central object occurs as the gas elements in the disc follow shrinking circular orbits. It is fair to wonder, how is it that elements orbiting in a central force field lose their angular momentum and inspiral inwards? Put another way, how a differentially rotating flow is disrupted into an accretion flow? It occurs when i) it is energetically favorable to do so and ii) a path to these lower energy states is

available. Indeed, given a Keplerian disc, a lower energy configuration do exist, characterized by all the disc mass being located at the minimum of the potential and all disc angular momentum being carried away by an infinitesimal mass at infinite distance. A mechanism for angular momentum transport is provided by the onset of instability that triggers and sustains turbulence, which dissipates the gas bulk kinetic energy and acts as an effective viscosity. In the case of accretion discs around BHs, the magneto-rotational-instability (MRI) has been shown to be an efficient mechanism for such an angular momentum transport [52]. This complex viscous angular momentum loss is usually simply modelled (both in analytical models and simulations) by means of the so called Shakura & Sunyaev α-prescription [53], in which gas kinematic viscosity is assigned to be

$$\nu = \alpha h c_{\rm s}, \tag{1.22}$$

where h is the disc thickness. This formulation neglects the details of the onset of instability and turbulence, which are hidden in the value of coefficient $\alpha < 1$.

Disc evolution If the accretion disc is axisymmetric and thin, its structure can be described by its surface density $\Sigma(R,t)$, where R is the cylindrical radius on the disc. The time evolution of $\Sigma(R,t)$ is governed by the conservation of mass and angular momentum [54] and can be expressed in terms of a diffusive partial differential equation for $\Sigma(R,t)$, which can be derived directly from the Navier-Stokes equations for a viscous fluid in cylindrical polar coordinates. From this equations, it is found that the timescale on which viscosity smooths out surface density gradients at R is

$$t_\nu \simeq \frac{R^2}{\nu}. \tag{1.23}$$

Assuming stationarity, the surface density of the disc is described by

$$\Sigma = \frac{\dot{M}_{\rm acc}}{3\pi\nu}\left(1 - \sqrt{\frac{r_{\rm isco}}{R}}\right), \tag{1.24}$$

which connects the disc surface density with viscosity and accretion rate. See [5, 54] for more details.

1.1.4.4 The growth of massive black holes

One important fact that any theory of AGN formation must take into account is that quasars are observed up to redshift ~ 7. The cosmic time at such a redshift is about 0.5 Gyr, and so the growth timescale of a MBH must be shorter than 0.5 Gyr. If the growth of a MBH is through radiative accretion, the mass accretion rate can be written as

$$\dot{M}_{\rm acc} = \frac{L}{\eta c^2} = \frac{L}{L_{\rm Edd}} \frac{M_\bullet}{\eta t_{\rm Slap}}, \tag{1.25}$$

where the first equation follows from Eq. (1.18) and the second from (1.13) and the definition of Salpeter time

$$t_{\rm Salp} = \frac{\sigma_{\rm T} c}{4\pi G m_{\rm p}} \sim 4.5 \cdot 10^8 {\rm yr}. \tag{1.26}$$

However, in the accretion process, a fraction ϵ of the accreting mass-energy is released into the environment. Then, the actual accretion rate on the MBH is

$$\frac{dM_\bullet}{dt} \equiv \dot{M}_\bullet = (1-\epsilon)\dot{M}_{\rm acc} = \frac{(1-\epsilon)}{\eta} \lambda_{\rm Edd} \frac{M_\bullet}{t_{\rm Slap}}. \tag{1.27}$$

In standard thin radiatively efficient discs it is usually assumed that $\epsilon = \eta$, as energy is released only in the form of radiation. If both $\lambda_{\rm Edd}$ and η are independent of time, we get a differential equation for MBH mass growth which is solved by

$$M_\bullet(t) = M_{\bullet,0} \exp\left(\frac{1-\eta}{\eta} \lambda_{\rm Edd} \frac{t}{t_{\rm Slap}} \right), \tag{1.28}$$

where $M_{\bullet,0}$ is the initial BH mass, which, in turn, depends on how the black hole was initially created. From Eq. (1.28), the Salpeter time can be understood as the time it would take for the MBH to increase its mass by an e-fold while accreting at a fraction $\lambda_{\rm Edd} = \eta(1-\eta)^{-1}$ of the Eddington limit. We note that, if $L = L_{\rm Edd}$ and $a = 0$ (corresponding to $\eta = 0.057$), then the timescale for accretion is $3 \cdot 10^7$ yrs, while if $a = 1$, we have that $\eta = 0.42$ and then the timescale of accretion is about one order of magnitude higher. For example, if $M_{\bullet,0} = 10^3 {\rm M}_\odot$, then in the Hubble time $T_{\rm H} = 10^4$ Myr, a MBH can easily grow up to $10^9 {\rm M}_\odot$ both in case of $a = 0$ or $a = 1$. However, the observation of quasars of $10^9 {\rm M}_\odot$ at $z = 6-7$ poses a challenge. At $z = 7$, where $T_{\rm H} \simeq 750$ Myr, if $a = 0$, MBHs can still grow of about a factor of $e^{25} \sim 10^{11}$, provided the MBH can support

Eddington accretion up to $z \sim 7$, whereas only by a factor of $e^{2.5} \sim 10$ if one assumes $\lambda_{\rm Edd} = 0.1$. The situation is even more problematic in the case of maximally spinning MBHs. In this case, even assuming Eddington accretion, MBHs can grow only by a factor of $\sim e^{2.5} \sim 10$. By taking into account the torque exerted by the radiation emitted by the disc on the MBH, [51] showed that the MBH spin cannot exceed the limiting value of 0.9982, which correspond to a radiative efficiency of $\eta \simeq 0.324$. In this case, we would still obtain $e^{3.5} \sim 33$. Then, if $a \geq 0.9982$, even heavy seeds of $10^5 {\rm M}_\odot$ cannot grow into massive $10^9 {\rm M}_\odot$ BHs at $z = 7$. This rises a problem since efficient prograde accretion tends to spin up the MBH (see § 1.1.4.6), hence increasing η and slowing down the accretion preventing the formation of MBHs at high redshift. Some solutions to this problem have been suggested:

- When including MHD in accretion disc models [55] the spin $a = 0.9982$ cannot be reached exactly. Similarly, as the emission of jets through Blandford-Znajek [56] mechanism is powered by the rotational energy of the MBH, it contributes in keeping the spin at low values during MBH accretion. Then, since the increase of $\eta(a)$ with the spin magnitude is steeper for higher spin values, it is possible to have high spin but η small enough to form MBHs at high redshift. For example, if $a = 0.9$, then $\eta = 0.15$, which allows MBHs to increase their mass by a factor of $\sim 10^4 {\rm M}_\odot$ in 750 Myr, which is enough to form $10^9 {\rm M}_\odot$ MBHs at $z \sim 7$ starting from heavy seeds.

- Another way is that Eddington limit works strictly for spherical systems. If the radiation emitted by the disc has not a spherical angular pattern, accretion can proceed unhindered in preferential directions allowing to exceed Eddington limit [57]. For example, [58] showed that by allowing for a mild super-Eddington accretion ($\lambda_{\rm Edd} = 2$) in the FABLE simulation, together with a reduced AGN feedback efficiency and earlier seeding, it is possible to grow $\sim 10^9 {\rm M}_\odot$ MBHs at redshift 7.

- Accretion episodes can be chaotic, i.e. some accretion events tends to spin up, others to spin down, with the net result of keeping the MBH spin close to zero [59].

Finally, I note that MBHs more massive than $10^{9.5} {\rm M}_\odot$ are rare, and so a MBH cannot accrete at the Eddington limit continuously over its entire lifetime. This is perhaps not surprising, given that AGN can release huge amounts of energy,

both in radiation and in kinetic forms, into its surrounding. Such energy feedback can heat the gas in the host galaxy or even drive the gas out of it, thereby quenching further gas accretion. From an observational perspective, [60] investigated the distribution of MBH accretion rates with redshift (up to $z \sim 4$) and galaxy stellar mass. They found that $\lambda_{\rm Edd}$ has a broad probability distribution function, consistent with the stochastic nature of AGN fuelling, characterized by a power law shape increasing towards lower $\lambda_{\rm Edd}$, a cutoff at $\gtrsim 0.1-1$, and a plateau for small $(10^{-3}-10^{-2})\ \lambda_{\rm Edd}$. The truncated shape close to Eddington accretion rate suggests that accretion is feedback regulated.
In a self-regulated MBH accretion it is possible that significant growth only occurs during the active (quasar) phase(s) of the AGN, while the mass remains more or less constant during the long dormant quiescent phase(s). The fraction of time spent by a MBH in an active state is referred to as duty cycle.

1.1.4.5 The Sołtan argument

A first important claim about MBH cosmic growth came with the Sołtan argument [61] (see also [62]), which illustrated that if quasars were powered by accretion onto a MBH, then such MBHs must be present in the local universe as quiescent MBHs. More in detail, given the number of observed quasars at various redshifts, i.e. the luminosity function of AGNs $n(L,z)$ as the density of AGNs at a given redshift and per unit luminosity, [61] computed the integral of the luminosity emitted by all AGNs at a given cosmic time, which is proportional to the rate at which MBHs grow at that redshift. By integrating further in time, he then obtained an estimate of the mass density of MBHs

$$\rho_{\rm MBH}(z) = \int_z^\infty \frac{dt}{dz'} dz' \int_0^\infty \frac{1-\eta}{\eta} \frac{L}{c^2} n(L,z) dL. \tag{1.29}$$

This computation revealed that i) the growth of MBHs occurred essentially at $z \sim 2$ (see also Fig. 1.12), as the bulk of the luminosity of AGN comes from that redshift, and that ii) in the local universe $\rho_{\rm MBH}(z=0) \sim 2 \cdot 10^5 (\eta/0.1)^{-1} {\rm M}_\odot/{\rm Mpc}^3$. Being the galaxy number density in the local universe approximately $n_{\rm gas} \sim 0.1 {\rm Mpc}^{-3}$, Sołtan result implies that in each galaxy, on average, there must be a MBH with mass $\sim 2 \cdot 10^6 {\rm M}_\odot$. Indirectly, this argument also suggests that the radiative efficiency should be, on average, $\eta \sim 0.1$, and hence MBHs spins should be low.

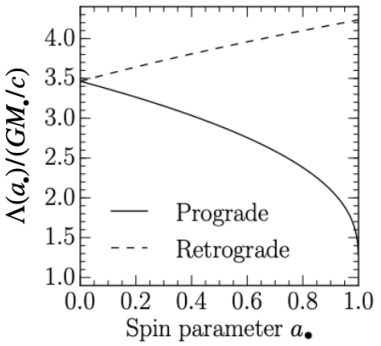

Figure 1.8: Specific angular momentum at the ISCO as a function of the spin parameter. Credit: [3].

1.1.4.6 MBH spin growth

AGN discs, while accreting mass on the central MBH and increasing its mass, they also accrete angular momentum and hence change the MBH spin. I can provide a rough estimate of the timescale needed to spin up an initially non-rotating (Schwarzschild) BH. I denote with $\Lambda_{\rm isco}$ the specific angular momentum of gas carried at the ISCO. A full GR calculation [63] reveals that

$$\Lambda_{\rm isco}(a) = \pm\frac{GM_\bullet}{c\xi}\frac{\xi^2 \mp 2a\sqrt{\xi}+a^2}{\sqrt{\xi-3\pm 2a/\sqrt{\xi}}}. \tag{1.30}$$

The function (1.30) is shown in Figure 1.8 for both the prograde and retrograde case. In particular $\Lambda_{\rm isco}/GM_\bullet c^{-1}$ is equal to $\sqrt{12}$ for a Schwarzschild BH and to $2/\sqrt{3}$ ($-22/3\sqrt{3}$) for a maximally spinning prograde (retrograde) BH (see also Fig 19 in [64]). In the following, for simplicity, I will consider a Newtonian approximation and assume the specific angular momentum at the ISCO for a non-spinning BH to be $\Lambda_{\rm isco} \simeq r_{\rm isco}\sqrt{GM_\bullet/r_{\rm isco}} = \sqrt{6}GM_\bullet/c$. Then, the accreted angular momentum on the BH reads

$$\dot{\mathbf{J}}_{\rm acc} = \dot{M}_{\rm acc}\Lambda_{\rm isco} \simeq \sqrt{6}\frac{GM_\bullet \dot{M}_{\rm acc}}{c}. \tag{1.31}$$

By combining Eq. 1.31 with the derivative of Eq. (1.5) we get an equation for spin evolution:

$$\dot{J}_\bullet = \frac{GM_\bullet^2}{c}\frac{da}{dt} + \frac{2aGM_\bullet}{c}\frac{dM_\bullet}{dt} = \sqrt{6}\frac{GM_\bullet \dot{M}_{\rm acc}}{c}, \tag{1.32}$$

which can be simplyfied into

$$\frac{da}{\sqrt{6}(1-\eta)-2a} = \frac{dM_\bullet}{M_\bullet}. \tag{1.33}$$

By integrating both sides and assuming $\eta = 0.057$, as for non-spinning BHs, we find that in order to spin up the MBH (reach $a = 1$), its final mass must be

$$M_{\bullet,f} = 2.73 M_{\bullet,i}, \tag{1.34}$$

i.e. the MBH needs to approximately triple its initial mass $M_{\bullet,i}$. However, I stress that in this computation I have assumed the $r_{\rm isco}$ and η to be constant during the spin growth, while in fact the former decreases and the latter increases with the spin. [34] and [51] carried out the correct GR computation and found the spin value a reached for a given increase of mass $M_{\bullet,f}/M_{\bullet,i}$ to be

$$a = \Big(\frac{2}{3}\Big)^{1/2}\frac{M_{\bullet,i}}{M_{\bullet,f}}\left[4 - \Big(\frac{18M_{\bullet,i}}{M_{\bullet,f}} - 2\Big)^{1/2}\right]. \tag{1.35}$$

Eq. (1.35) reveals that a complete spin-up is achieved once $M_{\bullet,f} = \sqrt{6}M_{\bullet,i} \simeq 2.45 M_{\bullet,i}$. Note also that in retrograde accretion, spin evolution would be faster because $r_{\rm isco}$ is larger and therefore the BH accretes more angular momentum per unit mass, i.e. an MBH requires to accrete less mass to spin down than to spin up.

Finally, if a non-spinning MBH has to roughly double its initial mass in order to become maximally spinning, the timescale $t_{\text{spin-up}}$ for this to occur can be estimated as

$$t_{\text{spin-up}} \sim \frac{\sqrt{6}M_\bullet - M_\bullet}{\dot{M}_{\rm acc}} = \big(\sqrt{6}-1\big)\frac{\eta}{\lambda_{\rm Edd}} t_{\rm Salp} \simeq 650\,{\rm Myr}\Big(\frac{\eta}{0.1}\Big)\Big(\frac{\lambda_{\rm Edd}}{0.1}\Big)^{-1}. \tag{1.36}$$

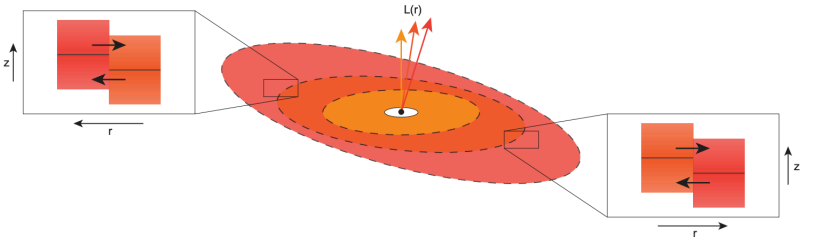

Figure 1.9: Illustration of the additional hydrodynamic effects present in a warped disc. Two neighboring and misaligned fluid annuli experience a vertical shear induced by the warp. The relative vertical displacements of the mid-planes of the annuli generate radial pressure gradients that act as a radial forcing, which is resonant with the disc epicyclic frequency if the potential is nearly Keplerian. Credit: [5].

1.1.5 Warped accretion discs

While accretion changes the magnitude of the MBH spin, it can also change its direction, provided the accretion disc angular momentum is misaligned with respect to the MBH spin. When this is the case, the disc annuli exchange torques with the MBH and with each other and disc looses its flat structure and gets warped (see Fig. 1.9).

The state of a warped disc is jointly described by the surface density $\Sigma(r)$ and the unit vector normal to the local disc plane $\hat{l}(r)$, where r is the radial coordinate. In addition, it is assumed that the disc is geometrically thin, that the fluid orbits are circular (modulo corrections due to radial gas flow), and that $\hat{l}(r)$ is a smooth, continuous function. Before discussing how the spin and disc structure evolve due to their reciprocal interaction, I briefly comment on the warped disc evolution as driven solely by internal torques.

Given two adjacent and misaligned disc annuli, their relative inclination causes both vertical and radial shear. Vertical shear, in turn, results in periodic vertical displacements of the annuli mid-planes, generating periodic radial pressure gradients, see e.g. [65]. If the potential is Keplerian, the forcing pressure gradients are resonant with the disc epicyclic frequency and launch waves. If the disc is sufficiently viscous, such waves are damped locally, and the warpe evolution is said to be in the viscous regime. The condition for viscous warp evolution is that [66]

$$\alpha \gtrsim \frac{h}{r}, \tag{1.37}$$

where h is the disc semi-thickness. In the opposite regime, radial propagation of the warp occurs via waves, provided that the potential is nearly Keplerian. The equations that describe the evolution of the warp in the viscous and wave-like regimes are different and they predict different qualitative behaviours. Discs around black holes and other compact objects are likely to be described by viscous warp dynamics, therefore in the following I will focus on this regime only. The equations for the evolution of warp structure in the viscous regime have been derived from conservation of mass and angular momentum by [67] and from fully non-linear hydrodynamic framework by [68].
According to [67] discussion, the evolution of an annulus angular momentum density (i.e. per unit area) $\mathbf{L} = \hat{l}\Sigma r^2\Omega$ is described by the equation

$$\begin{aligned}\frac{\partial}{\partial t}\mathbf{L} = &\frac{3}{r}\partial_r\left[\frac{r^{1/2}}{\Sigma}\partial_r(\nu_1\Sigma r^{1/2}\mathbf{L})\right]\\ &+\frac{1}{r}\partial_r\left[\left(\nu_2 r^2|\partial_r\hat{l}|^2-\frac{3}{2}\nu_1\right)\mathbf{L}\right]\\ &+\frac{1}{r}\partial_r\left[\frac{1}{2}\nu_2 r|\mathbf{L}|\partial_r\hat{l}\right],\end{aligned} \tag{1.38}$$

where the first term describes the angular momentum transport due to the azimuthal shear viscosity between differentially rotating annuli, while the second and third terms describe the alignment of misaligned annuli ($\partial_r\hat{l} \neq 0$) due to vertical shear viscosity. While the first process is regulated by the kinematic viscosity ν_1, which is the same as in Eq. (1.22) and discussed in § 1.1.4.3, the second is characterized by a kinematic viscosity ν_2, which, in principle, does not have a simple or obvious relationship with the former. The connection between the dissipative vertical (ν_2) and horizontal (ν_1) viscosities emerges from the full hydrodynamic derivation of the warped disc equations carried out by [68]. His analysis yields expressions for the kinematic viscosities in terms of the Shakura & Sunyaev α parameter and of the local strength of the warp $|\psi| = r|\partial_r\hat{l}|$. Both viscosities have a non-trivial form, typically decreasing as the warp amplitude becomes increasingly non-linear. In the small warp (linear) regime ($|\psi| \ll 1$), their relationship reads

$$\frac{\nu_2}{\nu_1} \simeq \frac{2(1+7\alpha^2)}{\alpha^2(4+\alpha^2)} \simeq \frac{1}{2\alpha^2}, \tag{1.39}$$

where the final expression is valid for the usual case where $\alpha \ll 1$. In reality, as discussed in § 1.1.4.3, it expected that disc viscosity is generated by MHD turbulence, triggered by the MRI. How this turbulence interacts in the vertical direction has yet to be fully determined.
Finally, from dimensional analysis of Eq. (1.38), the timescale for vertical disturbances diffusion and propagation reads

$$t_{\nu_2} = \frac{r^2}{\nu_2}. \tag{1.40}$$

Note that, given (1.39) and $\alpha \ll 1$, this timescale can be much shorter than the accretion timescale t_{ν_1} (1.23).

1.1.5.1 Bardeen-Petterson effect

Returning to Eq. (1.38), I now consider the effect of external torques $\mathbf{T}$ on the evolution of warped discs. The most famous example is the Lense-Thirring (LT) effect, which leads to the precession of orbits around Kerr black holes that are inclined with respect to the equatorial plane (see § 1.1.2). The precession frequency $\Omega_{\rm LT}$ is given in Eq. (1.12). Each annulus of the disc experiences a torque

$$\mathbf{T}_{\rm BP} = \frac{\boldsymbol{\omega}_{\rm LT} \times \mathbf{J}_{\rm annul.}}{r^3}, \tag{1.41}$$

where $\boldsymbol{\omega}_{\rm LT} = \boldsymbol{\Omega}_{\rm LT} r^3$. Then, the total torque experienced by the disc is given by

$$\frac{d\mathbf{J}_{\rm d}}{dt} = \int \frac{\boldsymbol{\omega}_{\rm LT} \times \mathbf{L}(r)}{r^3} 2\pi r dr. \tag{1.42}$$

[6] observed that *differential* precession due to the LT effect, acting on an initially planar but tilted disc, would rapidly warp the disc close to the black hole and drive up $|\psi|$ (see Fig. 1.10). We can define the characteristic warp radius $r_{\rm w}$, as the radius at which the timescale over which the disc is warped by LT effect equals the viscous timescale of diffusion of the warp disturbance. The first timescale is given by $t_{\rm LT} \sim r^3/\omega_{\rm LT}$, while the viscous timescale is (1.40). Equating these two timescales we find the warp radius as

$$r_{\rm w} = \frac{\omega_{\rm LT}}{\nu_2} = \frac{2GJ_\bullet}{c^2\nu_2}. \tag{1.43}$$

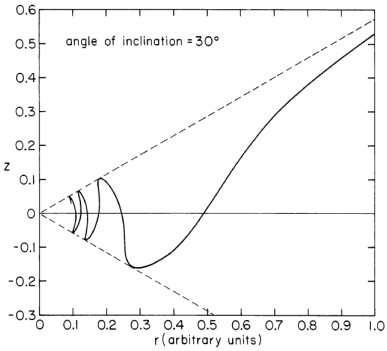

Figure 1.10: Disc mid-plane twisted structure as driven by LT precession. Credit: [6].

For larger radii $r > r_{\rm w}$, $t_{\nu_2} < t_{\rm LT}$ and any warped induced by the LT effect is immediately dissipated by viscosity and the disc keeps its initially flat misaligned shape. As we approach $r_{\rm w}$, viscosity is no longer able to redistribute and diffuse out the warps as they form on the same timescale $t_{\rm w} \equiv t_{\nu_2}(r_{\rm w}) = t_{\rm LT}(r_{\rm w})$. For $r < r_{\rm w}$, the LT torque is stronger than the viscous torque and any warped structure induced at $r < r_{\rm w}$ over a timescale $t_{\rm LT}(r)$ will be dumped by viscosity on a timescale $t_{\nu_2}(r) < t_{\rm w}$, in this way making the disc within the warp radius lay in the BH equatorial plane. This process of the disc acquiring an aligned orientation on the small scale while remaining misaligned on the large scale due to the LT precession is called Bardeen-Patterson effect.

1.1.5.2 Spin (counter)alignment

In the warp structure solution shown in the previous paragraph time evolution was neglected. However, as the spin exerts a torque on the disc, by inducing differential precession on its annuli, an opposite and equal torque must be experienced by the BH spin, according to Newton third law:

$$\frac{d\mathbf{J}_\bullet}{dt} = -\frac{d\mathbf{J}_{\rm d}}{dt}. \tag{1.44}$$

If the spin is parallel to the $\hat{z}$ axis, for each annulus, the LT torque lays in the xy plane, and hence the total torque on the disc does too. Since the torque acting on the MBH is perpendicular to the spin, it makes it change direction (inducing alignment and precession), but not magnitude. Therefore, as noted by [69], it is possible to decompose the torque experienced by the MBH into two components

as

$$\frac{d\mathbf{J}_\bullet}{dt} = -K_1(\mathbf{J}_\bullet \times \mathbf{J}_\mathrm{d}) - K_2\big(\mathbf{J}_\bullet \times (\mathbf{J}_\bullet \times \mathbf{J}_\mathrm{d})\big), \tag{1.45}$$

where K_1-term is responsible for precession and K_2-term for (counter)alignment, and both coefficients depend on the details of the disc structure. From simple geometrical analysis, by assuming that the spin modulus is constant, as well as the total (BH+disc) angular momentum, [69] found that the spin *always* aligns to the total angular momentum, without changing its magnitude. Conversely, the disc angular momentum is dissipated in this alignment process ($dJ_\mathrm{d}/dt \leq 0$). The BH spin and disc angular momentum counteralignment occurs if $J_\mathrm{total} < J_\bullet$, i.e.

$$\cos\theta < -\frac{J_\mathrm{d}}{2J_\bullet}, \tag{1.46}$$

where θ is the angle formed by the BH and disc angular momenta. From Eq. (1.46) counteralignment does occur if $\theta > \pi/2$ and $J_\mathrm{d} < 2J_\bullet$.

1.1.5.3 Timescale for spin alignment

I can provide an estimate for the timescale of spin alignment in the limit where the accretion disc has infinite extension and it is continually fed at its outer edge by matter whose angular momentum has constant direction $\hat{j}_\mathrm{disc,out}$. In this case, the BH aligns its spin to the outer disc direction. The alignment timescale t_al can be written as

$$t_\mathrm{al} \sim \frac{J_\bullet}{dJ_\bullet/dt} = \frac{J_\bullet}{|\int \boldsymbol{\omega}_\mathrm{LT} r^{-3} \times \mathbf{L} 2\pi r\, dr|} \sim \frac{J_\bullet}{\omega_\mathrm{LT} r_\mathrm{w}^{-3} J_\mathrm{w}}, \tag{1.47}$$

where J_w is the angular momentum of the annulus at the warp radius r_w and in the last passage I have assumed that most of the exchanged torque come from that disc-spin interaction at r_w. In fact, at smaller radii the disc lays in the spin equatorial plane due to the Bardeen-Patterson effect and no angular momentum is exchanged, whereas at larger scales the torque rapidly decays, as $\propto r^{-5/2}$ for a Keplerian disc, and its contribution can be neglected. Then, recalling that $t_\mathrm{w} = t_{\nu_2}(r_\mathrm{w}) = r_\mathrm{w}^2/\nu_2$ and using Eq. (1.40), the alignment timescale reads

$$t_\mathrm{al} \sim t_\mathrm{w} \frac{J_\bullet}{J_\mathrm{w}}. \tag{1.48}$$

Now, we can approximate $J_{\rm w}$ as

$$J_{\rm w} \simeq \pi r_{\rm w}^2 |\mathbf{L}| = \pi r_{\rm w}^2 \frac{\dot{M}_{\rm acc}}{3\pi\nu_1}\sqrt{GM_\bullet r_{\rm w}} = \lambda_{\rm Edd}\frac{M_\bullet}{3\eta}\frac{t_{\nu_1}(r_{\rm w})}{t_{\rm Salp}}\sqrt{GM_\bullet r_{\rm w}}, \qquad (1.49)$$

where in the second equality we used (1.24) for Σ and in the last one (1.25). Now, by replacing (2.16) in (1.48), and carrying out some algebra we obtain

$$t_{\rm al} \sim 3a\frac{\nu_1}{\nu_2}\sqrt{\frac{r_{\rm g}}{r_{\rm w}}}t_{\text{spin-up}}. \qquad (1.50)$$

The numerical value of the alignment time scale depends on the details of the disc model, but in general, as shown in (1.50) it works out to be short-compared to the Salpeter timescale on which accretion would change the magnitude of $\mathbf{J}_\bullet$. The ease with which a misaligned disc can change the spin axis of a black hole, compared to changing its magnitude, occurs because of the larger specific angular momentum of disc gas that drives the alignment (at $\sim r_{\rm w}$) compared to that responsible for spin growth (at $r_{\rm isco} \ll r_{\rm w}$), and because in the viscous regime $\nu_2 \gg \nu_1$ (Eq. 1.39).

1.2 AGN feedback

In this section I study how the presence of an AGN can affect its host galaxy, through the release of energy and momentum into the surrounding environment, a phenomenon known as AGN feedback. In these terms, AGN feedback can be seen as a by-product of accretion, which can influence galaxy evolution at a wide range of scales, from the AGN/BLR scale itself to the circum-galactic-medium CGM, through a wide range of phenomena, such as the driving of multi-phase outflows and the regulation of the host galaxy star formation (SF). AGN feedback is then a rich a complex phenomenon and shows that the study of AGN is not just for understanding AGN per se, but is an inseparable part of galaxy formation and evolution.

We can see this with a rough estimate. As shown above, the accretion process is associated with the release of large amounts of energy, whose power can be expressed by the relation

$$\frac{dE}{dt} = \epsilon \dot{M}_{\rm acc} c^2, \tag{1.51}$$

where $\epsilon = \eta + \eta_{\rm m}$ is an effective efficiency factor, η is the radiative efficiency defined in Eq. (1.20) and $\eta_{\rm m}$ the efficiency associated to the kinetic energy of mechanical feedback, e.g. jets. Now, assuming that the efficiency ϵ remains constant throughout the MBH growth process and that the MBH comes to acquire a mass $M_\bullet$ mainly through accretion (see Sec. § 1.1.4.5), then we obtain that the total energy released amounts to

$$E = \frac{\epsilon}{1-\epsilon} M_\bullet c^2. \tag{1.52}$$

Now, by comparing this energy with the binding energy of the host galaxy, it is possible to have a first indication of the effect that feedback may have on it. Assuming that the galaxy is an early type and is characterised by a mass $M_{\rm gal}$ and velocity dispersion σ, then its gravitational binding energy, in accordance with the viral theorem, can be expressed as $W \sim -M_{\rm gal}\sigma^2$. It then follows that

$$\frac{E}{|W|} \sim \frac{\epsilon}{1-\epsilon} \frac{M_\bullet}{M_{\rm gal}} \left(\frac{c}{\sigma}\right)^2. \tag{1.53}$$

According to the observed MBH-host galaxy scaling relations[4] $M_\bullet/M_{\rm gal} \sim 10^{-3}$,

[4]Note that in this relation $M_{\rm gal}$ is the mass of the central dispersion dominated spheroid

see e.g. [8]. Thus, by assuming that $\sigma \sim 300$ km/s, the ratio $E/|W|$ is about $10^3\epsilon(1-\epsilon)^{-1}$. If we assume ϵ to be around 0.1, as in radiative feedback (see e.g. § 1.1.4.5), the released energy is still orders of magnitude larger than that of the host. Consequently, if only a small fraction of this energy is able to couple to the gas, it will be capable of having an impact on the host galaxy, which points out how AGN feedback plays an important role in the formation and evolution of galaxies. In order to properly quantify the impact of AGN feedback on galaxy formation, there are two questions that need to be addressed. The first concerns the value of ϵ and the second the effectiveness with which the released energy couples with the gas in the galaxy, and both factors depend on the details of the type of feedback considered.

AGN feedback and MBH - galaxy co-evolution In the absence of AGN feedback, a MBH and its host galaxy would barely know about each other. The event horizon of a MBH is a billion times smaller than the size of a galaxy and its typical mass is less than 1 per cent of the galaxy stellar bulge mass. In this scenario the MBH has a negligible influence on its surrounding, limited to its sphere of dynamical influence (Eq. 1.1), and its growth is primarily determined by its galactic environment i.e. by the availability of cold gas, which is consumed and recycled by star formation, and by its ability of losing sufficient angular momentum to reach the inner sub-parsec region of the galaxy [70]. Put another way, MBH evolution is the result of its galactic environment, which instead is not influenced by the presence of the MBH. This corresponds to the situation illustrated in Figure 1.11, without the red and black arrows. The presence of AGN feedback, with the large amount of energy released in this process, allow to draw the remaining arrows, standing for the influence that the MBH exerts on its host galaxy. In other words, AGN feedback can serve as a connection between the MBH and the host galaxy and can drive their co-evolution, characterized by a reciprocal influence on each other [71, 72]. In this picture, both AGN activity and star formation are fuelled by the cold gas found in the common galaxy halo, which in turn can be supplied by various processes such as mergers between gas-rich galaxies, recycling of gas within the halo caused by baryonic feedback and accretion from intergalactic filaments [73]. In turn, AGN activity and star formation exert feedback on the surrounding environment in various forms, including winds, jets, radiation and cosmic rays [11, 74]. These feedback

of the galaxy, which, in case of ellipticals, constitutes the entire galaxy or the dominant part of it.

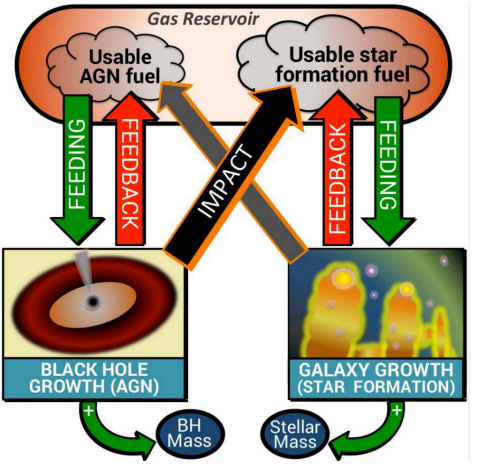

Figure 1.11: A sketch of the complex interplay between star formation, stellar feedback, BH growth and AGN feedback. Credit: [7]

processes have an impact on the cold gas that fuels the AGN and star formation in the first place, providing a complex self-regulatory feedback mechanisms. The detailed interaction between star formation, stellar feedback, BH growth and AGN feedback is probably the key to understanding the overall co-evolution of BHs and galaxies and, as a consequence, the properties of the galaxy population.

Observational evidence for co-evolution Indirect hints that a MBH-galaxy co-evolution does occur are provided by:

- the observed tight scaling relations between MBH and galaxy bulge properties, i.e. the $M_\bullet - \sigma$ and $M_\bullet - M_{\rm bulge}$ relations (See fig. 1.12, *left*) [8, 25, 75, 76]. It is worth mentioning that the sample from which these relations have been discovered or tested contains about 65 galaxies, and most of the MBHs in question are in the mass range of 10^7 to $10^9 M_\odot$, and the few that are above or below this range show departures from at least some of the correlations, or more scatter [77].

  However, I note that an alternative explanation of the $M_\bullet - M_{\rm bulge}$ relation has been suggested that does not require the effect of AGN feedback. This idea was formulated by [78] and subsequently developed by [79, 80] and predicts that the $M_\bullet - M_{\rm bulge}$ scaling relation is the result of the hierarchical assembly of MBH and stellar mass through galaxy merging,

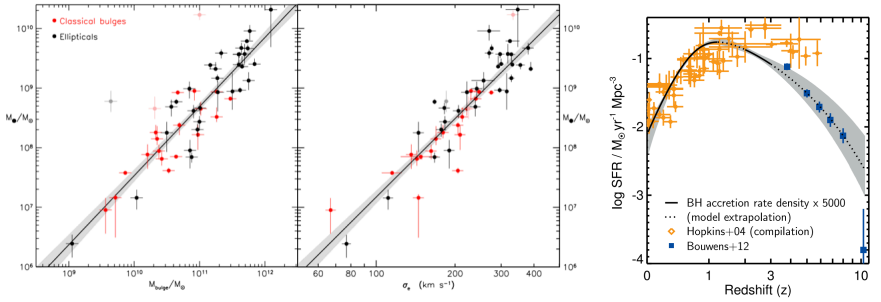

Figure 1.12: *Left*: MBH-stellar bulge scaling relations. The MBH mass is found to correlate with the stellar bulge mass and its velocity dispersion. *Right*: Evolution with redshift of the volume density of black hole accretion rate (black line with grey band), scaled up by a factor of 5000, and of cosmic star formation rate (blue and orange points). Credit: [8].

without implying the need for any physically coupled growth of MBHs and bulges through AGN feedback. Further supporting this idea is the fact that MBH mass correlates closely with the properties of bulges and ellipticals but not with those of pseudobulges, which indeed are not the result of galaxy mergers but of secular evolution [8].

- The similarity of the star-formation and MBH accretion histories [81] (Fig 1.12, *right*). Quasars and starbursts appear to be closely related. The most luminous starbursts always show signs of AGN activity, even if these do not dominate the bolometric output, and the host galaxies of AGNs often show sign of ongoing or recent star formation. [82] noted that the volume-averaged ratio of MBH accretion rate to SF rate today is $\sim 10^{-3}$, close to $M_\bullet/M_{\rm bulge}$. Whether this is a coincidence or the result of a deep causal connection between the evolution of MBHs and galaxies is still a subject of study.

While these evidences seems to indicate a co-evolution between MBH and host galaxy, some doubts have been raised as to the role AGN feedback plays in this process.

Is AGN feedback responsible for co-evolution? It remains one of the hottest topic in modern extra-galactic astrophysics understanding to what extent AGN feedback is responsible for such co-evolution and how it unfolds over

cosmic time. Indeed, similar SF and MBH accretion histories and the MBH-bulge correlation can be the result of processes that shape separately both MBH and galaxy growth, and by no means AGN feedback is the exclusive or the established main driver of these phenomena. As put by [83]:

> At the very root of the problem there is a crucial question: are the MBHs systematically found in massive galaxies nuclei a chance or a necessity? In other words, is the growth of a nuclear MBH the result of independent processes that produce both MBH and galaxy growth? If this is the case, BHs are a chance. Alternatively, do the two systems influence significantly their respective growth in a non-linear feedback loop? In this case MBHs may be a necessity.

In this respect, if MBHs are a necessity, AGN feedback stands as a crucial ingredient in determining the co-evolution. In this scenario, the MBH-host scaling relations are established as a result of reaching a limiting MBH mass and AGN luminosity such that the MBH drives powerful outflows that reach the halo escape velocity, thus sweeping away the surrounding gas and consequently halting both MBH growth and star formation in the galaxy [84, 85]. In the alternative view, the chance scenario, the galaxy sets the MBH mass by regulating the amount of gas that trickles to the MBH.
In addition, as emphasized by [9], besides the debated role of AGN feedback in regulating the co-evolution, it is not clear when the correlation is established. Three possibilities (Fig. 1.13) can be conceived: i) MBHs could have grown in symbiosis with their host galaxy; ii) the MBHs could have grown faster by dominating the process of co-evolution, with the galaxy catching up later, or, iii) on the contrary, the galaxy grew first determining the conditions for the evolution of the MBH, which later adjusted to its host. The second and third paths require that feedback and self-regulation were somehow different at early times.

Observational and theoretical evidences of AGN feedback Irrespective of the role of AGN feedback in establishing the MBH host scaling relation and the similarity in the MBH growth and SF histories, there is clear observational and theoretical evidence for AGN having a huge impact on its surrounding environment. Indeed, observations reveal

- large amounts of hot, X-ray-emitting gas in individual giant ellipticals and

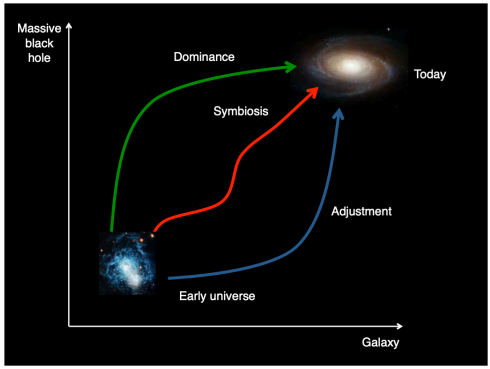

Figure 1.13: Possible routes to MBH and galaxy co-evolution, starting from black holes forming in distant galaxies in the early universe. Credit: [9].

groups and clusters of galaxies. These X-ray cavities or "bubbles" are believed to be inflated by AGN jets [11].

- Nuclear winds and galactic-scale outflows. Some bright quasars show blue-shifted X-ray spectral absorption lines interpreted as coming from winds with velocities $v \sim 0.1c$ and with mass loss rates of one to tens of $\mathrm{M}_{\odot}/\mathrm{yr}$ [86, 87]. Non-relativistic outflows with mass outflow rates of $\sim 1000\,\mathrm{M}_{\odot}\mathrm{yr}^{-1}$ at kpc scales are also observed [88, 89]. Such outflows can potentially clean a galaxy of cold gas in a single AGN episode.

AGN are also an attractive solution in models to supply the energy required to reproduce many key observables of galaxy populations and intergalactic material:

- episodic AGN feedback is believed to solve the "cooling flow" problem that, in the absence of energy input, X-ray halos in giant galaxies and in clusters of galaxies would cool quickly, but cool gas and star formation are not seen in the predicted large amounts. This phenomenon is sometimes referred to as "maintenance-mode AGN feedback".

- At high masses, the galaxy mass function drops more steeply than the mass function of dark halos that is predicted by our standard cosmology. The proposed solution is that higher mass AGNs are more efficient at preventing late galaxy growth, again through the action of radio jets that keep baryons suspended in hot gas [90], i.e AGN feedback is used to explain the high mass end of the galaxy stellar mass function.

- Mergers convert spiral galaxies into classical bulges and ellipticals. Since the former are gas-rich and star-forming whereas the latter are gas-poor and "red and dead", something connected with mergers presumably removes gas and quenches star formation. The observed bimodality in the color-magnitude correlation can be explained by a rapid quenching of star formation. Expulsion or heating of residual cold gas may be accomplished by AGN feedback [91].

1.2.1 AGN driven outflows and their impact on star formation

In this section I discuss more in depth the nature of AGN-driven outflows and how they affect the host galaxy star formation, both from a observational and theoretical perspective.

1.2.1.1 Galactic outflows

Galaxy-wide ($\gtrsim$ 0.1 - 10 kpc) energetic outflows and turbulences represent one way that AGN are known to be capable of interacting with their host galaxy multi-phase interstellar medium (ISM) [88, 89, 92, 93]. Observational signatures of outflows in the form of broadened (Doppler shifted) emission and absorption lines have been detected for a number of galaxies hosting an AGN. Detected outflows have characteristic speeds of 1000 km s^{-1}, spatial scales of $\sim 1-10$ kpc and often appear to consist of a complex multi-phase medium. This typically comprises a hot ionized component that can travel at speeds as high as $\simeq 3000$ km s^{-1} [92], a partially overlapping neutral atomic component at speeds not much exceeding $\simeq 1000$ km s^{-1} [94] and a substantial portion of cold molecular gas, as revealed by spatially resolved CO-emission and OH-emission/absorption features [94, 95]. As an example, Fig. 1.14 shows an object where both the AGN and outflow are seen is the low redshift ($z = 0.04$) quasar/merger Mrk 231 [10]. The outflow is characterized by a velocity of ~ 1100 km s^{-1} and a mass outflow rate of $420\,M_{\odot}yr^{-1}$, several times greater than the star formation rate. The outflow power is about one per cent of the bolometric luminosity of the AGN. Using CO observations of a sample of local Ultra Luminous Infrared Galaxies (ULIRGs) and QSOs, [95] have shown that the mass outflow rates, the kinetic luminosity, the momentum flux and the spatial extension of detected outflows all correlate with the fraction of the host galaxy bolometric luminosity attributed to a central AGN (see. also [96, 97]). This supports the idea that outflows are indeed powered by AGNs. In addition, both observations and theoretical

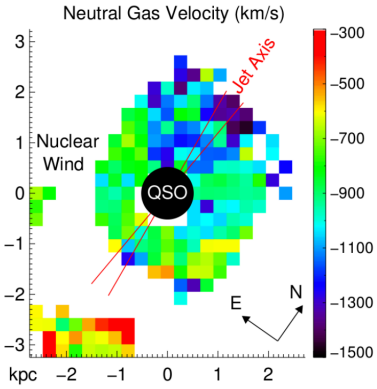

Figure 1.14: Neutral gas velocity map in the quasar/merger object Mrk231 [10]. Credit: [11].

modeling suggest that galaxy-scale AGN outflows have momentum fluxes well in excess of the radiative momentum flux output of the central AGN, $\dot{P}_{\rm rad} = L_{\rm AGN}/c$. Observationally, the "momentum boost" $\dot{P}_{\rm outflow}/\dot{P}_{\rm rad}$ ranges from ~ 2 to ~ 30 in local ULIRGs dominated by AGN [10, 94] and in luminous quasars. Although the uncertainties are large, collectively these measurements indicate that AGN-driven, galaxy-scale outflows may commonly have momentum fluxes $\sim 10 L_{\rm AGN}/c$.

I mention that besides AGN, also supernovae and star-bursts are capable to drive galactic outflows, though, theoretical models of supernova-driven feedback exclude outflow speeds much exceeding $\simeq 600$ km s^{-1} on energetic grounds. Therefore, most of the lower velocity winds are considered to be driven by stellar feedback and identifying the effects of AGN feedback in outflows often relies on observing higher winds velocity (e.g. > 500km s^{-1}) and an outflow power exceeding that predicted by any central starburst. Nonetheless, there is no clear distinction between AGN- and stellar- driven outflows, especially in dwarf galaxies.

1.2.1.2 Outflows driving mechanism

Theoretically, AGN galactic outflows may be driven by different mechanism:

- Radiative processes: as seen above, accretion discs release the energy dissipated by viscosity in the form of heat and then radiation, and for a

radiative efficiency of $\eta \sim 0.1$, the amount of energy made available in this way is enormous. This can affect the environment by both radiation pressure and radiative heating. In models, radiative energy injection is sometimes called "quasar" or "wind" mode and is usually associated with high Eddington ratios ($\lambda_{\rm Edd} \gtrsim 0.01$).

- Mechanical processes: the release of energy from an AGN can occur through the emission of a relativistic jet collimated along the direction of the MBH spin (see [98] for a review). Such jets can release an amount of kinetic energy comparable to the radiative energy of the source and can therefore have a significant impact on the host galaxy, up to the galaxy cluster scale. This type of feedback is associated with low Eddington ratios.

- Energetic particles (cosmic rays): Although there is currently no evidence that this feedback channel can have an impact comparable to the previous two, the production of energetic particles could in principle contribute to the overall feedback process exerted by the AGN on the surrounding environment, see [99] for a review.

Overall, radio jets are usually found in the most massive systems with old stellar populations, at least in the local universe, while radiative AGN are most common in galaxies with ongoing SF and younger stellar populations at all cosmic epochs. As a consequence, these two categories of AGN may represent distinct evolutionary phases and/or distinct MBH accretion mechanisms depending on the host galaxy mass and environment. Also, note that jets characterize a small fraction of the AGN population, contrary to AGN winds which are ubiquitous in AGNs.
In this thesis I am only concerned with the first of these mechanisms, i.e. with AGN radiative feedback. In this feedback mode, the interaction between the AGN radiation and the ISM that give rise to galaxy-wide outflows can occur though two main channels, i.e. via launching small scale winds that mediate the radiation-ISM interaction or through direct radiation-ISM coupling at galactic scales. In the next chapters I will focus solely on the first, channel, i.e. on radiation-driven AGN winds.

Now we turn our attention to the influence that galactic scale outflows and the overall AGN feedback process have on the galaxy host star formation rate history.

1.2.1.3 The impact of outflows on star formation

AGN feedback is widely believed to regulate the rate of star formation in AGN host galaxies. However, the details of how and when this occurs remain uncertain from both an observational and theoretical perspective.
For example, i) evidence that AGN-driven outflows may have a significant impact upon star formation is that the measured mass outflow rates of molecular outflows in low redshift ULIRGs and quasar host galaxies appear to exceed the concurrent SFRs [95]. Consequently star forming material appears to be being removed more rapidly than it can be formed into stars in these galaxies, i.e. star formation could be suppressed by the removal of star forming material. Alternatively ii) AGN might kinematically disturb, compress, shock and/or heat the gas and consequently reduce or enhance the efficiency of converting the available gas supply into stars without the need to remove it.
A more direct indication of AGN feedback regulation of SFR is provided by observations of a small number of distant luminous AGN ($z \sim 1-3$) that show evidence for an anti-correlation between the spatial location of an ionised outflow and the location of narrow H_α emission (a star formation tracer) [100] . These results may indicate that star formation has been reduced in the regions of the outflow, although an alternative possibility is that these diffuse outflows preferentially escape away from the dense star forming material. Instead, the observational evidences of AGN outflows triggering star formation are slim, but examples exist where star formation seems to occur within the AGN-driven outflow itself at kpc scales [101, 102, 103] [5]. A recent example of enhanced star formation due to AGN driven outflow or jet [12] is shown in Figure 1.15. In some cases, observational papers have also reported evidence of suppression and enhancement working simultaneously in the same galaxies [104], i.e. positive and negative AGN feedback do not necessarily act against one another. In particular, [104] used SINFONI nearIR integral field spectroscopy of an obscured quasar at $z \sim 1.6$ to show that a prominent outflow traced by [OIII] lines coincides with the location of an empty central cavity surrounded by star forming regions, suggesting that the outflow is removing gas from the cavity (negative feedback) while triggering star formation at the edge of the cavity (positive feedback).
[105] looked for signature of AGN on SF in the CARS sample and found no strong evidence for a *global* positive or negative AGN feedback. Or in other words, no

[5] Analyzing over 2.500 galaxies in MaNGA, [103] identified a sub-sample of 37 galaxies with outflows, of which $\sim 30\%$ show signs of star formation within the outflowing gas, ranging from $0.1-1 M_\odot/yr$ and contributing 5-30% of the total SFR in the galaxy.

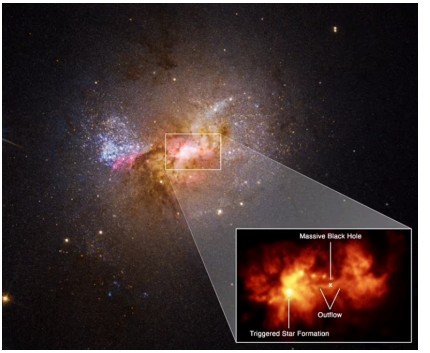

Figure 1.15: H_α map showing evidence of SF being triggered by an AGN jet in a dwarf galaxy. Credit: [12].

systematic suppression of SFR could be detected with respect to the non-AGN galaxy reference sample, and no specific trend of SFR with AGN luminosity has been found. Similarly, in a previous study, [106] considered a large galaxy sample of AGN host galaxies and by applying uniform techniques across the sample, found that average SFRs are independent of AGN luminosity. The lack of detection of any correlation between AGN luminosity and SFR, suggests that the AGN phase and SFR occur on different timescale. If AGN phase is short, there would be not enough time passed to see the impact on the global SFR when selecting AGN samples. This was already pointed out by [107], who showed that luminous AGNs are preferentially found in gas-rich SF galaxies, i.e. there is no direct causal link between instant MBH accretion and galaxy growth. More recently, also [108] emphasised that the observed influence of AGN feedback on SF is weak, i.e. they found no obvious galaxy wide signature of AGN feedback in the MANGA survey. They argue that the integrated AGN accretion is required for AGN feedback to suppress SF. To summarize, observations support the idea that instantaneous AGN activity and corresponding outflows do not necessarily translate into instantaneous quenching.

What do simulations teach us? The scenario emerging from observations suggests that luminous AGNs are preferentially found in gas-rich star forming galaxies, which is apparently in tension with the negative feedback scenario required by simulations. Indeed, from a numerical perspective, most galaxy formation models require some form of negative AGN feedback to eject existing ISM gas from massive galaxies and/or prevent CGM gas from cooling and accreting

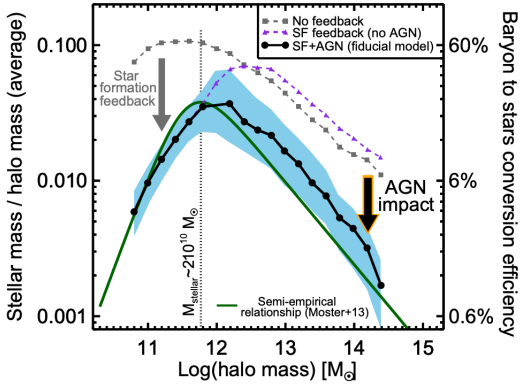

Figure 1.16: The ratio of stellar mass to halo mass as a function of halo mass for three different runs of a simulation (Sommerville & Hopkins 2008) and for the semi-empirical relationship (Moster & Naab, 2013). Credit: [7] The impact of including star formation feedback is to reduce the efficiency of converting baryons into stars in low mass haloes. For massive haloes, energy injection from AGN is required in order to reduce these efficiencies.

onto the galaxy, in this way suppressing star formation and quenching massive galaxies (Fig. 1.16). Otherwise, large-scale simulations of galaxy evolution show that the high-mass end of the galaxy stellar mass function is over-predicted [109]. In numerical models, AGN feedback is also crucial in order to properly recover galaxy sizes and central densities, and the observed bimodality in galaxy colours [90, 110, 111]

It is then informative to obtain a prediction on the SFR in AGN host galaxies from a cosmological simulation that requires the suppression of SF during periods of rapid MBH growth to reproduce such observable galaxy properties. For example, in agreement with the observation, the reference model of the EAGLE simulations [112] (that includes AGN feedback in the form of thermal energy injection) shows no evidence for reduced average SF rates with increasing MBH accretion rate. [113, 114] studied the correlation between the AGN activity and SFRs analysing high-resolution simulations of galaxy mergers, focusing on the phases pre-, during and after galaxy merger. They found that the MBH accretion rate does not correlate to the galaxy wide SFR, while it shows some level of correlation with the nuclear (within 100 pc) SFR. Similarly, by analyzing large scale cosmological simulations, [115] found no negative trends between the

AGN luminosity and SFR and that high AGN luminosity and SFR are found in galaxies with high gas fractions of molecular gas. Following the same line of reasoning, [116] studied the dependence of SF quenching on different parameters using a random forest approach, based on EAGLE, Illustris and IllustrisTNG and also galaxy-wide surveys SDSS & CANDELS and found that the MBH mass is the most predictive parameter of central galaxy quenching at all epochs (from cosmic noon to $z = 0$). Conversely, the AGN luminosity has little predictive power over galaxy quenching. That is, the current state of the AGN is not a useful proxy for the cumulative/integrated impact of historic AGN feedback on the galaxy, which is instead traced by MBH mass. In such a scenario, it is the energy released over long periods from AGN which really matters for quenching. Consequently, quiescence may emerge as a long term consequence of AGN heating preventing gas cooling and accretion from the CGM into massive galaxies, ultimately starving the system of fuel needed for further star formation. Instantaneous feedback may still trigger quenching (e.g., [117, 118]), but without long term heating of the CGM, gas cooling will inevitably re-kindle star formation in massive galaxies, removing them from the quenched state.
This discussion highlights that it is not possible to conclude a lack of impact by AGN upon star formation based purely on an empirical result where average SF rates are not reduced for galaxies that host the most instantaneously luminous AGN.

1.2.2 Simple outflow analytical models

Now I briefly discuss the impact of AGN winds on a spherically symmetric gaseous environment by means of simple analytical models. This discussion is based on works by [13, 14, 84, 85, 119, 120]. In these models it is usually assumed a quasi-spherical wind originating from the accretion disc scales, ignoring how this wind is launched in the first place. The wind mass, momentum and energy flux densities at a radius R from the MBH can be expressed as, respectively:

$$\begin{aligned} \dot{m}_{\rm w} &= \rho_{\rm w} v_{\rm w} = \frac{\dot{M}_{\rm w}}{4\pi R b}, \\ \dot{p}_{\rm w} &= \rho v_{\rm w}^2 + \mathcal{P}_{\rm w}, \\ \dot{e}_{\rm w} &= \frac{1}{2}\rho_{\rm w} v_{\rm w}^3 + \left(\frac{\gamma}{\gamma - 1}\right)\mathcal{P}_{\rm w} v_{\rm w}, \end{aligned} \tag{1.54}$$

where γ is the adiabatic index of the wind gas, $b = \Omega/4\pi \leq 1$ is the fractional solid angle and Ω the solid angle covered by the wind. The wind pressure $\mathcal{P}_{\rm w}$ can be expressed in terms of the wind sound speed as $\mathcal{P}_{\rm w} = \gamma^{-1}\rho_{\rm w}c_{\rm w}^2$ and in the supersonic limit ($v_{\rm w} \gg c_{\rm w}$) the terms involving $\mathcal{P}_{\rm w}$ in the equations above are subdominant and can be discarded. Now, by integrating the ram pressure $\rho_{\rm w}v_{\rm w}^2$ and the kinetic luminosity $1/2\rho_{\rm w}v_{\rm w}^3$ over the surface area at R, one obtains the total momentum flux $\dot{P}_{\rm w}$ and kinetic luminosity $\dot{E}_{\rm w}$ of the wind as

$$\begin{aligned} \dot{P}_{\rm w} &= \dot{M}_{\rm w}v_{\rm w}, \\ \dot{E}_{\rm w} &= \frac{1}{2}\dot{M}_{\rm w}v_{\rm w}^2. \end{aligned} \tag{1.55}$$

Then, the total wind momentum flux $\dot{P}_{\rm w}$ can be parameterized in terms of the impinging AGN radiation momentum flux L/c through $\dot{P}_{\rm w} = \tau(L/c)$, and the wind velocity in terms of the speed of light through $v_{\rm w} = \beta c$. Following this parameterization, the total mass, momentum and kinetic energy fluxes of the wind read

$$\dot{M}_{\rm w} = \frac{\tau}{\beta}\frac{L}{c^2}, \tag{1.56}$$

$$\dot{P}_{\rm w} = \tau\frac{L}{c}, \tag{1.57}$$

$$\dot{E}_{\rm w} = \frac{\tau\beta}{2}L. \tag{1.58}$$

The parameters τ, β and b, which allow to determine the properties of the AGN wind from its luminosity, in turn depend on the processes driving the winds and therefore require general-relativistic magneto/radiation-hydrodynamic simulations and observational constraints to be determined. We can compute the conversion efficiency of AGN luminosity into wind kinetic energy as

$$\dot{E}_{\rm w}/L = \frac{\tau\beta}{2} = 0.05\tau\Big(\frac{\beta}{0.1}\Big). \tag{1.59}$$

The further evolution of wind-driven outflows has been discussed in many papers [14, 85, 121, 122, 123] and textbooks [124], in the context of both stellar and AGN feedback. I briefly review some aspects here. Once launched, the AGN wind moves in the ambient medium shovelling the material it encounters along its path, forming a shell expanding at constant velocity $\sim v_{\rm w}$. This phase is referred to as free-expansion and lasts approximately until the swept-up mass

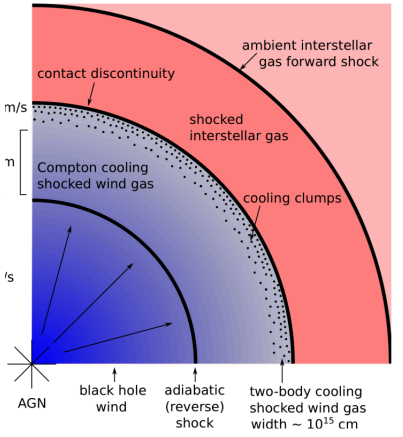

Figure 1.17: A sketch of the wind-driven outflow structure. Credit: [13].

equals the mass of the impinging wind. If the ambient medium has uniform density ρ_0, the free expansion timescale reads

$$t_{\rm free} = \left(\frac{3}{4\pi}\right)^{1/2} \left(\frac{\dot{M}_{\rm w}}{\rho_0 v_{\rm w}^3}\right)^{1/2}. \tag{1.60}$$

When the shell radius reaches a distance $\sim R_{\rm free} \equiv v_{\rm w} t_{\rm free}$, the momentum of the material added to the shell start causing it to slow down significantly and free-streaming brakes down. According to Eq. (1.60) and using (1.56) we can express this scale as

$$R_{\rm free} = 27.4 \left(\frac{\eta(a)}{\eta(0)}\right)^{1/2} \left(\frac{M_\bullet}{10^7 M_\odot}\right)^{1/2} \left(\frac{\mu n}{\rm cm^{-3}}\right)^{-1/2} \left(\frac{v_{\rm w}/c}{10^{-2}}\right)^{-1} {\rm pc}, \tag{1.61}$$

where μ is the gas mean-molecular-weight and n the gas number density. From now on, the incoming wind forms a strong reverse shock against the slowing down shell ($\dot{R}_{\rm sh} \ll v_{\rm w}$) and a significant fraction of the wind kinetic energy is thermalised. In the frame of the shock, the wind travels with the speed $|\dot{R}_{\rm sh} - v_{\rm w}| \sim v_{\rm w}$ and, as a result, the post-shock temperature $T_{\text{R-shock}}$ is given by

$$T_{\text{R-shock}} = \frac{3}{16} \frac{\mu m_{\rm p}}{k_{\rm B}} \left(\dot{R}_{\rm sh} - v_{\rm w}\right)^2 \simeq 1.2 \cdot 10^{10} \left(\frac{\beta}{0.1}\right) {\rm K}, \tag{1.62}$$

where $k_{\rm B}$ is the Boltzmann constant and I have assumed $\mu = 0.6$, i.e. a fully ionised hydrogen and helium plasma of primordial composition. Similarly, a forward shock is formed that propagates in the ambient medium. Under the assumption that such medium is static and that the shock is strong, from the Rankine-Hugoniot jump conditions it follows that the shock advances into the unperturbed ambient medium at velocity $(\gamma+1)/2\dot{R}_{\rm sh} = 4/3\dot{R}_{\rm sh}$. The temperature $T_{\rm F\text{-}shock}$ of the ambient medium after being invested by the forward shock is given by

$$T_{\rm F\text{-}shock} = \frac{1}{3}\frac{\mu m_{\rm p}}{k_{\rm b}}\dot{R}_{\rm sh}^2 \simeq 2.4\cdot 10^7 \left(\frac{\dot{R}_{\rm sh}}{1000{\rm km\ s^{-1}}}\right)^2 {\rm K}. \tag{1.63}$$

We can now distinguish a four-layers structure formed by the AGN wind, the shocked wind, the shocked ambient medium and finally the unperturbed environment (Fig. 1.17). The dynamics of this structured shell, or outflow, has been studied extensively both theoretically [13, 119, 120, 121, 122, 124] and numerically [14, 15]. In a nutshell, the subsequent evolution of the outflow depends on the ability of the shocked wind to preserve its thermal energy, which in turn depends on the cooling processes involved and on the associated timescales (see Fig. 1.18). If the radiative losses in the shocked wind are negligible, it expands adiabatically exerting a 'PdV' work on the overlying shell, i.e. the shocked ambient medium, driving an "energy driven" outflow [69]. On the other hand, if the cooling in the shocked wind is efficient, the gas rapidly loses its thermal energy and shrinks to form a thin layer and the shell of shocked ambient medium is driven only by the ram pressure of the wind [85]. These outflows are referred to as "momentum driven" [85]. In the intermediate situation, when the shocked wind undergoes radiative cooling but in an inefficient manner, the resulting outflow will have characteristics intermediate to the momentum and energy driven cases [120].

I briefly mention that the main cooling process that could make the momentum driven regime possible is the Compton cooling of free electrons in the shocked wind shell against the AGN photons, as discussed in [15, 85, 120, 123, 125, 126]. Following [127], assuming that the AGN radiation field has a nearly obscuration-independent Compton temperature $T_{\rm AGN} = 2\cdot 10^7$ K, the gas Compton heating/cooling rate for gas with temperatures $T < 10^9$ K (non relativistic regime) is

$$\Lambda_{\rm Cpt} = \frac{n_e \sigma_{\rm T} L}{m_e c^2 \pi r^2} k_{\rm B}(T - T_{\rm AGN}), \tag{1.64}$$

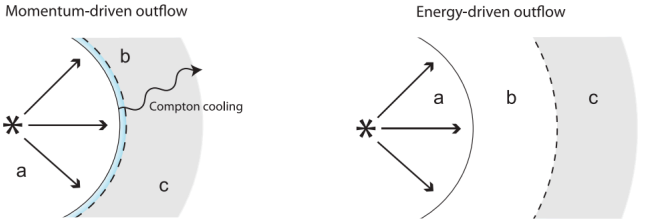

Figure 1.18: A sketch of the outflow propagation in the momentum- and energy-driven regimes. Credit: [14].

where T is the gas temperature, m_e the electron mass, $\sigma_{\rm T}$ the Thompson cross-section, n_e the electron number density (bound + free) and r the distance of the gas element from the AGN.

The evolution of the outflow, in both energy- and momentum-driven regimes, can be studied starting from energy and momentum conservation principles. In the momentum-driven regime, the momentum imparted by wind ram pressure is completely transferred to the thin radiatively cooling shell of shocked wind. This condition automatically yields and equation for the temporal evolution of the contact discontinuity between the shocked wind and shocked ambient medium, which is solved by $R_{\rm sh} \propto (L/\rho_0 c)^{1/4} t^{1/2}$. In the energy driven regime, taking into account the energy exchange within the shocked wind (due to wind injection and work performed on the overlying layer) and the momentum transfer through PdV work from the hot wind to the shocked environment, the solution $R_{\rm sh} \propto (L v_{\rm w}/\rho_0 c)^{1/5} t^{3/5}$ is derived. Starting from these simple solutions, one can compute the AGN luminosity needed so that the shell velocity exceeds the escape velocity of the system hosting the AGN, which, in the first place, can be simply modelled as an isothermal sphere. For such a luminosity all the gas in the host system is ripped off and no further accretion on the MBH takes place. If the AGN is assumed to shine at Eddington luminosity, this condition translates into a relation between the final mass of the MBH and the velocity dispersion of the isothermal sphere, which is proportional to its potential well. By means of this simple argument, [84, 85] showed that it is possible to recover the $M_\bullet - \sigma$ relation, which supports the idea that AGN feedback plays an active role in the establishment of the MBH-galaxy host scaling relations.

1.2.3 AGN feedback numerical models

Due to its relevance, AGN feedback has become an imperative ingredient in modern theories of galaxy formation to reproduce key observables of galaxy populations and it is routinely incorporated both in semi-analytic and hydrodynamical simulation models. In this section, I provide a brief review of the most popular approaches used to model AGN feedback Lagrangian (based on particles or moving-mesh) simulations. I begin noticing that despite their central importance, the physical processes governing AGN feedback and MBH accretion are only poorly understood and the modelling in cosmological hydrodynamic simulations is hence very sketchy, and typically encapsulated in heuristic sub-grid models. Indeed, with a typical mass resolution of $\sim 10^5 - 10^7 \mathrm{M}_\odot$ and spatial resolution of ~ 100 pc, black hole accretion and wind launching cannot be resolved in large scale cosmological simulations (see e.g. [128]), nor even in high resolution "zoom-in" simulations of massive galaxies with mass resolution of $\sim 10^3 \mathrm{M}_\odot$ and spatial resolution of ~ 1 pc (see e.g. [129]), and hence AGN feedback is treated in a simplified phenomenological fashion based on energy injection around accreting MBHs. More specifically, sub-grid feedback models in Lagrangian codes typically fall into two categories: thermal and kinetic energy injection modes. In thermal mode, AGN feedback is performed by injecting thermal energy in the BH neighbour gas particles at a rate proportional to the AGN luminosity [14, 91, 110]. With some modifications, this is the approach followed in most state-of-the-art cosmological simulations [112, 130, 131, 132, 133, 134, 135]. On the other hand, in kinetic mode, energy is injected in kinetic form into a number of cell/particle neighbours [132, 136, 137, 138, 139, 140]. Both these methods have some limitations (see [15], section 5.1, for a detailed discussion). In a nutshell, i) they fail to reproduce the correct AGN wind thermalization scale, provided this can be resolved, ii) they are accompanied by a decrease in the resolution around the accreting black hole, once the neighbour gas particles are driven outwards by the energy injection, and iii) the injection itself is anisotropic as it follows the mass distribution of such neighbours gas particles. Furthermore, in these models, the proportionality factor between AGN luminosity and injected energy is treated as a free parameter, calibrated to ensure that certain observables, such as the $M_\bullet - M_{\mathrm{bulge}}$ relation, are correctly reproduced by the simulation, thereby limiting the predictive power of the simulations with regard to the origin of these observables and the efficiency of the feedback. [15] proposed a novel sub-grid model in which wind mass is explicitly injected along with momentum and en-

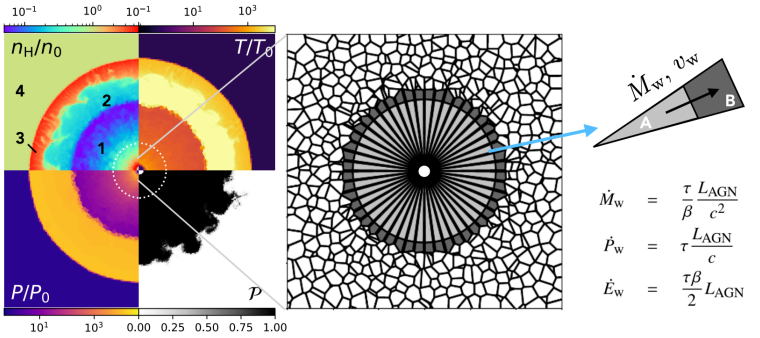

Figure 1.19: A schematic view of [15] "wind injection" technique. (*Left*): The the density, temperature and pressure, in units of the corresponding quantities of the background medium, and the wind tracer concentration. (*Right*): the Voronoi mesh of the ambient medium and of the "wind injection boundary" across which the small-scale wind is injected.

ergy at a fixed spatial scale across a desired solid angle, independently of the configuration of the gas cells surrounding the black hole (see Fig. 1.19). A similar approach is followed by [126], which consists in directly spawning wind particles and in ejecting them outward into the MBH surrounding resolved scales. Both these "wind injection" approaches do not suffer from the limitations mentioned above. Fig. 1.19 shows an example of an outflow resulting from the injection of a wind into a homogeneous density environment.

1.3 Massive Black Holes evolution across cosmic time

In this chapter I discuss the dynamical evolution of MBHs across cosmic time, with particular focus on the formation of dual MBHs in the aftermath of galaxy mergers, their Dynamical Friction (DF) driven inspiral in galactic nuclei, and the formation and evolution of pc scale bound MBH binaries (MBHBs). In doing so, I will discuss to what extent accounting for AGN feedback alters these processes and the efficiencies of MBHs pairing and coalescence.

Central MBHs are found in practically all observed galaxies with a significant bulge [8, 25]. This observational evidence, together with the fact that galactic mergers are a common occurrence [141], rises the interests in studying MBH pairs and binaries, their cosmic evolution and their ability to merge across cosmic epochs.

From an observational point of view, we have evidence of quasar pairs at tens of kpc separation [142, 143, 144, 145, 146, 147, 148, 149], of accreting MBHs with a separation of the order of or less than a kpc [150, 151, 152], and only one observation of a MBH binary with a separation of few pc [153]. In general, observations of bound MBHs when the binary separation is unresolved are elusive and rely on indirect techniques consisting of the observations of Doppler shifts in broad line UV spectra [154, 155] and quasi-periodic variability in the continuum [156], which, for most candidates, can be explained alternatively without invoking MBH binaries.

From a theoretical perspective, the dynamics of MBH pairs in merging galaxies has been first explored in a seminal work by [157], which first entertained the possibility of black hole mergers in galactic nuclei, provided the astrophysical environment yields a way to dissipate their angular momentum in less than a Hubble time. In this journey, MBHs will have to cross an impressive range of scales, from when they are hosted in separate galaxies at early times, to the end of their path, when they coalesce with each other. In their study [158] highlighted the occurrence of three steps that characterize MBHs pairing. In the initial phase, MBH are at kpc scale separation and they both will sink by dynamical friction to the innermost region of the core of the merger remnant losing orbital energy and angular momentum [159, 160, 161], leading to the formation of "paired" black holes in a common bulge. When the mass enclosed by the orbit of these two MBHs is smaller than the sum of their masses, they will form a MBH binary [162]. At this point the MBHs cannot shrink their orbital separation by means of dynamical friction and further loss of angular momentum is promoted

by three-body interactions with single background stars and/or gravitational interaction with a gaseous disc (the so-called "hardening" phase). In the final phase, when the MBHs reach a separation $a_{\rm GW} \sim 10^{-3}(M_{\rm MBHs}/10^6 M_\odot)$ pc, gravitational waves emission becomes the most efficient mechanism driving the binary shrinking and leading to coalescence. Gravitational waves from MBHs are a prime source in the frequency range of the future Laser Interferometer Space Antenna (LISA, [163]).
In the following I review some aspects of the first two phases and I refer the reader to the many existing reviews for a more complete presentation of the topic [160, 164, 165].

1.3.1 Dynamical Friction Regime

At kpc scales, when the MBHs are embedded in the galaxies merger remnant, their loss of angular momentum and consequent inspiral towrds the minimum of the potential well is driven by the interaction with the surrounding stellar and gaseous environment.

1.3.1.1 Interaction with collisionless media

In brief, stellar DF operates as follows: given an object of mass $M_\bullet$ moving in a medium of collisionless particles of mass $m_\star \ll M_\bullet$, it modifies their motion and deflects them leading to the formation of a trailing overdensity, referred to as "wake", which is dragged behind the moving massive object. The gravitational interaction between the wake and the moving object acts as a drag force that decelerates it. Such drag force is the so-called Dynamical Friction. [166] first calculated this force under idealised assumptions. Given a MBH of mass $M_\bullet$ and velocity $\mathbf{v}$ relative to the surrounding background of stars, the DF force experienced by the MBH assuming i) stellar homogeneous density $\rho_\star$, ii) stellar isotropic velocity distribution and velocity dispersion σ and iii) by accounting only the contribution from stars moving slower than the MBH, reads

$$\mathbf{F}_{\rm DF} \propto -M_\bullet^2 \rho_\star \mathcal{G}\left(\frac{v}{\sigma}\right) \ln\Lambda \frac{\mathbf{v}}{v^3}, \tag{1.65}$$

where $\ln\Lambda \sim 10$ is the Coulomb logarithm and the function $\mathcal{G}(x)$ depends on the stars velocity distribution. For a Maxwellian distribution $\mathcal{G}(x) \sim x^3$ for $x \ll 1$ and ~ 1 for $x \gtrsim 2$. A first rough estimate of the role played by DF in the process of MBHs pairing can be made by considering a MBH in a circular orbit at a

radius r in a stellar halo and by computing the orbital decay timescale as given by Eq. (1.65). Modelling the stellar background with an isothermal profile ($\rho_\star \propto \sigma^2 r^{-2}$) it can be shown [167] that the timescale required by the MBH to sink to the centre is

$$\tau_{\rm DF} \simeq \frac{8{\rm Gyr}}{\ln\Lambda}\left(\frac{r}{\rm kpc}\right)^2 \frac{\sigma}{200{\rm km/s}}\frac{10^7{\rm M}_\odot}{M_\bullet}, \tag{1.66}$$

which, being shorter than the Hubble time, reveals how stellar DF is an essential factor in promoting MBH binary formation after galaxy mergers. Note also that in the early stage of a galaxy merger, $M_\bullet$ may be replaced by the mass of a residual galactic core embedding the MBHs, resulting in much shorter timescales [62].
This calculation subtends many assumptions, which, if relaxed, can notably enrich this simplified picture and significantly widen the range of binary shrinking timescale as driven by DF:

- In the approach sketched above the DF is a local phenomenon and the contribution from global torques is neglected. Global torques may arise from global asymmetries in the host system triggered by the presence of the perturber [168] and can affect the MBH pairs orbital decay.

- In the above calculation (Eq.1.66) we assumed that the density profile is isothermal, which may not be the case for real galaxies, where in general the profile tends to be shallower. For example, if we only consider dark matter, its density profile is usually modelled with a Navarro-Frenk-and-White (NFW) profile, and for dwarf galaxies this may be even shallower due to baryonic feedback. In general, a more cored profile tends to slow down the orbital decay due to DF and thus the paring of MBHs after galaxy merger, to the point of preventing it altogether by stalling MBH orbits at tens of pc separation in the aftermath of equal mass dwarf galaxy mergers (see. e.g. [169]), which can be a problem as these are the galaxies expected to host the MBH binaries to which LISA will be mostly sensitive to.

- If the mass ratio between the two MBHs is small, then DF remains the main mechanism of shrinking separation even once the BHs are bound and form a binary. In this case the wake formed by the secondary is different from the case considered by [166], and there is also the formation of an

overdensity of stars leading the MBH, which tends to mitigate the overall DF force, delaying the decay.

- Bars are common features of galaxies and constitute a significant non-axisymmetric perturbation to the host potential, which can have an important effect on MBH pairs dynamics. [170] has recently shown that if a bar is present in host of a MBH pair, than it is likely to dominate the torque on the MBHs (compared to the local DF) and it can produce a wide range of decay timescales, both suppressing and enhancing the formation of a binary.

- A MBH moving in a clumpy medium where clumps masses are comparable to the MBH mass undergo a stochastic orbital decay, in which both enhancement and suppression of the pairing can occur [164]. This is likely to be relevant for high redshift galaxies where giant gas molecular clouds tend to be more massive (in the range of $\sim 10^7 \mathrm{M}_\odot - 10^8 \mathrm{M}_\odot$) and hence more capable to disturb MBHs orbits.

1.3.1.2 Interaction with gas

In the case where a galaxy is gas-rich, as is frequently the case at higher redshift [171], the gas too has an influence on MBH dynamics and participates in the dynamical friction process. Similarly to what happens when a MBH moves in a collisionless particles medium, a moving massive MBH in a gaseous medium perturbs its surroundings, leading to the formation of a trailing density wake, whose gravitational interaction with the MBH itself acts as a DF. [172] first carried out this computation assuming a homogeneous gas density background $\rho_{\rm gas}$ and found that

$$\mathbf{F}_{\rm DF,gas} \propto -M_\bullet^2 \rho_{\rm gas} \mathcal{G}_{\rm gas}\left(\frac{v}{c_{\rm s}}\right) \ln\Lambda \frac{\mathbf{v}}{v^3}, \tag{1.67}$$

where $c_{\rm s}$ is the sound speed and $\mathcal{G}_{\rm gas}(\mathcal{M}) \to 1$ for $\mathcal{M} \gg 1$ and $\sim \mathcal{M}^3$ for $\mathcal{M} \to 0$. It was shown by [172] that, if $\rho_{\rm gas} = \rho_\star$ and $c_{\rm s} = \sigma$, then, in the supersonic (subsonic) regime, the gaseous DF is stronger (weaker) than the stellar one. The relative role of gaseous and stellar dynamical friction has been tackled in numerical simulations too.
[173] and [174] studied the binary formation driven by DF that results from the merger of two equal mass spiral galaxies. In both of these studies the gas

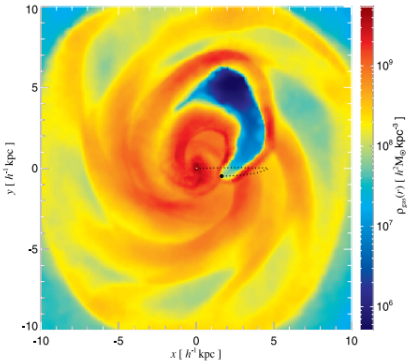

Figure 1.20: This image, taken from one of the [16] simulations, shows the effect of feedback from a recoiling MBH on the host galaxy. The formation of a low density bubble and its relative position to the MBH generate an anti-DF that causes the MBH to orbit in the opposite direction to the gas.

contribution appears to dominate over the stellar contribution to DF. However, this result can be attributed to the absence of AGN feedback in their simulations, which can cause excessive gas accumulation in the remnant center. In contrast, [162] found that orbital decay is driven primarily by stellar instead of gaseous dynamical friction, a result confirmed more recently by [175]. Notably, both papers included AGN feedback[6].

Effect of feedback Once AGN feedback is taken into account, the effect of gaseous DF on the MBH changes since feedback can heat and sweep away gas, altering its distribution around the MBH and consequently its dynamical effect on it. In a first study, considering Radiation Hydrodynamic simulations of an AGN moving in a uniform gaseous background, [176] showed that radiative feedback can lower the gas density partially destroying the density wake and promotes the formation of dense shell of gas in front of the MBH. These effects combined result in an acceleration of the MBH in it direction of motion, i.e. an anti-DF. Evidences of a sign reversal of the DF torque exerted by a rotating gaseous background affected by MBH feedback have been discussed on galactic scales by [16] (see e.g. Fig. 1.20). In particular, the authors found that recoiling MBHs on

[6]Besides that, in [162] the merger is between unequal mass galaxies, which compared to an equal mass merger involves less funneling of gas due to shocks and gravitational torques in the remnant nuclear region.

initially radial orbits tend to circularize corotating with the gaseous disc, and experience a fast orbital decay, when AGN feedback is not included, while settle on counter-rotating orbits, resulting long orbital decay timescales, when accretion-powered feedback is included. This early claim has been numerically confirmed in the contexts of MBH pair dynamics in galactic-scale simulations that involve mergers of gas rich disc galaxies ([175, 177]) and on circum-nuclear-disc (CND) scales [178], where the pairing efficiency of the MBH is significantly reduced by the AGN feedback and some small acceleration in the direction opposite to that of the standard DF is measured.

1.3.2 Hardening phase

When dynamical friction succeeds in bringing the separation of the MBHs at about pc scale, the two objects get bound and form a MBH binary (MBHB) and the subsequent shrinkage is known as binary hardening. As for the DF phase, both the interaction of the binary with gas and with stars can contribute to the hardening process. While many studies have focused on these mechanisms separately, only a few have considered them simultaneously [179, 180]. Below I briefly present both.

1.3.2.1 Stellar Hardening

When MBHs form a binary DF friction is no longer effective and shrinking in a stellar environment occurs through 3-body interactions with single stars, which remove energy and angular momentum from the binary. More generally, when there is a 3-body interaction between a binary and a third object approaching the two bound objects, several outcomes are possible: i) the third object performs a fly-by (single passage), or remains temporarily bound in a meta-stable triple system, and subsequently it is ejected with more or less energy than when it approached the binary; ii) it replaces one of the elements in the binary which instead gets ejected; iii) the system is ionised, i.e. the binary is unbound by the interaction with the third object. Under the assumption of a hard binary, i.e. that[7]

$$a \leq a_{\rm h} \equiv \frac{G\mu}{4\sigma^2}, \tag{1.68}$$

[7]In other words the binary becomes hard once its binding energy is larger than the average kinetic energy of the surrounding stars.

where a is the binary semi-major axis, μ is the binary reduced mass and σ the local stellar velocity dispersion, and assuming that the third object has a mass much smaller than the binary objects, as in the case of stars interacting with a MBHB, it has been shown that repeated encounters with surrounding stars make the binary shrink at a rate

$$\frac{d}{dt}\frac{1}{a} = \frac{G\rho_\star}{\sigma}H, \tag{1.69}$$

where $H \simeq 15-20$ is numerical coefficient weakly dependent on the properties of the binary [181]. As Eq. (1.69) shows, when σ and $\rho_\star$ are constant, binary hardening proceeds at a constant rate. However, as the binary becomes more bound and the stars with which it has interacted are ejected, $\rho_\star$ decreases, and with it the rate of shrinking. In other words, the loss cone, i.e. the region of phase-space containing stars with angular momentum low enough to interact with the binary, is depleted. This happens in the initial phase of hardening, in a time of the order of the orbital period of the stars. The effectiveness of hardening therefore depends on the possibility of repopulating the loss cone. As shown by [158] in their seminal paper, under the assumption of spherical symmetry, loss cone refilling can only occur through two-body relaxation, which takes longer than the Hubble time. Therefore, in the absence of other loss cone refilling mechanisms, the binary stalls at pc scale separation, an issue that led to the the expression *final parsec problem*. A number of solutions have been suggested in recent decades, and today the last parsec problem is no longer considered a problem. For example, by relaxing the assumption of spherical symmetry, as expected in real galaxy merger remnants, and by assuming a triaxial stellar bulge, it has been shown that the loss cone can be repopulated more rapidly, in less than one Hubble time [62]. In addition to this, it was shown that the rotation of the nuclear region of the galaxy (in the prograde direction with respect to the binary) can also facilitate the stellar hardening process, by promoting a more efficient extraction of energy from the binary.

1.3.2.2 Gaseous hardening

I now turn the attention to the evolution of MBHBs embedded in a gas-dominated galactic nucleus. After a merger between galaxies, the gas is funnelled into the nuclear region of the merger remnant by gravitational torques and is likely to retain an amount of angular momentum larger than that corresponding to the

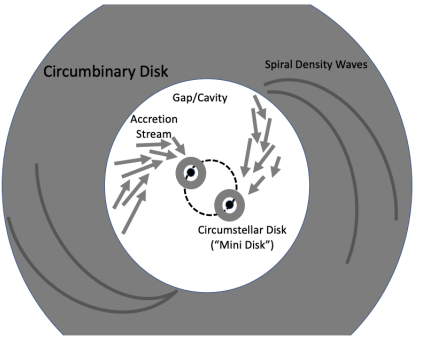

Figure 1.21: An illustration of the basic features of circumbinary accretion. Credit: Ryan Miranda (2017).

ISCO of the MBHs, and thus forms a disc around the binary: the so-called circum-binary disc (CBD). CBDs have been posited to be a gas-dynamical solution to the final parsec problem. This shrinking channel is likely to be effective in high-redshift gas-rich galaxies, where the existence of nuclear gaseous discs is supported by both theory [173, 182, 183] and observations [184, 185]. For example, in [173] two merging galaxies (each containing a MBH), initially separated at ~ 100 kpc, collide with each other, and eventually end up with two MBHs separated by ~ 10 pc and surrounded by an extended (~ 100 pc) disc/torus at the center of the merged galaxy. In the following I discuss some aspects of MBHB dynamical evolution in CBDs.

Circumbinary discs Figure 1.21 illustrates the basic features of a CBD: gas from large distances looses angular momentum due to viscous dissipation and spirals toward the binary; a central cavity might be present, with radius of few binary separations, cleared by the binary tidal torque; gas from the the edge of the cavity can spiral inward forming accretion streams that reach the MBHs and form "mini-discs", which buffer the accretion on individual MBHs.
Given the importance of CBDs, many numerical studies have been carried out to investigate the evolution of these systems and the role they play in the hardening of the binary and the growth of MBHs. These studies have been conducted using both SPH simulations [18, 186, 187] and Eulerian codes [188]. In recent years, several finite-volume moving mesh codes have been used to study circumbinary accretion, such as DISCO [189, 190], and mesh-free hybrid codes, such as GIZMO [191]. Most of the simulations deal with viscosity in an idealised parameterized

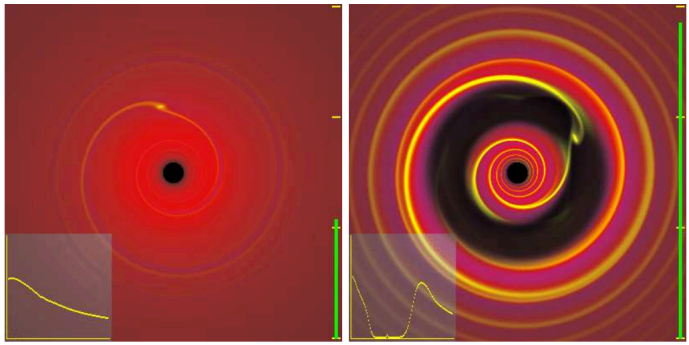

Figure 1.22: Illustration of type I (*left*) and type II (*right*) migration regimes. Credit: [17].

manner, while few resolve the MHD on the fly [192].
In the following I discuss how binary migration, as driven by the presence of a CBD, depends on the binary and CBD properties, in particular, on the binary mass ratio q and the CBD - secondary MBH mass ratio. I denote the binary mass with $M_{\rm bin}$, MBH masses and separation with M_1, M_2 and $a_{\rm bin}$, and the local measure of the CBD mass with $M(r) = 4\pi\Sigma(r)r^2$, where Σ is the CBD surface density.

- $M_2 \ll M(a_{\rm bin}) \ll M_1$
  This regime is typical of protoplanetary discs, and can be seen as the secondary perturbing the accretion disc of the primary object. This problem then is usually tackled with a linear perturbation theory approach. In this framework the gravitational potential of the secondary is decomposed in Fourier modes and each mode is treated as a linear perturbation separately. Angular momentum exchange can be expressed as the sum of torques exerted at discrete resonant locations within the disc. These resonances correspond to the locations within the disc at which the perturbation excites waves. What emerges from this analysis is that

  – interaction with gas exterior to the orbit increases the angular momentum of gas and decreases that of the perturber, i.e. the secondary migrates inward and gas is repelled from it;

  – interaction with gas interior to the orbit decreases angular momentum of gas and increases that of the perturber, i.e. the secondary migrates outward and gas is repelled from the secondary.

This can be understood also as the perturber interacting with an outer trailing density wave and with a leading inner density wake. The net effect is a negative torque on the perturber $T \propto -M_2^2 a_{\rm bin}\Sigma$, corresponding to a migration timescale $t_{\rm mig} \propto 1/M_2$. The type of migration outlined so-far it is usually referred to as "type I" migration, in the planetary community. In this regime the perturber mass is assumed to be low enough to leave the disc structure almost unperturbed. The secondary remains fully embedded within the disc and material to exchange torque with is present at all resonant locations.

For sufficiently large perturber masses this approximation breaks. As the perturber becomes more massive, the torque increases and starts to modify the disc structure and an annular gap within which Σ is reduced is opened in the disc. Resonances close to the perturbed are severely depleted of material and contribute little or nothing to the total torque

The treshold for this regime to occur, i.e. for a gap to be opened, can be computed by comparing the timescale of angular momentum transfer from the perturber to the disc with the timescale for the viscous loss of angular momentum. The gap opening regime is usually referred to as "type II" migration. In this regime the secondary behaves like a fluid element in the disc, evolving at viscous rate $t_{\rm min} = t_\nu(a_{\rm bin}) \sim a_{\rm bin}^2/\nu$, i.e. binary hardens on a timescale comparable to the viscous time-scale. The morphology of the disc in the type I and type II migration regimes is depicted in Fig. 1.22.

- $M_2 \gtrsim M(a_{\rm bin}) \ll M_1$
  When $q \ll 1$, but the secondary mass becomes of the order or grater then the local disc mass (whether you consider a more massive perturber or place it at a larger separation from the primary), the disc cannot efficiently redistribute the angular momentum acquired from the binary, and the shrinking rate decreases compared to the type II regime. This regime is sometimes referred to as type II migration "in the secondary-dominated limit". If the angular momentum of the perturber is f times larger than that of the disc, then it will take approximately $\sim f$ viscous times to exchange that angular momentum and migrate inward. The proper shrinking rate in this regime has been computed by [193, 194], and can be expressed

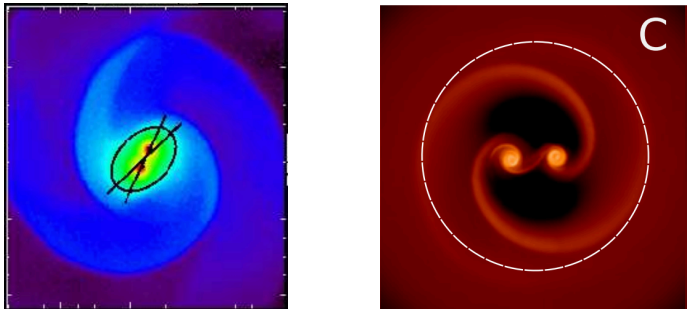

Figure 1.23: Illustration of the "no-cavity" (*left*) and "cavity" (*right*) migration regimes. In the first case the binary remains embedded in the disc and induces an ellipsoid-shaped density perturbation in the gas. In the second, the binary tidal torque clears a central cavity and induces spiral density perturbations in the disc. Credit: [18, 19].

as

$$t_{\rm mig} = \frac{M_2 + M(a_{\rm bin})}{M(a_{\rm bin})} t_\nu(a_{\rm bin}). \tag{1.70}$$

As noted by [195] or [194] this regime can occur at such a separation where the disc is self-gravitating.

- $M_1 \lesssim M_2$
  When the secondary mass becomes comparable to that of the primary, the migration timescale strongly depends on the ability of the binary to clear a central cavity in the disc (as the one shown in Fig. 1.21). [19, 196] investigated this problem and devised a cavity opening criterion for comparable mass binaries embedded in CBDs. The underlying idea is the same for gap opening in the limit $q \ll 1$. The binary induces a density non-axisymmetric perturbation in the disc, which has a shape of an ellipsoid (if $M_{\rm bin} \lesssim M(a_{\rm bin})$) or of a two arms spiral (if $M_{\rm bin} \gtrsim M(a_{\rm bin})$), and the tidal interaction between the binary and such perturbations acts as a positive torque on the gas, with the tendency of pushing it away from the binary and clearing a central cavity. The gas also experiences a negative viscous torque that makes it loose angular momentum and approach the binary. The critical binary mass for cavity opening is found by equating the timescale for cavity opening caused by the tidal interaction of the binary on the disc, and the timescale for cavity closing, caused by the viscous torque acting on the gas. This computation yields the following criterion

for cavity opening [19, 196]:

$$\frac{\Delta t_{\rm open}}{\Delta t_{\rm close}} = \frac{1}{f_q}\left(\frac{v_{\rm gas}}{v_{\rm bin}}\right)^2\left(\frac{c_{\rm s}}{v_{\rm gas}}\right)\left(\frac{H}{a_{\rm bin}}\right) \leq 1, \tag{1.71}$$

where f_q is a factor which depends on the disc viscosity and on the geometry of the density perturbation and its value increases with decreasing q, $v_{\rm gas}$ is the gas velocity, $c_{\rm s}$ its sound speed, $v_{\rm bin}$ the MBHs velocity, H the disc thickness and all quantities are evaluated at $a_{\rm bin}/2$. So, similarly to what discussed in the case of small mass ratios, hot and thick discs hosting low mass MBHs at small separations make the binary remain embedded in the disc, whereas cavity formation is fostered in the opposite region of parameter space (see Fig. 1.23). These two opposite regimes correspond to different binary migration timescales, which can be referred to as the analogs of type I and type II migration for comparable mass binaries. If a cavity is present (and $M_2 \gg M(a_{\rm bin})$), the binary attains a slow migration regime, and the migration timescale can be estimated as [197]:

$$t_{\rm mig} = \frac{M_1 M_2}{M_{\rm bin} M(a_{\rm bin})} t_\nu(a_{\rm bin}). \tag{1.72}$$

Conversely, if $M(a_{\rm bin}) \gtrsim M_{\rm bin}$ and the binary remains embedded in the disc, the tidal interaction with the off-axis ellipsoid density perturbation induced in the disc makes the binary migrate within few orbital times, i.e. the binary attains a fast migration regime e.g. [18, 198, 199].

The migration rates sketched above can be severely altered once other physical phenomena, e.g. AGN feedback, are taken into account, which makes numerical simulations a fundamental tool to reliably asses the shrinking timescales of MBH binaries in CBDs.

AGN feedback Regardless of the dominant hardening mechanism, the presence of AGN feedback can influence its effectiveness, just as it does for the DF inspiral phase. The effect of feedback in the hardening regime is largely unexplored and is limited to the case of pc scale separated binaries [199]. In a recent study, [199] considered different setups of binaries in CBDs, both in the regime where a cavity is present and in its absence. When the binary opens a cavity, shrinking takes place over a long time scale (slow migration regime) and little

gas accretes on the MBHs. Consequently, AGN winds carry little mass and due to the presence of the cavity they have little impact on the CBD. On the other hand, if the cavity is absent and the MBHs are embedded in the CBD, i.e. the fast migration regime, then the MBHs accretion is enhanced and AGN feedback efficiently expels the gas surrounding the binary, thus forming a "feedback cavity". Consequently, due to the lack of gas with which to exchange torque, the gaseous hardening is suppressed and the binary stalls. This shows that AGN feedback, in the regime where hardening is driven by a CBD, can have a crucial effect on the evolution of the binary. In the case of binaries that shrink due to stellar hardening, the effect of AGN feedback has not been explicitly studied but I can speculate that this may have a limited effect on existing stars, but may suppress the formation of new stars. Therefore, if binary evolution is slower than star formation, this can prevent loss con refill due to the formation of new stars and potentially it can slow down binary migration.

Chapter 2

Radiative feedback anisotropy and the MBH spin

In this chapter I present a novel implementation for AGN feedback through ultra-fast winds in the code GIZMO. This feedback recipe accounts for the angular dependence of radiative feedback upon black hole spin. Indeed, the MBH spin is an important parameter to be considered when modeling AGN feedback, and more generally MBH evolution, owing to the complex non-linear influence spin and feedback have on each other. In fact, on one hand the spin modulates radiative efficiency of AGN discs (Eq. 1.19), which influences the MBH accretion and the amount of energy released in radiation, and, for thick radiatively inefficient discs, it regulates the kinetic power and direction of jets [56]. On the other hand, feedback strongly impacts the MBH spin growth as it affects the gas reservoir that fuels MBH accretion which, together with MBH mergers, is the main channel for spin evolution [200] (see § 1.1.4.6). In addition to its relevance in the context of AGN feedback, the spin has a strong influence on the gravitational wave emission of merging BHs [201], and thus also on the expected recoil velocity of the merger remnant [202], which make the spin a fundamental parameter to be considered when we aim at understanding the cosmic evolution of MBHs. Due to its importance, some recent works started to include spin evolution in hydrodynamical simulations [3, 203, 204, 205] and semi-analytical models of galaxy formation [206, 207, 208, 209]. These studies, together with observations [210], have shown that the distribution of MBH spins depends on several quantities, such as host galaxy morphology, MBH mass, and redshift.
Recently, [211] first discussed the influence that the MBH spin has in shaping

the angular pattern of the AGN radiation, showing that more rapidly spinning black holes result in more isotropic radiation patterns, as the geodesics of photons emitted in inner region of the disc undergo a stronger gravitational bending. [212] and [213] first discussed the relevance of this effect in the context of radiation pressure-driven outflows in isolated spherical galaxies, by means of semi-analytic models. They showed that AGNs with rapidly spinning MBHs launch quasi-spherical outflows propagating on large scale at all inclination angles, opposite to MBHs with low spin values that produce weaker bipolar outflows driven in the polar direction. As a consequence, [213] argued that AGNs with slowly spinning MBHs should be accompanied by higher obscuration levels and higher accretion rates, being the AGN radiation less prone to remove gas from the disc equatorial plane. Numerical simulations also suggest that the AGN anisotropic radiation can have a dramatic effect on the outflow properties [214] and MBH pair dynamics [215] (see § 3), but in these studies the anisotropy factor remains unconstrained and simply left as a free parameter.
In this chapter, I present a new implementation of AGN radiative feedback in the code GIZMO [216] that takes into account the spin-dependence of feedback anisotropy. In this model, accretion from resolved scales onto an unresolved (sub-grid) AGN disc, spin evolution, the injection of AGN winds into resolved scales and their spin-induced anisotropy, are all self-consistently evolved. This implementation builds upon existing modules for MBH accretion and spin evolution [204] and AGN wind [126]. Equipped with this model, I investigate the role of AGN wind anisotropy in shaping AGN-driven outflows and the evolution of isolated disc galaxies hosting active MBHs. This chapter is organized as follows: in section § 2.1 I review the spin-dependence of AGN radiation angular pattern and I connect it to the anisotropy of AGN winds. The implementation of this effect in GIZMO is presented in section § 3.1, and section § 2.3 shows some tests of this model. I discuss an application of it in the context of isolated disc galaxies in section § 2.4, and I draw my conclusions in section § 2.5.

2.1 Theoretical Background

In this section, I review how the MBH spin influences the angular patter of the emitted radiation and I show how this reflects on the properties of AGN radiation-driven winds. Then, I discuss two analytic solutions of outflows driven by such anisotropic winds.

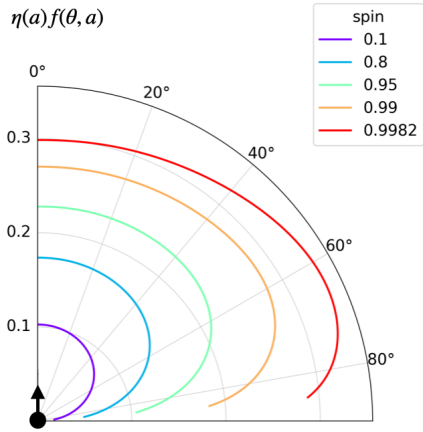

Figure 2.1: The luminosity angular pattern $\eta(a)f(\theta;a)$ for different spin values.

2.1.1 Radiation angular pattern from accretion discs

Recently, [211] and [213] pointed out that the BH spin not only influences the amount of energy released in radiation during the accretion process (Eqs. 1.19, 1.20) i.e., the disc luminosity, but also the angular pattern of such radiation. This is a consequence of the spin-dependence of the location of the ISCO (Eq. 1.7) and of the relativistic gravitational bending of photons being more effective closer to the BH, i.e., in a stronger gravitational field. Indeed, in the Newtonian case, with straight-lines photon geodesics, the luminosity angular distribution follows a simple cosine-like pattern, with the maximum luminosity observed when the disc is face-on and the minimum in the side-on configuration. If we take into account photon geodesics in full GR, due to the gravitational bending more radiation is capable to reach to observer's eye in the side-on configuration, and this occurs in a way that is sensitive to the BH spin. In particular, for larger BH spin values, the ISCO is located nearer to the BH and therefore the photons emitted by the inner annuli of the disc (the ones that dominate the disc luminosity) experience a stronger gravitational bending, funneling more radiation in the side-on direction, yielding a more isotropic radiation angular pattern.

[211] and [213] computed the precise emission pattern numerically by means of the KERRBB model implemented in XSPEC [217]. In addition, [211] proposed

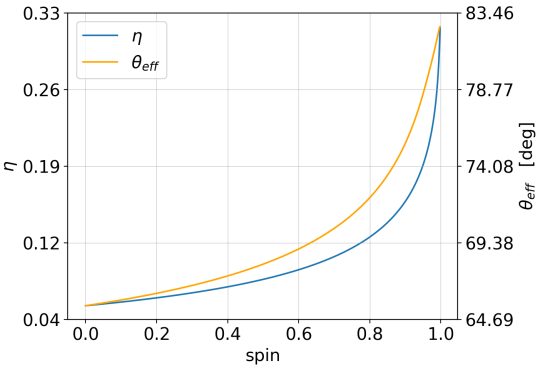

Figure 2.2: The radiative efficiency (left y-axis) and the effective radiation semi-opening angle (right y-axis) as a function of the spin parameter a.

a normalized fitting function $f(\theta;a)$ describing the luminosity angular pattern for different viewing angles θ and spin parameter a, so that

$$L(\theta;a) = f(\theta;a)L \tag{2.1}$$

is the luminosity measured by an observer whose line-of-sight forms an angle θ with the spin direction. With the above definition, the optically thick emission from a non-relativistic disc (i.e., when any light bending is neglected) would be described by $f(\theta,a) = f(\theta) = 2\cos\theta$. The term $f(\theta,a)\eta(a)$, in the relativistic case, is shown in Fig. 2.1.

In order to quantify the degree of anisotropy as a function of the BH spin, I define an *effective semi-opening angle* $\theta_{\rm eff}(a)$, as the truncation angle of the corresponding isotropic emission such that its angle-integrated output equals that of the actual angle-dependent emission. In Fig. 2.2 I show $\theta_{\rm eff}(a)$ together with $\eta(a)$. From this figure we see that we have a smaller $\theta_{\rm eff}$, i.e, a more collimated and anisotropic angular pattern, for low spin values, whereas the radiation distribution is more isotropic (larger $\theta_{\rm eff} \simeq 90^\circ$) for high spin values. Similarly, from Fig. 2.1 we see that in spin close to zero, the radiative flux is vertically focused along the spin axis and it decreases with increasing θ. On the other hand, the flux reduction for high $\theta \lesssim 90^\circ$ becomes less pronounced for increasing spin values, i.e., the flux collimation decreases moving towards a nearly isotropic radiation pattern.

As [212] and [213] pointed out, if the radiation from the accretion disc couples to

the surrounding material by exerting radiation pressure on dust or by launching line-driven AGN winds, then the emerging outflow inherits the anisotropy of the impinging radiation, which, in turn, it is shaped by the BH spin. This outflow spin-dependent anisotropy can affect the outflow ability to couple with the ISM and hence it may change the impact that AGN feedback has on the host galaxy and on the MBH growth. In this way, the MBH spin, through its influence on AGN feedback, can possibly play a role in the MBH-galaxy host co-evolution (see § 1.2).

2.1.2 AGN anisotropic winds

As discussed in § 1.2.2 (see Eq. 1.57), the total momentum carried by an AGN wind can be written as

$$\dot{P}_{\rm w} = \tau \frac{L}{c}. \tag{2.2}$$

Using Eq. (2.1) and by writing the momentum loading as $\dot{P}_{\rm w} \equiv \int \dot{p}_{\rm w}(\theta) r^2 \, d\Omega$, where $\dot{p}_{\rm w}(\theta)$ is the wind momentum flux in the direction θ at a distance r from the AGN, Eq. (2.2) yields

$$\dot{p}_{\rm w}(\theta; a) = \tau \frac{L}{c} \frac{f(\theta; a)}{4\pi r^2}. \tag{2.3}$$

That is, the momentum flux of the wind follows the same angular pattern of the radiation. Assuming that the wind is launched at a constant velocity $v_{\rm w}$, then the mass flux in the direction θ is simply $\dot{m}_{\rm w}(\theta; a) = \dot{p}_{\rm w}(\theta; a)/v_{\rm w}$, and hence the mass flux angular distribution of the wind follows the same angular pattern as well. By combining Equations (1.18) and (2.2) instead I obtain the total mass loading:

$$\dot{M}_{\rm w} \equiv \frac{\dot{P}_{\rm w}}{v_{\rm w}} = \eta_{\rm w} \dot{M}_{\rm acc}. \tag{2.4}$$

where I have defined the mass loading factor

$$\eta_{\rm w} = \eta(a) \tau \frac{c}{v_{\rm w}}. \tag{2.5}$$

I derive now the analytic solution for the propagation in an homogeneous medium of an outflow driven by an anisotropic wind, both in the energy- and momentum-driven scenarios (see the § 1.2.2 for a general overview in the case of isotropic winds). I characterize the evolution of the outflow by calculating the location $R(\theta, t)$ of the contact discontinuity that separates the shocked wind from the

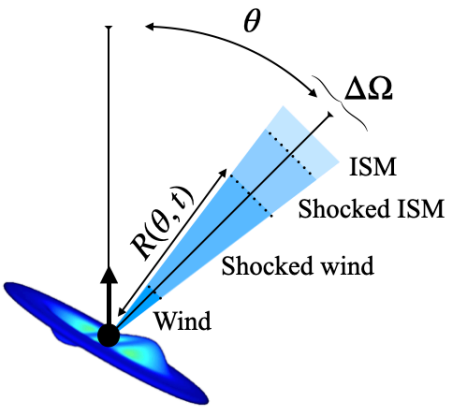

Figure 2.3: Schematic view of the outflow structure in a slice subtended by a solid angle $\Delta\Omega$ and centered in a direction forming an angle θ with the MBH spin. This stratified structure comprises the AGN wind, the shocked wind (which extends up to a distance $R(\theta,t)$ from the MBH), the shocked ISM, and the unperturbed ISM. The illustration also shows the warped accretion disc that feeds the spinning MBH.

shocked ambient medium (see Fig. 2.3). In the energy driven regime, the shocked wind shell is hot and thick and its thermal energy evolution is due to the energy injected by the wind (suddenly converted in thermal energy) and the work done on the above shocked ambient medium. Using Equations (1.18) and (2.4), we have that the thermal energy is added to the shock wind layer at a rate $1/2\dot{M}_{\rm w}v_{\rm w}^2 = 1/2\tau(v_{\rm w}/c)L \equiv \epsilon L$, where $\epsilon = (1/2)\tau v_{\rm w}/c$. Now, if we consider a single slice of the outflow, in the direction θ and subtended by a solid angle $\Delta\Omega$, as in Fig. 2.3, then the impinging disc luminosity in the slice direction is $Lf(\theta,a)\Delta\Omega/4\pi$ (see Eq. 2.1) and a fraction ϵ of it is converted in thermal energy in the shocked wind layer of the slice. Then, if P is the pressure of the shocked wind layer, the pressure force exerted on the layer above can be written as $P\Delta\Omega R^2$ and the PdV work as $P\Delta\Omega R^2 dR$. Assuming that the shocked wind layer is thick enough to neglect the portion of the slice occupied by the freely streaming wind, its volume can be approximated with that of the slice up to R, i.e. $\Delta\Omega R^3/3$, and hence its internal energy with $(3/2)P\Delta\Omega R^3/3$. Then, if ρ_0 the ambient medium density we can write the conservation of the shocked wind energy and the conservation of the shocked ambient medium momentum of the

slice as

$$\frac{d}{dt}\frac{3}{2}\left(\frac{\Delta\Omega}{3}R^3P\right) = \epsilon L f(\theta;a)\frac{\Delta\Omega}{4\pi} - \Delta\Omega R^2\dot{R}P, \tag{2.6}$$

$$\frac{d}{dt}\left(\rho_0\frac{\Delta\Omega}{3}R^3\dot{R}\right) = R^2\Delta\Omega P, \tag{2.7}$$

respectively. By solving Eq. (2.7) for P and replacing in Eq. (2.6) we get

$$10R^2\dot{R}^3 + 8R^3\dot{R}\ddot{R} + \frac{2}{3}R^4\dddot{R} = \frac{v_{\rm w}Lf(\theta;a)}{2c\pi\rho_0}, \tag{2.8}$$

which admits the self-similar solution

$$R_{\rm sh}(\theta,t) = \left(\frac{125}{308\rho_0\pi}\frac{v_{\rm w}}{c}Lf(\theta;a)\right)^{1/5} t^{3/5}. \tag{2.9}$$

Eq. (2.9) describes the evolution of the contact discontinuity in time, for each direction θ, in the energy driven regime.

In momentum-driven outflows, the energy of the shocked wind is quickly dissipated on small scales via radiation losses and the shocked wind shell collapses into a thin layer, as its thermal pressure support is radiated away. Then, the shocked ambient medium layer is driven outward directly by the ram pressure of the impinging AGN wind, which equals the momentum flux of the disc radiation if $\tau = 1$. In this case, we write the momentum conservation of the shocked ambient medium in the slice as

$$\frac{d}{dt}\left(\rho_0\frac{\Delta\Omega R^3}{3}\dot{R}\right) = \frac{Lf(\theta;a)\Delta\Omega}{4\pi c}, \tag{2.10}$$

which is solved by

$$R_{\rm sh}(r,\theta,t) = \left(\frac{3Lf(\theta;a)}{2\pi c\rho_0}\right)^{1/4} t^{1/2}. \tag{2.11}$$

Eq. (2.11) represents the evolution of the contact discontinuity in the momentum driven regime.

2.2 BH accretion and AGN feedback implementation

In order to investigate the role of anisotropic radiative feedback in more realistic scenarios, I implemented the anisotropic spin-dependent AGN wind discussed above in the code GIZMO [216]. GIZMO has been developed from the GADGET3 code, itself a descendant of GADGET2, and presents a new approach to solving hydrodynamics, aimed at capturing the advantages of both Lagrangian codes, such as adaptive resolution, and Eulerian codes, such as shock capturing, while avoiding their limitations. Specifically, in GIZMO the volume is discretized into particles/unstructured cells at which the fluid density is calculated in a kernel-weighted fashion. The properties of the fluid within a particle are then evolved via a Godunov scheme across effective faces among the particles in the target particle kernel. In the mesh-less finite-mass (MFM) method employed in this thesis, the effective faces are defined so that the mass fluxes vanish, i.e. the particles constitute a discretization of the fluid as in Lagrangian codes.
In the AGN model presented here, the MBH mass and spin are evolved in a sub-grid fashion according to the properties of an unresolved accretion disc, which are influenced by the resolved accretion flow on it. Once every timestep the unresolved system parameters are updated, they are used to model the effects of MBH feedback into resolved scales. In § 2.2.2 I present how this is done by means of the wind-spawning technique developed by [126], whose approach is similar to that devised by [15] for AREPO, i.e. the "wind-injection" approach described in § 1.2.3[1]. As AGN wind is ejected, it affects the inflow that in the first place powered it, and it does so in different ways depending on its magnitude and anisotropy. This results in a complex non-linear interplay between MBH fueling, feedback, its anisotropy and the MBH spin, which the sub-grid model presented here is aimed to capture.

2.2.1 Accretion and spin evolution

Here I provide more details about the accretion and spin evolution models. While the methods of unresolved accretion and spin evolution presented below will be the same as those used throughout the rest of this thesis, different approaches will be followed for resolved accretion.

[1] I anticipate that this AGN feedback approach is the same also employed in the simulations presented in § 4, whereas in § 3 a "kinetic energy injection model" will be used

2.2.1.1 Unresolved accretion

In this implementation, which is based on [204, 218] (see also [3]), the MBH particle is meant to represent a structured, sub-resolution system consisting of a MBH surrounded by an unresolved, warped accretion α-disc. The sub-grid accretion disc mass M_α evolves due to i) the accretion $\dot{M}_{\rm in}$ from resolved scales on the sub-grid disc, ii) the ejection of winds $\dot{M}_{\rm w}$, and iii) due to the accretion $\dot{M}_{\rm acc} = f_{\rm Edd}\dot{M}_{\rm Edd}$ within the sub-grid disc on the MBH. Instead, the time evolution of the MBH mass $M_\bullet$ is governed solely by the accretion rate in the disc. The equations that dictate the evolution of sub-grid masses are then:

$$\dot{M}_\bullet = (1-\eta)\dot{M}_{\rm acc}, \tag{2.12}$$

$$\dot{M}_\alpha = \dot{M}_{\rm in} - \dot{M}_{\rm acc} - \dot{M}_{\rm w}. \tag{2.13}$$

Similarly, the MBH angular momentum $\mathbf{J}_\bullet$ evolves due to the accreted angular momentum carried by the unresolved disc at the ISCO, which modifies the spin magnitude but not its direction. In general, $\mathbf{J}_\bullet$ and the sub-grid disc angular momentum $\mathbf{J}_\alpha$ are misaligned, i.e., the α-disc is warped, with the inner region laying in the MBH equatorial plane and the outer part aligned with $\mathbf{J}_\alpha$ [6]. The model then also accounts for the exchange of angular momentum between the MBH and the sub-grid disc due to the Bardeen-Petterson torque $\mathbf{T}_{\rm BP}$, in this way following the MBH spin (counter)alignment consistently with evolution of the sub-grid disc properties. The disc angular momentum evolution $d\mathbf{J}_\alpha/dt$ is set equal and opposite to $d\mathbf{J}_\bullet/dt$, according to angular momentum conservation, plus terms that account for the exchange of angular momentum with the resolved environment through winds $\dot{\mathbf{J}}_{\rm w}$ and inflows $\dot{\mathbf{J}}_{\rm in}$:

$$\frac{d\mathbf{J}_\bullet}{dt} = {\rm sign}\big(\mathbf{J}_\bullet\cdot\mathbf{J}_\alpha\big)\Lambda_{\rm ISCO}\dot{M}_{\rm acc} - \mathbf{T}_{\rm BP}, \tag{2.14}$$

$$\frac{d\mathbf{J}_\alpha}{dt} = -\frac{d\mathbf{J}_\bullet}{dt} + \dot{\mathbf{J}}_{\rm in} - \dot{\mathbf{J}}_{\rm w}. \tag{2.15}$$

Here $\Lambda_{\rm ISCO}$ is the specific angular momentum of the gas at the ISCO and $\mathbf{T}_{\rm BP}$ is modelled as in [3]. The angular momentum carried by the wind is given by

$$\dot{\mathbf{J}}_{\rm w}dt = \mathbf{J}_\alpha\left(1-\left(1-\frac{\dot{M}_{\rm w}dt}{M_\alpha}\right)^{7/5}\right), \tag{2.16}$$

which is computed assuming that the wind arises as ejecta from the outskirt of the disc i.e. $\dot{\mathbf{J}}_{\rm w}dt = \int_{R'}^{R_{\rm out}} \Sigma\sqrt{GM_\bullet R} 2\pi R\, dR$ where the inner integration boundary R' satisfies $\dot{M}_{\rm w}dt = \int_{R'}^{R_{\rm out}} \Sigma 2\pi R\, dR$, with $\Sigma \propto R^{-3/4}$ being the disc surface density and $R_{\rm out}$ the disc external radius, defined as the radius where the disc becomes self-gravitating (see [219]).
The accretion in the disc $\dot{M}_{\rm acc}$ is self-consistently evolved according to the evolution of the sub-grid quantities determined by Eqs. (2.12)-(2.15). In particular, at any given MBH timestep, $f_{\rm Edd}$ is computed as

$$f_{\rm Edd} \simeq 0.76 \left(\frac{\eta}{0.1}\right) \left(\frac{M_\alpha}{10^4 M_\odot}\right)^5 \left(\frac{M_\bullet}{10^6 M_\odot}\right)^{-47/7} \left(\frac{a|\mathbf{J}_\alpha|}{3|\mathbf{J}_\bullet|}\right)^{-25/7}, \qquad (2.17)$$

see [3] for its derivation.
While all sub-grid quantities evolve smoothly in time, instead, the growth of the MBH *particle* mass $M_{\bullet,\rm dyn}$, i.e. the mass used in the computation of the gravitational force, is performed in a discrete fashion by selecting stochastically the gas particles in the BH vicinity (i.e. in its kernel, see § 2.2.1.2) to be accreted, with probability $p \propto \max[M_\bullet + M_\alpha - (M_{\bullet,\rm dyn} + \sum_k^N m_k), 0]$, where m_k is the mass of the k-th gas particle among the N selected. This guarantees that at every timestep, on average, $M_{\bullet,\rm dyn} \simeq M_\bullet + M_\alpha$. I note that in this implementation there are no measures to handle the situation where the accretion from resolved scales in a timestep exceeds the mass contained in the BH kernel. However, with an estimate we can verify a posteriori that this never occurs in simulations of § 2.4. Indeed, even assuming the maximum inflow rate found in those simulations $\sim 10 {\rm M}_\odot/{\rm yr}$, and a long BH timestep of $dt_\bullet \sim 5 \cdot 10^2$ yr, I note that the accreted mass amounts to $\sim 5 \cdot 10^3 {\rm M}_\odot$, which is much smaller than the employed gas mass resolution (see § 2.4). Therefore there is no risk that the mass available in the kernel is not sufficient to sustain the accretion estimated with the modified Bondi prescription.
Below I discuss more in detail how the inflows $\dot{M}_{\rm in}$ and $\dot{\mathbf{J}}_{\rm in}$ are computed.

2.2.1.2 Resolved accretion

The accretion rate $\dot{M}_{\rm in}$ from resolved scales on the sub-grid disc is estimated based on the properties of the gas particles within the MBH smoothing length $h_\bullet$, which is defined as a spherical region centered on the MBH enclosing a given effective number of particles $N_{\rm ngb}$ capped to a maximum size $R_{\rm max}$. The kernel

function adopted throughout this thesis is the standard cubic-spline. In particular, the inflow $\dot{M}_{\rm in}$ is estimated through a modified Bondi-Hoyle prescription that accounts for the angular momentum of gas in the BH kernel, as proposed by [131]. The argument suggested by [131], similarly to the classical Bondi-Holye derivation, is based on the definition of a characteristic accretion radius $R_{\rm acc}$, relative to the MBH, within which gas is bound to the MBH, and from which the accretion rate is computed as $\dot{M}_{\rm in} \sim \pi R_{\rm acc}^2 \rho v$, where v is the characteristic velocity of gas nearby the MBH and ρ its the density. The accretion radius is defined as the radial distance at which the gravitational potential of the MBH balances the internal and bulk energetics of the gas, but differently from the classical Bondi-Hoyle derivation, the computation is carried out in the reference frame of rotating gas, where the gas angular momentum provides an effectively lower gravitational potential: $U_{\rm eff}(r) = -GM_\bullet/r + \Lambda(r)^2/2r^2$, where $\Lambda(r)$ is the angular momentum per unit mass of the gas at distance r from the MBH. If the dominant motion of the gas is rotational rather than a bulk flow, the energy balance reduces to the requirement that the effective potential balances with the thermal energy of the gas, i.e. $U_{\rm eff} \sim c_s^2/2$. This allows to get $R_{\rm acc}$ and then, assuming that the characteristic velocity of gas can be approximated as $v \sim c_{\rm s}$, one obtains

$$\dot{M}_{\rm in} = \frac{4\pi (GM)^2 \rho c_{\rm s}}{(v_\varphi^2 + c_{\rm s}^2)^2}, \tag{2.18}$$

where $v_\varphi \equiv \Lambda(r)/r$ encapsulates the amount of angular momentum support the gas has on the smallest resolved scales. Numerically, v_φ is computed by estimating the specific angular momentum $\mathbf{\Lambda}$ of gas close to the MBH (i.e. prone to accrete) as the ratio between the kernel weighted averages of angular momentum and mass of particles in the MBH kernel. Then, assuming that angular momentum on the larger scales is conserved once the gas reaches the smallest resolved scale, $v_\varphi = |\mathbf{\Lambda}|/R_{\rm in}$, where $R_{\rm in} \equiv h_\bullet/3$ is a proxy of the smallest resolved scale in the MBH kernel. Then, if $v_\varphi < v_{\rm bulk}$, where $v_{\rm bulk}$ is the mass averaged velocity of gas in the MBH kernel, the usual Bondi-Hoyle formula (see § 1.1.4.2) [91, 110, 204] is adopted

$$\dot{M}_{\rm in} = \frac{4\pi (GM)^2 \rho}{(v_{\rm bulk}^2 + c_{\rm s}^2)^{3/2}}, \tag{2.19}$$

otherwise Eq. (2.18). Both in Eq. (2.18) and (2.19) ρ and $c_{\rm s}$ are computed as mass-weighted averages on the gas particles within the MBH kernel. As

an example, in Fig. 2.4 I show the evolution of the ratio between $\dot{M}_{\rm in}$ and the corresponding classical Bondi-Hoyle (Eq. 2.19) prescription in one of the simulations discussed in § 2.4. This ratio is always much smaller than one, i.e. Eq. (2.19) is never employed to compute the accretion on the sub-grid disc as in the setup employed in § 2.4 gas kinematics is dominated by rotation instead of bulk motion. The Bondi-Hoyle accretion is about two orders of magnitude larger than the modified Bondi (Eq. 2.18) accretion, in agreement with other works (e.g. [70, 131, 220, 221]), which showed that the classical Bondi-Hoyle accretion has the tendency to overestimate the accretion on the MBH. Once the accretion rate $\dot{M}_{\rm in}$ is computed, it is used to update the mass of the sub-grid disc, which evolves smoothly over time, as outlined in § 2.2.1.1.

I remark that both in the computation of the accretion rate $\dot{M}_{\rm in}$ and in the stochastic accretion of $M_{\bullet,\rm dyn}$, only non-wind particles are accounted, i.e. particles not spawned from the sub-grid disc (see section § 2.2.2), since such particles are initialized as outflowing and hence they do not contribute to the accretion flow on the MBH.

From the accretion $\dot{M}_{\rm in}$ on the sub-grid disc, the accreted angular momentum on the sub-grid disc is computed as $\dot{\mathbf{J}}_{\rm in} = \dot{M}_{\rm in}\mathbf{\Lambda}dt$, where $|\mathbf{\Lambda}|$ is limited as in [204] in order to account for not resolved processes like shocks and torques that make the accreting gas further loose angular momentum before accreting on the sub-grid disc at not resolved scales.

While the sub-grid disc mass is capped in order to avoid it from becoming self-gravitating, it is allowed to become zero, i.e. quiescent MBH, due to the accretion on the MBH and wind ejection. Once M_α vanishes, the disc is refilled with probability $p = (\sum \dot{M}_{\rm in}dt)/M_{\rm seed}$, where $\sum \dot{M}_{\rm in}dt$ is the mass inflow collected since the MBH became quiescent and $M_{\rm seed}$ is a free parameter. If refilling occurs, the new sub-grid disc is initialized with $M_\alpha = \max[M_{\rm seed}, \sum \dot{M}_{\rm in}dt]$, $f_{\rm Edd} = 0.1$, angular momentum set by Eq. (5) of [204] and its direction equal to that of the angular momentum in the MBH kernel.

2.2.2 AGN wind injection

As mentioned before, the implementation of AGN winds is based on the "wind injection" technique[2] by [15] and [126]. While in their models the wind injection is assumed isotropic, here I force the wind momentum (Eq. 2.3) and mass

[2]For the sake of completeness, I mention that the spawning particle technique has also been used with the GIZMO code in the context of stellar feedback [222], AGN jets [223], and AGN winds in zoom-in simulation [224].

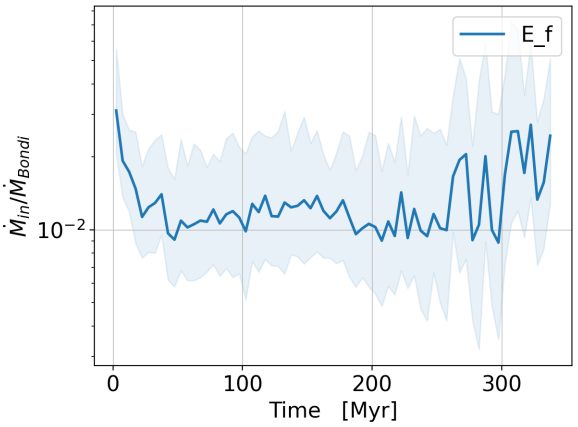

Figure 2.4: Ratio between the modified-Bondi accretion rate (Eq. 2.18) $\dot{M}_{\rm in}$ and the classical Bondi rate (Eq. 2.19) in simulation **`E_f`**.

fluxes to follow the sub-grid disc luminosity angular pattern resulting from gravitational bending, which is ultimately set by the MBH spin. I mention that another source of AGN feedback anisotropy does exist when AGN winds are accelerated at relativistic velocities. Indeed, an isotropic AGN radiation source driving a nuclear wind with relativistic velocity is perceived as anisotropic by the wind gas itself due relativistic beaming [225]. However, this effect translates in angular variations of $v_{\rm w}$ of a few percent for $v_{\rm w} = 0.01c$, as I will assume later, which is negligible compared to the variation in the wind momentum attributed to the photons gravitational bending.

Following [126] and [15], I assume that a factor τ of the radiation momentum flux is transferred to the gas at sub-grid scales, generating an AGN wind which is directly injected into the resolved scales. The wind mass outflow rate $\dot{M}_{\rm w}$ is computed from the unresolved disc accretion rate as shown in Eq. (2.4), where both $v_{\rm w}$ and τ, appearing in the definition of $\eta_{\rm w}$ (Eq. 2.5), are free parameters of the model. In practice, the wind is simulated by removing mass from the sub-grid disc and by spawning $N_{\rm w}$ new gas particles at a rate $\dot{M}_{\rm w}$. The newborn wind particles are distributed uniformly on a sphere centered on the MBH and with radius equal to the minimum between one tenth of the MBH gravitational softening $\epsilon_\bullet$ and half of the smallest MBH-gas particle separation. The mass distribution of the spawned particles follows the sub-grid disc luminosity angular

pattern. More precisely, the mass of the $i-$th spawned particle, with polar angle θ_i from the MBH spin direction, is assigned as

$$m_i = \frac{f(\theta_i, a)}{\sum_j f(\theta_j, a)} M_{\rm spawn}, \tag{2.20}$$

where the sum at denominator spans over all the spawned particles, $M_{\rm spwn}$ is the total mass to be spawned and $f(\theta, a)$ is the luminosity angular pattern defined in Eq. (2.1)

The wind particles are then launched radially outward with constant velocity $v_{\rm w}$ and by interacting with the other surrounding gas particles they generate an outflow. During their evolution, the wind particles can be merged into non-wind (or ISM) gas particles, properly transferring to them their mass, momentum, and energy as in an inelastic collision, see Appendix E of [216]. I required that such a merger occurs once the velocity of the target wind particle falls below five times[3] the mean velocity of the non-wind particles in its kernel. I provide more details about wind particles mass resolution and their merger to non-wind particles in Appendix C. In order to track the propagation of the wind into the environment, I introduced a scalar wind tracer ζ, similarly to [15], that represents the wind mass fraction of a gas particle. Therefore $\zeta = 1$ for wind particles, non-wind particles are initialized with $\zeta = 0$ and $0 < \zeta < 1$ values characterize non-wind particles that experienced mergers with wind particles.

In order to be able to capture the formation of a momentum-driven outflow I include gas Compton cooling in the model. I assume that the AGN photons interact with the surrounding gas at sub-grid scale, launching the AGN wind, and then they are remitted isotropically. Then, such reprocessed photons can scatter with the high energy electrons of the shocked wind layer of the outflow, making it loose energy and cool. In practice, following [226], a contribution $\Lambda_{\rm Cpt}$ as in Eq. (1.64) is included when computing radiative cooling/heating of gas particles, where now r is the distance between the gas particle and the MBH and L is the instantaneous sub-grid disc luminosity computed from Eq. (1.18).

[3]The choice of this parameter is not restrictive. In the development phase, I tried using other parameters in the range $\sim [1-10]$ without finding any significant difference. Similarly, I tried imposing conditions on the number of non-wind neighbours a wind particle must have before it undergoes a merger, but these also proved irrelevant. In principle, by increasing the treshold velocity for merger and decreasing the number of neighbours required for this to occur, mergers could occur more frequently and the simulation could get rid of wind particles faster, potentially speeding up, but even in these terms I did not notice any significant improvement.

In the sub-grid model described in this section, the MBH timestep $dt_\bullet$ is taken small enough to resolve the sub-grid accretion, wind launching and spin evolution and large enough to guarantee that the disc attains a steady-state warped profile, as assumed in our prescriptions.

2.3 Tests

In order to compare the simulated evolution of the wind-driven outflows against the analytical predictions given by Eqs. (2.9, 2.11), I first adopt an idealized setup. I consider an active MBH embedded in a gas with uniform density and temperature, so to ensure that the outflow anisotropy is the result of the intrinsic anisotropy of the wind, rather than of the ambient density distribution. In order to compare the simulated outflows with Eqs. (2.9,2.11), I switch off gravitational forces and gas self-gravity so that the outflow evolution is purely hydrodynamical. For all the duration of the simulations I keep the AGN luminosity and angular pattern constant, i.e., I force the properties of the sub-grid disc and MBH not to vary.
In order to test both energy- and momentum-driven outflows, I consider two different setups. In the first case, I assume a gas number density $\mu n = 1\,\mathrm{cm}^{-3}$, where μ is the mean-molecular-weight, and a MBH mass 10^7 $\mathrm{M}_\odot$, while in the second $\mu n = 10^6\,\mathrm{cm}^{-3}$ and MBH mass 10^{10} $\mathrm{M}_\odot$. In both cases the gas temperature is set at $T = 2\cdot 10^4$ K. In order to test different outflow anisotropies, for each setup I consider three different values of the MBH spin, $a = \{0.01, 0.95, 0.9982\}$. In the energy-driven simulation with $a = 0.01$, I assume $f_{\rm Edd} \equiv \dot{M}_{\rm acc}/\dot{M}_{\rm Edd} =$

	a	η	$\log(M_\bullet/M_\odot)$	$f_{\rm Edd}$	L[erg/s]	μn[cm^{-3}]	$\epsilon_{\rm grav}$[pc]	$N_{\rm w}$
En.	0.01	0.057	7	0.1	$1.2\cdot 10^{44}$	1	0.11	588
	0.95	0.190	7	0.332	$3.98\cdot 10^{44}$	1	0.11	588
	0.9982	0.323	7	0.567	$6.8\cdot 10^{44}$	1	0.11	588
Mom.	0.01	0.057	10	0.3	$3.6\cdot 10^{47}$	10^6	0.08	108
	0.95	0.190	10	0.997	$1.2\cdot 10^{48}$	10^6	0.08	108
	0.9982	0.323	10	1.7	$2.04\cdot 10^{48}$	10^6	0.08	108

Table 2.1: Summary of the parameters adopted in the test simulations: in order, I show the spin, the radiative efficiency, the MBH mass, the dimensionless accretion rate, the AGN luminosity, the gas number density, the gravitational softening and the number of particles spawned at each spawning episode. In all simulations I employed 10^7 gas particles and wind particles velocity and temperature are initialized with $v_{\rm w} = 0.01c$ and $T_{\rm w} = 2\cdot 10^4$ K.

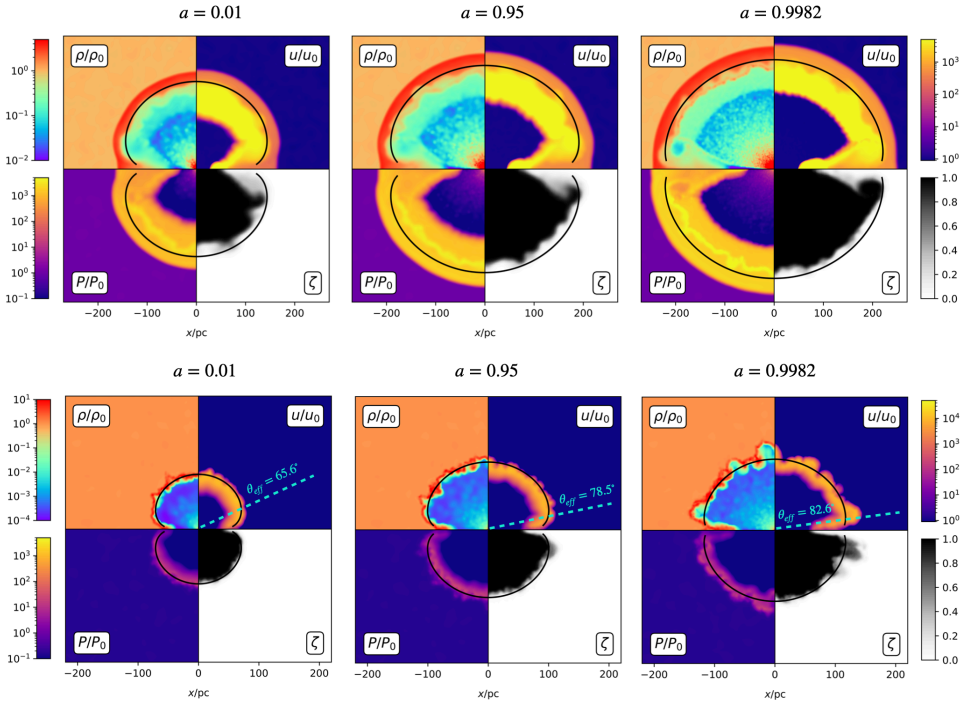

Figure 2.5: Final snapshots of the propagation of an AGN wind-driven outflow for different spin values (increasing from left to right) and the two considered regimes (energy-driven in the top row and momentum-driven in the bottom one). Each panel illustrates the density, temperature and pressure fields in units of the corresponding quantities of the assumed background medium as well as the wind mass fraction. In the energy-driven simulations the outflow can be divided into four distinct sections: (1) the freely-expanding wind, (2) the shocked wind, (3) the shocked ambient medium and (4) the undisturbed ambient medium. In the momentum-driven simulations radiative cooling makes the shocked wind layer cool and regions (2) and (3) are condensed into a thin shell. The wind tracer is injected together with the wind and is therefore only present in regions (1) and (2). The black lines correspond to the analytical location of the contact discontinuity between regions (2) and (3), as computed in Eq. (2.9-2.11). In momentum-driven simulations the cyan dashed lines indicate the effective aperture of the radiation as defined in 2.1.1.

0.1, while $f_{\rm Edd} = 0.3$ in the corresponding momentum-driven simulation. In the simulations with higher MBH spin I keep the same sub-grid disc properties as for $a = 0.01$, therefore the corresponding $f_{\rm Edd}$ values scale as $\eta(a)/\eta(a = 0.01)$, according to Eq. (2.17). Energy-driven simulations run up to $t_{\rm end} \sim 0.22$ Myr, while momentum-driven ones for $t_{\rm end} \sim 1.5$ Myr. The values of the main parameters of all runs are summarized in Table 2.1.

Figure 2.5 shows the final snapshots for all six simulations, with energy-driven runs in the top panels and momentum-driven in the bottom ones. For each snapshot, the figure reports the density, temperature and pressure fields in units of the corresponding quantities of the background medium as well as well as the wind mass fraction. Superimposed to all maps, I draw as a black curve the location $R_{\rm sh}(t_{\rm end}, \theta)$ of the contact discontinuity, as computed via Eqs. (2.9,2.11). In the energy-driven simulations (top panels) the typical stratified structure of outflows described in § 1.2.2 can be recognized, with the free propagation wind layer, the shock wind, the shocked ambient medium and the unperturbed ambient medium. The simulated location of the contact discontinuity approximates very well its theoretical prediction (Eq. 2.9). In the momentum-driven simulations (bottom panels) Compton cooling makes the shocked wind layer cool and collapse, forming a thin shell that separates the free expanding wind from the unperturbed medium. Again, the location of the separating shell is in good agreement with the theoretical estimate (Eq. 2.11).

In both energy- and momentum-driven simulations, as the spin increases, the angular pattern of the emerging outflow becomes more spherical and spreads at larger distance from the MBH. This is expected, as larger spin values yield more isotropic luminosity angular patterns as well as more luminous discs.

2.4 Isolated galaxy simulations

I employ now the sub-grid model for spin-dependent AGN winds described in Section 3.1 to study the role of wind anisotropy in shaping AGN-driven galactic outflows, and then the impact such outflows have on the host galaxy. I start by constructing an isolated galaxy setup similarly to [15]. I first initialize a gaseous halo of mass $M_g = f_g M_{200}$, where $M_{200} = 10^{12} M_\odot$ is the halo (dark matter + gas) virial mass and $f_g = 0.17$ the gas mass fraction, with a Navarro-Frenk-White [NFW; 227] density profile. A $M_\bullet = 10^8 M_\odot$ MBH is placed at the center of the system and the gas internal energy is set to guarantee hydrostatic equilibrium in

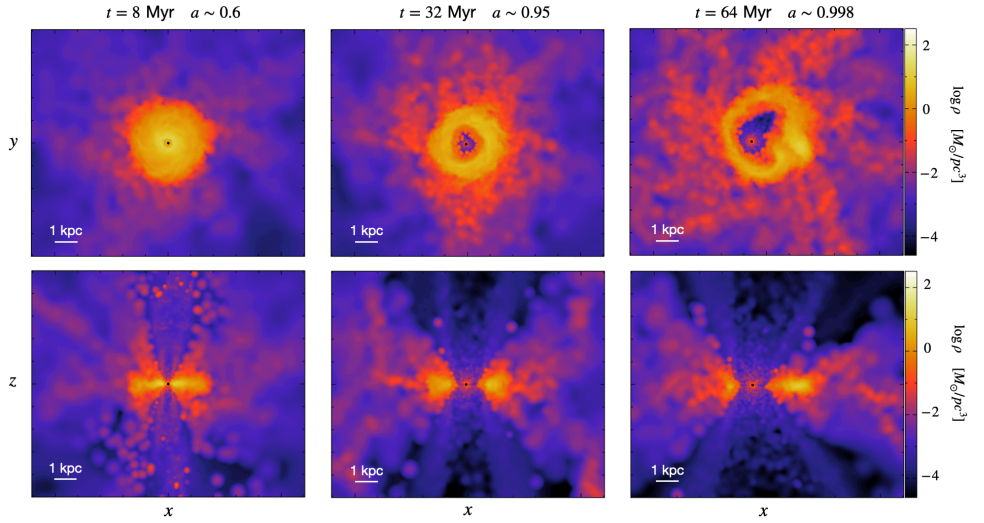

Figure 2.6: Density slices of three snapshots from simulation **C_f**, with the disc face-on in the top panels and side-on in the bottom panels. The MBH location is marked by a black dot.

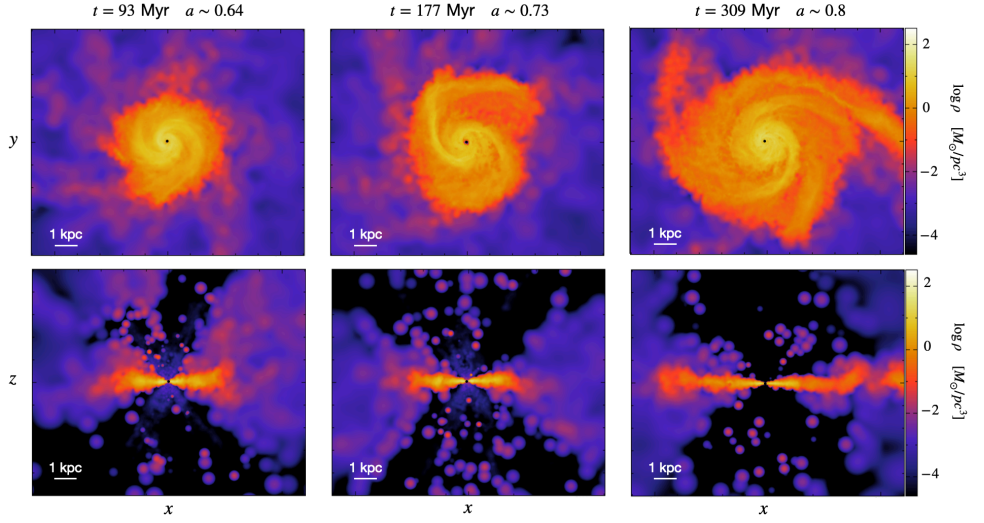

Figure 2.7: Density slices of three snapshots from simulation **E_f**, with the disc face-on in the top panels and side-on in the bottom panels. The MBH location is marked by a black dot.

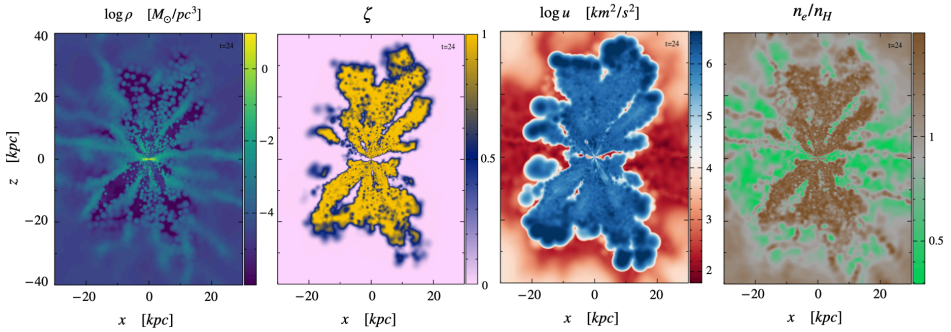

Figure 2.8: From left to right, edge-on maps of the gas density, the wind mass fraction, the internal energy, and the electron abundance fraction of simulation **E_f** at $t = 24$ Myr.

the absence of cooling. The pressure profile has been computed numerically from the gas density and total potential profiles. The halo concentration parameter is $\mathcal{C} = 7.2$, which gives a halo scale radius $a_{\rm halo} = 28.54$ kpc and a virial radius $r_{200} = \mathcal{C} a_{\rm halo} = 205.5$ kpc. These parameters were chosen to recreate a setup similar to that of [15], so that their simulations could be used as a reference. The gas initial specific angular momentum follows a profile $j(r,\theta)$, where r and θ are the spherical radial and polar coordinates, as in Eqs. (12-15) of [228]. Such profile is characterized by the halo spin parameter $\lambda_{\rm sim}$, introduced by [229] (their Eq. 5), which is set to $\lambda_{\rm sim} = 0.035$.

Radiative cooling is modelled as described in [230], assuming initial metallicity $0.1 Z_\odot$ and ignoring radiative cooling processes below $T < 10^4$ K. Due to the loss of pressure support following radiative cooling, at $t = 0$ the spinning gaseous halo starts to collapse towards the center and the inner region settles into a galactic disc continuously fed by the outermost falling layers. I emphasize that this initial gas inflow and the subsequent galaxy formation and star formation history are sensitive to the initial halo density profile. In particular, a NFW profile, as assumed here, is likely to enhance these processes compared to other shallower profiles, see e.g. [231, 232].

The gaseous halo is sampled with $N = 3 \cdot 10^5$ particles only up to a radius of $0.6 r_{200}$. Note that the presence of a sharp pressure gradient at $0.6 r_{200}$ causes an artificial outflow. Nonetheless, this occurs on spatial scales far away from those considered in our analysis, which focus on the central ~ 10 kpc region. In addition, the radius of $0.6 r_{200}$ within which we sample the gas is tailored to

ensure that over the simulated time the boundary effects of this sampling cannot propagate within the central region of interest, as gas particles above $0.6\,r_{200}$ take more than ~ 0.7 Gyr to fall within ~ 5 kpc from the center of the system. The mass resolution of our simulations is $m_{\rm gas} = 3.44 \cdot 10^5 M_\odot$. Dark matter is not sampled and enters the simulation as a static analytic potential.

Star formation is treated following [233], where the effects of unresolved physical processes operating within the interstellar medium (ISM) are captured by an effective equation of state that is applied to all gas with hydrogen number density $n_{\rm H} > n_{\rm th}$. This effective equation of state is stiffer than that of isothermal gas, because it accounts for additional pressure provided by supernova explosions within the ISM. Stellar particles are spawned stochastically from gas with $n_{\rm H} > n_{\rm th}$ at a rate

$$\frac{d\rho_\star}{dt} = (1-\beta)\frac{\rho_{\rm c}}{t_\star}, \tag{2.21}$$

where $\beta = 0.1$ is the mass fraction of massive stars assumed to instantly explode as supernovae, $\rho_{\rm c}$ is the density of cold clouds [see 233, for details] and $t_\star = t_{\star,0}(n_{\rm H}/n_{\rm th})^{-1/2}$ is the star formation timescale, with $t_{\star,0} = 1.5$ Gyr and $n_{\rm th} = 0.5{\rm cm}^{-3}$. Supernova-driven winds are not modelled, as they would add a further layer of complexity affecting both star formation, the MBH growth and hence AGN feedback [see, e.g., 234]. Therefore, our simulations should be regarded as idealised experiments aimed at illustrating how AGN wind modelling affects the impact of MBH feedback on the host galaxy and on the MBH evolution, without "contamination" from supernova-driven winds.

After the first 150 Myr, once a galactic disc has formed and star formation has already reached its peak, MBH accretion and feedback are "switched on". I denote this instant with t_0. Then, I perform six different simulations divided in two sets (labelled with **C** and **E**) corresponding to different MBH accretion prescriptions, each set consisting of three different simulations characterized by different feedback anisotropies (indicated with labels **f**, **iso**, **a0**). In the simulation set labelled with **C**, the sub-grid accretion disc is forced to maintain the same properties for the entire duration of the simulations, i.e., the disc mass and angular momentum do not change because of accretion onto the MBH and wind ejection. In these simulations, the Eddington factor $f_{\rm Edd} \equiv \dot{M}_{\rm acc}/\dot{M}_{\rm Edd}$ is kept constant equal to 1 (similarly to [15, 126, 224]), corresponding to a sub-grid disc of constant luminosity $L = 1.2 \cdot 10^{46}$ erg/s. On the contrary, in **E** simulations, $f_{\rm Edd}$ is allowed to evolve and its value is set by the instantaneous MBH + subgrid disc properties (Eq. 2.17), which, in turn, are determined by the inflow

on the disc, the accretion on the MBH and wind ejection (see Eqs. 2.12-2.15). In this way, **E**-simulations are able to capture the mutual non-linear influence that inflows and outflows have on each other, that lead to a self-regulated MBH growth.[4] In addition to these simulation sets, I prolonged the simulation for the spinning halo collapse beyond 150 Myr without switching on the AGN, so that the sets **C** and **E** can be compared to the case in which the MBH is not active. I indicate this simulation with **NoFb**.

Both **C** and **E** sets consist of three simulations, accounting for a different wind anisotropy. Simulations **f** have an angular pattern $f(\theta;a)$, as illustrated in section 2.1.1, that evolves according to the evolution of the spin parameter a; **iso**-simulations are characterized by an isotropic angular pattern, i.e. $f=1$; **a0**-simulations assume instead a fixed angular pattern corresponding to the one of $a\simeq 0$, $f=f(\theta;0.01)$. Note that, independent of the anisotropy pattern, the MBH spin and $\eta(a)$ are allowed to evolve in these runs. The motivation for these choices of angular patterns is the following: real outflows anisotropy can result from the wind "intrinsic" anisotropy imparted by the radiation angular pattern and linked to the MBH spin, i.e. the anisotropy discussed in section § 2.1.1 and seen in Fig. 2.5, or it can be induced by the anisotropy of the medium in which the outflow propagates as, for example, in a spiral galaxy where the gas density is higher in the midplane of the galaxy than perpendicular to it. In this way, an "intrinsically" spherical outflow expands more easily along the galaxy axis, i.e., along the least resistance path, turning into a bipolar (anisotropic) outflow [15, 123, 235].[5] Since outflow anisotropy is shaped by these two factors, both present in simulations **f**, a comparison with simulations **iso** allows to disentangle these effects and to properly assess the relevance of radiation pattern anisotropy in galactic outflows. Instead, simulations **a0** represent the opposite term of comparison, in which the angular pattern is maximally anisotropic, i.e. $f(\theta;0.01)\simeq 2\cos\theta$ as in (Newtonian) α-discs, as if all the isotropy coming from gravitational bending were removed. I summarize the main features of the six simulations performed in Table 2.2.

In both **C** and **E** sets, I start the simulations at t_0 with $f_{\rm Edd}=1$, $a=0.01$, $M_\alpha=0.005M_\bullet$ and $M_\bullet+M_\alpha=10^8M_\odot$. Following [15], the wind velocity and radiation-wind coupling parameter are fixed to $v_{\rm w}=0.01\,c$ and $\tau=1$, accord-

[4] [126] showed that an Eddington accreting AGN generates wide cavities in its surroundings, but noted that this lower density should reflect in decreased inflow on the AGN in turn reducing his power and the cavity size itself, letting the system self-regulate.

[5] This may explain, for example, the presence of the Fermi bubbles in the Milky Way [236].

	$f_{\rm Edd}(t)$	$M_\alpha(t)$
E	variable	variable
C	1	$4.975 \cdot 10^5$ $M_\odot$

	angular pattern
f	$f\left(a(t);\theta\right)$
a0	$f\left(a=0.01;\theta\right)$
iso	1

Table 2.2: Main features of the isolated galaxy simulations: (*left*) the dimensionless accretion rate and sub-grid disc mass for the **E** and **C** simulation sets. Note that while sub-grid disc quantities are evolved only in **E** simulations, the MBH mass and spin evolve according to the prescriptions detailed in 2.2.1.1 in both simulation sets. (*right*) the AGN radiation angular patterns used in each simulation set.

ing to radiation hydrodynamics simulations of thin discs centred on MBHs with mass $10^6 - 10^9 M_\odot$ [237, 238], which showed that the AGN wind reaches velocities of the order of $10^3 - 10^4$ km/s at ~ 50 gravitational radii from the MBH and that $\tau \sim 1$. $N_{\rm w} = 48$ wind particles are spawned at each spawning event their temperature is fixed to $T_{\rm w} = 2 \cdot 10^4$ K. In all simulations the gravitational softening for all particle species is 2 pc.

In the following sub-sections, I will discuss the impact of AGN feedback in our setups, focusing on the one hand on its effect on the host galaxy, in particular on the central gas reservoir and star formation, and on the other hand on its influence on the MBH evolution in mass and spin. Before entering in details, we give a qualitative glimpse on how the galaxy-MBH evolution looks like in simulations **C_f** and **E_f**.

Figure 2.6 shows three snapshots of the simulation **C_f**, both face on (top panels) and side-on (bottom panels). In the side-on view, we see that after $t \simeq 8$ Myr from the AGN "switch on", a collimated wind is piercing the circum-galactic-medium (CGM), its opening angle widening over time. Correspondingly, in the face-on view, a ∼kpc-scale cavity is cleared in the central region surrounding the MBH, becoming increasingly larger with time. Both these effects are accompanied by an increase of the spin value, which reaches ~ 0.998 after $\simeq 64$ Myr, and hence by an increase in the disc radiative efficiency and in the isotropy of the radiation angular pattern (see discussion in § 2.1.1). I remark that in this simulation the accretion rate on the MBH is forced to be constant, equal to the Eddington rate. However, as noted by [126], once the gas reservoir feeding the MBH diminishes with the formation of a central cavity, the accretion on the MBH should decrease as well, reducing the AGN power and hence its ability to further enlarge the cavity. I show this effect in Fig. 2.7, which is the analogous of Fig. 2.6 for the simulation **E_f**, in which the MBH accretion is consistently evolved with the

inflow on the disc and the wind ejection from it. In this case, no cavity formation can be seen in the face-on view and a milder wind (compared to Fig. 2.6) is seen in the side-on view. This suggests that a much lower accretion (and hence outflow) rate is achieved once that the disc is allowed to adjust itself through its interaction with the environment. In particular, we will see in section 2.4.1.1 that, in this simulation, $f_{\rm Edd}$ indeed drops by $\sim 1 \div 2$ orders of magnitude from its initial value.

In Figure 2.8 I show a zoom-out of the side-on view of simulation **E_f** at $t =$ 24 Myr. The four columns illustrate, from left to right, the gas density, the wind mass fraction, the gas internal energy and the electron abundance fraction $n_e/n_{\rm H}$. Even though the AGN wind doesn't seem to affect much the host galaxy (Fig. 2.7), it propagates deeply in the CGM creating a hot, low density, ionized bipolar outflow that extends in the polar directions and regulates the inflow onto the galaxy, hence its growth.

I now discuss more quantitatively the impact of feedback both on the MBH and the galaxy host, turning the attention to the relevance of the spin-dependent wind anisotropy.

2.4.1 The impact of AGN feedback on the MBH

In order to understand how the MBH mass and spin evolve and to what extend their growth is influenced by AGN feedback, we need to understand its back-reaction on $f_{\rm Edd}$, which characterizes the rate of such growth.

2.4.1.1 Evolution of $f_{\rm Edd}$

In **C** simulations, the growth of MBH mass and spin is completely determined by the constrain $f_{\rm Edd} = 1$, so it is independent on any effect feedback might have on the gas surrounding the MBH. Conversely, in **E** simulations, $f_{\rm Edd}$ varies with time according to the evolution of the sub-grid disc+MBH system (Eq. 2.17), which is influenced by the action of feedback on the nuclear environment. Indeed, in this case, AGN feedback diminishes the gas density in the vicinity of the MBH, lowering the mass inflow rate on it and hence the AGN power.

In order to have a better understanding of how $f_{\rm Edd}$ evolves, I computed the time derivative $df_{\rm Edd}/dt$ (see Appendix A), finding that it can be approximated as

$$\frac{df_{\rm Edd}}{dt} \simeq 5 f_{\rm Edd} \left(-C_{\rm w} \frac{\dot{M}_{\rm w}}{M_\alpha} + C_{\rm in} \frac{\dot{M}_{\rm in}}{M_\alpha} \right), \tag{2.22}$$

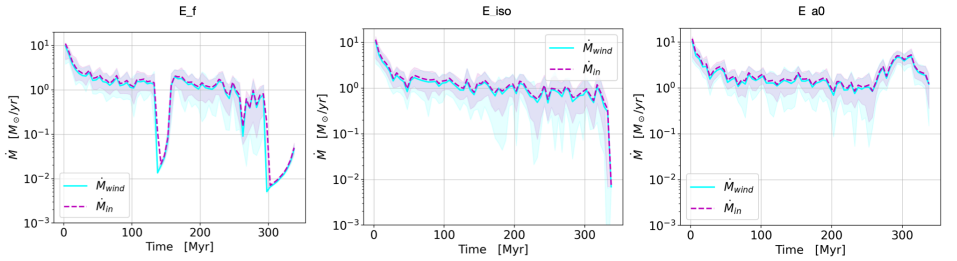

Figure 2.9: The evolution of the mass inflow rate $\dot{M}_{\rm in}$ on the sub-grid disc and the mass outflow rate $\dot{M}_{\rm w}$ ejected in winds for the three **E** simulations. The solid and dashed lines correspond to the median values of these quantities over time bins of 5 Myr, while the shaded regions span from the 16th to the 84th percentiles of $\dot{M}_{\rm in}$ and $\dot{M}_{\rm w}$ within the bins.

where $\dot{M}_{\rm in}$ is the mass inflow rate on the sub-grid disc from resolved scales, as defined in § 2.2.1.2, and the coefficients $C_{\rm w}$ and $C_{\rm in}$ are both found to be $\simeq 0.1$, as detailed in Appendix A. Equation (2.22) describes the evolution of $f_{\rm Edd}$ as driven by the disc mass loss, proportional to $\dot{M}_{\rm w}$, and by the inflow $\dot{M}_{\rm in}$ that supplies mass to the disc; in other words, the disc accretion rate is regulated by the balance between outflows and inflows. Because of the different signs in front of $C_{\rm w}$ and $C_{\rm in}$, the disc tends to evolve towards a stationary $df_{\rm Edd}/dt \sim 0$ regime. Indeed, if the inflow exceeds the outflow, i.e. $C_{\rm in}\dot{M}_{\rm in} > C_{\rm w}\dot{M}_{\rm w}$, then the accretion rate $f_{\rm Edd}$ increases and $\dot{M}_{\rm w}$ grows as well (see Eq. 2.4). By contrast, if the disc mass consumption outpaces the external mass supply, $C_{\rm w}\dot{M}_{\rm w} > C_{\rm in}\dot{M}_{\rm in}$, the accretion rate decreases and hence $\dot{M}_{\rm w}$ diminishes too. In this way inflows and outflows tend to adjust each other such that $C_{\rm w}\dot{M}_{\rm w} \sim C_{\rm in}\dot{M}_{\rm in}$, i.e. $df_{\rm Edd}/dt \sim 0$. Figure 2.9 shows the evolution of $\dot{M}_{\rm w}$ and $\dot{M}_{\rm in}$ in the three simulations **E** and reveals that in all cases $\dot{M}_{\rm w} \sim \dot{M}_{\rm in}$ and both quantities settle around $\sim 1\,{\rm M}_\odot/{\rm yr}$ after a transient of ~ 50 Myr. As a result, in all **E** simulations, $f_{\rm Edd}$ decreases from its initial value $f_{\rm Edd,0} = 1$ and, after ~ 50 Myr, attains a value ~ 0.05 (see Fig. 2.10), which is consistent with observed Seyfert galaxies [239] and corresponds to a moderate luminous AGN with $L \simeq 6 \cdot 10^{44}$ erg/s.

The final value $f_{\rm Edd} \sim 0.05$ can be also roughly predicted directly from Eq. (2.22). By imposing $df_{\rm Edd}/dt = 0$ I find the equilibrium value attained by the dimensionless accretion rate to be

$$f_{\rm Edd}^{\rm teo} = \frac{\dot{M}_{\rm in}}{\dot{M}_{\rm Edd}} C_{\rm in}, \tag{2.23}$$

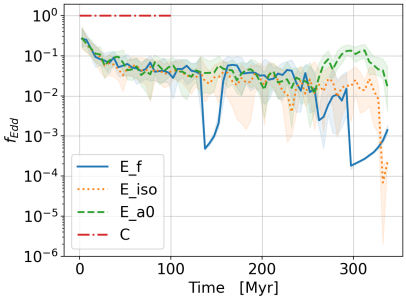

Figure 2.10: Evolution of $f_{\rm Edd}$ in **E** and **C** simulations. The lines correspond to the median values of $f_{\rm Edd}$ over time bins of 5 Myr, while the shaded regions represent the fluctuations within the bins from the 16-th to 84-th percentiles.

where I used $C_{\rm w} = \eta_{\rm w}^{-1}$ (see § 2.2.1.2) and Eq. (2.4). This equation shows that the sub-grid accretion rate is ultimately set by the resolved accretion rate $\dot{M}_{\rm in}$ and by the coefficient $C_{\rm in}$, which contains information on the resolved accretion of angular momentum (see § 2.2.1.2). In order to obtain a specific value to compare with the simulations, I assume that $\dot{M}_{\rm in} \sim 0.01 \cdot 4\pi G^2 M_\bullet^2 \rho c_{\rm s}^{-3}$, using the classical Bondi formula with zero bulk velocity (Eq. 2.19) and the factor 0.01 coming from Fig. 2.4. To obtain a rough estimate of this expression, as ρ I take the value of $\sim 100\,{\rm M}_\odot/{\rm pc}^3$, as seen in the nuclear region of the galaxy in Fig. 2.7, and the value of $\sim$ few$10^{-4}c$ for $c_{\rm s}$ (corresponding to a temperature of $T \sim 2 \cdot 10^6 \mu ({\rm few}/4)^2 {\rm K}$), inferred similarly from sound speed contourmaps. Then, by replacing these values in the expression for $\dot{M}_{\rm in}$ and in Eq. (2.23), and by using $C_{\rm in} \sim 0.1$, I obtain $f_{\rm Edd}^{\rm teo} \sim 0.069$, in reasonable agreement with the outcome of the simulation. The major limitation in using Eq. (2.23) to predict the accretion rate on the MBH lies in the fact that the values of ρ and $c_{\rm s}$ used here are those extracted from the simulation once self-regulation has been achieved, and thus these values are the result of the effect that feedback is having on the surrounding environment. Predicting these values before self-regulation takes place (e.g. from our initial condition at t_0) requires detailed knowledge of the interaction of the AGN winds with the surrounding environment, which is inherently a complex non-linear problem and requires simulations.

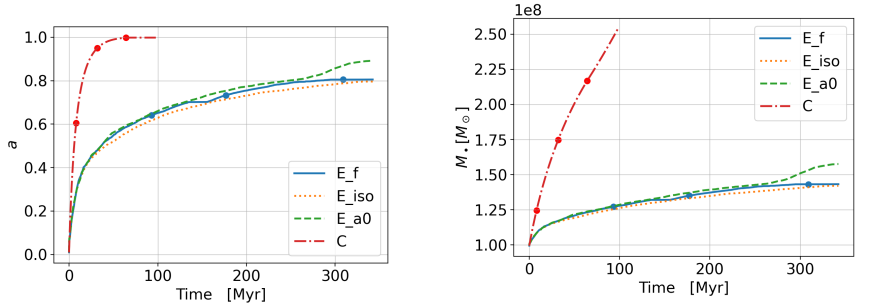

Figure 2.11: MBH spin and mass growth in **E** and **C** simulations. The red and blue bullets mark the instants corresponding to the snapshots shown in Figures 2.6 and 2.7.

2.4.1.2 MBH mass and spin growth

The mass and spin evolution of the MBH in all simulations is shown in Figure 2.11. In **C** simulations, the growth of MBH mass and spin is constrained by $f_{\rm Edd} = 1$, whereas in **E** simulations $f_{\rm Edd}$ varies with time (Fig. 2.10), according to the interplay between inflows and outflows. In this second case $f_{\rm Edd}$ lowers down to ~ 0.05, in this way the MBH mass and spin growth is severely delayed compared to the $f_{\rm Edd} = 1$ case.
While the disc luminosity is directly linked to the MBH mass and spin growth rates (Eq. 1.18), its angular pattern has a negligible impact on them. Nonetheless, in **E** simulations we notice a small dependence of these growth rates with the radiation angular pattern, i.e. the more isotropic the angular pattern is (where isotropy rises with **a0** $\rightarrow$ **f** $\rightarrow$ **iso**), the slower the mass and spin growth is. This can be attributed to the wind-ISM coupling increasing with isotropy (see § 2.4.2), thus yielding smaller mass inflow rates on the MBH and hence lower AGN power.

2.4.2 The impact of AGN feedback on the galaxy host

I now quantify the impact of AGN feedback on the host galaxy by probing the galaxy star formation history, the size of the central cavity and the AGN wind opening angle and the CGM properties.

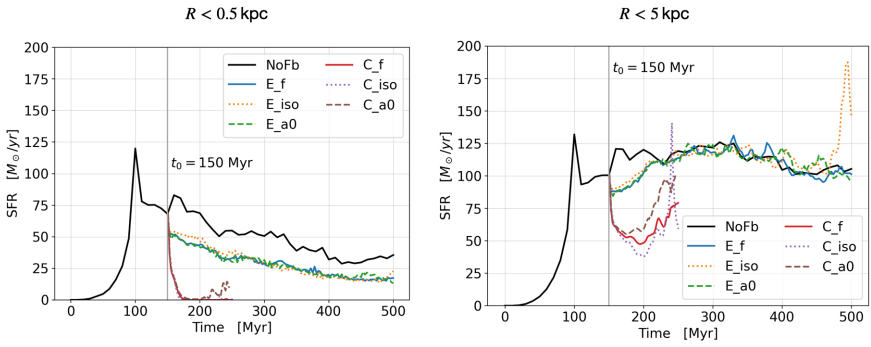

Figure 2.12: Star Formation Rate (SFR) in the nuclear region (left) and at galactic scale (right) for **E**, **C** and **NoFb** simulations. $t = 0$ corresponds to the initial condition with the spinning gasous halo in hydrostatic equilibrium and $t_0 = 150$ Myr (when AGN feedback is turned on) is marked with a grey vertical line.

2.4.2.1 Star formation rate history

In Figure 2.12 I show the evolution of the star formation rate (SFR) with time. In order to differentiate the effect of the AGN feedback on nuclear and galactic scales, in the left panel I consider the SFR of the gas particles within 0.5 kpc from the MBH, while in the right panel the SFR of the gas particles within 5 kpc. In both panels I show results from the simulations sets **C** and **E** and from simulation **NoFb**, that with no feedback.

The **NoFb** simulation traces the evolution of the SFR starting from the initial condition with the spinning halo in hydrostatic equilibrium. At this time the SFR is zero, but as soon as the gaseous halo collapses, getting denser and cooler, the SFR grows and peaks at $\sim$ 100 Myr, both on nuclear and galactic scales. At this point, while in the central region the SFR starts to decline, in the whole galaxy stars continue to be formed at a rate of 100 $M_\odot$/yr $\div$125 $M_\odot$/yr. The switch-on of AGN feedback at $t_0 = 150$, in **C** and **E** runs, modifies these trends. In the central 0.5 kpc, the SFR is reduced by a factor of $\lesssim 2$ in **E** simulations, while it is completely shut off in **C** simulations. The imprint of AGN feedback on galactic scales is less marked: in **E**-simulations the SFR within 5 kpc is not appreciably altered, except for a $\lesssim 20\%$ decrease during the first ~ 50 Myr of AGN activity, and a burst of SFR at the end of **E_iso** due to a clump in a spiral arm, whereas it diminishes by a factor of $\lesssim 2$ in **C** runs. Overall, these trends do not show any significant dependence on the AGN radiation angular pattern,

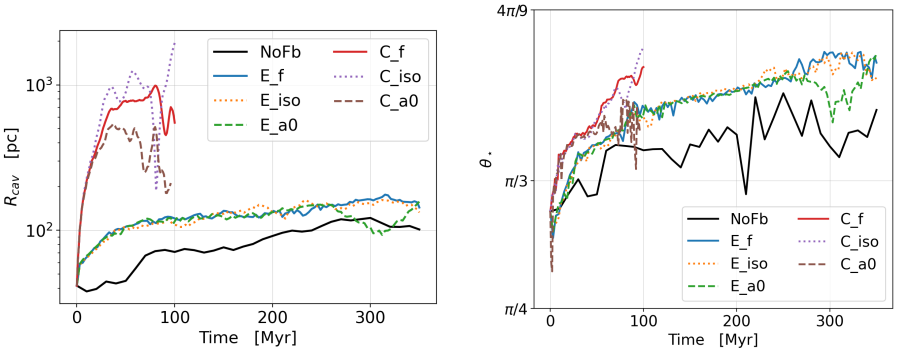

Figure 2.13: Evolution of the central cavity size (*left*) and outflow opening angle (*right*) in **E**, **C** and **NoFb** simulations.

except for **C** simulations at galactic scale. In this case, we see that the more isotropic the luminosity angular pattern is, the more the SFR is suppressed, due to the increase of wind-ISM coupling. However, this appears as a second order effect and the impact of AGN feedback on the SFR is mainly driven by the AGN luminosity, rather than by its angular pattern.

2.4.2.2 The size of the central cavity

The trends seen in the SFR(t) history are closely related to those seen in the size of the central cavity cleared by AGN feedback. Here the cavity size is measured as the radius $R_{\rm cav}$ of the sphere centered in the MBH containing a gas mass equal to the MBH mass. Figure 2.13 shows that in the simulation without feedback this quantity is initially (at t_0) about 50 pc and overall grows up to ~ 100 pc. In simulations with AGN feedback, AGN winds tends to push the gas away from the MBH, lowering the gas density in its surroundings and thus increasing $R_{\rm cav}$. Such an increase is modest in **E** simulations, by a factor less than 2, while it is about an order of magnitude larger in **C** simulations. In this second case, we can distinguish a dependence of the cavity size with the feedback radiation angular pattern, where a more isotropic pattern results in a larger cavity.
As for the SFR(t), the cavity size seems to be determined at first order by the disc luminosity and only for high (Eddington) luminosities (**C** runs) by the radiation angular pattern, at least partially. In addition, the increase in the cavity size with disc luminosity and with disc radiation angular pattern mirrors

what I found for the SFR, i.e., larger cavities are associated with lower SFRs. This suggests that star formation suppression in the galaxy nuclear region occurs via gas removal caused by AGN winds.

2.4.2.3 The outflow opening angle

Finally, I measure the opening angle of the region within which the SFR is maintained below 1 $M_\odot$/yr, which provides information about the anisotropy (or angular amplitude) of the bipolar outflow. In order to compute this quantity, I first determine, at any time t, the SFR angular profile $\mathrm{SFR}(\theta;t)$, where θ is the polar angle from the galaxy axis [6]. For all simulations, $\mathrm{SFR}(\theta;t) \simeq 10^{-2} \div 10^{-1}$ $M_\odot$/yr for small θ, i.e. perpendicular to the galaxy disc plane, and rapidly increases at $\theta \gtrsim \pi/3$, reaching $\simeq 10 \div 10^2$ $M_\odot$/yr for $\theta \lesssim \pi/2$, i.e. in the galactic disc mid-plane. Given this trend, I define $\theta_\star$ as the angle below which the $\mathrm{SFR}(\theta;t) < 1$ $M_\odot$/yr. Then, the larger $\theta_\star$, the wider the angular region where the outflow manages to keep the SFR below our treshold of 1 $M_\odot$/yr. In this sense, $\theta_\star$ measures the outflow semi-opening angle.
In Figure 2.13, I show how $\theta_\star$ evolves in our simulations and we notice a trend similar to that of $\mathrm{SFR}(t)$ and $R_{\rm cav}(t)$. Indeed, $\theta_\star(t) \gtrsim \pi/3$ in **NoFb** simulation, then becomes larger in **E** simulations and increases further in **C** runs. No particular trend of $\theta_\star$ is seen with the feedback radiation angular pattern, except for the final part of **C** simulations, which suggest that $\theta_\star$ is larger for more isotropic radiation angular patterns. Therefore, similarly to what I discussed for $\mathrm{SFR}(t)$ and $R_{\rm cav}(t)$, the disc luminosity, more than its angular pattern, determines the angular amplitude of the outflow, measured as the ability of AGN winds to hamper the SFR at large polar angles.

2.4.2.4 The impact on the CGM

While on galactic (~ 10 kpc) scales there is a mild or absent dependence of the outflow opening angle on the AGN radiation anisotropy, this is not the case if we look at the larger CGM (~ 100 kpc) scales, where an imprint of the feedback anisotropy on the CGM temperature and entropy can be appreciated. In Figure 2.14 I show the time averages of the CGM temperature and entropy (left and right of each panel respectively) for the three simulations in the set **E**. Entropy is

[6] I defined $\mathrm{SFR}(\theta;t)$ as the sum of the SFR of all gas particles with polar coordinate $\theta_i \in [\theta - \Delta\theta/2, \theta + \Delta\theta/2]$, or $\pi - \theta_i$ in the same interval, and within a distance of 5 kpc from the MBH. We used $\Delta\theta = \pi/40$.

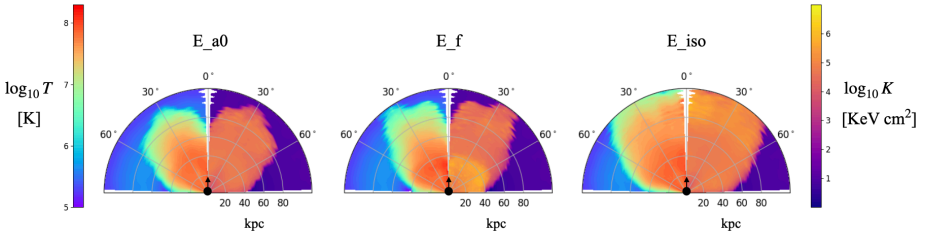

Figure 2.14: Polar plots of the time averages of CGM temperature and entropy for **E** simulations. Time averages are taken considering snapshots up to 180 Myr from t_0.

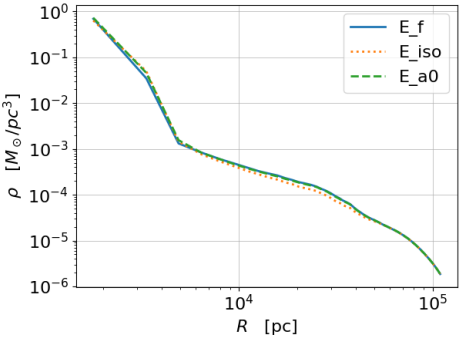

Figure 2.15: Time averages of the density radial profile of the CGM for the **E** simulations.

computed as $K = k_{\rm B} T n_e^{-2/3}$ and the time averages only consider snapshots up to 180 Myr from t_0 in order to avoid boundary condition effects caused by the finite size of the sampled halo. Fig. 2.14 emphasises that while the opening angle of the outflow on a small scale does not seem to be affected by the anisotropy of the radiation emitted by the AGN, on a larger scale, the more isotropic the radiation angular pattern, the larger the volume fraction of the CGM that is affected by the outflow. This in turn may have implications on the CGM metal enrichment, on the outflow ability to prevent cooling flows on the galaxy and thus on the galaxy cold gas growth and its star formation history on longer timescales. Despite these effects on the energetics of the gas in the CGM, the radial density profile is not affected by feedback anisotropy, as illustrated in figure 2.15, where the time averages of these profiles for the **E** simulations are shown. I provide more details on the CGM energetic balance in Appendix B.

In the analysis above, I have not considered the effect of varying the wind velocity and the radiation-wind coupling parameter, however I can speculate what the effects of this parameter space investigation might be. By changing the wind speed, an immediate effect is to change the post shock temperature in the outflow driven by such winds. As shown in Eq. (1.62), the post-shock temperature scales as the velocity squared, consequently a faster wind would result in greater 'PdV' work of the shocked wind on the outer layers and thus in greater ease of the wind to sweep away the ISM. The dependence of the effects of feedback on wind velocity was investigated by [126], who showed that indeed faster winds are able to open larger cavities at the center of galaxies and suppress SF more efficiently. Instead, I note that changing τ would correspond to modulating L. Therefore, a hint of the effect of varying τ can be inferred from the results of simulations with different luminosities, i.e. from comparing simulation sets **C** and **E**. I note that actually a $\tau < 1$ should correspond to the situation where part of the radiation escapes from the disc sub-grid scale and only a fraction τ transfers its momentum to gas at that scale. The radiation pressure of escaping radiation in such a case is not dealt in my implementation of AGN feedback and would require radiation hydrodynamics simulations.

2.5 Summary and Discussion

In this chapter, I investigated the role that spin-dependent anisotropy of AGN winds [212, 213] has in shaping the evolution of MBHs and their host galaxies. To this purpose, I implemented in the code GIZMO a sub-grid model for AGN feedback that takes into account the spin dependence of feedback anisotropy, linking and integrating existing modules for MBH accretion and spin evolution [204] and AGN wind [126]. In doing so, I assumed that the AGN disc radiation couples with gas at the disc (sub-grid) scale, completely transferring its momentum. In this way, the nuclear wind that is launched inherits the luminosity angular pattern of the impinging radiation, which is set by the MBH spin. I initially tested this novel implementation by following the propagation of an AGN wind driven outflow into a homogeneous medium, and I compared the results against simple analytical models. Then, I considered an isolated galaxy setup, thought to be formed from the collapse of a spinning gaseous halo, and there I studied the impact of AGN feedback on the MBH and galaxy evolution. I considered different prescriptions for the MBH accretion rate, i.e., constant and

equal to the Eddington rate or self-consistently evolved according to the resolved gas inflow onto the MBH. I also considered different degrees of anisotropy of the angular pattern of the launched AGN wind.
The most relevant results of this work can be summarised as follows:

- MBH feedback and fueling are tightly intertwined. On the one hand, the AGN wind affects the gas reservoir that feeds the MBH and, on the other hand, gas flowing onto the MBH supplies material and power the wind. The disc-wind system is a complex, self-regulating system [83]. We found that accounting for such self-regulated evolution or not makes a crucial difference. In our simulations with an evolving MBH accretion rate, the AGN luminosity, initially set equal to Eddington $L_{\rm Edd} = 1.2 \cdot 10^{46}$ erg/s, drops down by $1 \div 2$ orders of magnitude to $\simeq 6 \cdot 10^{44}$ erg/s, exactly because the AGN feedback limits the inflow that powers itself. Such reduced luminosity corresponds to an Eddington factor $f_{\rm Edd} \sim 0.05$, consistent with what estimated in Seyfert galaxies [239]. Such decrease in luminosity implies both a much slower MBH growth and a much weaker impact of the AGN on the host, when compared with simulations with constant Eddington MBH accretion rate. This highlights the importance of self-consistently evolving MBH accretion and feedback.

- Once MBH accretion is allowed to evolve, I found that AGN feedback has a limited impact on the host galaxy, except for the central, $\simeq$kpc scale region. A smaller, $\simeq 100$ pc cavity is cleared around the AGN. At the same time the SFR is approximately halved within the inner 0.5 kpc, while it remains at values typical of non active galaxies on larger scales. Put another way, my simulations indicate that isolated disc galaxies may be able to host luminous AGN activity without undergoing any significant star formation suppression on larger galaxy-scales[7]. I emphasise that due to the simulated timescales, the star formation suppression witnessed in

[7] I emphasise that the absence of quenching is the result of the type of setup and feedback adopted in these simulations. Indeed, in the case of an early-type galaxy in a "cooling flow" atmosphere, the presence of a jet mode feedback has been shown to be efficient in suppressing star formation and quenching the galaxy. For example, [240] performed zoom-in cosmological simulations and found that AGN jets can transform galaxies at the center of clusters in red dispersion dominated quenched galaxies, and [241] revealed how quenching of massive central galaxies happens coincidently with jet mode feedback in large scale cosmological simulations. This view is also supported by semi-analytical models [90] and observations [11, 242], which show that AGN jets can efficiently couple with the surrounding gaseous atmosphere in early type galaxies and keep the specific star formation rates low.

these simulations is the result of the AGN wind ejection of the existing ISM, while star formation suppression owing to CGM heating that prevents cooling and accreting flows on the galaxy is at most mildly captured as such process unfolds on longer $\sim$ Gyr timescales. These results agree with many observational studies that find no systematic signature of AGN feedback on the host galaxy SFR [105, 107, 108, 243] (see discussion in § 1.2.1.3 for more details). In addition, [108] remarked that AGNs, despite not showing evidence for galaxy-wide quenching, have significantly suppressed central ($\sim$ kpc scale) SFR, lying up to a factor of 2 below those of the control non active galaxies, in agreement with my findings. These results suggest that the integrated effect of secular AGN feedback, which is traced by the MBH mass, rather than an instantaneous AGN driven outflow, is required to significantly affect SF on galactic scales. In other words, the instantaneous AGN luminosity is not a proxy for the cumulative impact of AGN feedback on SF [116].

- The impact of AGN feedback on the host galaxy and on MBH growth is primarily determined by the AGN disc luminosity, rather than by its angular pattern. I found that MBHs accreting with constant Eddintong rate, corresponding to a bolometric luminosity of $L \sim 1.2 \cdot 10^{46}$ erg/s, are capable to clear kpc-scale cavities, suppressing SF by a factor of two on galactic scale, and driving outflows with large $\sim \pi/3 \div \pi/2$ semi-opening angles. For lower luminosities, $L \sim 6 \cdot 10^{44}$, achieved once self-regulation is allowed, such effects are milder and restricted to the nuclear region. This is consistent with [126] who found that increasing luminosity allows for further growth of the central cavity and suppression of SFR.

- Conversely, the imprint of the AGN luminosity angular pattern on the MBH-galaxy evolution is less marked, and can be appreciated only in cases with high (Eddington) constant accretion rate, in which the AGN impact is overall stronger. For maximally anisotropic $\sim \cos\theta$ angular pattern (**a0** simulations), most of the wind momentum and energy are funnelled in the MBH spin direction, i.e., perpendicularly to the galaxy disc, without much affecting the host galaxy. With more isotropic angular patterns, as occurring for higher MBH spin becauese of relativistic light bending, a larger fraction of the wind energy and momentum is distributed perpendicular to the spin, i.e., into the galactic disc, yielding a higher coupling between the wind and the galaxy ISM. Indeed, in the simulations with Ed-

dington accretion, I observed that AGNs with isotropic luminosity more efficiently suppress the host SFR, up to a factor of two compared to the maximally anisotropic case, and more easily sweep away gas in the nuclear region, clearing cavities up to ten times larger. However, in simulations with smaller ($f_{\rm Edd} \sim 0.05$) accretion rate, differences in the response of the galaxy to different AGN radiation anisotropies are negligible, with the exception of the CGM, on which the impact of the outflow shows small but appreciable differences with AGN feedback angular pattern. As a consequence, I expect the spin-dependent anisotropy of AGN radiation to be relevant in those scenarios characterized by high and prolonged MBH accretion episodes and by high opening angle of the ISM disc as seen by the central MBH, as both features would increase the wind-galaxy coupling and make the galaxy response more sensitive to the radiation angular pattern. These conditions might be satisfied during galaxy mergers, where large amounts of gas are funnelled into the galactic nucleus, resulting in elevated MBH accretion rates and quasi-isotropic central gas geometries, or in high redshift galaxies, characterized by thick discs and by MBH accretion rates close to the Eddington limit over long periods of time [e.g. 134, 135, 244, 245].

- The spin growth itself is influenced by the AGN angular pattern. Given a constant accretion rate, the spin growth naturally slows down due the distance of the ISCO from the MBH becoming smaller with increasing spin. In addition, as the spin becomes larger, both AGN luminosity and its isotropy increase and make the AGN feedback more capable to reduce the inflow on the MBH itself, further delaying its spin and mass growth. I witnessed a hint of this trend in the simulations with self regulated accretion, noting that more isotropic angular patterns yield slower MBH mass and spin growths. Although in these simulations this effect seems negligible. In this respect, I might speculate that, because of the angular pattern anisotropy, high-redshift slowly spinning MBHs might more easily attain accretion rates above the Eddington limit, as they would be less prone to alt accretion flows in the AGN disc equatorial plane via winds [246], but also because the efficiency of the jets potentially suppressing super-Eddington accretion rates is lower for lower MBH spins [247, 248].

While in this paper I discussed the role of the spin-dependent anisotropy of AGN winds in the context of isolated disc galaxies, I remark that this effect might be

crucial in other astrophysical scenarios where AGN feedback intervenes, such as the pairing and migration of MBH binaries, which will be the subject of the next chapters.

Chapter 3

Dynamics of MBH pairs in the presence of spin dependent radiative feedback

In this chapter I consider another application of the spin-induced raidative feedback anisotropy presented in § 2. Beyond its role in influencing the growth of MBHs and the overall impact of feedback on host galaxies, feedback anisotropy can also play a crucial role in shaping the dynamics of MBHs. It can influence their ability to pair and form bound binaries, ultimately impacting the cosmological coalescence rate of these systems, a phenomenon that the Laser Interferometer Space Antenna (LISA) is poised to investigate.

More specifically, as outlined in § 1.3.1.2, AGN feedback from accreting MBHs can alter the local properties of the surrounding gas and, therefore, its dynamical friction effect. Early indications of a sign reversal of the DF torque exerted by a rotating gaseous background affected by MBH feedback has been discussed on galactic scales by [16]. This early claim has been numerically confirmed in the context of MBH pair dynamics on CND scales [see, e.g., 249], where the pairing efficiency of the MBHs is significantly reduced by the AGN feedback anti-DF, which makes the MBHs accelerate in the direction opposite to that of the standard DF. In these studies, the energy or momentum injection has been assumed to be isotropic. However, at sufficiently small scales, the feedback may have significant deviations from isotropy, both in case of direct radiative feedback from the MBH accretion disc, as shown in § 2, as well as kinetic feedback from relativistic jets. An anisotropic feedback would increase significantly the complexity of the problem and, for some specific configurations, it may decrease the effect of feedback onto the local gaseous environment if the majority of the

energy-momentum of the outflows escapes through a minimal-resistance path before altering the gas dynamics.
Here, I consider the impact of spin-dependent radiative feedback on the dynamics of a MBH pair embedded in a CND. I explore different feedback models based on an anisotropic momentum injection in the gas. The work presented in this chapter was carried out before that shown in § 2, so the feedback model used here is different from that presented in § 2.2.2. In particular, I anticipate that here feedback anisotropy is left as a constant free parameter, decoupled from the spin magnitude, which instead can evolve following the prescriptions discussed in [250]. Moreover, while in § 2.2.2 the AGN wind is simulated by spawning gas particles from the accretion disc, here it is created by kicking gas particles in the MBH kernel. In § 3.1, I describe more in detail the model of spin-dependent feedback I adopt in this chapter. The specific setup of simulations is presented in § 3.2, while results are discussed in § 3.3. Finally, § 3.4 is devoted to summary and concluding remarks.

3.1 Methods

Here I review the sub-grid model for MBH accretion, spin evolution and AGN feedback employed in this study. The prescriptions for BH accretion and spin evolution are mostly the same presented in § 2.2.1, except for minor differences. In particular, here i) there is no angular momentum removal in (2.15) due to wind ejection, because wind is not spawned from the accretion disc, and ii) the resolved accretion is performed by means of the classical Bondi prescription of Eq. (2.19), instead of Eq. (2.18) which also accounted for the angular momentum of accreting gas. In this way here the accretion rate on the MBHs is significantly overestimated (see Fig. 2.4) compared to the simulations in § 2. Consequently, I expect that in the simulations presented in this chapter the feedback effect is also overestimated since the wind rate is proportional to the accretion rate (Eq. 2.4). This in turn may facilitate the formation of low density bubbles in the gas and thus accentuate the dynamic effect these have on MBHs inspiral.
The major difference between the model employed here and that of § 2 concerns feedback implementation. In § 2.2.2 the AGN wind is simulated by spawning gas particles from the accretion disc, distributing them uniformly on a sphere centered in the MBH, and then by kicking them outward with constant velocity. The spawned wind particles have an angular mass distribution that follows the

AGN luminosity angular pattern set by the spin, which guarantees that AGN winds anisotropy and direction is always tied to the evolving MBH spin.
In the feedback implementation used in the present study, a "kinetic energy injection" approach (see § 1.2.3) has been employed. In this model, gas particles within the MBH kernel are selected stochastically, a fraction f of their mass is accreted on the MBH, and the remaining is kicked outward with constant velocity $v_{\rm w}$ along specific directions. The fraction f is defined as $f = 1 - \dot{M}_{\rm w}\Delta t/(\sum_k^N m_k)$, where m_k is the mass of the k-th gas particle among the N selected and Δt is the BH timestep. This choice of f guarantees that the entire amount of ejected mass $(1-f)\sum^N m_k$ is, at every time-step, equal to $\dot{M}_{\rm w}\Delta t$. The probabilities to select particles are chosen to guarantee that the dynamical mass $M_{\bullet,\rm dyn}$ follows, on average, the sub-grid mass $M_\bullet + M_\alpha$ (see [140] for further details)[1].
By varying the kick direction, the outflow anisotropy can be tuned to reproduce different feedback mechanisms. In particular, the outflow can be either modelled as an isotropic wind, where the selected particles receive a kick along the radial direction, as a collimated jet parallel to the gas angular momentum, as implemented by [251], or it can be assumed to have a biconical shape, as implemented by [140]. In the latter case, the kick direction is randomly sampled within a cone of given semi-aperture $\theta_{\rm bic}$, with the cone axis either fixed in time or consistently evolved during the simulation (e.g., parallel to the MBH spin). Thus, while the direction of feedback can be chosen to be bound to that of spin, its anisotropy is completely determined by $\theta_{\rm bic}$, which is a constant free parameter, independent of spin magnitude.

3.2 Numerical simulation setup

In order to simulate the dynamics of MBH pairs in presence of spin-dependent radiative feedback, in this work I employed the publicly available N-body, meshless hydrodynamic code GIZMO [252] supplied with the implementations by [250] and [140]. This enabled me to investigate the role of feedback in the orbital evolution of MBH pairs placed in a gaseous and stellar environment.
Here I discuss the setup of the numerical simulations I performed, consisting in a MBH pair embedded in a gaseous CND and in a stellar bulge. The initial con-

[1] In order to ensure that the dynamical mass follows on average the physical mass, when $M_{\bullet,t+\Delta t} < M_{\bullet,\rm dyn}$ I only change the momentum of the selected particles, and leave the MBH dynamical mass unchanged.

ditions have been created by first initializing the stellar and gaseous components in dynamical equilibrium with the primary MBH (placed at the center of the system) and by subsequently adding the secondary MBH to the relaxed system. I achieved the first step by using the publicly available code GD_BASIC [253], building up a 'Bulge+CND+Primary' (BCP hereinafter) system characterized by:

- a spherical stellar bulge described by an [254] profile

$$\rho_{\rm b}(r) = \frac{M_\star}{2\pi}\frac{r_\star}{r(r+r_\star)^3}, \tag{3.1}$$

  where r is the spherical radial coordinate, $M_\star = 5\times10^8 M_\odot$ the total bulge mass and $r_\star = 100$ pc the bulge scale radius;

- a rotationally supported exponential disc in vertical hydrostatic equilibrium whose surface density profile is

$$\Sigma(R) = \frac{M_{\rm d}}{2\pi R_{\rm d}^2} e^{-R/R_{\rm d}}, \tag{3.2}$$

  where R is the cylindrical radial coordinate, $R_{\rm d} = 50$ pc the disc scale radius and $M_{\rm d} = 10^8 M_\odot$ the disc total mass;

- a primary MBH with dynamical mass $M_1 = 10^7 M_\odot$ at rest in the center of the system.

The stellar and gaseous components are sampled by $N_\star = 5\times10^6$ and $N_{\rm d} = 10^6$ particles respectively, corresponding to a mass resolution of $10^2 M_\odot$ for both. The spatial resolution is determined by the Plummer equivalent gravitational softening $\epsilon_{\rm soft}$. For stellar and MBH particles it is fixed at 0.1 pc and 0.33 pc, respectively, while for gas particles it is adaptively set equal to the hydrodynamic kernel size, i.e., the radius encompassing an effective number of neighbours $N_{\rm ngb} = 32$, down to a minimum allowed value $\epsilon_{\rm soft,\ min} = 0.1$. The gas particles are also initialized with a uniform temperature $T = 2\times10^4$ K, assuming an ideal equation of state with adiabatic index $\gamma = 5/3$. Once created, in order to relax the system, the BCP is evolved for 20 Myr, corresponding to ~ 6 orbits at $R_{\rm d}$ and ~ 3.22 orbits at $r_\star$. After relaxation, I introduced a secondary MBH with dynamical mass M_2 in the disc plane ($z = 0$) at a separation of 80 pc from the BCP center of mass. After the introduction of the secondary, the

position of the total center of mass shifts from the center of coordinates and its velocity is no longer vanishing, therefore the positions and velocities of all the particles are then suitably shifted in order to move back the center of mass of the BCP+secondary system at rest in the origin. Additionally, the presence of the secondary affects locally the previous equilibrium by perturbing the surrounding gas and star particle trajectories and by triggering the formation of an overdensity around the MBH soon after its introduction. Different initial conditions are created depending on the initial mass ratio $q = M_2/M_1$ and initial eccentricity e. These initial conditions are aimed at modeling the final stages of the MBHs DF-driven inspiral that brings the MBHs separation from kpc to pc scales [165, 173]. In the fiducial simulations (indicated with **f**) I initialized the secondary with $q = 1/2$ and $e = 0$ (w.r.t. the center of mass of the BCP) and initial velocity $\mathbf{v}_2(t = 0) = \sqrt{R|d\Phi/dR|}\,\hat{\varphi}$, where $\hat{\varphi}$ is the azimuthal unit vector and Φ is the gravitational potential of the BCP. Compered to this fiducial runs, simulations labelled as **q** all have a lower mass ratio ($q = 1/6$), simulations labelled as **e** have a non-vanishing initial radial velocity component that sets the initial eccentricity to $e = 0.5$ (see Table 3.1). For each of these three initial setups (**f, q** and **e**) I performed four simulations considering different feedback models: i) the case without feedback (labelled as **nofb**), ii) isotropic feedback (labelled as **iso**), iii) biconical feedback with the cone axis fixed and parallel to the vertical direction $\hat{z}$ (labelled as **z**) and iv) biconical feedback with the cone axis aligned to the evolving MBH spin direction (labelled as **a**). In the latter two cases I fixed $\theta_{\rm bic} = 45°$ and, whenever feedback is present, I used $\tau = 1$, i.e., the radiation momentum flux is entirely transferred to the wind, and $v_{\rm w} = 500$ km/s. I highlight that the wind velocity used in this chapter is a factor of 6 smaller than that used in § 2. The choice of this value has been dictated by a practical factor, namely speeding up the simulations. Indeed, a lower wind velocity corresponds to a lower post-shock temperature (Eq. 1.62) and hence lower sound speed, and both this and the wind velocity itself enter the Courant timestep criterion (Eq. 24-25 in [216]), such that a smaller wind velocity yields higher timesteps. Although this wind velocity was determined by the practical need to make the simulations faster, it is still consistent with expected values of AGN winds velocities of warm absorbers, which are characterised by wind speeds of $100 - 1000$ km/s [72]. Our complete simulation suite therefore comprises a total of 12 runs.

I remark that the modules for sub-grid accretion plus spin-evolution and stochastic feedback (if present) are switched on for the secondary MBH only. This means

Table 3.1: Summary of the parameters adopted in the simulations. *Top:* parameters that vary across our simulation suite. The following parameters are the same for all runs: for feedback launching $\theta_{\rm bic} = 45^\circ$, $p = 1$, $v_{\rm w} = 500$ km/s and for the sub-grid system $a = 0.5$, $f_{\rm Edd,0} = 0.01$, $M_\alpha/M_\bullet = 0.005$ and $\alpha = 0.1$. This choice of M_α guarantees that the initial disc mass is smaller than the disc self-gravitating mass $M_{\rm sg}$. *Bottom:* gravitational softening for the different components.

	q	e	$\frac{J_\alpha}{J_\bullet}$	$\frac{M_\alpha}{M_{\rm sg}}$	$R_{\bullet,\rm max}$ [pc]
f	1/2	0	2.85	0.52	3
q	1/6	0	4.84	0.40	1
e	1/2	0.5	2.85	0.52	3

type	$\epsilon_{\rm soft}$ [pc]
gas	0.1
bulge	0.1
MBH	0.33

I am considering the impact of feedback from the secondary on its own dynamics without accounting for the possible effects the feedback from the primary MBH may have on the secondary one. This is justified by the fact that we are in a regime where the relative separations of the two MBHs is large compared to the local regions possibly affected by feedback, but see § 3.4 if this is not the case. In all simulations, I initialise the secondary MBH mass as $M_\bullet = M_2/1.005$, $M_\alpha = 0.005 M_\bullet$, such that $M_\bullet + M_\alpha = M_2 (\equiv M_{\bullet,\rm dyn})$. The disc angular momentum direction is along the $z-$axis, while the initial MBH spin is "flipped downwards" at an angle $5\pi/6$, with magnitude $a = 0.5$. The initial retrograde orientation of the spin has been chosen so as to cause an initial alignment of the spin towards the $z-$axis. This alignment causes the spin to be momentarily aligned in the plane of the CND and thus can potentially enhance the coupling between gas and feedback in those simulations (**a**) in which the direction of feedback is tied to spin. The initial Eddington ratio is set at $f_{\rm Edd,0} = 0.01$, which together with the other sub-grid parameters constrains the value of $J_\alpha/J_\bullet$ (Eq. 5 in [250]).

3.3 Results

I discuss now the outcome of the simulations I carried out, starting from **f**-simulations in § 3.3.1. In the subsequent sections I perform the same analysis for **e**- and **q**-simulations. Some snapshots (at 1 and 4 Myr) are shown in the

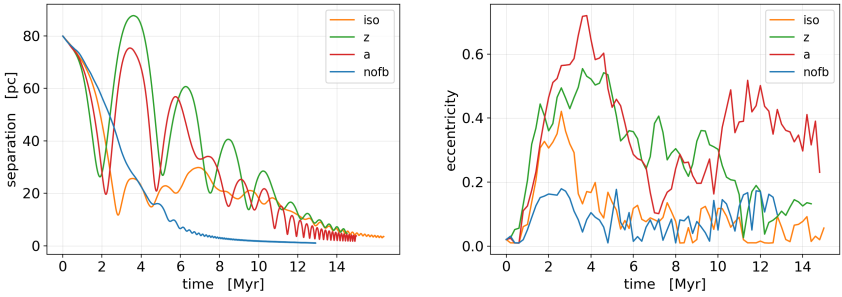

Figure 3.1: Time evolution of the MBH separation (*left*) and eccentricity (*right*) in **f**-simulations.

Appendix for the entire suite of simulations.

3.3.1 f-simulations

3.3.1.1 Qualitative analysis

The time evolution of the MBH separation and M_2 eccentricity is shown in Fig. 3.1, for the four tested different feedback models in **f**-simulations. Overall, I observe that in presence of feedback the timescale of orbital decay of M_2 is larger and the orbits tend to develop higher eccentricities. We can get some insights into such behavior from the evolution of the torques acting on M_2 shown in Fig. 3.2. The torque in **f_nofb** is always negative, indicating that efficient DF is acting on M_2, hence causing a net loss of angular momentum and energy, leading to rapid inspiral towards M_1. On the other hand, switching feedback on, the torques on M_2 can become positive, indicating in these phases an inefficient (or even reversed) DF, i.e., a positive acceleration, and hence an orbital decay at slower pace.

In more details, as shown in Fig. 3.2, the z-component of the torque acting on M_2 initially quickly drops to negative values. In this phase, lasting ~ 2 Myrs, in **f_iso, f_z** and **f_a** the torque is twice as large (in magnitude) than that in **f_nofb**, i.e., DF is initially enhanced by feedback processes. In all cases, the initial larger loss of angular momentum in the presence of feedback is accompanied by an increase in eccentricity (Fig. 3.1). Later on, the z-component of the torque becomes positive, i.e., the angular momentum increases, something not seen in **f_nofb**, where the torque is always negative.

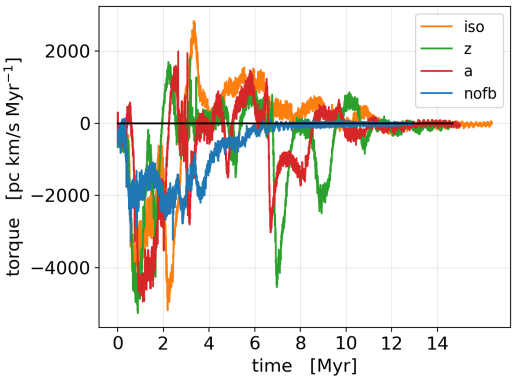

Figure 3.2: Time evolution of the z-component of the total torque acting on M_2 in **f**-simulations.

I notice (see Fig. 3.2) that in **f_iso** the initial negative torque phase is prolonged slightly further compared to the other feedback simulations, causing the first pericenter to be closer to M_1 (~ 10 pc), and to occur at a later time (~ 3 Myr). Because of such longer journey to the pericenter, M_2 looses more energy compared to the **f_z** and **f_a** cases, consequently acquiring a smaller eccentricity, $e \simeq 0.1$, with the separation stalled around $\simeq 20$ pc for the subsequent $\simeq 10$ Myr. In this phase, M_2 is subject to a net positive torque that traces a 'reversed' DF. Then, the system enters a further phase in which the separation decreases again.
In **f_z**, the eccentricity grows to $e \simeq 0.5$ when M_2 reaches the first apocenter, and then slowly decays. I also observe that the first apocenter is located at a distance larger than the initial MBHs separation, signaling a net gain of energy.
In **f_a**, M_2 orbits follow a similar trend, with an initial rapid rise in eccentricity followed by a slower circularization along M_2 orbital decay.
Finally, the two MBHs form a binary, at ~ 5 Myr in **f_nofb**, and between 10-12 Myr in feedback simulations. I comment the convergence of these results in § E.

3.3.1.2 Quantitative analysis

DF is generally attributed to the many two-body encounters between a massive object (M_2 in the present context) and background stars [166]. In the case of a

gaseous background, DF can be understood in terms of the gravitational interaction between M_2 and the density wake generated by its motion in the gaseous background. In fact, the relative motion of M_2 with respect to the background creates an overdensity on the side opposite to the relative velocity between M_2 and fluid. The gaseous DF acts in all respect as a non-conservative drag force [172]. However, the gas around the MBH can be (partially) blown away by radiative feedback, thus hampering the formation of the density wake itself. The density enhancement trailing M_2 is, in this case, replaced by an underdensity, I refer to it as "density bubble", affecting M_2 dynamics in a decisive manner.
In order to quantify the effects the radiative feedback has on M_2 orbital decay, I introduce an "anisotropy vector" defined as

$$\mathbf{A} \equiv \sum_i m_i \, w(r_i) \frac{\mathbf{r}_i}{r_i}. \tag{3.3}$$

Here, the sum is intended over all particles (with mass m_i and position vector $\mathbf{r}_i$ in the CND plane centered in M_2) within a distance from M_2 equal to the minimum between 30 pc and the MBHs separation. Each particle is weighted by the force softening function implemented in GIZMO, w. As $\mathbf{A}$ evolves in time through coordinates $\mathbf{r}_i$, I consider the (normalised) difference $\Delta\mathbf{A} \equiv \mathbf{A}_0 - \mathbf{A}$, where $\mathbf{A}_0$ is the anisotropy vector computed by considering, at each time, the current M_2 position but the initial distribution of gas. This allows us to quantify the time evolution of the anisotropy due to the MBH-gas interaction independently of any possible anisotropy already present at the beginning of the simulation.[2] The direction of $\Delta\mathbf{A}$ indicates the axis along which the anisotropy develops, pointing towards the lower density side. Therefore, in the presence of feedback, $\Delta\mathbf{A}$ indicates the bubble location, while, in absence of feedback, $\Delta\mathbf{A}$ points in the direction opposite to the over-density wake. Fig 3.3 shows $\Delta\mathbf{A}$ in a snapshot of **`f_iso`**.
If I now consider $A_2 \equiv \Delta\mathbf{A} \cdot \mathbf{v}_2$, i.e., the projection of $\Delta\mathbf{A}$ along the M_2 velocity vector $\mathbf{v}_2$, we see that a positive value of A_2 would indicate that the bubble lies in front of M_2 (or that the overdensity lies behind M_2 in **`nofb`**-type simulations). In this case the gas distribution around M_2 exerts a gravitational force opposite to the direction of motion, resulting in an efficient DF. On the other hand, the underdense bubble lies behind M_2 for negative values of A_2, thus imparting a net acceleration to M_2 (see Fig. 3.3).

[2] I note that this choice would be slightly affected by the Poisson noise in the initial distribution of the gas.

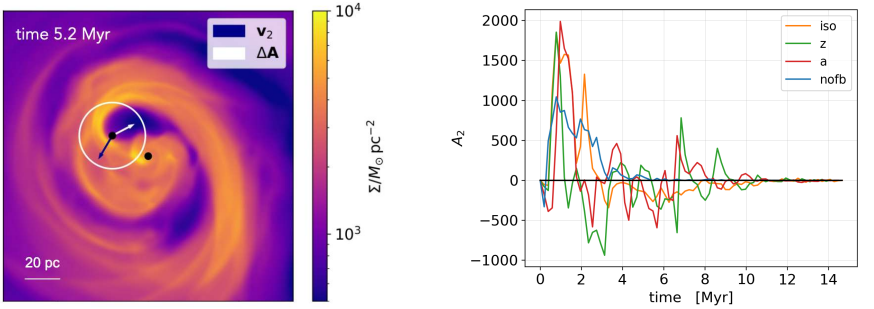

Figure 3.3: *Left*: The surface density Σ (in $M_\odot/\mathrm{pc}^2$) in a snapshot of run **f_iso**. The two black dots indicate the positions of the MBHs. The white circle bounds the region around M_2 used to define the anisotropy vector $\mathbf{A}$, indicated by the white arrow. The dark-blue arrow indicates $\mathbf{v}_2$, the M_2 velocity. *Right*: Time evolution of the anisotropy projection A_2 in **f**-simulations.

I can now use A_2 to interpret the dynamics of M_2 described in 3.3.1. Fig. 3.3 shows the evolution of A_2 for all four **f**-simulations. First, I observe that in **nofb** A_2 is positive, meaning that an overdensity is present behind the MBH. This produces a negative torque that forces M_2 to rapidly inspiral towards M_1. Conversely, when feedback is switched on, A_2 has initially positive values (and larger compared to **nofb**), suggesting that DF is enhanced in the early inspiral phase by the action of feedback. In Fig. 3.4 I compare snapshots taken at the same time (2 Myr after the start of the simualtion) for **f_nofb** and **f_iso**. In the first case, the formation of a spiral wave in the disc is accompanied by the presence of a moderately low-density region in front of M_2. When feedback is included, this region exerts a weaker resistance to the gas particles blown away by radiation pressure, allowing the bubble to expand in such direction. As a consequence, the gas surrounding M_2 exhibits a larger anisotropy, i.e., an initially larger value of A_2 corresponding to a larger negative torque. From Fig. 3.3, I also notice that in **f_iso** the phase during which the bubble lies in front of M_2 ($A_2 > 0$) lasts longer compared to the other feedback models, consistently with the more prolonged negative torque observed in Fig. 3.2. Indeed, isotropic feedback is more efficient than anisotropic models (**z** and **a**) in keeping the low density bubble "open", as particles are more easily kicked in the CND plane (where the gas density is higher), hence more likely able to prolong the dynamical effect of the preceding bubble.

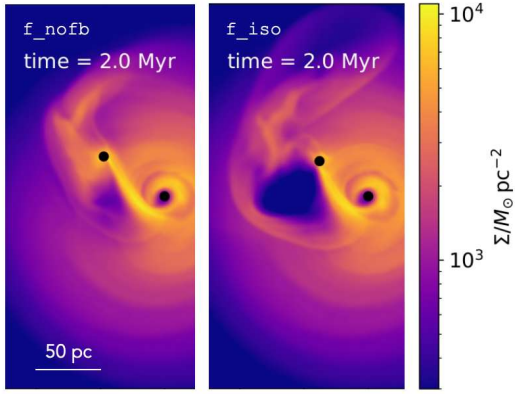

Figure 3.4: Two snapshots at time $t = 2$ Myr of runs **f_nofb** (*left*) and **f_iso** (*right*).

After the initial preceding-bubble ($A_2 > 0$) phase, all simulations with feedback show a drop and eventually a sign change in A_2. This turning point approximately corresponds to M_2 reaching the pericenter. Indeed, as M_2 approaches the pericenter, its orbital speed exceeds that of the gas, overtaking the bubble which then lags behind. In this configuration, A_2 is negative, and M_2 accelerates, increasing its eccentricity. In particular, **f_z** displays the most negative value of A_2, implying that M_2 receives more energy in the process. In this case, M_2 reaches the first apocenter at a distance which is actually larger than the initial MBHs separation. In **f_iso** A_2 remains negative in the time interval $\simeq [3-10]$ Myr, i.e., M_2 keeps being accelerated by the trailing bubble. Interestingly, in our simulations such feedback-driven acceleration is approximately balanced by stellar DF, and the semi-major axis remains approximately constant during this phase (see Fig. 3.3 for a snapshot from this evolutionary phase).

3.3.2 e-simulations

M_2 orbits corresponding to simulations with an eccentric initial condition are shown in Fig. 3.5 (top panel), together with the evolution of A_2 (bottom panel). In **e_nofb**, the MBH separation rapidly decays and orbit circularizes. This occurs as M_2 produces a density wake on the side opposite to the relative velocity between itself and the fluid. Therefore, since the orbital speed of M_2 close to

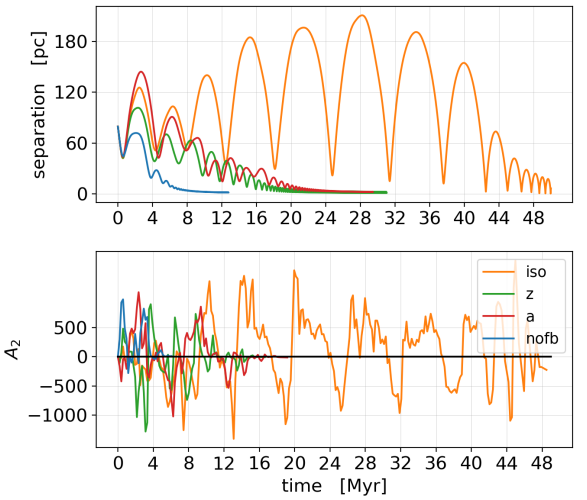

Figure 3.5: Time evolution of the MBHs separation (top) and anisotropy projection A_2 (bottom) in **e**-simulations.

the pericenter is larger than the local gas rotational velocity, the wake lags behind and M_2 slows down. On the other hand, near the apocenter the MBH velocity is smaller than the disc one and the wake is dragged in front of M_2, increasing its angular momentum and accelerating it. The combination of these two opposite effects at pericenter and apocenter results in orbit circularization [255, 256]. When radiative feedback is switched on, the density wake is somewhat destroyed and a low density bubble is created instead. Circularization is thus less effective, as it can be seen in Fig. 3.5, top panel, in the cases of **e_z** and **e_a**. In **e_iso**, because of the stronger impact of feedback on the surrounding gas, the density wake is more efficiently blown away and replaced by a low density bubble, which now follows the same trend of the wake in **e_nofb**, but with the opposite gravitational effect. Therefore, at apocenter the bubble falls in front of the MBH, enhancing DF, while at pericenter it trails behind, accelerating the MBH, with the net effect of increasing the eccentricity. This behavior is illustrated in Fig. 3.5 where, in **e_iso**, M_2 develops relatively high ($0.5 \lesssim e \lesssim 0.9$) eccentricities. Correspondingly, A_2 is positive (i.e., bubble lies ahead) at apocenter and negative (i.e., bubble lies behind) at pericenter, supporting our interpretation (see Fig.3.5, bottom panel).

3.3.3 q-simulations

Fig. 3.6 illustrates the time evolution of MBHs separation and of A_2 in the case of a $q = 1/6$ mass ratio. Overall, we can see that, in the feedback runs, M_2 orbits differ more from the **nofb** case, compared to what we have seen in **f** and **e** cases. The evolution of the orbital separation is again associated with the effects induced by the feedback. In **q_z**, M_2 eccentricity increases up to ~ 0.5 in the first ~ 15 Myr, with the growth associated to an oscillating behaviour of A_2, positive at apocenter and negative at pericenter, as discussed in § 3.3.2. By contrast, in **q_iso** and **q_a** M_2 orbits are quasi-circular, with an average eccentricity $e \lesssim 0.1$. In these cases, M_2 orbit is not going to shrink appreciably by the end of the simulation. Again, the increasing/decreasing trends of the MBHs separation due to positive/negative torques are linked to feedback, as they correspond, respectively, to negative/positive values of A_2 (Fig. 3.6, bottom). Interestingly, in **q_a**, after $\simeq 25$ Myr the distance of M_2 from M_1 shows, on average, a slightly increasing trend. I can explain this behavior as follows: due to the pressure gradient in the disc, the gas circular velocity is smaller than that of the MBH, settled on a quasi-circular orbit, and hence the bubble created in the disc by feedback is overtaken by the MBH, favoring its acceleration. Therefore, it may happen that stellar dynamical friction counterbalances this feedback acceleration, helping to keep M_2 on a quasi-circular orbit.

3.3.4 Angular pattern

In this analysis, I have shown through the quantity A_2 how radiative feedback is linked to the torques experienced by M_2, and how it can have an impact on orbital eccentricity and decay timescale. Here, I will discuss in a more quantitative way the relation existing between gas density perturbations due to feedback and the orbital decay timescale and eccentricity.
If I consider the angle θ between $\Delta\mathbf{A}$ and $\mathbf{v}_2$, I do see that in the absence of feedback M_2 creates a trailing density wake, i.e., $\Delta\mathbf{A}$ tends to be directed parallel to $\mathbf{v}_2$, resulting in $\theta \lesssim \pi/2$. On the other hand, when feedback effects are considered, the low density bubble in the disc can be either trailing or leading with respect to M_2, depending on the relative velocity between the disc and M_2. This corresponds to $\theta \gtrsim \pi/2$ and $\theta \lesssim \pi/2$, respectively. For all simulations, I follow the time evolution of θ, and compute its weighted probability distribution. In practice, any occurrence of a given angle is weighted with the current value of $|\Delta\mathbf{A}|$, and the resulting frequency distribution of θ is then normalised. Results

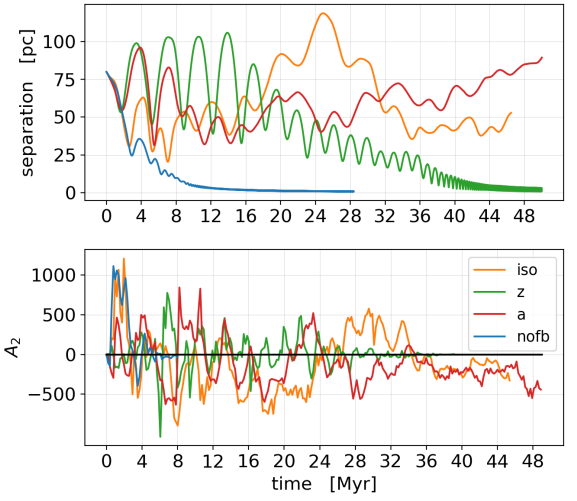

Figure 3.6: Same as Fig. 3.5 but for **q**-simulations.

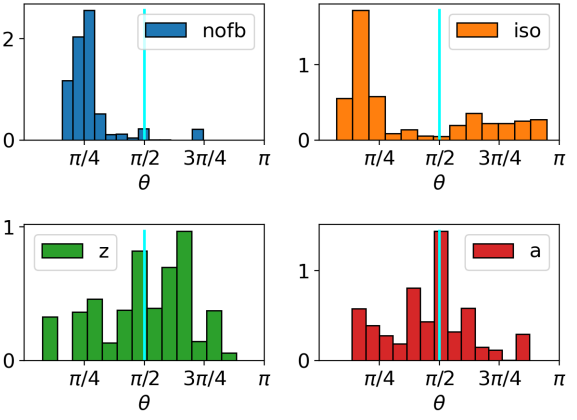

Figure 3.7: Probability distribution of the (weighted) angle θ between the anisotropy difference $\mathbf{\Delta A}$ and M_2 velocity $\mathbf{v}_2$ (see text for details) in the **f**-simulations.

are shown in Fig. 3.7 for **f** simulations (the cases **q** and **e** are reported in § F). As expected, the distribution in **nofb** is peaked at small angles ($\lesssim \pi/2$), whereas the feedback cases exhibit much more spread values, across the entire range. In particular, the more the peak of the distribution shifts to larger values, the more frequently the secondary will be accelerated by feedback, making DF inefficient. Therefore I consider $\langle\theta\rangle$, the mean of θ, as a proxy for DF efficiency and, for each simulation, I compare its value with the orbital decay timescale and the mean eccentricity.

In Fig. 3.8 (top panel), I plot $\langle\theta\rangle$ against the orbital decay timescale, defined here as the time required by M_2 to reach an orbital semi-major axis < 10 pc. Simulations without feedback present lower mean values of θ and lower values of decaying timescale, while both quantities are larger in feedback simulations, confirming that a feedback-induced trailing bubble delays the inspiral of M_2 toward M_1.

In particular, if I compare **f** and **q** simulations, both with initial circular orbits but different mass ratios, I observe that by lowering the mass ratio by a factor of 1/3 (i.e., moving from **f** to **q**) the decay timescale is significantly delayed. This indicates that feedback is more likely to affect lighter MBHs dynamics, or, in other words, that the feedback accelerating force has a softer scaling with the perturber mass M compared to the DF force (which is $\propto M^2$). This is consistent with [257] and [258], who showed that the feedback-induced force acting on a pertuber moving in an homogeneous medium scales as $\propto M^{3/2}$.

Similarly, in Fig. 3.8 (bottom panel) I compare $\langle\theta\rangle$ with the mean eccentricity. In the absence of feedback, DF is efficient and both $\langle\theta\rangle$ and mean eccentricity are small (< 0.2), even for **e_nofb**, which started eccentric. On the other hand, when feedback is turned on, the majority of simulations exhibits excited eccentricities (or hindered circularization, as in **e_z** or **e_a**). By contrast, in three cases (**f_iso**, **q_iso** and **q_z**), the secondary mean eccentricity remains small (~ 0.1), comparable with those found without feedback. The reason behind this different behaviour is that these simulations are characterized by prolonged stages of trailing bubbles in which feedback acceleration is counteracted by stellar DF.

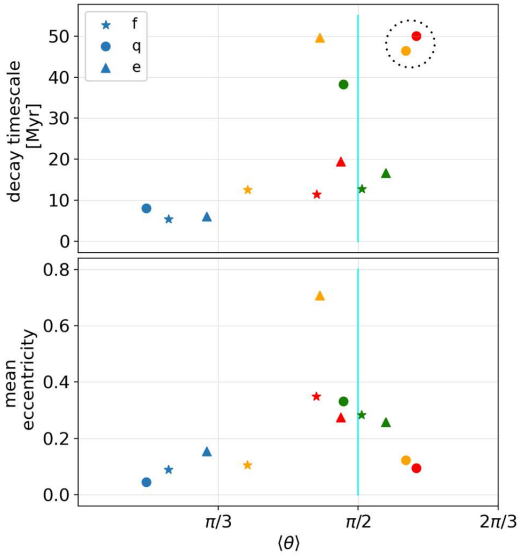

Figure 3.8: (*top*) The decay timescale of M_2 vs the mean value of the angle θ between the anisotropy difference $\mathbf{\Delta A}$ and M_2 velocity $\mathbf{v}_2$, for the entire simulation suite. The decay time is estimated as the time that the semi-major axis of M_2 takes to reach an orbital distance to M_1 of 10 pc. The different colors label the different type of feedback with the same legend of previous figures. Note that for the two runs in the dotted circle (**`q_a`** and **`q_z`**) the time indicated is the stop time of the simulation, as in these two cases M_2 did not reach an orbital separation of 10 pc within the simulation time. (*bottom*) The mean eccentricity of M_2 vs the mean of θ. The legend is the same as in top panel.

3.4 Summary and Conclusions

Using the publicly available code GIZMO, I have run a suite of simulations aimed at studying the dynamics of a MBH pair embedded in a gaseous circumnuclear disk. By means of dedicated sub-resolution prescriptions, I could model the dynamics in the presence of spin-dependent feedback, and compare results obtained with different feedback models, and to a benchmark case with no feedback at all. Overall, I observed that feedback significantly alters the MBHs dynamics and different feedback models produce large differences in the orbital evolution of the MBH pair.
Our results can be summarized as follows:

- feedback can both raise and suppress DF with the net effect of delaying the shrinking timescale of a MBH pair. This very fact bears important consequences when we are to model the cosmic population of MBH binaries, and their detectability via electromagnetic *and* gravitational waves;
- feedback has also a relevant effect on the eccentricity of MBHs orbits, exciting it or weakening the circularization process. Again, this fact is relevant for an assessment of the properties of MBH pairs as a cosmological population;
- finally, the effect of feedback on the dynamics of MBH pairs is more pronounced for smaller MBH masses.

These results then highlight that MBHs dynamics strongly depends on the feedback model assumed, i.e. whether we are considering isotropic or anisotropic feedback, with fixed or spin-dependent collimation axis. It is therefore crucial to model the anisotropy and direction of feedback consistently with the MBH spin in order to reliable assess the role of feedback in the evolution of MBH pairs. This is the only way to consistently capture the interplay between feeding and feedback, allowing a proper modeling of MBHs pairing, which is essential in view of forthcoming low-frequency GW missions such as LISA [259].
Due to simplified modeling, a number of caveats that we have to keep in mind when interpreting these results do exist. Specifically:

- This analysis is limited to coplanar orbits, an assumption justified by the fact that both the CBD and the MBHs inherit their angular momentum from the parent merging galaxies, leading to orbits likely laying in the same

orbital plane [173, 260]. Nonetheless, if coplanarity is not guaranteed, the pair inspiral is initially driven mainly by the DF exerted by the stellar bulge, while gaseous DF dominates once the MBHs separation becomes small enough that the MBHs spend most of their time in the disc [18]. As a consequence, for non-coplanar orbits, I expect the feedback-induced eccentricity and delayed decay to be initially negligible and to become progressively more important as the pair shrinks and gets closer to binary formation.

- Another important element overlooked here is the feedback from the primary. The primary has a mass two (six) times larger than the secondary in **f** and **e** (**q**) simulations and thus it can support Eddington limited accretion rates as many times larger. As a consequence, the primary is likely to form larger low density bubbles and to mitigate the dynamical impact of gas on the secondary simply by expelling it from its surrounding. More in detail, I expect that once the secondary spirals within the cavity cleared by the primary, both the proper and reversed gaseous DF would severely drop, leaving further inspiral to be driven by interaction of stars only. In this scenario, the eccentricity build up by the presence of feedback at separations larger than the primary cavity could be partially diminished once the secondary enters the central cavity where only stellar DF operates. Similarly, the effect of delaying the orbital decay attributed to the feedback-induced reversed DF ceases once the secondary enters the inner cavity of the primary, likely resulting in shorter pairing timescales than those observed in my simulations.

- In **z** and **a** feedback models the anisotropy has been realized by kicking the gas particles within a well-defined cone, as if the driving radiation emitted by the subgrid disc had a step-like angular pattern, non-vanishing within the cone. In reality, the disc radiation angular pattern can be described with a continuous function which depends upon the MBH spin and therefore evolves with it, as shown in § 2.

- I have not included any form of cooling in the simulations. Cooling can potentially make the low density bubbles expand as momentum-driven structures, hence more slowly, since the shock wind thermal energy that swells the bubbles is radiated away. Therefore, cooling may have an impact on the bubbles formation/expansion which, in turn, may reflect on the

MBH dynamics;

- the MBH wind has been simulated via injection of kinetic energy only, by adding momentum to gas particles within the MBH kernel. The lack of thermal energy injection tends to postpone the wind thermalization, as discussed in § 1.2.3, thus speeding up the bubble expansion, which, again, may affect the MBH dynamics;

- If the region within $R_{\bullet,\max}$ (the maximum MBH kernel size) is emptied, i.e. density vanishes because a sufficiently large bubble has formed around the MBH, feedback is artificially shut off since no more particles are eligible to be kicked, until the MBH kernel is refilled. This can weaken bubbles expansion thus influencing the MBH orbital evolution.

Some of the limitations listed above are naturally overcome by the feedback model presented in § 2.2.2. I expect that feedback model to affect the formation of low density bubbles and hence the MBHs inspiral rates, compared to the work of this chapter. Indeed, on the one hand, i) § 2 model would tend to produce wider bubbles because feedback is not artificially shut off once gas particles escape the BH kernel and ii) wind launching covers the whole solid angle, irrespective of anisotorpy. On the other hand, i) the accretion prescription adopted here tends to largely overestimate the accretion rate, and hence feedback, compared to the modified Bondi of Eq. (2.18) and ii) the kinetic energy injection feedback model employed in this chapter would be prone to generate stronger feedback also because of the delayed wind thermalisation intrinsic to this approach, than achieved via launching spawned wind particles. It is therefore not obvious how and by how much bubble formation and MBHs dynamics would differ due to using these different feedback models.

Chapter 4

Does anisotropic AGN feedback hamper the migration of MBH binaries?

In this chapter I present another astrophysical context in which the spin-dependent feedback anisotropy plays an active role: the migration of MBH binaries in circumbinary discs (CBDs). As discussed in § 1.3 and § 3 the evolution of MBH pairs and binaries in a gaseous environment is altered once AGN feedback is taken into account. AGN feedback affects the gas distribution surrounding the MBHs, altering the gravitational interaction with it and hence mitigating the resulting drag force on the MBHs. This reflects in delayed/reversed inspiral in the DF regime (when MBHs have tens of pc separations), and in stalling orbital shrinkage in gaseous hardening regime [199] (where MBH have pc scale separations and are bound). In particular, [199] found that if the binary clears a cavity, AGN feedback escapes through the cavity having little impact on the binary dynamics, which is already in a slow migration regime. By contrast, if no cavity forms and the MBHs are embedded in the disc gas, AGN feedback manages to clear a "feedback cavity" around the MBHs, and the binary migration is stalled by the lack of gas to exchange torques with, restoring slow migration. However, [199] limited to isotropic feedback, which might overestimate the impact of AGN feedback on the surrounding gas and hence its ability to hamper the binary migration. Anisotropic, i.e. collimated radiative feedback, may reduce the feedback coupling with the CBD, yielding a smaller feedback cavity and possibly allowing to recover fast binary migration when it is predicted to occur in the absence of feedback. Therefore, the MBH spin, through its influence on feedback anisotropy, could have an important impact on binary dynamics. I recall that

besides this effect, the MBH spin also affects the emission of GWs in the late inspiral and the MBH merger remnant recoil velocity, and hence its evolution has been included both in semi-analytical [261, 262] and numerical [263, 264] models of binary dynamics.
In the work presented in this chapter I aim at improving the investigation carried out by [199], by accounting for the spin-dependence of feedback anisotropy and by self-consistently evolving spin, accretion and feedback. In doing so I will employ the dedicated sub-grid model developed in § 2, with minor modifications. This would enable to address to what extend feedback anisotropy, as naturally set by the spin, can affect the ability of AGN feedback to hamper MBH migration. This chapter is structured as follows: in section § 4.1 I present some improvements of the numerical model, while in § 4.2 I present the setup and simulation suite. Results are shown in § 4.3 and their discussion and conclusion in § 4.4.

4.1 Methods

The accretion and feedback model used in this work is the same as that presented in § 2, with some modifications dictated by the different physical scales involved in the present context, where we can resolve down to hundredths of a pc, compared to the galaxy-scale application in § 2, where the minimum resolution was on the pc scale. In particular, the novelty with respect to the version in § 2.2.1 consists in how the inflow $\dot{M}_{\rm in}$ onto the sub-grid disc from resolved scales is modelled. Now the MBH particle is treated as a sink, such that all gas particles bound to the MBH and orbiting around the it with apocentric radius smaller than $R_{\rm sink}$ are captured in the sub-grid system. In particular, if the disc mass is zero, i.e. the MBH is quiescent, then the mass and angular momentum of the captured particles are added to sub-grid variables $M_{\rm capt}$ and $\mathbf{J}_{\rm capt}$. Then, a sub-grid disc is created (i.e. AGN activity is turned on) and initialised with $M_\alpha = M_{\rm capt}$ and $\mathbf{J}_\alpha = \mathbf{J}_{\rm capt}$ only once the accretion rate $\dot{M}_{\rm acc}$ computed from these quantities exceeds or is equal to one tenth of the Eddington accretion rate. At this point, at each time-step, the mass and angular momentum of the captured gas particles are directly added to M_α and $\mathbf{J}_\alpha$. In addition, in order to account for unresolved processes that make the gas loose angular momentum close to the MBH, I force the gas particles within a distance $R_{\rm ext} \geq R_{\rm sink}$ from the MBH to loose their angular momentum (with respect to it) in an orbital

time. The radius $R_{\rm sink}$ is defined as the self-gravitating radius of the subgrid disc, or of a disc with $f_{\rm Edd} = 0.1$ is the MBH is quiescent, and $R_{\rm ext}$ as the self-gravitating radius of a disc with $f_{\rm Edd} = 0.01$. The self-gravitating radii are computed from Eq.(A6) in [3]. In addition, the sink and external radii are required to fulfill the constraint $\epsilon_\bullet \leq R_{\rm sink} \leq R_{\rm ext} \leq R_{\rm Hill}$, where $\epsilon_\bullet$ is the MBH gravitational softening and $R_{\rm Hill}$ is the MBH Hill radius[1].
In addition, since gas dynamics in the CBD and the opening a central cavity are influenced by the competition between the binary tidal torque and the viscous torque (see § 1.3.2.2), I included the effect of gas viscosity in the Navier-Stokes fluid equations, similarly to [265]. More precisely, I set the gas particles kinematic shear viscosity to be

$$\nu = \alpha R c_{\rm s}^2 / v_\varphi, \tag{4.1}$$

where $\alpha = 0.1$ is the Shakura & Sunyaev viscosity parameter, $c_{\rm s}$ the sound speed of the particle, R its distance from the binary center of mass and v_φ its azimuthal velocity (with respect to it). Bulk viscosity is set to zero. This viscosity prescription is meant to capture the turbulence-driven loss of angular momentum triggered by the magneto-rotational-instability, typical of magnetized and differentially rotating discs [52] (see § 1.1.4.3), therefore it does not apply to outflowing gas, pushed radially outward by AGN feedback. As a consequence, I use Eq. (4.1) only for non-wind particles that have $v_r < 1/2 v_\varphi$, where v_r is the gas particle radial velocity, and ν is set to zero otherwise. In addition, since gas particles within a MBH Hill radius have closed orbits around it and form a minidisc, for such particles R, v_r and v_φ in the above formulae are taken as relative to the closest MBH, instead of to the binary center of mass.

4.2 Setup and simulations

In this work, I use [19, 196] criterion to select binary - CBD systems in different migration regimes and I study how the binary dynamics is altered by the presence of AGN anisotropic feedback. According to [19, 196] criterion (Eq. 1.71), binary migration is fostered by hot and thick discs hosting low mass MBHs at small separations, as all these properties concur in preventing the formation of a cavity ("no-cavity" regime), whereas binary migration is slown down in the

[1]The Hill radius is defined as the radius of the sphere around the MBH where its own gravity dominates over that of the companion. For and equal mass binary, according to Eq. (8.89) in [167], it is equal to half of the binary separation.

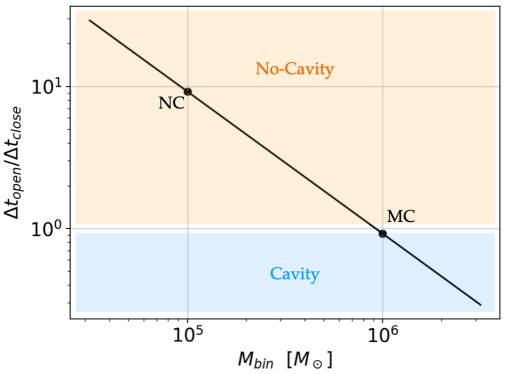

Figure 4.1: The black line shows the [19] gap-opening criterion and bullet points the simulations setups.

opposite region of parameter space, which instead favours the formation of a cavity ("cavity" regime).
In the following I will consider two sets of simulations, the first, denoted with **NC**, with the system lying in the no-cavity regime, and the second, indicated with **MC**, chosen so that a mild cavity forms and the system falls in between the two aforementioned regimes. The reason for this choice is the following: on the one hand, in the no-cavity regime, isotropic feedback has been shown to efficiently hamper migration due to the formation of a feedback cavity [199], which rises the question whether in this regime anisotropy could diminish such effect and reestablish fast binary migration. On the other hand, [199] found that isotropic feedback in the cavity regime has little impact on binary dynamics, suggesting anisotropy not to be relevant in this case, as it would mitigate the effect of an already not effective isotropic feedback, which leads us to consider its impact in an intermediate (mild-cavity) regime.
For both **NC** and **MC** simulation sets I create a binary+CBD+bulge system for the initial condition in the following way. The CBD extends up to $R_{\rm out} = 10\, a_{\rm bin0}$ and contains a central cavity of radius $R_{\rm in} = 2\, a_{\rm bin0}$, where $a_{\rm bin0}$ is the initial MBHs separation. The CBD surface density profile follows a Mestel profile

$$\Sigma(R) = \frac{M_{\rm d}}{2\pi R_{\rm in}(R_{\rm out} - R_{\rm in})} \frac{R_{\rm in}}{R}, \quad R_{\rm in} \leq R \leq R_{\rm out} \tag{4.2}$$

where $M_{\rm d}$ the CBD mass. I determined the gas azimuthal velocity and verti-

cal density profile using the code GD_BASIC [253] assuming the CBD to be in dynamical equilibrium with a central point-like potential of mass $M_{\rm bin}$ and an external potential that mimics the presence of a spherical stellar bulge.
In both simulation sets I used $a_{\rm bin0} = 2$ pc, $M_{\rm d} = 10^5$ $M_\odot$ and gas particles are initialized with uniform temperature of $6 \cdot 10^3$ K, solar metallicity. In **NC** I set $M_{\rm bin} = 10^5$ $M_\odot$, whereas $M_{\rm bin} = 10^6$ $M_\odot$ in **MC**. I modelled the bulge with a Plummer potential of core radius 65 pc and total mass $3 \cdot 10^8$ $M_\odot$, consistent with the black hole mass-bulge mass relation [75]. The two simulations sets are shown as bullet points in Fig. 4.1, together with the cavity opening criterion (Eq. 1.71) computed from our CBD parameters and expressed a function of the binary mass.[2] I note that with these choices of parameter, in both setups the CBD is stable against fragmentation due to gravitational instability, which avoids the formation of clumps that can perturb the binary orbit, an effect potentially difficult to be disentangled from the effect of AGN feedback.
Once the disc gas particles are initialized, an equal mass binary is placed at the center of the system and the two MBHs are initialized with circular orbits in the same rotation direction of gas. The MBHs are initially quiescent, i.e. the sub-grid disc mass is zero, and I let the accretion from the resolved scale create and fill the unresolved disc, as described in § 4.1. In order to explore the relevance of feedback anisotropy and its collimation direction in shaping binary dynamics, I considered different spin configurations, since the spin determines both feedback properties. In table 4.1 I report the simulations I performed in **NC** and **MC** sets, and for each of them I indicate the corresponding label, the spin moduli and their inclinations θ with respect to the CBD axis. In the following, I will indicate simulations with their set and spin configuration labels, such that, for example, **NC_fid** denotes a simulation with $M_{\rm bin} = 10^5$ $M_\odot$ (i.e., no cavity) and both spin with moduli 0.5 and inclination $\theta = 0°$. The choice of these spin values is based on the indications of [266], who showed that merging MBH are expected to be highly spinning. Furthermore, since anisotropy becomes a steep function of spin for high spin values, as shown in Fig 2.2, the two chosen moduli, despite being both high, correspond to significant differences in anisotropy.
The number of gas particles in our simulations is $N = 5 \cdot 10^5$ (which increases as wind particles are spawned from the sub-grid disc) and the gravitational softening $\epsilon_{\rm gas} = 0.005$ pc, while the bulge is note sampled but enters the simulation as a static analytic potential. The MBH gravitational $\epsilon_\bullet = 0.015$.

[2] The terms in Eq. (1.71) are evaluated at $R_{\rm in}$ and I used $H/a_{\rm bin} = c_{\rm s}/v_{\rm bin}$.

Table 4.1: For all simulations $\theta_1 = 0$, i.e. the primary MBH spin is aligned with the orbital angular momentum axis.

label	a_1	a_2	θ_2 [deg]	AGN FB
NoFb	0.5	0.5	0	✗
fid	0.5	0.5	0	✓
a1	0.5	0.9982	0	✓
aa1	0.9982	0.9982	0	✓
5pi6	0.5	0.5	150	✓
5pi12	0.5	0.5	75	✓

Table 4.2: Some paramters of **MC** and **NC** sets.

label	$\log M_{\rm bin}$ [pc]	$R_{\rm sink}$ [pc]	$R_{\rm ext}$ [pc]	$t_{\rm dyn0}$ [Myr]
NC	5	0.051	0.158	0.271
MC	6	0.036	0.11	0.857

4.3 Results

As the simulations start, the gas at the inner edge of the CBD cavity inspirals towards the center, due to the external and unbalanced pressure forces pushing it inwards. Gas particles passing close to the MBHs begin to be captured and eventually sub-grid discs are created out of them, according to the prescriptions in § 4.1. The subsequent binary-CBD dynamics depends both on the choice of no/mild-cavity regime and on the effect feedback may have on the CBD, which in turn depends on the spins configuration.
In the following I describe binary dynamics and MBHs mass and spin evolution in **MC** and **NC** sets.

4.3.1 Mild cavity regime

In the mild-cavity regime, sub-grid discs are created after ~ 0.16 Myr. After that, in the simulation without feedback, gas keeps approaching the MBHs and minidiscs of diameter $\lesssim 1$ pc form, which continuously feed the unresolved discs. Such minidiscs, can be appreciated in Fig. 4.2 first-panel, which shows the face-on view of the CBD in **MC_NoFb** run. The other three panels show simulations with feedback, **MC_fid**, **MC_aa1** and **MC_a5pi12** respectively, from which it is clear that the impact of feedback strongly depends on the spins configuration. Indeed, when both spins are aligned to the orbital angular momentum (second

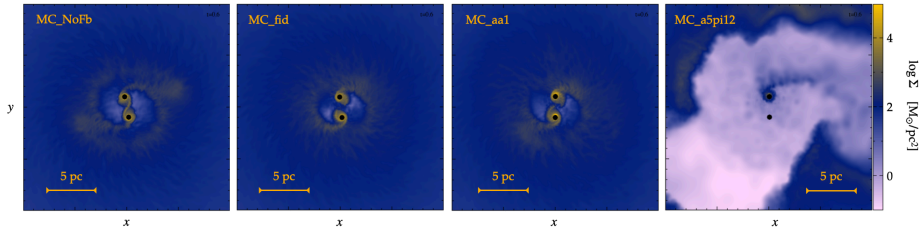

Figure 4.2: Face-on view of the snapshots at $t = 0.6$ Myr of four of the simulations in **MC** set.

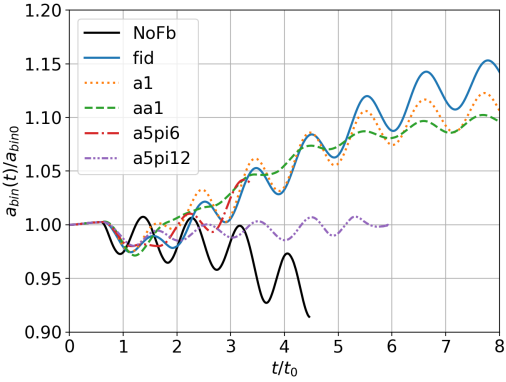

Figure 4.3: Evolution of the MBHs orbital separation in **MC** simulations.

and third panels) the CBD does not seem to be much affected by the presence of feedback, while in the presence of one spin flipped in the disc (fourth panel), AGN feedback inhibits further gas inflow towards the MBHs, preventing the formation of minidiscs. These different feedback effects then reflect in different MBHs dynamics, accretion and spin evolution, as I discuss more in detail below.

4.3.1.1 Dynamics

Figure 4.3 illustrates the evolution of the MBHs separation with time for all **MC** simulations. The separation is expressed in units of its initial value and time in units of the initial orbital period. We can distinguish three main behaviours: slow binary migration, which occurs only without feedback (**MC_NoFb**), orbital stalling, seen in **MC_a5pi12**, and orbital expansion, occurring for all other sim-

ulations.

Interestingly, simulations that look similar in the density maps (first three panels of Fig. 4.2) can have opposite dynamical behaviours, i.e. shrinking and expanding orbits. While slow binary migration in **MC_NoFb** is expected by construction, being **MC** setup at the border between the cavity and no-cavity regimes, the outspiral of the binary can be explained as the result of AGN feedback interacting with the the CBD. In fact, AGN feedback affects the CBD gas away from the MBHs ($r > a_{\rm bin}$), which exerts a negative torque on the binary, while the gas closer to the binary ($r < a_{\rm bin}$), responsible for a positive torque, remains almost unperturbed. This is simply due to the AGN feedback being anisotropic and the CBD being thicker at larger radii and consequently having there a higher coupling with the AGN wind. More specifically, we can think about AGN wind as being collimated towards the spin direction within a cone of semi-opening angle $\theta_{\rm eff}$, and the CBD to be semi-subtended by an angle $\theta_{\rm d} \sim h/r$. Then, AGN wind-CBD coupling occurs if the wind cone partly overlaps with the CBD, i.e. if $\theta_{\rm eff} + \theta_{\rm d} > 90°$, provided that the spin and CBD mid-plane are perpendicular. The CBD angle $\theta_{\rm d}$ computed at the characteristic scale $a_{\rm bin,0}$ reads

$$\theta_{\rm d} = \frac{h}{r}\Big|_{\rm 2pc} \sim c_{\rm s}\sqrt{\frac{r}{GM_{\rm bin}}}\Big|_{\rm 2pc} \sim 7.8° M_{\rm bin,6}^{-1/2}, \tag{4.3}$$

where I used $h/r = c_{\rm s}/v_{\rm gas}$, $c_{\rm s}(T = 6 \cdot 10^3\,{\rm K}) \simeq 6.4$ km/s, and $M_{\rm bin,6} = M_{\rm bin}/10^6$ $M_\odot$. The feedback effective angle for spin 0.9982, for which $\theta_{\rm eff}$ is maximum and feedback almost isotorpic, reads $\theta_{\rm eff} \sim 82.6°$ (see Fig. 2.2), hence $\theta_{\rm d} + \theta_{\rm eff} \sim 90°$. Since $\theta_{\rm d}$ is an increasing function of r, I expect the wind to have an effect only on the gas exterior to ~ 2 pc, and to leave mostly unperturbed the thin minidiscs. In simulation **MC_a5pi12**, one of the spins points almost in the CBD plane, hence the direction where most of the wind energy and momentum are collimated directly intercepts the CBD, yielding the maximum AGN wind-CBD coupling compared to previous simulations. As a result, the gas in the CBD is efficiently removed from the binary vicinity and a wide feedback cavity is cleared in the center, similarly to [199]. The lack of gas close to the MBHs to exchange torque with, significantly mitigates the CBD ability to drive orbital evolution and the binary separation stalls.

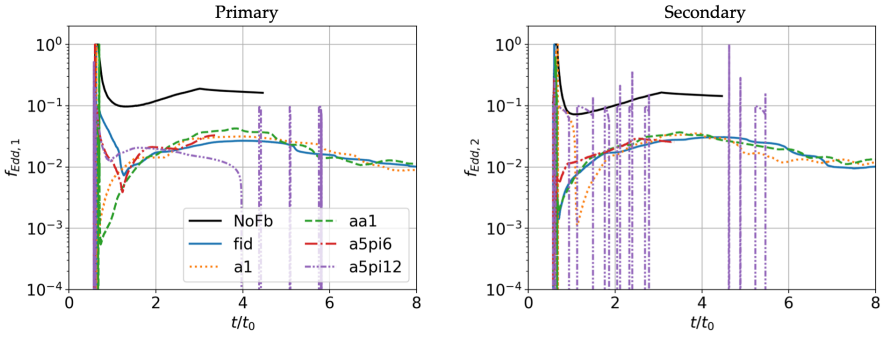

Figure 4.4: Sub-grid accretion rates on the primary (*left*) and secondary (*right*) MBHs in **MC** simulations.

4.3.1.2 MBHs accretion

In all simulations, except for **MC_a5pi12**, the minidiscs around MBHs survive for all the duration of the runs and coherently feed the unresolved discs. After a transient of about two binary orbits, the sub-grid accretion rate of both MBHs reaches a quasi-stationary value, which is about $f_{\rm Edd} \gtrsim 0.1$ for **MC_NoFb** and $f_{\rm Edd} \gtrsim 0.01$ for the simulations with feedback (**MC_a5pi12** excluded), see Fig. 4.4. In these simulations the MBH growth is negligible and by the end of the runs both MBHs have accreted only about on thousandth of their initial mass. By contrast, in **MC_a5pi12**, as soon as the resolved accretion on the secondary MBH (the one with misaligned spin) initializes a sub-grid disc, AGN feedback hinders the inflow of further particles, and the unresolved disc ends up being rapidly drained by wind ejection and sub-grid accretion on the MBH. During this active phase, gas particles are pushed away from the secondary MBH (e.g. fourth panel in Fig 4.2), and only after AGN activity ceases, the gas falls back and kindles a new active phase. This duty cycle, absent in all other **MC** simulations, repeats 10 times, with active phases $f_{\rm Edd} \lesssim 0.1$ lasting on average $\langle t_{\rm active} \rangle \simeq 0.035$ Myr, and quiescent phases $\langle t_{\rm qscnt} \rangle \simeq 0.19$ Myr. The primary MBH accretion is affected by the AGN activity of its companion, as feedback from the secondary tends to sweep away the primary minidisc as well as the gas streams accreting on it (fourth panel in Fig 4.2). In this phase, the primary is characterized by a low accretion rate, $f_{\rm Edd} \sim 0.01$, until after ~ 1.1 Myr, its minidisc is completely ripped off and a duty cycle of bursty $f_{\rm Edd} \lesssim 0.1$ accretion episodes is established. I remark that the duty cycle of the primary is regulated

solely by the AGN activity of the secondary, since feedback from the primary weakly couples to CBD being it vertically oriented in the spin direction, as seen in the other **MC** simulations. Due to this asymmetry in the accretion, by the end of the simulation the secondary has accreted about twice the mass accreted by the primary, though still a negligible fraction, i.e. few 10^{-4}, of the initial MBH mass. I highlight that this asymmetry in the accretion in an equal mass binary arises as a consequence of the asymmetry in the orientation of the spins, which, through their influence on feedback, regulate in different ways the MBHs feeding.

4.3.1.3 Spin evolution

I discuss now how the MBH accretion affects spin evolution. In all simulations, except for **MC_a5pi12**, the angles between MBHs sub-grid discs angular momenta and the binary orbital angular momentum are approximately zero. Therefore, in those simulations in which the spins are aligned with the binary angular momentum, the accretion is coherent and the spins grow in magnitude, even though negligibly, due to the small amount of accreted mass. Conversely, in **a5pi6**, the spin of the secondary MBH is initially flipped down of $5\pi/6$ rad with respect to the binary angular momentum, hence the sub-grid disc is counter-rotating with respect to the spin and makes it decrease in magnitude. In addition, the Bardeen-Patterson torque reorients the spin, aligning it to the angular momentum of the gas feeding the MBH. In this path towards alignment, the spin will eventually cross the CBD plane, attaining a configuration similar to that of **a5pi12**, which can prevent the spin to complete its reorientation, as discussed below.

In **MC_a5pi12**, each accretion episode on the secondary is characterized by the creation of a new sub-grid disc with initial mass M_α and angular momentum $\mathbf{J}_\alpha$, which is in general misaligned with respect to the MBH spin direction. Indeed, Figure 4.5 shows the distribution of the angle ψ between a newly formed disc angular momentum $\mathbf{J}_\alpha$ and the MBH angular momentum $\mathbf{J}_\bullet$, weighted on the initial mass M_α of the accretion episode. This plot indicates that the newly formed sub-grid discs, at the moment of their creation, are mostly misaligned with respect to the MBH spin, and even counter-rotating, i.e. with $\psi > \pi/2$. According to [69], in each accretion episode, the spin tends to align to the total (spin+disc) angular momentum (see § 1.1.5.2), therefore, given the orientation of the accretion events, the spin direction undergoes an erratic path, with no net

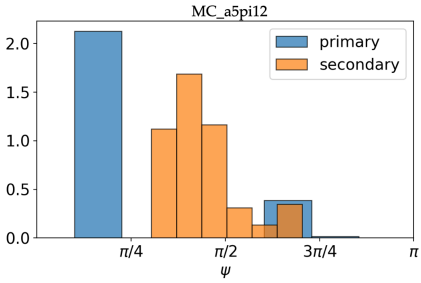

Figure 4.5: Angular distributions of accretion episodes on the MBHs in **MC_a5pi12**.

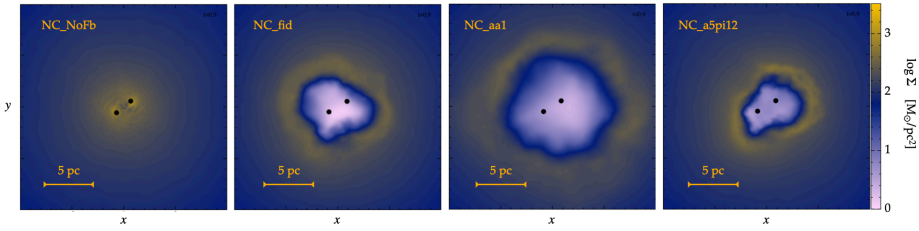

Figure 4.6: Face-on view of the snapshots of four of the simulations in **NC** set.

alignment. By contrast the accretion events on the primary are mostly coherent, i.e. characterized by $\psi \lesssim \pi/4$, similarly to MBHs in other simulations. Similarly to what we saw for the accretion, in **a5pi12**, the two spins undergo a different evolution, which is driven by the initial relative misalignment and feedback being dependent on the spin direction.

4.3.2 No cavity regime

I now discuss simulations in the no-cavity regime, i.e. **NC** set. As we saw in **MC**, the gas initially fills the cavity present in the initial condition, but now, since binary tidal torque is not able to counteract the viscous torque, in the absence of feedback the binary remains fully embedded in the CBD and no tidal cavity forms, e.g. first panel in Fig. 4.6. Though, in this regime, due to the lack of a cavity and being the CBD thicker, the coupling between AGN wind and the CBD is higher and hence the effect of AGN feedback is more pronounced (e.g. last three panels in Fig. 4.6), with a significant effect on the binary dynamics. I examine these effects more in detail below.

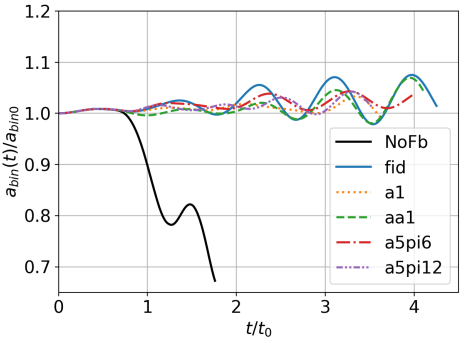

Figure 4.7: Evolution of the MBHs orbital separation in **NC** simulations.

4.3.2.1 Dynamics

More specifically, in the no-cavity regime, AGN feedback always manages to clear a central feedback cavity enclosing the binary, similarly to [199]. The simulation **NC_fid**, having both spins aligned to the binary angular momentum and moduli 0.5, is expected to be the one characterized by the weaker AGN wind-CBD coupling, because AGN wind is collimated in the direction perpendicular to the CBD and its effective anisotropy $\theta_{\rm eff}(a = 0.5) \simeq 68°$ is the smallest among the considered spin configurations. Nonetheless, in the no-cavity regime, the gas attains a thick configuration that fills the space within the binary, providing an high CBD-wind geometrical coupling, therefore even in **NC_fid** simulation AGN feedback manages to clear a central cavity surrounding the binary. The same then occurs with other spin configurations, since they are characterised by higher wind-CBD coupling, due to misaligned spins or higher spin moduli .
The presence of a feedback cavity makes the binary dynamical evolution depart from the fast migration expected in the absence of feedback (see Fig. 4.7), and the MBHs migrate on a much longer timescale (no shrinking can be appreciated in the simulated time). Since the cavity that causes orbits to stall is present for all spin configurations, they leave no specific trace on the dynamics, regardless of orientation and magnitude.

4.3.2.2 Accretion and spin evolution

In all **NC** simulations with feedback, AGN winds create low density bubbles in the CBD that affect gas accretion on the MBHs in a way similar to that

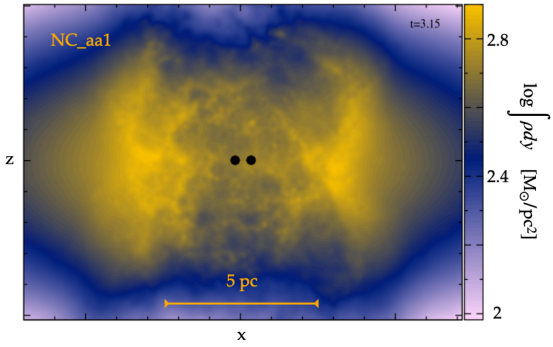

Figure 4.8: Side on view of a snapshot of **NC_aa1**.

observed in **MC_a5pi12**. Short active phases are separated by longer quiescent ones, resulting in bursty accretion episodes. In addition, we found that spin configurations characterized by higher AGN wind-CBD coupling, i.e. with higher spin moduli or a spin tilted towards the CBD, create larger bubbles in the CBD and hence longer quiescent phases due to the longer time required by the gas to fall back and trigger a new accretion event. In this way, the spin configuration, through its influence on AGN feedback, has an imprint on the feedback cavity sizes and hence on MBHs accretion duty cycles.
In addition, the accretion episodes on the MBHs are mostly misaligned with respect to the spin directions, as suggested by the complex gas distribution around the binary, as shown in Fig. 4.8. Therefore, as already seen in **MC_a5pi12**, the spin directions undergo a stochastic evolution, with no net (counter)alignment to the binary angular momentum direction, as a result of the interaction of the spin with randomly oriented accretion episodes.

4.4 Discussion

In this work, I investigated the role that spin-dependent anisotropy of AGN winds has in shaping the evolution of MBH binaries in CBDs. To this purpose, I used the sub-grid model for AGN feedback, MBH accretion and spin evolution I developed in the code GIZMO. According to [19] criterion, I selected binary-CBD initial conditions characterized by different binary migration regimes, i.e. slow and fast migration, and I studied how binary dynamics, MBHs accretion and spins evolution are altered by the presence of AGN anisotropic feedback. In order

to assess the relevance of the AGN feedback spin dependence in these processes, in both migration regime setups I considered different spins configurations, in terms of moduli and inclinations.
The most relevant results of this work can be summarised as follows:

- The spin modulus and direction, through their influence on AGN feedback, can affect the gas in the CBD in very different ways. On the one hand, if the binary is embedded in a thick disc with no cavity or if it is embedded in a thin disc with a cavity but at least one of the spin is oriented towards the CBD, the AGN wind-CBD coupling is high and results in the formation of a "feedback cavity" around the binary. On the other hand, if the binary is embedded in a thin disc and the spins, which set the directions where anisotropic winds are headed to, form small $\lesssim 30°$ angles with the CBD axis, the AGN wind-CBD coupling is weak: the CBD gas is swept away only far from the binary, while close to it can still reach the MBHs and form minidiscs. In addition, if the CBD is thick (no-cavity regime), I found that cavities are wider for those spins configurations that enhance the wind-CBD coupling, that is spins with higher moduli, associated to more isotropic feedback, and/or more tilted towards the CBD.

- The impact that AGN feedback has on the CBD reflects on the binary dynamics, since it affects the gas that drives the binary orbital evolution. As a consequence, different AGN feedback effects on the CBD, due to different spin configurations, result in different effects on binary dynamics. If the AGN wind-CBD coupling is high and a feedback cavity is present, due to the lack of gas close to the binary to exchange torque with, the binary orbits stall within the simulated time, and, on longer timescales, they likely attain a slow "typeII" migration regime, similarly to what observed by [199]. Conversely, if the AGN wind-CBD coupling is weak and no feedback cavity forms, AGN feedback mostly removes the gas outside the binary, responsible for a negative torque, while the gas in the thin minidiscs, which causes orbital expansion, remains almost unperturbed, with the net result of the binary migrating outwards.

  I remark that in all our simulations with feedback, despite accounting for anisotropic feedback, and hence a weaker AGN wind-CBD coupling compared to isotropic feedback prescriptions [199], no orbital migration is observed.

- MBHs accretion is severely influenced by the impact AGN feedback as on the CBD. Indeed, if feedback clears a central cavity, AGN discs are eventually drained by wind ejection and, after that, the gas in the CBD can stream back on the MBHs and kindle new AGN active phases, and so on and so forth. MBHs accretion proceeds in a bursty way and a duty cycle is established, characterised by short active phases interspersed by longer quiescent periods. Moreover, these accretion episodes are typically misaligned with respect to spin, which therefore does not undergo a clear alignment in the direction of orbital angular momentum. As I discussed above, by virtue of the different spin orientations, AGN feedback from the two MBHs can have very different effects on their common gas reservoir (the CBD) and their duty cycle can result being completely regulated by AGN feedback from one of the two MBHs, i.e. the one with higher wind-CBD coupling. This, in turn, can cause one of the MBHs grow faster than the other and make the binary depart from equal mass. Put another way, the asymmetry in the spin orientations, through feedback, translates in an asymmetry in the MBHs growth. In, addition, MBHs with spins yielding higher AGN wind-CBD coupling end up clearing wider cavities, therefore they experience longer quiescent phases and hence an overall slower mass growth.

  By contrast, if AGN wind-CBD coupling is weak e no feedback cavity forms, the minidiscs continue to feed coherently the MBHs and their accretion is characterized by a prolonged and coherent active phase that never expires in the simulated time. The accretion rate in this phase is $f_{\rm Edd} \sim 0.01$, about an order of magnitude smaller compared to the corresponding non-AGN feedback simulations.

Chapter 5

Final remarks

5.1 Summary of the results

In this thesis, I have been studying the effect of AGN radiative feedback in the evolution of MBHs, focusing on the impact of spin dependence of feedback anisotropy. In doing so, I considered different stages of the MBHs cosmic evolution: i) the co-evolution of MBHs in an isolated galaxy, ii) the pairing of MBHs in circumbinary discs, iii) The final shrinking that preludes coalescence of bound MBH binaries. While the effect of feedback in these regimes has already been addressed in the literature, its dependence on spin and how this dependence reflects on MBH evolution represents the novelty of this work. In order to investigate the consequences of this effect in numerical simulations, I developed a sub-grid model for the code GIZMO that self-consistently evolves in time i) the gas accretion process from resolved scales to a smaller scale, unresolved AGN disc, ii) the evolution of the spin of the MBH, iii) the injection of AGN-driven winds into the resolved scales, and iv) the spin-induced anisotropy of the overall feedback process. For each astrophysical problem/scale, I then considered an idealised setup and studied the evolution of the MBH(s) in the presence of spin-dependent radiative feedback. I found that this effect can leave a trace on the MBH host galaxy, on the MBH accretion and on its dynamics. Below I summarise the major results of this thesis.
AGN feedback has an impact on the surrounding gaseous environment:

- In the case of a MBH at the centre of an isolated galaxy the host response to different angular feedback patterns, as dictated by different spin

magnitudes, can be appreciated for high (Eddington) accretion rates and high AGN wind - ISM coupling. In particular, under these conditions, more rapidly spinning MBH more easily suppress the host galaxy SFR by sweeping away gas from the nuclear region. Both high accretion rates and high AGN wind-ISM coupling are found during galaxy mergers and/or in high redshift galaxies, which therefore represent ideal astrophysical environments to appreciate the effect of feedback spin-dependent anisotropy.

- If the MBHs are in a circumbinary disc, the direction of the spin can be crucial in determining the impact that the feedback has on the gas itself, precisely because of the anisotropy. Indeed, in the presence of a thin CBD, AGN feedback can sweep away gas and clear cavities around the binary only for highly tilted spins, almost laying in the MBH equatorial plane. If the disc is thicker the coupling with the wind is naturally enhanced and feedback has a more effective impact on the surrounding gas, always managing to open central cavities around the binary, irrespective of the spin direction.

The ability of feedback to sweep away the surrounding material, and thus impact the gas reservoir that feeds the MBH, reflects on MBH accretion:

- The MBH growth itself is influenced by the AGN feedback angular pattern. As the spin becomes larger, both AGN luminosity and its isotropy increase and make the AGN feedback more capable to reduce the inflow on the MBH itself, delaying its mass and spin growth. In this respect, slowly spinning high-redshift MBHs are more likely to attain accretion rates above the Eddington limit, as they would be less prone to alt accretion flows in the AGN disc equatorial plane via winds.

- In the context of MBH binaries in CBDs, the opening of a feedback cavity determines a transition from a coherent continuous accretion mode, mediated by minidiscs, to a bursty non-coherent stochastic accretion mode. In addition, the spin configuration, through its influence on feedback, i) can cause unequal growth of an initially equal mass binary, ii) can inhibit the spin alignment to the binary orbital angular momentum and iii) regulates the MBHs duty cycles.

Finally, the impact of feedback on the MBHs gaseous surroundings affects their dynamics:

- If MBHs are ispiralling towards the center of a CND, as driven by gaseous and stellar dynamical friction, AGN feedback can severely delay the orbital decay and enhance eccentricity, in a way that is strongly dependent on feedback direction and anisotropy.

- At smaller scales, when the MBHs are bound and form a binary, the presence of feedback always has the effect of preventing or significantly delaying the inspiral or possibly even favouring the the binary expansion, irrespective of the anisotropy and direction of the feedback. This poses an intriguing challenge in view of detection campaigns of GW signals from merging MBHs, such as LISA.

Due to simplified modeling, a number of caveats that we have to keep in mind when interpreting these results do exist. Specifically:

- The sub-grid accretion model used throughout this thesis does not include the geometrically thick, radiatively inefficient accretion mode [267] that occurs below $\lesssim f_{\rm Edd} \sim 0.01$. For such low accretion rates the disc is still modelled as an α-disc. Moreover, once the disc enters such low accretion regime, it becomes prone to launch a jet, a phenomenon not included in our model. Due to these limitations, I could not capture any transition from quasar to jet mode, which can potentially influence MBHs at all stages of their evolution. Similarly, the model presented in this thesis does not include super-Eddington accretion, which might be interesting as in § 2 I showed that the impact of AGN feedback on the host galaxy and the imprint of feedback angular pattern are more relevant for high (Eddington) accretion rates.

- In both AGN feedback models discussed in this thesis, i.e. based on spawning (§ 2 and § 4) and kicking (§ 3), the wind velocity has been assumed to be constant. However, from an observational point of view it has been shown that velocity scales with luminosity as $v_{\rm w} \propto L^{1/2}$ [268], and from a theoretical/numerical point of view wind speed varies depending on the region of the disc from which it is driven [267] and on the viewing angle, with higher velocities edge on [237, 238].

- In all simulations presented in this thesis, the coupling coefficient $\tau = \dot{M}_{\rm w} v_{\rm w}/(L/c)$ between AGN radiation and gas is assumed to be constant and equal to one. All the AGN radiation momentum flux is assumed to be

completely transferred to the gas in the MBH vicinity (at unresolved scale in § 2 and § 4 and in the MBH kernel in § 3). In a more realistic model the radiation-gas coupling should evolve according to the ionization level of the gas, a fraction of the AGN radiation should be allowed to escape the nuclear region and interact directly with the resolved ISM gas, exerting radiation pressure on it. This would require performing Radiation-Hydrodynamics simulations, something beyond the aim of this thesis.

- Stellar physics has been treated with different levels of approximation in the three papers presented in this thesis. In the binary hardening regime (§ 4), the stellar particles were not sampled and the stellar bulge was simply included as static analytical potential, despite the importance of stellar hardening in this regime. At circum-nuclear disc scale (§ 3), stellar dynamics was resolved with particles, but the formation of new stars from CND gas has not been enabled, which in principle can influence MBH inspiral. Finally, In the simulations of isolated galaxies (§ 2), I accounted for star formation but I did not model stellar winds and supernovae which, together with AGN feedback, contribute in driving galactic outflows, especially in dwarf galaxies, and in regulating the amount of gas present in the central region of a galaxy, thus further modulating the AGN fueling. At each stage considered, an improvement in stellar physics modeling would add a further level of complexity beyond the scope of this thesis, but nonetheless important in order to understand the details of MBH dynamics, growth and feedback.

- Magnetic fields and magneto-hydro-dynamics (MHD) have been neglected throughout this thesis. While MHD on the galactic and circum-nuclear-disc scales plays a secondary role, on the circum-binary-disc (pc) scale it is crucial in the treatment of viscosity, which in the study on binary migration was treated with a simple model based on Shakura & Sunyaev α-prescription.

5.2 Future prospects

Given the limitations highlighted in this chapter and the potential of the model developed in this thesis, I would like to conclude this work by listing a number of possible improvements and applications.

- The physics of MBH accretion discs changes depending on the accretion rate, from advection-dominated-accretion-flows for low accretion rates, passing through standard Shakura & Sunyaev discs close to Eddington rates, to slim-discs for super Eddington accretion regimes. Each accretion mode is characterised by a different type of feedback, which can manifest itself not only through radiation (the type discussed in this thesis) but also through MHD winds and jets. A natural improvement of the model presented in this thesis would be to extend it to other accretion regimes with their respective feedback modes. For example, for the sub-Eddington regime, a direct way to improve the model would therefore be to extend it to lower accretion rates following [269], who recently developed such an extension for the α-disc model developed by [3] in AREPO. In addition, the launch of a jet could be implemented from the spawning technique presented in this thesis, appropriately modifying the opening angle of the spawned particles and taking into account the appropriate efficiency of this process [57, 270, 271]. Finally, for a self-consistent model, I would include the spin-down effect of the jet [205, 270, 271] and more generally the evolution of the spin in a thick discs [270]. For the super-Eddington regime the approach would be very similar. Firstly, such an extension would require replacing the α-disc with another model: the slim disc [272, 273]. In addition, similar to the sub-Eddington regime, the disc is thick and prone to launching a jet, which can again be done by spawning particles and adopting the appropriate efficiency in this regime. The functional form of this efficiency with the spin can be taken from the fits performed by [274] (see also [57] and [275]) to the GRMHD simulations of [276]. Finally, the next step would be to include the back reaction of the jet on the spin characteristic of this regime [277] and the spin evolution proper to slim discs.

- In all simulations presented in this work, the setup is represented by an idealised system. A natural extension of this work would be to perform zoom-in cosmological simulations and study the co-evolution of galaxies and MBHs and their insprial down to the the binary formation in a cosmological context. In doing so, one could also introduce a particle-splitting prescription so as to resolve the accretion down to the scale of the radius of the accretion disc. In this way one could model the accretion on the unresolved disc by direct particle capture (as I did in § 4), instead of by

Bondi-like prescriptions. This improvement, combined with the extension of the sub-grid model to different accretion (and feedback) regimes, would provide an excellent and competitive framework to study MBH accretion, feedback and evolution in cosmological simulations.

- There are currently no binary hardening simulations that jointly account for the contribution of gas and stars. An interesting followup to the work shown in § 4 would be to include a bulge (triaxial or rotating so as to ensure replenishment of the loss cone) by resolving individual stars. This would make it possible to quantify the relative contribution of gas and stars directly from the simulation. A further step would be to repeat the experiment, but starting from initial conditions provided by cosmological simulations, as suggested in the point above.

- A further interesting possibility is to perform an exploration of the parameter space of the binary (e.g. mass ratio and eccentricity) with both the present model and its extension that includes sub- and super-Eddington accretion regimes. Recent 2D simulations [278, 279] have shown that depending on q, the binary evolves towards a different equilibrium eccentricity $e_{\rm eq}$ (with $e_{\rm eq} \sim 0.5$ for $q \to 1$) and has a different probability of migrating (with inspiral for $q \lesssim 0.2$ and outspiral for $q \gtrsim 0.2$). However, in the presence of feedback, we expect these results to change. As shown by [189, 190], when $q < 1$, there is preferential accretion on the secondary, which will then be characterised by a higher wind mass loading that is likely to influence the evolution towards a possible equilibrium eccentricity. Preferential accretion also drives faster spin (counter-)alignment (e.g. [261] but see [280]), which has an influence on feedback direction and its coupling with the disc. Similarly, when orbits are eccentric, during an orbital period the MBH passes through regions of different density that modulate both accretion and feedback, and this effect can have an interesting back reaction on the MBH dynamics itself. Finally, the problem becomes further complicated in the extended version of the model, when the disc can support different accretion regimes (as in [269]). In that case, during evolution, feedback can switch from quasar/wind to jet mode, thus varying the coupling with CBD and how this affects the MBHs.

Appendices

A The derivative of $f_{\rm Edd}$

Here I compute the derivative of $f_{\rm Edd}$ and find an approximate expression suitable for interpreting results shown in section 2.4.1. Starting from Eq. (2.17) and replacing $a/J_\bullet = c/GM_\bullet^2$, the time derivative of $f_{\rm Edd}$ reads

$$\begin{aligned}\frac{df_{\rm Edd}}{dt} &= f_{\rm Edd}\left(\frac{\dot\eta}{\eta}+5\frac{\dot M_\alpha}{M_\alpha}+\frac{3}{7}\frac{\dot M_\bullet}{M_\bullet}-\frac{25}{7}\frac{\dot J_\alpha}{J_\alpha}\right)\simeq\\ &\simeq f_{\rm Edd}\left(\frac{\dot\eta}{\eta}+5\frac{\dot M_{\rm in}-\dot M_{\rm acc}-\dot M_{\rm w}}{M_\alpha}+\frac{3}{7}\frac{(1-\eta)\dot M_{\rm acc}}{M_\bullet}\dots\right.\\ &\qquad\left.\dots-\frac{25}{7}\frac{\dot J_{\rm in}-\dot J_\bullet-\dot J_{\rm w}}{J_\alpha}\right),\end{aligned}\tag{A.1}$$

where in the second row, I plugged in Eqs. (2.12, 2.13), and (2.15) in place of $\dot M_\alpha$, $\dot M_\bullet$ and $\dot J_\alpha$ and, for Eq. (2.15), I approximated all vectors as lying along the same direction. Eq. (A.1) can be simplified as follows. First, I note that $-5\dot M_{\rm w}/M_\alpha + 25/7\dot J_{\rm w}/J_\alpha = 0$, according to the definition of $\dot J_{\rm w}$ (Eq. 2.16). In other words, the removal of mass and angular momentum from the disc due to the wind ejection does not affect the disc accretion rate. In addition, $3/7(1-\eta)\dot M_{\rm acc}/M_\bullet$ and $\dot\eta/\eta \propto \dot M_{\rm acc}/M_\bullet$ are both $\ll \dot M_{\rm acc}/M_\alpha$, being $M_\alpha \ll M_\bullet$. Similarly, noting that $\mathbf{T}_{\rm BP}$ in Eq. (2.14) doesn't affect affect the spin modulus but only its direction, we can write $|\dot J_\bullet/J_\alpha| = \Lambda_{\rm ISCO}/(J_\alpha/M_\alpha)\cdot\dot M_{\rm acc}/M_\alpha \ll \dot M_{\rm acc}/M_\alpha$ since the specific angular momentum of gas orbiting at the ISCO is much smaller than the disc

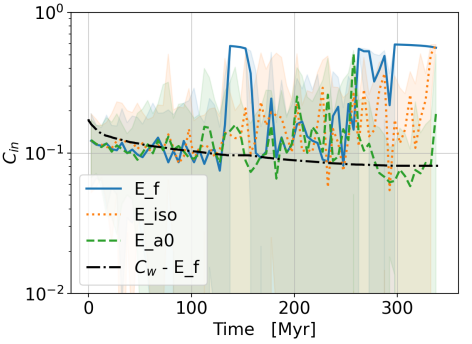

Figure 1: Coefficients $C_{\rm in}$ in **E** simulations. The lines correspond to the median values over time bins of 5 Myr, while the shaded regions span from the 16th to the 84th percentiles over these bins. The coefficient $C_{\rm w}$ is also shown for the **E_f** run.

total specific angular momentum J_α/M_α. In this way, Eq. (A.1) reduces to

$$\frac{df_{\rm Edd}}{dt} \simeq f_{\rm Edd}\left(-5\frac{\dot{M}_{\rm acc}}{M_\alpha}+5\frac{\dot{M}_{\rm in}}{M_\alpha}-\frac{25}{7}\frac{\dot{J}_{\rm in}}{J_\alpha}\right). \tag{A.2}$$

Now, by writing $\dot{J}_{\rm in}=\langle\Lambda\rangle\dot{M}_{\rm in}$ (see Section 2.2.1.2) and $\dot{M}_{\rm acc}=\eta_{\rm w}^{-1}\dot{M}_{\rm w}$ (using Eq. 2.4), I obtain

$$\frac{df_{\rm Edd}}{dt} \simeq 5f_{\rm Edd}\left(-\frac{1}{\eta_{\rm w}}\frac{\dot{M}_{\rm w}}{M_\alpha}+\left(1-\frac{5}{7}\frac{\langle\Lambda\rangle}{J_\alpha/M_\alpha}\right)\frac{\dot{M}_{\rm in}}{M_\alpha}\right). \tag{A.3}$$

This equation points out that the leading terms driving the evolution of $f_{\rm Edd}$ are the loss of mass due to accretion, here expressed in terms of $\dot{M}_{\rm w}$, and the replenishment of mass from resolved scales, represented by $\dot{M}_{\rm in}$. by defining the coefficients $C_{\rm w}=\eta_{\rm w}^{-1}$ and $C_{\rm in}=(1-5\langle\Lambda\rangle/7(J_\alpha/M_\alpha))$ I get Eq. (2.22). For this choice of parameters, being $v_{\rm w}/c=0.01$, we have that $C_{\rm w}=0.1(\eta/0.1)^{-1}$ is of the same order of $C_{\rm in}$, whose value is shown in Fig. 1 for the three simulations **E**.

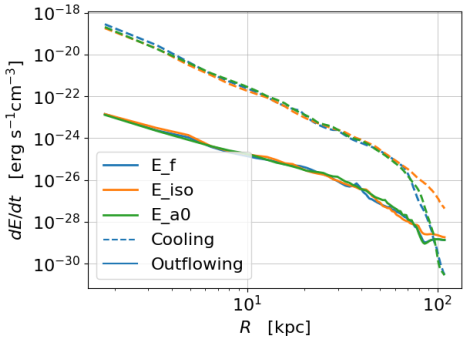

Figure 2: Time averages of the cooling luminosity (dashed) and outflow energy flux (solid) radial profiles for the **E** simulations. Time averages are taken considering snapshots up to 180 Myr from t_0.

B CGM energetic balance

In this section I discuss more in detail the energetic balance in the CGM, i.e. I compare the cooling luminosity of the gas and the energy flux of the outflow. The cooling luminosity is defined as $\dot{\varepsilon}_{\rm cool}(r) = \Sigma_i n^2_{{\rm H},i} \Lambda_{{\rm cool},i}/N$, where $\Lambda_{{\rm cool},i}$ is the total cooling function of the $i-$th particle and the sum spans over the N gas particles in the radial bin $[r-\Delta R/2, r+\Delta R/2)$, where I used $\Delta R = 1.5$ kpc. I defined the energy flux of the outflow as $\dot{\varepsilon}_{\rm outflow}(r) = \Sigma_i \rho_i \left(0.5 v_i^2 + u_i\right) v_{r,i}/N\Delta R$, where v_i, u_i and $v_{r,i}$ are the i-th particle velocity, internal energy and radial velocity. In Fig. 2 I show the time averages (over the same snapshots accounted in 2.4.2.4) of these quantities for the **E** simulations. For each simulation, the location where the two energy rates become comparable roughly coincides with the maximum radius within which the CGM is affected by the outflow, as shown in the Fig. 2.14. While for anisotropic feedback (**E_f** and **E_a0**) this occurs at $R \sim 100$ kpc, for isotropic feedback (**E_iso**) the region impacted by the outflow extends beyond the radial range considered.

C Wind particles

In this section I study the mass resolution of wind particles and the location where such particles are merged to non-wind particles for **E_f** simulation. In Fig. 3 (*left*) I show the normalized histograms of the wind particles masses

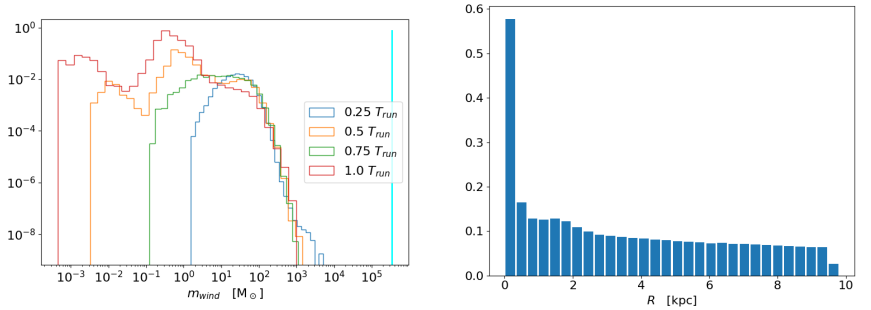

Figure 3: (*Left*): normalised histograms of wind particles masses at four snapshots of **E_f** simulation. The cyan line indicates the mass of non-wind particles at the beginning of the simulation. (*Right*): Normalised histogram of the radii where winds particles merge with ISM particles in **E_f** simulation.

at four snapshots of **E_f**: at one quarter, one half, three quarters and at the end of the simulation. The vertical cyan line shows the value of the non-wind particle mass resolution. According to this figure, wind particles throughout the simulation have masses orders of magnitude smaller than the initial ISM resolution, reason why I exclude the possibility that at the time of spawning these particles could result in a significant and instantaneous perturbation of the gas density surrounding the MBH. In addition, I considered the location where wind particles are merged into ISM particles. Figure 3 (*right*) shows the normalized histogram of the radii where such mergers occur throughout all **E_f** simulation. It follows that wind particles capture is much more likely to occur within the first few hundreds pc from the MBH, but still takes place up to a distance of ∼10 kpc.

D Density maps of the simulations of § 3

Figures 5, 6, and 7 show the density maps of the CND at 1 and 4 Myr, for all feedback models and all setups. From these images, we can understand some of the characteristics of the feedback effect on the CND. The cavities (or low density bubbles) tend to vary considerably in size, from a few pc to tens of pc, to have different shapes, both circular or very elongated, and to be in different positions relative to the MBH. This suggests that understanding the dynamic effect these have on the MBH is very complicated and requires the use

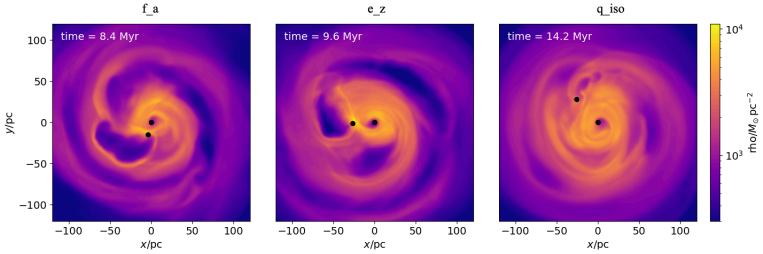

Figure 4: Density maps of three simulations at "late" times, when numerous feedback episodes already occurred.

of simulations. More specifically, we can sketch some trends. For each setup, the CND seems to be most affected by the effect of feedback in **a** and **iso**, followed by **z**. This is not surprising since in the first case the feedback energy and momentum are collimated along the evolving spin direction (within a cone that partially intercepts the CND), in the second the energy and momentum are uniformly distributed over the entire solid angle, while in the last they are collimated in the direction perpendicular to the CND, the one giving the least wind-disc coupling. However, this trend is not very marked and in some cases the differences are minimal. Among the different setups, we note that the **q** setup tends to have smaller bubbles and that the CND remains more intact, as is to be expected since the secondary is smaller and can therefore sustain smaller Eddington limited accretion rates than the **f** and **e** setups. Finally, I note that in all simulations the CND perturbation at 1 Myr is much less pronounced than at 4 Myr. In fact, as the system evolves and the secondary creates cavities in the disc, these may merge together, be closed by the pressure of the external gas, be swollen by new feedback episodes, and over time the CND takes on an increasingly pierced and irregular appearance (see e.g. Fig 4).

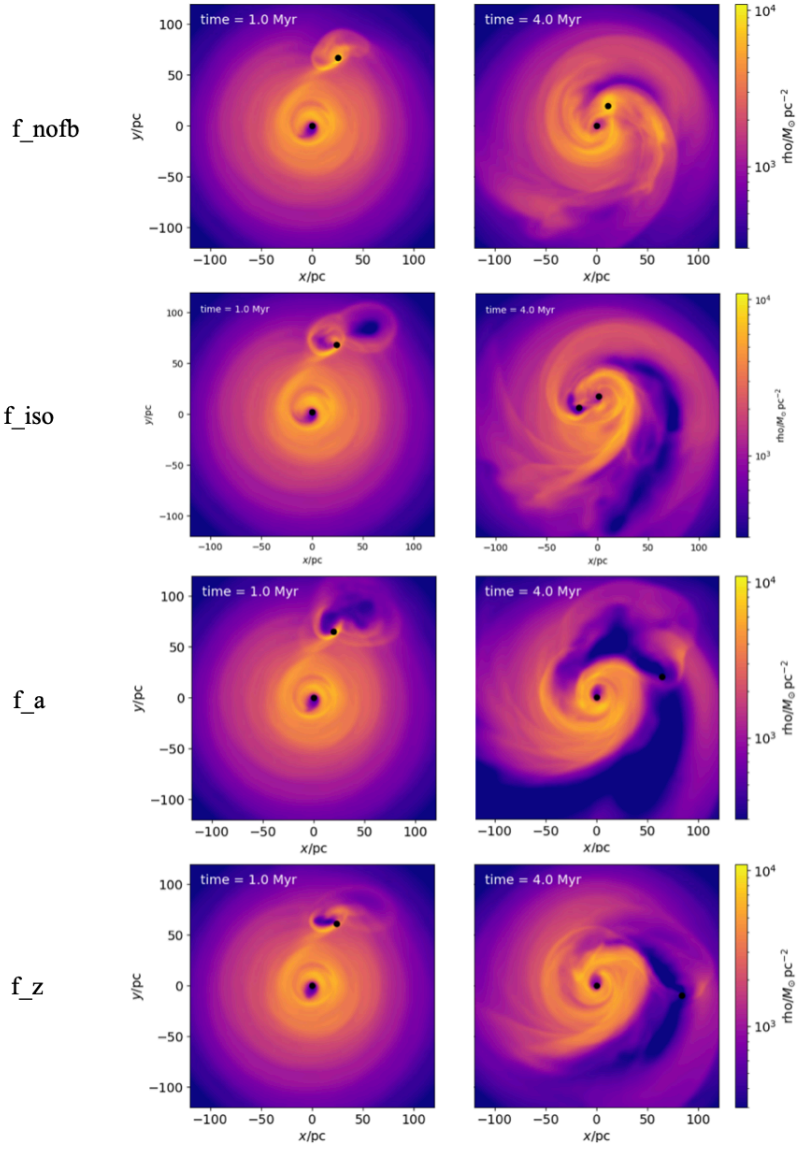

Figure 5: Density maps of **f** simulations at 1 Myr and 4 Myr.

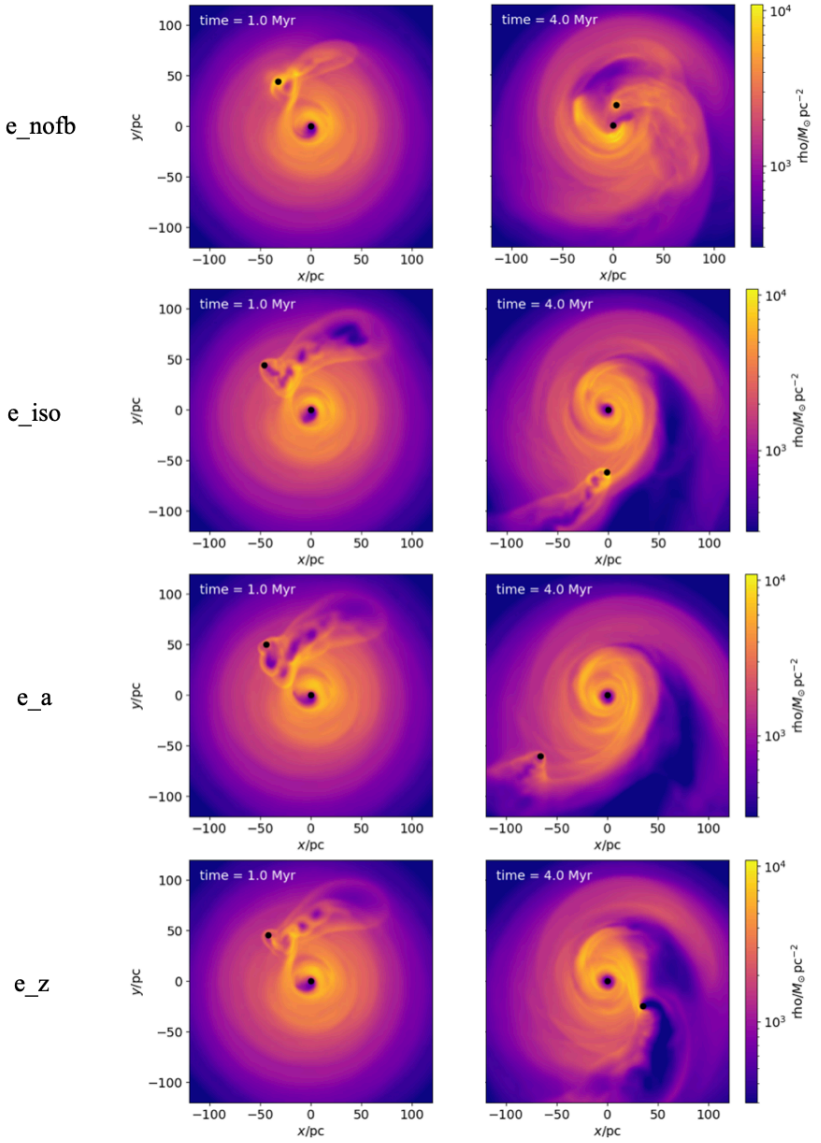

Figure 6: Density maps of **e** simulations at 1 Myr and 4 Myr.

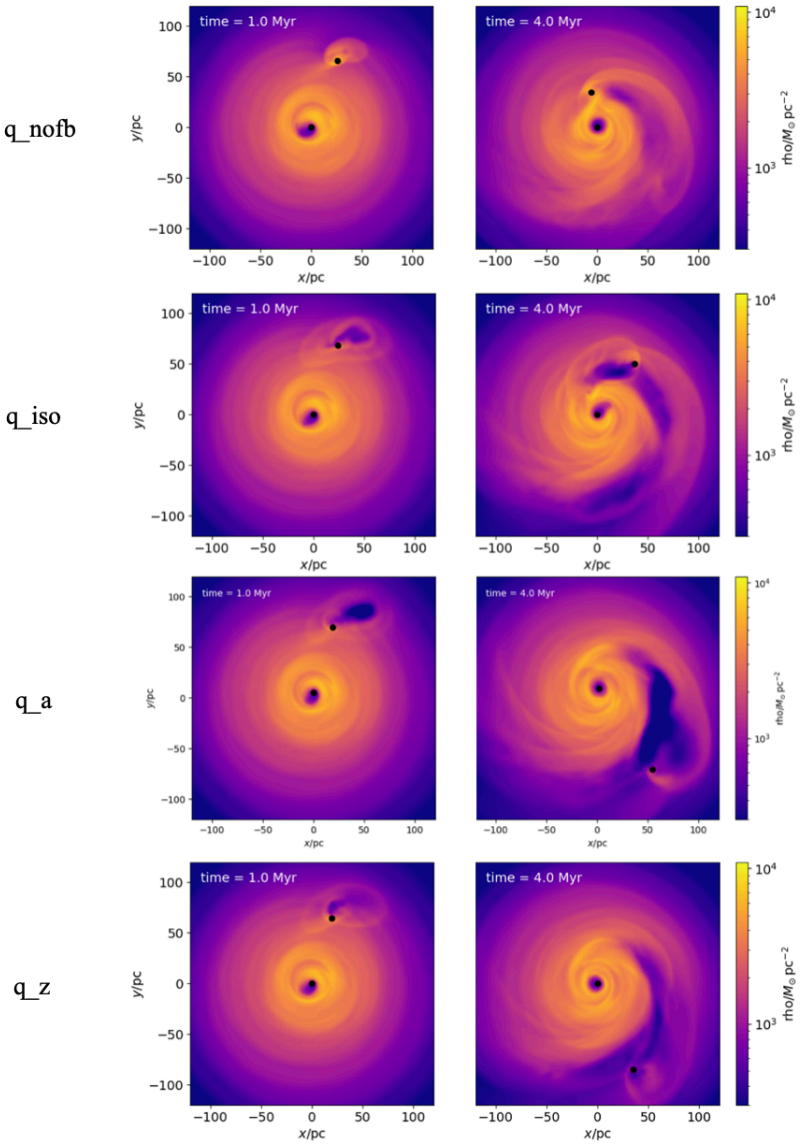

Figure 7: Density maps of **q** simulations at 1 Myr and 4 Myr.

E Convergence of MBH pairs simulations

In order to discuss the convergence of our results we performed additional simulations, with both smaller and higher resolution, in the cases **f_nofb** and **f_a**. In particular, we sampled the CND with 10^5, $3\cdot10^5$ and $3\cdot10^6$ gas particles, in addition to the 10^6 case presented in 3.3.1. For all these resolutions the number of star particles is five times that of the gas. Figure 8 shows how the evolution of the MBHs separation in **f_nofb** changes with resolution and reveals that the dynamics converges by increasing the number of particles. On the other hand, we do not expect convergence in simulations with feedback due to the stochastic nature of our subgrid feedback model. Indeed, depending on which gas particles receive a kick at a given timestep, the resulting bubbles can display morphological differences, such that their cumulative effect in time can lead to very different trajectories, i.e. different realizations of the same stochastic process (see Fig **??** for the **f_a** case).

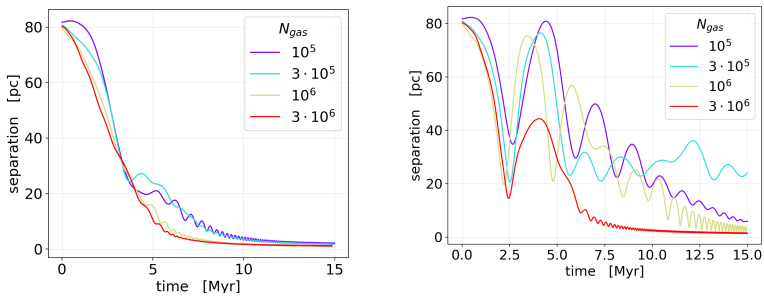

Figure 8: Time evolution of the MBHs separation for different resolutions in the case **f_nofb**.

F Bubbles angular distributions in MBH pairs simulations

In Fig. 9 we report the histograms of the quantity θ for **e** and **q** simulations. As pointed out in 3.3.4, the distribution of θ, peaked at small angles ($< \pi/2$) in **nofb** simulations, spreads over the whole range $[0, \pi]$ when feedback is turned on, due to the presence of low density bubbles trailing the MBH, which tend to accelerate it, hampering DF. We note that the simulations in which the peak of the distribution is more shifted to the right (i.e. more frequent feedback acceleration) are **q_iso** and **q_a**, which are also the only two simulations whose orbits do not decay over the simulated time.

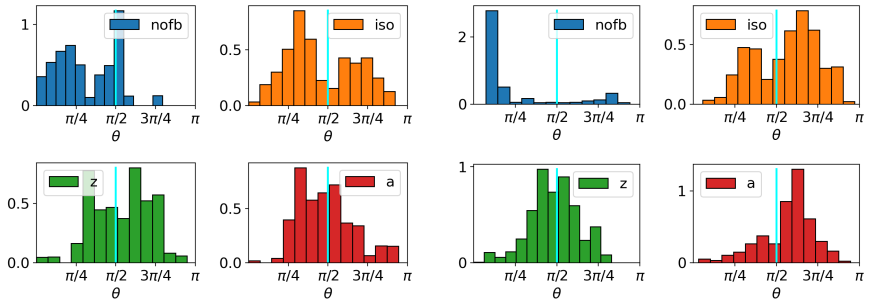

Figure 9: Histograms of θ in **e** (*left*) and **q** (*right*) simulations.

References

[1] Pedro R. Capelo. Astrophysical black holes. In Muhammad Latif and Dominik Schleicher, editors, *Formation of the First Black Holes*, pages 1–22. 2019.

[2] Marianne Vestergaard and Kayhan Gültekin. Massive black holes in galactic nuclei: Observations. *arXiv e-prints*, page arXiv:2304.10233, April 2023.

[3] Davide Fiacconi, Debora Sijacki, and J. E. Pringle. Galactic nuclei evolution with spinning black holes: method and implementation. , 477(3):3807–3835, July 2018.

[4] Houjun Mo, Frank C. van den Bosch, and Simon White. *Galaxy Formation and Evolution*. 2010.

[5] Philip J. Armitage. Lecture notes on accretion disk physics. *arXiv e-prints*, page arXiv:2201.07262, January 2022.

[6] James M. Bardeen and Jacobus A. Petterson. The Lense-Thirring Effect and Accretion Disks around Kerr Black Holes. , 195:L65, January 1975.

[7] C. M. Harrison. Impact of supermassive black hole growth on star formation. *Nature Astronomy*, 1:0165, July 2017.

[8] John Kormendy and Luis C. Ho. Coevolution (Or Not) of Supermassive Black Holes and Host Galaxies. , 51(1):511–653, August 2013.

[9] M. Volonteri. The Formation and Evolution of Massive Black Holes. *Science*, 337(6094):544, August 2012.

[10] David S. N. Rupke and Sylvain Veilleux. Integral Field Spectroscopy of Massive, Kiloparsec-scale Outflows in the Infrared-luminous QSO Mrk 231. , 729(2):L27, March 2011.

[11] A. C. Fabian. Observational Evidence of Active Galactic Nuclei Feedback. , 50:455–489, September 2012.

[12] Zachary Schutte and Amy E. Reines. Black-hole-triggered star formation in the dwarf galaxy Henize 2-10. , 601(7893):329–333, January 2022.

[13] Andrew King and Ken Pounds. Powerful Outflows and Feedback from Active Galactic Nuclei. , 53:115–154, August 2015.

[14] Tiago Costa, Debora Sijacki, and Martin G. Haehnelt. Feedback from active galactic nuclei: energy- versus momentum-driving. , 444(3):2355–2376, November 2014.

[15] Tiago Costa, Rüdiger Pakmor, and Volker Springel. Powering galactic superwinds with small-scale AGN winds. , 497(4):5229–5255, October 2020.

[16] Debora Sijacki, Volker Springel, and Martin G. Haehnelt. Gravitational recoils of supermassive black holes in hydrodynamical simulations of gas-rich galaxies. , 414(4):3656–3670, July 2011.

[17] Philip J. Armitage and W. K. M. Rice. Planetary migration. *arXiv e-prints*, pages astro–ph/0507492, July 2005.

[18] Andrés Escala, Richard B. Larson, Paolo S. Coppi, and Diego Mardones. The Role of Gas in the Merging of Massive Black Holes in Galactic Nuclei. II. Black Hole Merging in a Nuclear Gas Disk. , 630(1):152–166, September 2005.

[19] Luciano del Valle and Andrés Escala. Binary-Disk Interaction. II. Gap-opening Criteria for Unequal-mass Binaries. , 780(1):84, January 2014.

[20] Francesco Bollati, Alessandro Lupi, Massimo Dotti, and Francesco Haardt. On the connection between AGN radiative feedback and massive black hole spin. *arXiv e-prints*, page arXiv:2311.07576, November 2023.

[21] Francesco Bollati, Alessandro Lupi, Massimo Dotti, and Francesco Haardt. Dynamical evolution of massive black hole pairs in the presence of spin-dependent radiative feedback. , 520(3):3696–3705, April 2023.

[22] Andrew C. Fabian and Anthony N. Lasenby. Astrophysical Black Holes. *arXiv e-prints*, page arXiv:1911.04305, November 2019.

[23] Riccardo Giacconi, Herbert Gursky, Frank R. Paolini, and Bruno B. Rossi. Evidence for x Rays From Sources Outside the Solar System. , 9(11):439–443, December 1962.

[24] B. P. Abbott, R. Abbott, T. D. Abbott, S. Abraham, F. Acernese, K. Ackley, C. Adams, R. X. Adhikari, V. B. Adya, C. Affeldt, M. Agathos, K. Agatsuma, N. Aggarwal, O. D. Aguiar, L. Aiello, A. Ain, P. Ajith, G. Allen, A. Allocca, M. A. Aloy, P. A. Altin, A. Amato, A. Ananyeva, S. B. Anderson, W. G. Anderson, S. V. Angelova, S. Antier, S. Appert, K. Arai, M. C. Araya, J. S. Areeda, M. Arène, N. Arnaud, K. G. Arun, S. Ascenzi, G. Ashton, S. M. Aston, P. Astone, F. Aubin, P. Aufmuth, K. AultONeal, C. Austin, V. Avendano, A. Avila-Alvarez, S. Babak, P. Bacon, F. Badaracco, M. K. M. Bader, S. Bae, P. T. Baker, F. Baldaccini, G. Ballardin, S. W. Ballmer, S. Banagiri, J. C. Barayoga, S. E. Barclay, B. C. Barish, D. Barker, K. Barkett, S. Barnum, F. Barone, B. Barr, L. Barsotti, M. Barsuglia, D. Barta, J. Bartlett, I. Bartos, R. Bassiri, A. Basti, M. Bawaj, J. C. Bayley, M. Bazzan, B. Bécsy, M. Bejger, I. Belahcene, A. S. Bell, D. Beniwal, B. K. Berger, G. Bergmann, S. Bernuzzi, J. J. Bero, C. P. L. Berry, D. Bersanetti, A. Bertolini, J. Betzwieser, R. Bhandare, J. Bidler, I. A. Bilenko, S. A. Bilgili, G. Billingsley, J. Birch, R. Birney, O. Birnholtz, S. Biscans, S. Biscoveanu, A. Bisht, M. Bitossi, M. A. Bizouard, J. K. Blackburn, C. D. Blair, D. G. Blair, R. M. Blair, S. Bloemen, N. Bode, M. Boer, Y. Boetzel, G. Bogaert, F. Bondu, E. Bonilla, R. Bonnand, P. Booker, B. A. Boom, C. D. Booth, R. Bork, V. Boschi, S. Bose, K. Bossie, V. Bossilkov, J. Bosveld, Y. Bouffanais, A. Bozzi, C. Bradaschia, P. R. Brady, A. Bramley, M. Branchesi, J. E. Brau, T. Briant, J. H. Briggs, F. Brighenti, A. Brillet, M. Brinkmann, V. Brisson, P. Brockill, A. F. Brooks, D. D. Brown, S. Brunett, A. Buikema, T. Bulik, H. J. Bulten, A. Buonanno, R. Buscicchio, D. Buskulic, C. Buy, R. L. Byer, M. Cabero, L. Cadonati, G. Cagnoli, C. Cahillane, J. Calderón Bustillo, T. A. Callister, E. Calloni, J. B. Camp, W. A. Campbell, M. Canepa, K. C. Cannon, H. Cao, J. Cao, E. Capocasa, F. Carbognani, S. Caride, M. F. Carney, G. Carullo, J. Casanueva Diaz, C. Casentini, S. Caudill, M. Cavaglià, F. Cavalier, R. Cavalieri, G. Cella, P. Cerdá-Durán, G. Cerretani, E. Cesarini, O. Chaibi, K. Chakravarti, S. J.

Chamberlin, M. Chan, S. Chao, P. Charlton, E. A. Chase, E. Chassande-Mottin, D. Chatterjee, M. Chaturvedi, K. Chatziioannou, B. D. Cheeseboro, H. Y. Chen, X. Chen, Y. Chen, H. P. Cheng, C. K. Cheong, H. Y. Chia, A. Chincarini, A. Chiummo, G. Cho, H. S. Cho, M. Cho, N. Christensen, Q. Chu, S. Chua, K. W. Chung, S. Chung, G. Ciani, A. A. Ciobanu, R. Ciolfi, F. Cipriano, A. Cirone, F. Clara, J. A. Clark, P. Clearwater, F. Cleva, C. Cocchieri, E. Coccia, P. F. Cohadon, D. Cohen, R. Colgan, M. Colleoni, C. G. Collette, C. Collins, L. R. Cominsky, Jr. Constancio, M., L. Conti, S. J. Cooper, P. Corban, T. R. Corbitt, I. Cordero-Carrión, K. R. Corley, N. Cornish, A. Corsi, S. Cortese, C. A. Costa, R. Cotesta, M. W. Coughlin, S. B. Coughlin, J. P. Coulon, S. T. Countryman, P. Couvares, P. B. Covas, E. E. Cowan, D. M. Coward, M. J. Cowart, D. C. Coyne, R. Coyne, J. D. E. Creighton, T. D. Creighton, J. Cripe, M. Croquette, S. G. Crowder, T. J. Cullen, A. Cumming, L. Cunningham, E. Cuoco, T. Dal Canton, G. Dálya, S. L. Danilishin, S. D'Antonio, K. Danzmann, A. Dasgupta, C. F. Da Silva Costa, L. E. H. Datrier, V. Dattilo, I. Dave, M. Davier, D. Davis, E. J. Daw, D. DeBra, M. Deenadayalan, J. Degallaix, M. De Laurentis, S. Deléglise, W. Del Pozzo, L. M. DeMarchi, N. Demos, T. Dent, R. De Pietri, J. Derby, R. De Rosa, C. De Rossi, R. DeSalvo, O. de Varona, S. Dhurandhar, M. C. Díaz, T. Dietrich, L. Di Fiore, M. Di Giovanni, T. Di Girolamo, A. Di Lieto, B. Ding, S. Di Pace, I. Di Palma, F. Di Renzo, A. Dmitriev, Z. Doctor, F. Donovan, K. L. Dooley, S. Doravari, I. Dorrington, T. P. Downes, M. Drago, J. C. Driggers, Z. Du, J. G. Ducoin, P. Dupej, S. E. Dwyer, P. J. Easter, T. B. Edo, M. C. Edwards, A. Effler, P. Ehrens, J. Eichholz, S. S. Eikenberry, M. Eisenmann, R. A. Eisenstein, R. C. Essick, H. Estelles, D. Estevez, Z. B. Etienne, T. Etzel, M. Evans, T. M. Evans, V. Fafone, H. Fair, S. Fairhurst, X. Fan, S. Farinon, B. Farr, W. M. Farr, E. J. Fauchon-Jones, M. Favata, M. Fays, M. Fazio, C. Fee, J. Feicht, M. M. Fejer, F. Feng, A. Fernandez-Galiana, I. Ferrante, E. C. Ferreira, T. A. Ferreira, F. Ferrini, F. Fidecaro, I. Fiori, D. Fiorucci, M. Fishbach, R. P. Fisher, J. M. Fishner, M. Fitz-Axen, R. Flaminio, M. Fletcher, E. Flynn, H. Fong, J. A. Font, P. W. F. Forsyth, J. D. Fournier, S. Frasca, F. Frasconi, Z. Frei, A. Freise, R. Frey, V. Frey, P. Fritschel, V. V. Frolov, P. Fulda, M. Fyffe, H. A. Gabbard, B. U. Gadre, S. M. Gaebel, J. R. Gair, L. Gammaitoni, M. R. Ganija, S. G. Gaonkar, A. Garcia, C. García-Quirós, F. Garufi, B. Gateley, S. Gaudio, G. Gaur, V. Gayathri, G. Gemme, E. Genin,

A. Gennai, D. George, J. George, L. Gergely, V. Germain, S. Ghonge, Abhirup Ghosh, Archisman Ghosh, S. Ghosh, B. Giacomazzo, J. A. Giaime, K. D. Giardina, A. Giazotto, K. Gill, G. Giordano, L. Glover, P. Godwin, E. Goetz, R. Goetz, B. Goncharov, G. González, J. M. Gonzalez Castro, A. Gopakumar, M. L. Gorodetsky, S. E. Gossan, M. Gosselin, R. Gouaty, A. Grado, C. Graef, M. Granata, A. Grant, S. Gras, P. Grassia, C. Gray, R. Gray, G. Greco, A. C. Green, R. Green, E. M. Gretarsson, P. Groot, H. Grote, S. Grunewald, P. Gruning, G. M. Guidi, H. K. Gulati, Y. Guo, A. Gupta, M. K. Gupta, E. K. Gustafson, R. Gustafson, L. Haegel, O. Halim, B. R. Hall, E. D. Hall, E. Z. Hamilton, G. Hammond, M. Haney, M. M. Hanke, J. Hanks, C. Hanna, M. D. Hannam, O. A. Hannuksela, J. Hanson, T. Hardwick, K. Haris, J. Harms, G. M. Harry, I. W. Harry, C. J. Haster, K. Haughian, F. J. Hayes, J. Healy, A. Heidmann, M. C. Heintze, H. Heitmann, P. Hello, G. Hemming, M. Hendry, I. S. Heng, J. Hennig, A. W. Heptonstall, Francisco Hernandez Vivanco, M. Heurs, S. Hild, T. Hinderer, D. Hoak, S. Hochheim, D. Hofman, A. M. Holgado, N. A. Holland, K. Holt, D. E. Holz, P. Hopkins, C. Horst, J. Hough, E. J. Howell, C. G. Hoy, A. Hreibi, E. A. Huerta, D. Huet, B. Hughey, M. Hulko, S. Husa, S. H. Huttner, T. Huynh-Dinh, B. Idzkowski, A. Iess, C. Ingram, R. Inta, G. Intini, B. Irwin, H. N. Isa, J. M. Isac, M. Isi, B. R. Iyer, K. Izumi, T. Jacqmin, S. J. Jadhav, K. Jani, N. N. Janthalur, P. Jaranowski, A. C. Jenkins, J. Jiang, D. S. Johnson, A. W. Jones, D. I. Jones, R. Jones, R. J. G. Jonker, L. Ju, J. Junker, C. V. Kalaghatgi, V. Kalogera, B. Kamai, S. Kandhasamy, G. Kang, J. B. Kanner, S. J. Kapadia, S. Karki, K. S. Karvinen, R. Kashyap, M. Kasprzack, S. Katsanevas, E. Katsavounidis, W. Katzman, S. Kaufer, K. Kawabe, N. V. Keerthana, F. Kéfélian, D. Keitel, R. Kennedy, J. S. Key, F. Y. Khalili, H. Khan, I. Khan, S. Khan, Z. Khan, E. A. Khazanov, M. Khursheed, N. Kijbunchoo, Chunglee Kim, J. C. Kim, K. Kim, W. Kim, W. S. Kim, Y. M. Kim, C. Kimball, E. J. King, P. J. King, M. Kinley-Hanlon, R. Kirchhoff, J. S. Kissel, L. Kleybolte, J. H. Klika, S. Klimenko, T. D. Knowles, P. Koch, S. M. Koehlenbeck, G. Koekoek, S. Koley, V. Kondrashov, A. Kontos, N. Koper, M. Korobko, W. Z. Korth, I. Kowalska, D. B. Kozak, V. Kringel, N. Krishnendu, A. Królak, G. Kuehn, A. Kumar, P. Kumar, R. Kumar, S. Kumar, L. Kuo, A. Kutynia, S. Kwang, B. D. Lackey, K. H. Lai, T. L. Lam, M. Landry, B. B. Lane, R. N. Lang, J. Lange, B. Lantz, R. K. Lanza, A. Lartaux-Vollard, P. D. Lasky, M. Laxen, A. Lazzarini, C. Laz-

zaro, P. Leaci, S. Leavey, Y. K. Lecoeuche, C. H. Lee, H. K. Lee, H. M. Lee, H. W. Lee, J. Lee, K. Lee, J. Lehmann, A. Lenon, N. Leroy, N. Letendre, Y. Levin, J. Li, K. J. L. Li, T. G. F. Li, X. Li, F. Lin, F. Linde, S. D. Linker, T. B. Littenberg, J. Liu, X. Liu, R. K. L. Lo, N. A. Lockerbie, L. T. London, A. Longo, M. Lorenzini, V. Loriette, M. Lormand, G. Losurdo, J. D. Lough, C. O. Lousto, G. Lovelace, M. E. Lower, H. Lück, D. Lumaca, A. P. Lundgren, R. Lynch, Y. Ma, R. Macas, S. Macfoy, M. MacInnis, D. M. Macleod, A. Macquet, F. Magaña-Sandoval, L. Magaña Zertuche, R. M. Magee, E. Majorana, I. Maksimovic, A. Malik, N. Man, V. Mandic, V. Mangano, G. L. Mansell, M. Manske, M. Mantovani, M. Mapelli, F. Marchesoni, F. Marion, S. Márka, Z. Márka, C. Markakis, A. S. Markosyan, A. Markowitz, E. Maros, A. Marquina, S. Marsat, F. Martelli, I. W. Martin, R. M. Martin, D. V. Martynov, K. Mason, E. Massera, A. Masserot, T. J. Massinger, M. Masso-Reid, S. Mastrogiovanni, A. Matas, F. Matichard, L. Matone, N. Mavalvala, N. Mazumder, J. J. McCann, R. McCarthy, D. E. McClelland, S. McCormick, L. McCuller, S. C. McGuire, J. McIver, D. J. McManus, T. McRae, S. T. McWilliams, D. Meacher, G. D. Meadors, M. Mehmet, A. K. Mehta, J. Meidam, A. Melatos, G. Mendell, R. A. Mercer, L. Mereni, E. L. Merilh, M. Merzougui, S. Meshkov, C. Messenger, C. Messick, R. Metzdorff, P. M. Meyers, H. Miao, C. Michel, H. Middleton, E. E. Mikhailov, L. Milano, A. L. Miller, A. Miller, M. Millhouse, J. C. Mills, M. C. Milovich-Goff, O. Minazzoli, Y. Minenkov, A. Mishkin, C. Mishra, T. Mistry, S. Mitra, V. P. Mitrofanov, G. Mitselmakher, R. Mittleman, G. Mo, D. Moffa, K. Mogushi, S. R. P. Mohapatra, M. Montani, C. J. Moore, D. Moraru, G. Moreno, S. Morisaki, B. Mours, C. M. Mow-Lowry, Arunava Mukherjee, D. Mukherjee, S. Mukherjee, N. Mukund, A. Mullavey, J. Munch, E. A. Muñiz, M. Muratore, P. G. Murray, A. Nagar, I. Nardecchia, L. Naticchioni, R. K. Nayak, J. Neilson, G. Nelemans, T. J. N. Nelson, M. Nery, A. Neunzert, K. Y. Ng, S. Ng, P. Nguyen, D. Nichols, S. Nissanke, F. Nocera, C. North, L. K. Nuttall, M. Obergaulinger, J. Oberling, B. D. O'Brien, G. D. O'Dea, G. H. Ogin, J. J. Oh, S. H. Oh, F. Ohme, H. Ohta, M. A. Okada, M. Oliver, P. Oppermann, Richard J. Oram, B. O'Reilly, R. G. Ormiston, L. F. Ortega, R. O'Shaughnessy, S. Ossokine, D. J. Ottaway, H. Overmier, B. J. Owen, A. E. Pace, G. Pagano, M. A. Page, A. Pai, S. A. Pai, J. R. Palamos, O. Palashov, C. Palomba, A. Pal-Singh, Huang-Wei Pan, B. Pang, P. T. H. Pang, C. Pankow, F. Pannarale,

B. C. Pant, F. Paoletti, A. Paoli, A. Parida, W. Parker, D. Pascucci, A. Pasqualetti, R. Passaquieti, D. Passuello, M. Patil, B. Patricelli, B. L. Pearlstone, C. Pedersen, M. Pedraza, R. Pedurand, A. Pele, S. Penn, C. J. Perez, A. Perreca, H. P. Pfeiffer, M. Phelps, K. S. Phukon, O. J. Piccinni, M. Pichot, F. Piergiovanni, G. Pillant, L. Pinard, M. Pirello, M. Pitkin, R. Poggiani, D. Y. T. Pong, S. Ponrathnam, P. Popolizio, E. K. Porter, J. Powell, A. K. Prajapati, J. Prasad, K. Prasai, R. Prasanna, G. Pratten, T. Prestegard, S. Privitera, G. A. Prodi, L. G. Prokhorov, O. Puncken, M. Punturo, P. Puppo, M. Pürrer, H. Qi, V. Quetschke, P. J. Quinonez, E. A. Quintero, R. Quitzow-James, F. J. Raab, H. Radkins, N. Radulescu, P. Raffai, S. Raja, C. Rajan, B. Rajbhandari, M. Rakhmanov, K. E. Ramirez, A. Ramos-Buades, Javed Rana, K. Rao, P. Rapagnani, V. Raymond, M. Razzano, J. Read, T. Regimbau, L. Rei, S. Reid, D. H. Reitze, W. Ren, F. Ricci, C. J. Richardson, J. W. Richardson, P. M. Ricker, K. Riles, M. Rizzo, N. A. Robertson, R. Robie, F. Robinet, A. Rocchi, L. Rolland, J. G. Rollins, V. J. Roma, M. Romanelli, R. Romano, C. L. Romel, J. H. Romie, K. Rose, D. Rosińska, S. G. Rosofsky, M. P. Ross, S. Rowan, A. Rüdiger, P. Ruggi, G. Rutins, K. Ryan, S. Sachdev, T. Sadecki, M. Sakellariadou, L. Salconi, M. Saleem, A. Samajdar, L. Sammut, E. J. Sanchez, L. E. Sanchez, N. Sanchis-Gual, V. Sandberg, J. R. Sanders, K. A. Santiago, N. Sarin, B. Sassolas, B. S. Sathyaprakash, P. R. Saulson, O. Sauter, R. L. Savage, P. Schale, M. Scheel, J. Scheuer, P. Schmidt, R. Schnabel, R. M. S. Schofield, A. Schönbeck, E. Schreiber, B. W. Schulte, B. F. Schutz, S. G. Schwalbe, J. Scott, S. M. Scott, E. Seidel, D. Sellers, A. S. Sengupta, N. Sennett, D. Sentenac, V. Sequino, A. Sergeev, Y. Setyawati, D. A. Shaddock, T. Shaffer, M. S. Shahriar, M. B. Shaner, L. Shao, P. Sharma, P. Shawhan, H. Shen, R. Shink, D. H. Shoemaker, D. M. Shoemaker, S. ShyamSundar, K. Siellez, M. Sieniawska, D. Sigg, A. D. Silva, L. P. Singer, N. Singh, A. Singhal, A. M. Sintes, S. Sitmukhambetov, V. Skliris, B. J. J. Slagmolen, T. J. Slaven-Blair, J. R. Smith, R. J. E. Smith, S. Somala, E. J. Son, B. Sorazu, F. Sorrentino, T. Souradeep, E. Sowell, A. P. Spencer, M. Spera, A. K. Srivastava, V. Srivastava, K. Staats, C. Stachie, M. Standke, D. A. Steer, M. Steinke, J. Steinlechner, S. Steinlechner, D. Steinmeyer, S. P. Stevenson, D. Stocks, R. Stone, D. J. Stops, K. A. Strain, G. Stratta, S. E. Strigin, A. Strunk, R. Sturani, A. L. Stuver, V. Sudhir, T. Z. Summerscales, L. Sun, S. Sunil, J. Suresh, P. J. Sutton, B. L. Swinkels, M. J. Szczepańczyk, M. Tacca,

S. C. Tait, C. Talbot, D. Talukder, D. B. Tanner, M. Tápai, A. Taracchini, J. D. Tasson, R. Taylor, F. Thies, M. Thomas, P. Thomas, S. R. Thondapu, K. A. Thorne, E. Thrane, Shubhanshu Tiwari, Srishti Tiwari, V. Tiwari, K. Toland, M. Tonelli, Z. Tornasi, A. Torres-Forné, C. I. Torrie, D. Töyrä, F. Travasso, G. Traylor, M. C. Tringali, A. Trovato, L. Trozzo, R. Trudeau, K. W. Tsang, M. Tse, R. Tso, L. Tsukada, D. Tsuna, D. Tuyenbayev, K. Ueno, D. Ugolini, C. S. Unnikrishnan, A. L. Urban, S. A. Usman, H. Vahlbruch, G. Vajente, G. Valdes, N. van Bakel, M. van Beuzekom, J. F. J. van den Brand, C. Van Den Broeck, D. C. Vander-Hyde, L. van der Schaaf, J. V. van Heijningen, A. A. van Veggel, M. Vardaro, V. Varma, S. Vass, M. Vasúth, A. Vecchio, G. Vedovato, J. Veitch, P. J. Veitch, K. Venkateswara, G. Venugopalan, D. Verkindt, F. Vetrano, A. Viceré, A. D. Viets, D. J. Vine, J. Y. Vinet, S. Vitale, T. Vo, H. Vocca, C. Vorvick, S. P. Vyatchanin, A. R. Wade, L. E. Wade, M. Wade, R. Walet, M. Walker, L. Wallace, S. Walsh, G. Wang, H. Wang, J. Z. Wang, W. H. Wang, Y. F. Wang, R. L. Ward, Z. A. Warden, J. Warner, M. Was, J. Watchi, B. Weaver, L. W. Wei, M. Weinert, A. J. Weinstein, R. Weiss, F. Wellmann, L. Wen, E. K. Wessel, P. Weßels, J. W. Westhouse, K. Wette, J. T. Whelan, B. F. Whiting, C. Whittle, D. M. Wilken, D. Williams, A. R. Williamson, J. L. Willis, B. Willke, M. H. Wimmer, W. Winkler, C. C. Wipf, H. Wittel, G. Woan, J. Woehler, J. K. Wofford, J. Worden, J. L. Wright, D. S. Wu, D. M. Wysocki, L. Xiao, H. Yamamoto, C. C. Yancey, L. Yang, M. J. Yap, M. Yazback, D. W. Yeeles, Hang Yu, Haocun Yu, S. H. R. Yuen, M. Yvert, A. K. Zadrożny, M. Zanolin, T. Zelenova, J. P. Zendri, M. Zevin, J. Zhang, L. Zhang, T. Zhang, C. Zhao, M. Zhou, Z. Zhou, X. J. Zhu, A. B. Zimmerman, Y. Zlochower, M. E. Zucker, J. Zweizig, LIGO Scientific Collaboration, and Virgo Collaboration. Binary Black Hole Population Properties Inferred from the First and Second Observing Runs of Advanced LIGO and Advanced Virgo. , 882(2):L24, September 2019.

[25] John Magorrian, Scott Tremaine, Douglas Richstone, Ralf Bender, Gary Bower, Alan Dressler, S. M. Faber, Karl Gebhardt, Richard Green, Carl Grillmair, John Kormendy, and Tod Lauer. The Demography of Massive Dark Objects in Galaxy Centers. , 115(6):2285–2305, June 1998.

[26] A. M. Ghez, S. Salim, N. N. Weinberg, J. R. Lu, T. Do, J. K. Dunn, K. Matthews, M. R. Morris, S. Yelda, E. E. Becklin, T. Kremenek,

M. Milosavljevic, and J. Naiman. Measuring Distance and Properties of the Milky Way's Central Supermassive Black Hole with Stellar Orbits. , 689(2):1044–1062, December 2008.

[27] Reinhard Genzel, Frank Eisenhauer, and Stefan Gillessen. The Galactic Center massive black hole and nuclear star cluster. *Reviews of Modern Physics*, 82(4):3121–3195, October 2010.

[28] John Michell. On the Means of Discovering the Distance, Magnitude, &c. of the Fixed Stars, in Consequence of the Diminution of the Velocity of Their Light, in Case Such a Diminution Should be Found to Take Place in any of Them, and Such Other Data Should be Procured from Observations, as Would be Farther Necessary for That Purpose. By the Rev. John Michell, B. D. F. R. S. In a Letter to Henry Cavendish, Esq. F. R. S. and A. S. *Philosophical Transactions of the Royal Society of London Series I*, 74:35–57, January 1784.

[29] K. Schwarzschild. On the Gravitational Field of a Mass Point According to Einstein's Theory. *Abh. Konigl. Preuss. Akad. Wissenschaften Jahre 1906,92, Berlin,1907*, 1916:189–196, January 1916.

[30] E. T. Newman, E. Couch, K. Chinnapared, A. Exton, A. Prakash, and R. Torrence. Metric of a Rotating, Charged Mass. *Journal of Mathematical Physics*, 6(6):918–919, June 1965.

[31] Werner Israel. Event Horizons in Static Vacuum Space-Times. *Physical Review*, 164(5):1776–1779, December 1967.

[32] Roy P. Kerr. Gravitational Field of a Spinning Mass as an Example of Algebraically Special Metrics. , 11(5):237–238, September 1963.

[33] G. Nordström. On the Energy of the Gravitation field in Einstein's Theory. *Koninklijke Nederlandse Akademie van Wetenschappen Proceedings Series B Physical Sciences*, 20:1238–1245, January 1918.

[34] James M. Bardeen. Kerr Metric Black Holes. , 226(5240):64–65, April 1970.

[35] A. Buonanno and T. Damour. Effective one-body approach to general relativistic two-body dynamics. , 59(8):084006, April 1999.

[36] Josef Lense and Hans Thirring. Über den Einfluß der Eigenrotation der Zentralkörper auf die Bewegung der Planeten und Monde nach der Einsteinschen Gravitationstheorie. *Physikalische Zeitschrift*, 19:156, January 1918.

[37] M. Schmidt. 3C 273 : A Star-Like Object with Large Red-Shift. , 197(4872):1040, March 1963.

[38] D. Lynden-Bell. Galactic Nuclei as Collapsed Old Quasars. , 223(5207):690–694, August 1969.

[39] A. L. Kinney, H. R. Schmitt, C. J. Clarke, J. E. Pringle, J. S. Ulvestad, and R. R. J. Antonucci. Jet Directions in Seyfert Galaxies. , 537(1):152–177, July 2000.

[40] John N. Bahcall, Sofia Kirhakos, David H. Saxe, and Donald P. Schneider. Hubble Space Telescope Images of a Sample of 20 Nearby Luminous Quasars. , 479(2):642–658, April 1997.

[41] Robert Antonucci. Unified models for active galactic nuclei and quasars. , 31:473–521, January 1993.

[42] C. Megan Urry and Paolo Padovani. Unified Schemes for Radio-Loud Active Galactic Nuclei. , 107:803, September 1995.

[43] Hagai Netzer. Revisiting the Unified Model of Active Galactic Nuclei. , 53:365–408, August 2015.

[44] E. E. Salpeter. Accretion of Interstellar Matter by Massive Objects. , 140:796–800, August 1964.

[45] F. Hoyle and R. A. Lyttleton. The effect of interstellar matter on climatic variation. *Mathematical Proceedings of the Cambridge Philosophical Society*, 35(3):405415, 1939.

[46] H. Bondi and F. Hoyle. On the mechanism of accretion by stars. , 104:273, January 1944.

[47] H. Bondi. On spherically symmetrical accretion. , 112:195, January 1952.

[48] E. Shima, T. Matsuda, H. Takeda, and K. Sawada. Hydrodynamic calculations of axisymmetric accretion flow. , 217:367–386, November 1985.

[49] Richard Edgar. A review of Bondi-Hoyle-Lyttleton accretion. , 48(10):843–859, September 2004.

[50] I. D. Novikov and K. S. Thorne. Astrophysics of black holes. In *Black Holes (Les Astres Occlus)*, pages 343–450, January 1973.

[51] Kip S. Thorne. Disk-Accretion onto a Black Hole. II. Evolution of the Hole. , 191:507–520, July 1974.

[52] Steven A. Balbus and John F. Hawley. A Powerful Local Shear Instability in Weakly Magnetized Disks. I. Linear Analysis. , 376:214, July 1991.

[53] N. I. Shakura and R. A. Sunyaev. Reprint of 1973A&A....24..337S. Black holes in binary systems. Observational appearance. , 500:33–51, June 1973.

[54] J. E. Pringle. Accretion discs in astrophysics. , 19:137–162, January 1981.

[55] Stuart L. Shapiro. Spin, Accretion, and the Cosmological Growth of Supermassive Black Holes. , 620(1):59–68, February 2005.

[56] R. D. Blandford and R. L. Znajek. Electromagnetic extraction of energy from Kerr black holes. , 179:433–456, May 1977.

[57] Alessandro Lupi, Giada Quadri, Marta Volonteri, Monica Colpi, and John A. Regan. Sustained super-Eddington accretion in high-redshift quasars. *arXiv e-prints*, page arXiv:2312.08422, December 2023.

[58] Jake S. Bennett, Debora Sijacki, Tiago Costa, Nicolas Laporte, and Callum Witten. The growth of the gargantuan black holes powering high-redshift quasars and their impact on the formation of early galaxies and protoclusters. , 527(1):1033–1054, January 2024.

[59] A. R. King, J. E. Pringle, and J. A. Hofmann. The evolution of black hole mass and spin in active galactic nuclei. , 385(3):1621–1627, April 2008.

[60] J. Aird, A. L. Coil, and A. Georgakakis. X-rays across the galaxy population - II. The distribution of AGN accretion rates as a function of stellar mass and redshift. , 474:1225–1249, January 2018.

[61] A. Soltan. Masses of quasars. , 200:115–122, July 1982.

[62] Qingjuan Yu and Scott Tremaine. Observational constraints on growth of massive black holes. , 335(4):965–976, October 2002.

[63] James M. Bardeen, William H. Press, and Saul A. Teukolsky. Rotating Black Holes: Locally Nonrotating Frames, Energy Extraction, and Scalar Synchrotron Radiation. , 178:347–370, December 1972.

[64] R. Ruffini and J. A. Wheeler. Relativistic cosmology and space platforms. *ESRO*, 52:45–174, January 1971.

[65] C. P. Dullemond, C. N. Kimmig, and J. J. Zanazzi. On the equations of warped disc dynamics. , 511(2):2925–2947, April 2022.

[66] J. C. B. Papaloizou and J. E. Pringle. The time-dependence of non-planar accretion discs. , 202:1181–1194, March 1983.

[67] J. E. Pringle. A simple approach to the evolution of twisted accretion discs. , 258(4):811–818, October 1992.

[68] G. I. Ogilvie. Nonlinear Fluid Dynamics of Warped Discs. In J. A. Sellwood and Jeremy Goodman, editors, *Astrophysical Discs - an EC Summer School*, volume 160 of *Astronomical Society of the Pacific Conference Series*, page 61, April 1999.

[69] Andrew King. The AGN-Starburst Connection, Galactic Superwinds, and M_{BH}-σ. , 635(2):L121–L123, December 2005.

[70] Philip F. Hopkins and Eliot Quataert. An analytic model of angular momentum transport by gravitational torques: from galaxies to massive black holes. , 415(2):1027–1050, August 2011.

[71] Timothy M. Heckman and Philip N. Best. The Coevolution of Galaxies and Supermassive Black Holes: Insights from Surveys of the Contemporary Universe. , 52:589–660, August 2014.

[72] Pedro R. Capelo, Chiara Feruglio, Ryan C. Hickox, and Francesco Tombesi. Black Hole-Galaxy Co-evolution and the Role of Feedback. In *Handbook of X-ray and Gamma-ray Astrophysics. Edited by Cosimo Bambi and Andrea Santangelo*, page 126. 2023.

[73] Robert A. Crain, Yannick M. Bahé, Claudia del P. Lagos, Alireza Rahmati, Joop Schaye, Ian G. McCarthy, Antonino Marasco, Richard G. Bower, Matthieu Schaller, Tom Theuns, and Thijs van der Hulst. The EAGLE simulations: atomic hydrogen associated with galaxies. , 464(4):4204–4226, February 2017.

[74] Dong Zhang. A Review of the Theory of Galactic Winds Driven by Stellar Feedback. *Galaxies*, 6(4):114, November 2018.

[75] Nadine Häring and Hans-Walter Rix. On the Black Hole Mass-Bulge Mass Relation. , 604(2):L89–L92, April 2004.

[76] Laura Ferrarese and David Merritt. A Fundamental Relation between Supermassive Black Holes and Their Host Galaxies. , 539(1):L9–L12, August 2000.

[77] Jenny E. Greene, Chien Y. Peng, Minjin Kim, Cheng-Yu Kuo, James A. Braatz, C. M. V. Impellizzeri, James J. Condon, K. Y. Lo, Christian Henkel, and Mark J. Reid. Precise Black Hole Masses from Megamaser Disks: Black Hole-Bulge Relations at Low Mass. , 721(1):26–45, September 2010.

[78] Chien Y. Peng. How Mergers May Affect the Mass Scaling Relation between Gravitationally Bound Systems. , 671(2):1098–1107, December 2007.

[79] Michaela Hirschmann, Sadegh Khochfar, Andreas Burkert, Thorsten Naab, Shy Genel, and Rachel S. Somerville. On the evolution of the intrinsic scatter in black hole versus galaxy mass relations. , 407(2):1016–1032, September 2010.

[80] Knud Jahnke and Andrea V. Macciò. The Non-causal Origin of the Black-hole-galaxy Scaling Relations. , 734(2):92, June 2011.

[81] Piero Madau and Mark Dickinson. Cosmic Star-Formation History. , 52:415–486, August 2014.

[82] Timothy M. Heckman, Guinevere Kauffmann, Jarle Brinchmann, Stéphane Charlot, Christy Tremonti, and Simon D. M. White. Present-Day Growth of Black Holes and Bulges: The Sloan Digital Sky Survey Perspective. , 613(1):109–118, September 2004.

[83] Fabrizio Fiore, Massimo Gaspari, Alfredo Luminari, Paolo Tozzi, and Lucilla De Arcangelis. Dynamical complexity in micro-scale disk-wind systems. *arXiv e-prints*, page arXiv:2304.12696, April 2023.

[84] Joseph Silk and Martin J. Rees. Quasars and galaxy formation. , 331:L1–L4, March 1998.

[85] Andrew King. Black Holes, Galaxy Formation, and the M_{BH}-σ Relation. , 596(1):L27–L29, October 2003.

[86] J. N. Reeves, P. T. O'Brien, V. Braito, E. Behar, L. Miller, T. J. Turner, A. C. Fabian, S. Kaspi, R. Mushotzky, and M. Ward. A Compton-thick Wind in the High-luminosity Quasar, PDS 456. , 701(1):493–507, August 2009.

[87] F. Tombesi, M. Meléndez, S. Veilleux, J. N. Reeves, E. González-Alfonso, and C. S. Reynolds. Wind from the black-hole accretion disk driving a molecular outflow in an active galaxy. , 519(7544):436–438, March 2015.

[88] Claudia Cicone, Marcella Brusa, Cristina Ramos Almeida, Giovanni Cresci, Bernd Husemann, and Vincenzo Mainieri. The largely unconstrained multiphase nature of outflows in AGN host galaxies. *Nature Astronomy*, 2:176–178, February 2018.

[89] A. Fluetsch, R. Maiolino, S. Carniani, S. Arribas, F. Belfiore, E. Bellocchi, S. Cazzoli, C. Cicone, G. Cresci, A. C. Fabian, R. Gallagher, W. Ishibashi, F. Mannucci, A. Marconi, M. Perna, E. Sturm, and G. Venturi. Properties of the multiphase outflows in local (ultra)luminous infrared galaxies. , 505(4):5753–5783, August 2021.

[90] Darren J. Croton, Volker Springel, Simon D. M. White, G. De Lucia, C. S. Frenk, L. Gao, A. Jenkins, G. Kauffmann, J. F. Navarro, and N. Yoshida. The many lives of active galactic nuclei: cooling flows, black holes and the luminosities and colours of galaxies. , 365(1):11–28, January 2006.

[91] Volker Springel, Tiziana Di Matteo, and Lars Hernquist. Black Holes in Galaxy Mergers: The Formation of Red Elliptical Galaxies. , 620(2):L79–L82, February 2005.

[92] N. P. H. Nesvadba, F. Boulanger, M. D. Lehnert, P. Guillard, and P. Salome. Dense gas without star formation: the kpc-sized turbulent molecular disk in 3C 326 N. , 536:L5, December 2011.

[93] Sylvain Veilleux, Roberto Maiolino, Alberto D. Bolatto, and Susanne Aalto. Cool outflows in galaxies and their implications. , 28(1):2, April 2020.

[94] E. Sturm, E. González-Alfonso, S. Veilleux, J. Fischer, J. Graciá-Carpio, S. Hailey-Dunsheath, A. Contursi, A. Poglitsch, A. Sternberg, R. Davies, R. Genzel, D. Lutz, L. Tacconi, A. Verma, R. Maiolino, and J. A. de Jong. Massive Molecular Outflows and Negative Feedback in ULIRGs Observed by Herschel-PACS. , 733(1):L16, May 2011.

[95] C. Cicone, R. Maiolino, E. Sturm, J. Graciá-Carpio, C. Feruglio, R. Neri, S. Aalto, R. Davies, F. Fiore, J. Fischer, S. García-Burillo, E. González-Alfonso, S. Hailey-Dunsheath, E. Piconcelli, and S. Veilleux. Massive molecular outflows and evidence for AGN feedback from CO observations. , 562:A21, February 2014.

[96] F. Fiore, C. Feruglio, F. Shankar, M. Bischetti, A. Bongiorno, M. Brusa, S. Carniani, C. Cicone, F. Duras, A. Lamastra, V. Mainieri, A. Marconi, N. Menci, R. Maiolino, E. Piconcelli, G. Vietri, and L. Zappacosta. AGN wind scaling relations and the co-evolution of black holes and galaxies. , 601:A143, May 2017.

[97] A. Fluetsch, R. Maiolino, S. Carniani, A. Marconi, C. Cicone, M. A. Bourne, T. Costa, A. C. Fabian, W. Ishibashi, and G. Venturi. Cold molecular outflows in the local Universe and their feedback effect on galaxies. , 483(4):4586–4614, March 2019.

[98] Roger Blandford, David Meier, and Anthony Readhead. Relativistic Jets from Active Galactic Nuclei. , 57:467–509, August 2019.

[99] Mateusz Ruszkowski and Christoph Pfrommer. Cosmic ray feedback in galaxies and galaxy clusters. , 31(1):4, December 2023.

[100] M. Cano-Díaz, R. Maiolino, A. Marconi, H. Netzer, O. Shemmer, and G. Cresci. Observational evidence of quasar feedback quenching star formation at high redshift. , 537:L8, January 2012.

[101] Dominika Wylezalek and Nadia L. Zakamska. Evidence of suppression of star formation by quasar-driven winds in gas-rich host galaxies at $z < 1$? , 461(4):3724–3739, October 2016.

[102] R. Maiolino, H. R. Russell, A. C. Fabian, S. Carniani, R. Gallagher, S. Cazzoli, S. Arribas, F. Belfiore, E. Bellocchi, L. Colina, G. Cresci, W. Ishibashi, A. Marconi, F. Mannucci, E. Oliva, and E. Sturm. Star formation inside a galactic outflow. , 544(7649):202–206, March 2017.

[103] R. Gallagher, R. Maiolino, F. Belfiore, N. Drory, R. Riffel, and R. A. Riffel. Widespread star formation inside galactic outflows. , 485(3):3409–3429, May 2019.

[104] G. Cresci, V. Mainieri, M. Brusa, A. Marconi, M. Perna, F. Mannucci, E. Piconcelli, R. Maiolino, C. Feruglio, F. Fiore, A. Bongiorno, G. Lanzuisi, A. Merloni, M. Schramm, J. D. Silverman, and F. Civano. Blowin' in the Wind: Both "Negative" and "Positive" Feedback in an Obscured High-z Quasar. , 799(1):82, January 2015.

[105] I. Smirnova-Pinchukova, B. Husemann, T. A. Davis, C. M. A. Smith, M. Singha, G. R. Tremblay, R. S. Klessen, M. Powell, T. Connor, S. A. Baum, F. Combes, S. M. Croom, M. Gaspari, J. Neumann, C. P. O'Dea, M. Pérez-Torres, D. J. Rosario, T. Rose, J. Scharwächter, and N. Winkel. The Close AGN Reference Survey (CARS). No obvious signature of AGN feedback on star formation, but subtle trends. , 659:A125, March 2022.

[106] T. Taro Shimizu, Richard F. Mushotzky, Marcio Meléndez, Michael J. Koss, Amy J. Barger, and Lennox L. Cowie. Herschel far-infrared photometry of the Swift Burst Alert Telescope active galactic nuclei sample of the local universe - III. Global star-forming properties and the lack of a connection to nuclear activity. , 466(3):3161–3183, April 2017.

[107] D. J. Rosario, P. Santini, D. Lutz, H. Netzer, F. E. Bauer, S. Berta, B. Magnelli, P. Popesso, D. M. Alexander, W. N. Brandt, R. Genzel, R. Maiolino, J. R. Mullaney, R. Nordon, A. Saintonge, L. Tacconi, and S. Wuyts. Nuclear Activity is More Prevalent in Star-forming Galaxies. , 771(1):63, July 2013.

[108] Caleb Lammers, Kartheik G. Iyer, Hector Ibarra-Medel, Camilla Pacifici, Sebastián F. Sánchez, Sandro Tacchella, and Joanna Woo. Active Galactic Nuclei Feedback in SDSS-IV MaNGA: AGNs Have Suppressed Central Star Formation Rates. , 953(1):26, August 2023.

[109] C. Scannapieco, M. Wadepuhl, O. H. Parry, J. F. Navarro, A. Jenkins, V. Springel, R. Teyssier, E. Carlson, H. M. P. Couchman, R. A. Crain, C. Dalla Vecchia, C. S. Frenk, C. Kobayashi, P. Monaco, G. Murante, T. Okamoto, T. Quinn, J. Schaye, G. S. Stinson, T. Theuns, J. Wadsley, S. D. M. White, and R. Woods. The Aquila comparison project: the effects

of feedback and numerical methods on simulations of galaxy formation. , 423(2):1726–1749, June 2012.

[110] Tiziana Di Matteo, Volker Springel, and Lars Hernquist. Energy input from quasars regulates the growth and activity of black holes and their host galaxies. , 433(7026):604–607, February 2005.

[111] Sarah Wellons, Claude-André Faucher-Giguère, Philip F. Hopkins, Eliot Quataert, Daniel Anglés-Alcázar, Robert Feldmann, Christopher C. Hayward, Dušan Kereš, Kung-Yi Su, and Andrew Wetzel. Exploring supermassive black hole physics and galaxy quenching across halo mass in FIRE cosmological zoom simulations. , 520(4):5394–5412, April 2023.

[112] Joop Schaye, Robert A. Crain, Richard G. Bower, Michelle Furlong, Matthieu Schaller, Tom Theuns, Claudio Dalla Vecchia, Carlos S. Frenk, I. G. McCarthy, John C. Helly, Adrian Jenkins, Y. M. Rosas-Guevara, Simon D. M. White, Maarten Baes, C. M. Booth, Peter Camps, Julio F. Navarro, Yan Qu, Alireza Rahmati, Till Sawala, Peter A. Thomas, and James Trayford. The EAGLE project: simulating the evolution and assembly of galaxies and their environments. , 446(1):521–554, January 2015.

[113] Marta Volonteri, Pedro R. Capelo, Hagai Netzer, Jillian Bellovary, Massimo Dotti, and Fabio Governato. Growing black holes and galaxies: black hole accretion versus star formation rate. , 449(2):1470–1485, May 2015.

[114] Marta Volonteri, Pedro R. Capelo, Hagai Netzer, Jillian Bellovary, Massimo Dotti, and Fabio Governato. Black hole accretion versus star formation rate: theory confronts observations. , 452(1):L6–L10, September 2015.

[115] S. R. Ward, C. M. Harrison, T. Costa, and V. Mainieri. Cosmological simulations predict that AGN preferentially live in gas-rich, star-forming galaxies despite effective feedback. , 514(2):2936–2957, August 2022.

[116] Asa F. L. Bluck, Joanna M. Piotrowska, and Roberto Maiolino. The Fundamental Signature of Star Formation Quenching from AGN Feedback: A Critical Dependence of Quiescence on Supermassive Black Hole Mass, Not Accretion Rate. , 944(1):108, February 2023.

[117] Elad Zinger, Annalisa Pillepich, Dylan Nelson, Rainer Weinberger, Rüdiger Pakmor, Volker Springel, Lars Hernquist, Federico Marinacci, and

Mark Vogelsberger. Ejective and preventative: the IllustrisTNG black hole feedback and its effects on the thermodynamics of the gas within and around galaxies. , 499(1):768–792, November 2020.

[118] Bryan A. Terrazas, Eric F. Bell, Annalisa Pillepich, Dylan Nelson, Rachel S. Somerville, Shy Genel, Rainer Weinberger, Mélanie Habouzit, Yuan Li, Lars Hernquist, and Mark Vogelsberger. The relationship between black hole mass and galaxy properties: examining the black hole feedback model in IllustrisTNG. , 493(2):1888–1906, April 2020.

[119] Kastytis Zubovas and Andrew King. Clearing Out a Galaxy. , 745(2):L34, February 2012.

[120] Claude-André Faucher-Giguère and Eliot Quataert. The physics of galactic winds driven by active galactic nuclei. , 425(1):605–622, September 2012.

[121] R. Weaver, R. McCray, J. Castor, P. Shapiro, and R. Moore. Interstellar bubbles. II. Structure and evolution. , 218:377–395, December 1977.

[122] Bon-Chul Koo and Christopher F. McKee. Dynamics of Wind Bubbles and Superbubbles. I. Slow Winds and Fast Winds. , 388:93, March 1992.

[123] Tilman Hartwig, Marta Volonteri, and Gohar Dashyan. Active galactic nucleus outflows in galaxy discs. , 476(2):2288–2307, May 2018.

[124] J. E. Dyson and D. A. Williams. *The physics of the interstellar medium.* 1997.

[125] Alexander J. Richings and Claude-André Faucher-Giguère. The origin of fast molecular outflows in quasars: molecule formation in AGN-driven galactic winds. , 474(3):3673–3699, March 2018.

[126] Paul Torrey, Philip F. Hopkins, Claude-André Faucher-Giguère, Daniel Anglés-Alcázar, Eliot Quataert, Xiangcheng Ma, Robert Feldmann, Dusan Keres, and Norm Murray. The impact of AGN wind feedback in simulations of isolated galaxies with a multiphase ISM. , 497(4):5292–5308, October 2020.

[127] S. Yu. Sazonov, J. P. Ostriker, and R. A. Sunyaev. Quasars: the characteristic spectrum and the induced radiative heating. , 347(1):144–156, January 2004.

[128] Annalisa Pillepich, Dylan Nelson, Volker Springel, Rüdiger Pakmor, Paul Torrey, Rainer Weinberger, Mark Vogelsberger, Federico Marinacci, Shy Genel, Arjen van der Wel, and Lars Hernquist. First results from the TNG50 simulation: the evolution of stellar and gaseous discs across cosmic time. , 490(3):3196–3233, December 2019.

[129] Philip F. Hopkins, Andrew Wetzel, Dušan Kereš, Claude-André Faucher-Giguère, Eliot Quataert, Michael Boylan-Kolchin, Norman Murray, Christopher C. Hayward, Shea Garrison-Kimmel, Cameron Hummels, Robert Feldmann, Paul Torrey, Xiangcheng Ma, Daniel Anglés-Alcázar, Kung-Yi Su, Matthew Orr, Denise Schmitz, Ivanna Escala, Robyn Sanderson, Michael Y. Grudić, Zachary Hafen, Ji-Hoon Kim, Alex Fitts, James S. Bullock, Coral Wheeler, T. K. Chan, Oliver D. Elbert, and Desika Narayanan. FIRE-2 simulations: physics versus numerics in galaxy formation. , 480(1):800–863, October 2018.

[130] Mark Vogelsberger, Shy Genel, Debora Sijacki, Paul Torrey, Volker Springel, and Lars Hernquist. A model for cosmological simulations of galaxy formation physics. , 436(4):3031–3067, December 2013.

[131] M. Tremmel, M. Karcher, F. Governato, M. Volonteri, T. R. Quinn, A. Pontzen, L. Anderson, and J. Bellovary. The Romulus cosmological simulations: a physical approach to the formation, dynamics and accretion models of SMBHs. , 470(1):1121–1139, September 2017.

[132] Rainer Weinberger, Volker Springel, Lars Hernquist, Annalisa Pillepich, Federico Marinacci, Rüdiger Pakmor, Dylan Nelson, Shy Genel, Mark Vogelsberger, Jill Naiman, and Paul Torrey. Simulating galaxy formation with black hole driven thermal and kinetic feedback. , 465(3):3291–3308, March 2017.

[133] Nicholas A. Henden, Ewald Puchwein, Sijing Shen, and Debora Sijacki. The FABLE simulations: a feedback model for galaxies, groups, and clusters. , 479(4):5385–5412, October 2018.

[134] Alessandro Lupi, Marta Volonteri, Roberto Decarli, Stefano Bovino, Joseph Silk, and Jacqueline Bergeron. High-redshift quasars and their host galaxies - I. Kinematical and dynamical properties and their tracers. , 488(3):4004–4022, September 2019.

[135] Alessandro Lupi, Marta Volonteri, Roberto Decarli, Stefano Bovino, and Joseph Silk. High-redshift quasars and their host galaxies - II. Multiphase gas and stellar kinematics. , 510(4):5760–5779, March 2022.

[136] Ena Choi, Jeremiah P. Ostriker, Thorsten Naab, and Peter H. Johansson. Radiative and Momentum-based Mechanical Active Galactic Nucleus Feedback in a Three-dimensional Galaxy Evolution Code. , 754(2):125, August 2012.

[137] Paramita Barai, Giuseppe Murante, Stefano Borgani, Massimo Gaspari, Gian Luigi Granato, Pierluigi Monaco, and Cinthia Ragone-Figueroa. Kinetic AGN feedback effects on cluster cool cores simulated using SPH. , 461(2):1548–1567, September 2016.

[138] Daniel Anglés-Alcázar, Romeel Davé, Claude-André Faucher-Giguère, Feryal Özel, and Philip F. Hopkins. Gravitational torque-driven black hole growth and feedback in cosmological simulations. , 464(3):2840–2853, January 2017.

[139] Romeel Davé, Daniel Anglés-Alcázar, Desika Narayanan, Qi Li, Mika H. Rafieferantsoa, and Sarah Appleby. SIMBA: Cosmological simulations with black hole growth and feedback. , 486(2):2827–2849, June 2019.

[140] Luca Sala, Elia Cenci, Pedro R. Capelo, Alessandro Lupi, and Massimo Dotti. Non-isotropic feedback from accreting spinning black holes. , 500(4):4788–4800, January 2021.

[141] Simon D. M. White and Carlos S. Frenk. Galaxy Formation through Hierarchical Clustering. , 379:52, September 1991.

[142] Joseph F. Hennawi, Michael A. Strauss, Masamune Oguri, Naohisa Inada, Gordon T. Richards, Bartosz Pindor, Donald P. Schneider, Robert H. Becker, Michael D. Gregg, Patrick B. Hall, David E. Johnston, Xiaohui Fan, Scott Burles, David J. Schlegel, James E. Gunn, Robert H. Lupton, Neta A. Bahcall, Robert J. Brunner, and Jon Brinkmann. Binary Quasars in the Sloan Digital Sky Survey: Evidence for Excess Clustering on Small Scales. , 131(1):1–23, January 2006.

[143] G. Foreman, M. Volonteri, and M. Dotti. Double Quasars: Probes of Black Hole Scaling Relationships and Merger Scenarios. , 693(2):1554–1562, March 2009.

[144] Xin Liu, Yue Shen, Michael A. Strauss, and Lei Hao. Active Galactic Nucleus Pairs from the Sloan Digital Sky Survey. I. The Frequency on ∼5-100 kpc Scales. , 737(2):101, August 2011.

[145] Julia M. Comerford, Kyle Schluns, Jenny E. Greene, and Richard J. Cool. Dual Supermassive Black Hole Candidates in the AGN and Galaxy Evolution Survey. , 777(1):64, November 2013.

[146] C. Vignali, E. Piconcelli, M. Perna, J. Hennawi, R. Gilli, A. Comastri, G. Zamorani, M. Dotti, and S. Mathur. Probing black hole accretion in quasar pairs at high redshift. , 477(1):780–790, June 2018.

[147] John D. Silverman, Shenli Tang, Khee-Gan Lee, Tilman Hartwig, Andy Goulding, Michael A. Strauss, Malte Schramm, Xuheng Ding, Rogemar A. Riffel, Seiji Fujimoto, Chiaki Hikage, Masatoshi Imanishi, Kazushi Iwasawa, Knud Jahnke, Issha Kayo, Nobunari Kashikawa, Toshihiro Kawaguchi, Kotaro Kohno, Wentao Luo, Yoshiki Matsuoka, Yuichi Matsuda, Tohru Nagao, Masamune Oguri, Yoshiaki Ono, Masafusa Onoue, Masami Ouchi, Kazuhiro Shimasaku, Hyewon Suh, Nao Suzuki, Yoshiaki Taniguchi, Yoshiki Toba, Yoshihiro Ueda, and Naoki Yasuda. Dual Supermassive Black Holes at Close Separation Revealed by the Hyper Suprime-Cam Subaru Strategic Program. , 899(2):154, August 2020.

[148] Yang-Wei Zhang, Yang Huang, Jin-Ming Bai, Xiao-Wei Liu, Jian-guo Wang, and Xiao-bo Dong. A Systematic Search for Dual AGNs in Merging Galaxies (Astro-daring): III: Results from the SDSS Spectroscopic Surveys. , 162(6):276, December 2021.

[149] Yang-Wei Zhang, Yang Huang, Jin-Ming Bai, Xiao-Wei Liu, Jian-guo Wang, and Xiao-bo Dong. A Systematic Search for Dual Active Galactic Nuclei in Merging Galaxies (ASTRO-DARING) II: First Results from Long-slit Spectroscopic Observations. , 162(6):289, December 2021.

[150] Stefanie Komossa. Observational evidence for supermassive black hole binaries. In Joan M. Centrella, editor, *The Astrophysics of Gravitational Wave Sources*, volume 686 of *American Institute of Physics Conference Series*, pages 161–174, October 2003.

[151] G. Fabbiano, Junfeng Wang, M. Elvis, and G. Risaliti. A close nuclear black-hole pair in the spiral galaxy NGC3393. , 477(7365):431–434, September 2011.

[152] Julia M. Comerford, Brian F. Gerke, Daniel Stern, Michael C. Cooper, Benjamin J. Weiner, Jeffrey A. Newman, Kristin Madsen, and R. Scott Barrows. Kiloparsec-scale Spatial Offsets in Double-peaked Narrow-line Active Galactic Nuclei. I. Markers for Selection of Compelling Dual Active Galactic Nucleus Candidates. , 753(1):42, July 2012.

[153] C. Rodriguez, G. B. Taylor, R. T. Zavala, A. B. Peck, L. K. Pollack, and R. W. Romani. A Compact Supermassive Binary Black Hole System. , 646(1):49–60, July 2006.

[154] Michael Eracleous, Todd A. Boroson, Jules P. Halpern, and Jia Liu. A Large Systematic Search for Close Supermassive Binary and Rapidly Recoiling Black Holes. , 201(2):23, August 2012.

[155] P. Tsalmantza, R. Decarli, M. Dotti, and David W. Hogg. A Systematic Search for Massive Black Hole Binaries in the Sloan Digital Sky Survey Spectroscopic Sample. , 738(1):20, September 2011.

[156] Massimo Dotti, Matteo Bonetti, Daniel J. D'Orazio, Zoltán Haiman, and Luis C. Ho. Binary black hole signatures in polarized light curves. , 509(1):212–223, January 2022.

[157] M. C. Begelman, R. D. Blandford, and M. J. Rees. Massive black hole binaries in active galactic nuclei. , 287(5780):307–309, September 1980.

[158] M. C. Begelman, R. D. Blandford, and M. J. Rees. Massive black hole binaries in active galactic nuclei. , 287(5780):307–309, September 1980.

[159] S. Chandrasekhar. Dynamical Friction. I. General Considerations: the Coefficient of Dynamical Friction. , 97:255, March 1943.

[160] Monica Colpi. Massive Binary Black Holes in Galactic Nuclei and Their Path to Coalescence. , 183(1-4):189–221, September 2014.

[161] Marta Volonteri, Tamara Bogdanović, Massimo Dotti, and Monica Colpi. Massive Black Holes in Merging Galaxies. *IAU Focus Meeting*, 29B:285–291, January 2016.

[162] Hugo Pfister, Alessandro Lupi, Pedro R. Capelo, Marta Volonteri, Jillian M. Bellovary, and Massimo Dotti. The birth of a supermassive black hole binary. , 471(3):3646–3656, November 2017.

[163] Pau Amaro-Seoane, Jeff Andrews, Manuel Arca Sedda, Abbas Askar, Quentin Baghi, Razvan Balasov, Imre Bartos, Simone S. Bavera, Jillian Bellovary, Christopher P. L. Berry, Emanuele Berti, Stefano Bianchi, Laura Blecha, Stéphane Blondin, Tamara Bogdanović, Samuel Boissier, Matteo Bonetti, Silvia Bonoli, Elisa Bortolas, Katelyn Breivik, Pedro R. Capelo, Laurentiu Caramete, Federico Cattorini, Maria Charisi, Sylvain Chaty, Xian Chen, Martyna Chruślińska, Alvin J. K. Chua, Ross Church, Monica Colpi, Daniel D'Orazio, Camilla Danielski, Melvyn B. Davies, Pratika Dayal, Alessandra De Rosa, Andrea Derdzinski, Kyriakos Destounis, Massimo Dotti, Ioana Dutan, Irina Dvorkin, Gaia Fabj, Thierry Foglizzo, Saavik Ford, Jean-Baptiste Fouvry, Alessia Franchini, Tassos Fragos, Chris Fryer, Massimo Gaspari, Davide Gerosa, Luca Graziani, Paul Groot, Melanie Habouzit, Daryl Haggard, Zoltan Haiman, Wen-Biao Han, Alina Istrate, Peter H. Johansson, Fazeel Mahmood Khan, Tomas Kimpson, Kostas Kokkotas, Albert Kong, Valeriya Korol, Kyle Kremer, Thomas Kupfer, Astrid Lamberts, Shane Larson, Mike Lau, Dongliang Liu, Nicole Lloyd-Ronning, Giuseppe Lodato, Alessandro Lupi, Chung-Pei Ma, Tomas Maccarone, Ilya Mandel, Alberto Mangiagli, Michela Mapelli, Stéphane Mathis, Lucio Mayer, Sean McGee, Barry McKernan, M. Coleman Miller, David F. Mota, Matthew Mumpower, Syeda S. Nasim, Gijs Nelemans, Scott Noble, Fabio Pacucci, Francesca Panessa, Vasileios Paschalidis, Hugo Pfister, Delphine Porquet, John Quenby, Angelo Ricarte, Friedrich K. Röpke, John Regan, Stephan Rosswog, Ashley Ruiter, Milton Ruiz, Jessie Runnoe, Raffaella Schneider, Jeremy Schnittman, Amy Secunda, Alberto Sesana, Naoki Seto, Lijing Shao, Stuart Shapiro, Carlos Sopuerta, Nicholas C. Stone, Arthur Suvorov, Nicola Tamanini, Tomas Tamfal, Thomas Tauris, Karel Temmink, John Tomsick, Silvia Toonen, Alejandro Torres-Orjuela, Martina Toscani, Antonios Tsokaros, Caner Unal, Verónica Vázquez-Aceves, Rosa Valiante, Maurice van Putten, Jan van Roestel, Christian Vignali, Marta Volonteri, Kinwah Wu, Ziri Younsi, Shenghua Yu, Silvia Zane, Lorenz Zwick, Fabio Antonini, Vishal Baibhav, Enrico Barausse, Alexander Bonilla Rivera, Marica Branchesi, Graziella Branduardi-Raymont, Kevin Burdge, Srija Chakraborty, Jorge Cuadra, Kristen Dage, Benjamin Davis, Selma E. de Mink, Roberto Decarli, Daniela Doneva, Stephanie Escoffier, Poshak Gandhi, Francesco Haardt, Carlos O. Lousto, Samaya Nissanke, Jason Nordhaus, Richard O'Shaughnessy, Simon Portegies Zwart, Adam Pound, Fabian Schussler,

Olga Sergijenko, Alessandro Spallicci, Daniele Vernieri, and Alejandro Vigna-Gómez. Astrophysics with the Laser Interferometer Space Antenna. *Living Reviews in Relativity*, 26(1):2, December 2023.

[164] Alessandra De Rosa, Cristian Vignali, Tamara Bogdanović, Pedro R. Capelo, Maria Charisi, Massimo Dotti, Bernd Husemann, Elisabeta Lusso, Lucio Mayer, Zsolt Paragi, Jessie Runnoe, Alberto Sesana, Lisa Steinborn, Stefano Bianchi, Monica Colpi, Luciano del Valle, Sándor Frey, Krisztina É. Gabányi, Margherita Giustini, Matteo Guainazzi, Zoltan Haiman, Noelia Herrera Ruiz, Rubén Herrero-Illana, Kazushi Iwasawa, S. Komossa, Davide Lena, Nora Loiseau, Miguel Perez-Torres, Enrico Piconcelli, and Marta Volonteri. The quest for dual and binary supermassive black holes: A multi-messenger view. , 86:101525, December 2019.

[165] Pau Amaro-Seoane, Jeff Andrews, Manuel Arca Sedda, Abbas Askar, Razvan Balasov, Imre Bartos, Simone S. Bavera, Jillian Bellovary, Christopher P. L. Berry, Emanuele Berti, Stefano Bianchi, Laura Blecha, Stéphane Blondin, Tamara Bogdanović, Samuel Boissier, Matteo Bonetti, Silvia Bonoli, Elisa Bortolas, Katie Breivik, Pedro R. Capelo, Laurentiu Caramete, Federico Catorini, Maria Charisi, Sylvain Chaty, Xian Chen, Martyna Chruślińska, Alvin J. K. Chua, Ross Church, Monica Colpi, Daniela D'Orazio, Camilla Danielski, Melvyn B. Davies, Pratika Dayal, Alessandra De Rosa, Andrea Derdzinski, Kyriakos Destounis, Massimo Dotti, Ioana Duţan, Irina Dvorkin, Gaia Fabj, Thierry Foglizzo, Saavik Ford, Jean-Baptiste Fouvry, Tassos Fragkos, Chris Fryer, Massimo Gaspari, Davide Gerosa, Luca Graziani, Paul J. Groot, Melanie Habouzit, Daryl Haggard, Zoltan Haiman, Wen-Biao Han, Alina Istrate, Peter H. Johansson, Fazeel Mahmood Khan, Tomas Kimpson, Kostas Kokkotas, Albert Kong, Valeriya Korol, Kyle Kremer, Thomas Kupfer, Astrid Lamberts, Shane Larson, Mike Lau, Dongliang Liu, Nicole Lloyd-Ronning, Giuseppe Lodato, Alessandro Lupi, Chung-Pei Ma, Tomas Maccarone, Ilya Mandel, Alberto Mangiagli, Michela Mapelli, Stefan Mathis, Lucio Mayer, Sean McGee, Berry McKernan, M. Coleman Miller, David F. Mota, Matthew Mumpower, Syeda S. Nasim, Gijs Nelemans, Scott Noble, Fabio Pacucci, Francesca Panessa, Vasileios Paschalidis, Hugo Pfister, Delphine Porquet, John Quenby, Fritz Röpke, John Regan, Stephan Rosswog, Ashley Ruiter, Milton Ruiz, Jessie Runnoe, Rafaella Schneider, Jeremy Schnittman, Amy Secunda, Alberto Sesana, Naoki Seto, Lijing

Shao, Stuart Shapiro, Carlos Sopuerta, Nick Stone, Arthur Suvorov, Nicola Tamanini, Tomas Tamfal, Thomas Tauris, Karel Temmink, John Tomsick, Silvia Toonen, Alejandro Torres-Orjuela, Martina Toscani, Antonios Tsokaros, Caner Unal, Verónica Vázquez-Aceves, Rosa Valiante, Maurice van Putten, Jan van Roestel, Christian Vignali, Marta Volonteri, Kinwah Wu, Ziri Younsi, Shenghua Yu, Silvia Zane, Lorenz Zwick, Fabio Antonini, Vishal Baibhav, Enrico Barausse, Alexander Bonilla Rivera, Marica Branchesi, Graziella Branduardi-Raymont, Kevin Burdge, Srija Chakraborty, Jorge Cuadra, Kristen Dage, Benjamin Davis, Selma E. de Mink, Roberto Decarli, Daniela Doneva, Stephanie Escoffier, Poshak Gandhi, Francesco Haardt, Carlos O. Lousto, Samaya Nissanke, Jason Nordhaus, Richard O'Shaughnessy, Simon Portegies Zwart, Adam Pound, Fabian Schussler, Olga Sergijenko, Alessandro Spallicci, Daniele Vernieri, and Alejandro Vigna-Gómez. Astrophysics with the Laser Interferometer Space Antenna. *arXiv e-prints*, page arXiv:2203.06016, March 2022.

[166] S. Chandrasekhar. Dynamical Friction. I. General Considerations: the Coefficient of Dynamical Friction. , 97:255, March 1943.

[167] James Binney and Scott Tremaine. *Galactic Dynamics: Second Edition*. 2008.

[168] S. Tremaine and M. D. Weinberg. Dynamical friction in spherical systems. , 209:729–757, August 1984.

[169] Tomas Tamfal, Pedro R. Capelo, Stelios Kazantzidis, Lucio Mayer, Douglas Potter, Joachim Stadel, and Lawrence M. Widrow. Formation of LISA Black Hole Binaries in Merging Dwarf Galaxies: The Imprint of Dark Matter. , 864(1):L19, September 2018.

[170] Elisa Bortolas, Pedro R. Capelo, Tommaso Zana, Lucio Mayer, Matteo Bonetti, Massimo Dotti, Melvyn B. Davies, and Piero Madau. Global torques and stochasticity as the drivers of massive black hole pairing in the young Universe. , 498(3):3601–3615, November 2020.

[171] Roberto Decarli, Manuel Aravena, Leindert Boogaard, Chris Carilli, Jorge González-López, Fabian Walter, Paulo C. Cortes, Pierre Cox, Elisabete da Cunha, Emanuele Daddi, Tanio Díaz-Santos, Jacqueline A. Hodge, Hanae Inami, Marcel Neeleman, Mladen Novak, Pascal Oesch, Gergö Popping, Dominik Riechers, Ian Smail, Bade Uzgil, Paul van der Werf, Jeff Wagg,

and Axel Weiss. The ALMA Spectroscopic Survey in the Hubble Ultra Deep Field: Multiband Constraints on Line-luminosity Functions and the Cosmic Density of Molecular Gas. , 902(2):110, October 2020.

[172] Eve C. Ostriker. Dynamical Friction in a Gaseous Medium. , 513(1):252–258, March 1999.

[173] L. Mayer, S. Kazantzidis, P. Madau, M. Colpi, T. Quinn, and J. Wadsley. Rapid Formation of Supermassive Black Hole Binaries in Galaxy Mergers with Gas. *Science*, 316(5833):1874, June 2007.

[174] Damien Chapon, Lucio Mayer, and Romain Teyssier. Hydrodynamics of galaxy mergers with supermassive black holes: is there a last parsec problem? , 429(4):3114–3122, March 2013.

[175] Shihong Liao, Dimitrios Irodotou, Peter H. Johansson, Thorsten Naab, Francesco Paolo Rizzuto, Jessica M. Hislop, Ruby J. Wright, and Alexander Rawlings. RABBITS – II. The impact of AGN feedback on coalescing supermassive black holes in disc and elliptical galaxy mergers. *arXiv e-prints*, page arXiv:2311.01493, November 2023.

[176] KwangHo Park and Tamara Bogdanović. Gaseous Dynamical Friction in Presence of Black Hole Radiative Feedback. , 838(2):103, April 2017.

[177] Rosie Y. Talbot, Debora Sijacki, and Martin A. Bourne. Simulations of spin-driven AGN jets in gas-rich galaxy mergers. , 528(3):5432–5451, March 2024.

[178] Rafael Souza Lima, Lucio Mayer, Pedro R. Capelo, and Jillian M. Bellovary. The Pairing of Accreting Massive Black Holes in Multiphase Circumnuclear Disks: the Interplay Between Radiative Cooling, Star Formation, and Feedback Processes. , 838(1):13, March 2017.

[179] Elisa Bortolas, Alessia Franchini, Matteo Bonetti, and Alberto Sesana. The Competing Effect of Gas and Stars in the Evolution of Massive Black Hole Binaries. , 918(1):L15, September 2021.

[180] Luke Zoltan Kelley, Laura Blecha, Lars Hernquist, Alberto Sesana, and Stephen R. Taylor. The gravitational wave background from massive black hole binaries in Illustris: spectral features and time to detection with pulsar timing arrays. , 471(4):4508–4526, November 2017.

[181] Alberto Sesana, Francesco Haardt, and Piero Madau. Interaction of Massive Black Hole Binaries with Their Stellar Environment. I. Ejection of Hypervelocity Stars. , 651(1):392–400, November 2006.

[182] Joshua E. Barnes and Lars E. Hernquist. Fueling Starburst Galaxies with Gas-rich Mergers. , 370:L65, April 1991.

[183] Joshua E. Barnes. Formation of gas discs in merging galaxies. , 333(3):481–494, July 2002.

[184] D. B. Sanders and I. F. Mirabel. Luminous Infrared Galaxies. , 34:749, January 1996.

[185] D. Downes and P. M. Solomon. Rotating Nuclear Rings and Extreme Starbursts in Ultraluminous Galaxies. , 507(2):615–654, November 1998.

[186] J. Cuadra, P. J. Armitage, R. D. Alexander, and M. C. Begelman. Massive black hole binary mergers within subparsec scale gas discs. , 393(4):1423–1432, March 2009.

[187] Enrico Ragusa, Giuseppe Lodato, and Daniel J. Price. Suppression of the accretion rate in thin discs around binary black holes. , 460(2):1243–1253, August 2016.

[188] Daniel J. D'Orazio, Zoltán Haiman, and Andrew MacFadyen. Accretion into the central cavity of a circumbinary disc. , 436(4):2997–3020, December 2013.

[189] Brian D. Farris, Paul Duffell, Andrew I. MacFadyen, and Zoltan Haiman. Binary Black Hole Accretion from a Circumbinary Disk: Gas Dynamics inside the Central Cavity. , 783(2):134, March 2014.

[190] Paul C. Duffell, Daniel D'Orazio, Andrea Derdzinski, Zoltan Haiman, Andrew MacFadyen, Anna L. Rosen, and Jonathan Zrake. Circumbinary Disks: Accretion and Torque as a Function of Mass Ratio and Disk Viscosity. , 901(1):25, September 2020.

[191] Alessia Franchini, Alessandro Lupi, and Alberto Sesana. Resolving Massive Black Hole Binary Evolution via Adaptive Particle Splitting. , 929(1):L13, April 2022.

[192] Ji-Ming Shi and Julian H. Krolik. Three-dimensional MHD Simulation of Circumbinary Accretion Disks. II. Net Accretion Rate. , 807(2):131, July 2015.

[193] D. Syer and C. J. Clarke. Satellites in discs: regulating the accretion luminosity. , 277(3):758–766, December 1995.

[194] G. Lodato, S. Nayakshin, A. R. King, and J. E. Pringle. Black hole mergers: can gas discs solve the 'final parsec' problem? , 398(3):1392–1402, September 2009.

[195] Zoltán Haiman, Bence Kocsis, and Kristen Menou. The Population of Viscosity- and Gravitational Wave-driven Supermassive Black Hole Binaries Among Luminous Active Galactic Nuclei. , 700(2):1952–1969, August 2009.

[196] Luciano del Valle and Andrés Escala. Binary-Disk Interaction: Gap-opening Criteria. , 761(1):31, December 2012.

[197] Roman R. Rafikov. Structure and Evolution of Circumbinary Disks around Supermassive Black Hole Binaries. , 774(2):144, September 2013.

[198] Massimo Dotti, Monica Colpi, and Francesco Haardt. Laser Interferometer Space Antenna double black holes: dynamics in gaseous nuclear discs. , 367(1):103–112, March 2006.

[199] Luciano del Valle and Marta Volonteri. The effect of AGN feedback on the migration time-scale of supermassive black holes binaries. , 480(1):439–450, October 2018.

[200] Emanuele Berti and Marta Volonteri. Cosmological Black Hole Spin Evolution by Mergers and Accretion. , 684(2):822–828, September 2008.

[201] Antoine Klein, Enrico Barausse, Alberto Sesana, Antoine Petiteau, Emanuele Berti, Stanislav Babak, Jonathan Gair, Sofiane Aoudia, Ian Hinder, Frank Ohme, and Barry Wardell. Science with the space-based interferometer eLISA: Supermassive black hole binaries. , 93(2):024003, January 2016.

[202] M. Dotti, M. Volonteri, A. Perego, M. Colpi, M. Ruszkowski, and F. Haardt. Dual black holes in merger remnants - II. Spin evolution and gravitational recoil. , 402(1):682–690, February 2010.

[203] Sebastian Bustamante and Volker Springel. Spin evolution and feedback of supermassive black holes in cosmological simulations. , 490(3):4133–4153, December 2019.

[204] Elia Cenci, Luca Sala, Alessandro Lupi, Pedro R. Capelo, and Massimo Dotti. Black hole spin evolution in warped accretion discs. , 500(3):3719–3727, January 2021.

[205] Yohan Dubois, Ricarda Beckmann, Frédéric Bournaud, Hoseung Choi, Julien Devriendt, Ryan Jackson, Sugata Kaviraj, Taysun Kimm, Katarina Kraljic, Clotilde Laigle, Garreth Martin, Min-Jung Park, Sébastien Peirani, Christophe Pichon, Marta Volonteri, and Sukyoung K. Yi. Introducing the NEWHORIZON simulation: Galaxy properties with resolved internal dynamics across cosmic time. , 651:A109, July 2021.

[206] Marta Volonteri, Piero Madau, Eliot Quataert, and Martin J. Rees. The Distribution and Cosmic Evolution of Massive Black Hole Spins. , 620(1):69–77, February 2005.

[207] N. Fanidakis, C. M. Baugh, A. J. Benson, R. G. Bower, S. Cole, C. Done, and C. S. Frenk. Grand unification of AGN activity in the ΛCDM cosmology. , 410(1):53–74, January 2011.

[208] Enrico Barausse. The evolution of massive black holes and their spins in their galactic hosts. , 423(3):2533–2557, July 2012.

[209] A. Sesana, E. Barausse, M. Dotti, and E. M. Rossi. Linking the Spin Evolution of Massive Black Holes to Galaxy Kinematics. , 794(2):104, October 2014.

[210] Christopher S. Reynolds. Observational Constraints on Black Hole Spin. , 59:117–154, September 2021.

[211] Samuele Campitiello, Gabriele Ghisellini, Tullia Sbarrato, and Giorgio Calderone. How to constrain mass and spin of supermassive black holes through their disk emission. , 612:A59, April 2018.

[212] W. Ishibashi, A. C. Fabian, and C. S. Reynolds. Radiation pattern and outflow geometry: a new probe of black hole spin? , 486(2):2210–2214, June 2019.

[213] W. Ishibashi. AGN anisotropic radiative feedback set by black hole spin. , 495(2):2515–2523, June 2020.

[214] David Williamson, Sebastian Hönig, and Marta Venanzi. 3d radiation hydrodynamics of a dynamical torus. *The Astrophysical Journal*, 876(2):137, may 2019.

[215] Francesco Bollati, Alessandro Lupi, Massimo Dotti, and Francesco Haardt. Dynamical evolution of massive black hole pairs in the presence of spin-dependent radiative feedback. , February 2023.

[216] Philip F. Hopkins. A new class of accurate, mesh-free hydrodynamic simulation methods. , 450(1):53–110, June 2015.

[217] Li-Xin Li, Erik R. Zimmerman, Ramesh Narayan, and Jeffrey E. McClintock. Multitemperature Blackbody Spectrum of a Thin Accretion Disk around a Kerr Black Hole: Model Computations and Comparison with Observations. , 157(2):335–370, April 2005.

[218] Luca Sala, Elia Cenci, Pedro R. Capelo, Alessandro Lupi, and Massimo Dotti. Non-isotropic feedback from accreting spinning black holes. , 500(4):4788–4800, January 2021.

[219] Davide Fiacconi, Debora Sijacki, and J. E. Pringle. Galactic nuclei evolution with spinning black holes: method and implementation. , 477(3):3807–3835, July 2018.

[220] Michael Curtis and Debora Sijacki. Resolving flows around black holes: the impact of gas angular momentum. , 463(1):63–77, November 2016.

[221] Nina Akerman, Stephanie Tonnesen, Bianca M. Poggianti, Rory Smith, and Antonino Marasco. How Ram Pressure Drives Radial Gas Motions in the Surviving Disk. *arXiv e-prints*, page arXiv:2301.09652, January 2023.

[222] Michael Y. Grudić, Dávid Guszejnov, Philip F. Hopkins, Stella S. R. Offner, and Claude-André Faucher-Giguère. STARFORGE: Towards a comprehensive numerical model of star cluster formation and feedback. , 506(2):2199–2231, September 2021.

[223] Kung-Yi Su, Philip F. Hopkins, Greg L. Bryan, Rachel S. Somerville, Christopher C. Hayward, Daniel Anglés-Alcázar, Claude-André Faucher-Giguère, Sarah Wellons, Jonathan Stern, Bryan A. Terrazas, T. K. Chan,

Matthew E. Orr, Cameron Hummels, Robert Feldmann, and Dušan Kereš. Which AGN jets quench star formation in massive galaxies? , 507(1):175–204, October 2021.

[224] Jonathan Mercedes-Feliz, Daniel Anglés-Alcázar, Christopher C. Hayward, Rachel K. Cochrane, Bryan A. Terrazas, Sarah Wellons, Alexander J. Richings, Claude-André Faucher-Giguère, Jorge Moreno, Kung Yi Su, Philip F. Hopkins, Eliot Quataert, and Dušan Kereš. Local positive feedback in the overall negative: the impact of quasar winds on star formation in the FIRE cosmological simulations. *arXiv e-prints*, page arXiv:2301.01784, January 2023.

[225] A. Luminari, F. Tombesi, E. Piconcelli, F. Nicastro, K. Fukumura, D. Kazanas, F. Fiore, and L. Zappacosta. The importance of special relativistic effects in modelling ultra-fast outflows. , 633:A55, January 2020.

[226] Philip F. Hopkins, Paul Torrey, Claude-André Faucher-Giguère, Eliot Quataert, and Norman Murray. Stellar and quasar feedback in concert: effects on AGN accretion, obscuration, and outflows. , 458(1):816–831, May 2016.

[227] Julio F. Navarro, Carlos S. Frenk, and Simon D. M. White. A Universal Density Profile from Hierarchical Clustering. , 490(2):493–508, December 1997.

[228] Shihong Liao, Jianxiong Chen, and M. C. Chu. A Universal Angular Momentum Profile for Dark Matter Halos. , 844(1):86, July 2017.

[229] J. S. Bullock, A. Dekel, T. S. Kolatt, A. V. Kravtsov, A. A. Klypin, C. Porciani, and J. R. Primack. A Universal Angular Momentum Profile for Galactic Halos. , 555(1):240–257, July 2001.

[230] Philip F. Hopkins, Andrew Wetzel, Dušan Kereš, Claude-André Faucher-Giguère, Eliot Quataert, Michael Boylan-Kolchin, Norman Murray, Christopher C. Hayward, and Kareem El-Badry. How to model supernovae in simulations of star and galaxy formation. , 477(2):1578–1603, June 2018.

[231] Matthew J. Miller and Joel N. Bregman. The Structure of the Milky Way's Hot Gas Halo. , 770(2):118, June 2013.

[232] Matthew J. Miller and Joel N. Bregman. Constraining the Milky Way's Hot Gas Halo with O VII and O VIII Emission Lines. , 800(1):14, February 2015.

[233] Volker Springel and Lars Hernquist. Cosmological smoothed particle hydrodynamics simulations: a hybrid multiphase model for star formation. , 339(2):289–311, February 2003.

[234] Yohan Dubois, Marta Volonteri, Joseph Silk, Julien Devriendt, Adrianne Slyz, and Romain Teyssier. Black hole evolution - I. Supernova-regulated black hole growth. , 452(2):1502–1518, September 2015.

[235] Kastytis Zubovas and Gediminas Maskeliūnas. Life after AGN switchoff: Evolution and properties of fossil galactic outflows. , June 2023.

[236] Kastytis Zubovas and Sergei Nayakshin. Fermi bubbles in the Milky Way: the closest AGN feedback laboratory courtesy of Sgr A*? , 424(1):666–683, July 2012.

[237] Mariko Nomura, Ken Ohsuga, Hiroyuki R. Takahashi, Keiichi Wada, and Tessei Yoshida. Radiation hydrodynamic simulations of line-driven disk winds for ultra-fast outflows. , 68(1):16, February 2016.

[238] M. Nomura and K. Ohsuga. Line-driven disc wind model for ultrafast outflows in active galactic nuclei - scaling with luminosity. , 465(3):2873–2879, March 2017.

[239] Luis C. Ho. Radiatively Inefficient Accretion in Nearby Galaxies. , 699(1):626–637, July 2009.

[240] Yohan Dubois, Raphaël Gavazzi, Sébastien Peirani, and Joseph Silk. AGN-driven quenching of star formation: morphological and dynamical implications for early-type galaxies. , 433(4):3297–3313, August 2013.

[241] Rainer Weinberger, Volker Springel, Rüdiger Pakmor, Dylan Nelson, Shy Genel, Annalisa Pillepich, Mark Vogelsberger, Federico Marinacci, Jill Naiman, Paul Torrey, and Lars Hernquist. Supermassive black holes and their feedback effects in the IllustrisTNG simulation. , 479(3):4056–4072, September 2018.

[242] N. Werner, B. R. McNamara, E. Churazov, and E. Scannapieco. Hot Atmospheres, Cold Gas, AGN Feedback and the Evolution of Early Type Galaxies: A Topical Perspective. , 215(1):5, January 2019.

[243] J. Scholtz, C. M. Harrison, D. J. Rosario, D. M. Alexander, C. C. Chen, D. Kakkad, V. Mainieri, A. L. Tiley, O. Turner, M. Cirasuolo, R. M. Sharples, and S. Stach. KASHz: No evidence for ionised outflows instantaneously suppressing star formation in moderate luminosity AGN at z $\sim$ 1.4-2.6. , 492(3):3194–3216, March 2020.

[244] Tiziana Di Matteo, Rupert A. C. Croft, Yu Feng, Dacen Waters, and Stephen Wilkins. The origin of the most massive black holes at high-z: BlueTides and the next quasar frontier. , 467(4):4243–4251, June 2017.

[245] Paramita Barai and Elisabete M. de Gouveia Dal Pino. Intermediate-mass black hole growth and feedback in dwarf galaxies at high redshifts. , 487(4):5549–5563, August 2019.

[246] A. Lupi, F. Haardt, M. Dotti, D. Fiacconi, L. Mayer, and P. Madau. Growing massive black holes through supercritical accretion of stellar-mass seeds. , 456(3):2993–3003, March 2016.

[247] John A. Regan, Turlough P. Downes, Marta Volonteri, Ricarda Beckmann, Alessandro Lupi, Maxime Trebitsch, and Yohan Dubois. Super-Eddington accretion and feedback from the first massive seed black holes. , 486(3):3892–3906, July 2019.

[248] Warren Massonneau, Marta Volonteri, Yohan Dubois, and Ricarda S. Beckmann. How the super-Eddington regime regulates black hole growth in high-redshift galaxies. , 670:A180, February 2023.

[249] Rafael Souza Lima, Lucio Mayer, Pedro R. Capelo, and Jillian M. Bellovary. The Pairing of Accreting Massive Black Holes in Multiphase Circumnuclear Disks: the Interplay Between Radiative Cooling, Star Formation, and Feedback Processes. , 838(1):13, March 2017.

[250] Elia Cenci, Luca Sala, Alessandro Lupi, Pedro R. Capelo, and Massimo Dotti. Black hole spin evolution in warped accretion discs. , 500(3):3719–3727, January 2021.

[251] Daniel Anglés-Alcázar, Romeel Davé, Claude-André Faucher-Giguère, Feryal Özel, and Philip F. Hopkins. Gravitational torque-driven black hole growth and feedback in cosmological simulations. , 464(3):2840–2853, January 2017.

[252] Philip F. Hopkins. A new class of accurate, mesh-free hydrodynamic simulation methods. , 450(1):53–110, June 2015.

[253] Alessandro Lupi, Francesco Haardt, and Massimo Dotti. Massive black hole and gas dynamics in galaxy nuclei mergers - I. Numerical implementation. , 446(2):1765–1774, January 2015.

[254] Lars Hernquist. An Analytical Model for Spherical Galaxies and Bulges. , 356:359, June 1990.

[255] M. Dotti, M. Colpi, F. Haardt, and L. Mayer. Supermassive black hole binaries in gaseous and stellar circumnuclear discs: orbital dynamics and gas accretion. , 379(3):956–962, August 2007.

[256] Matteo Bonetti, Elisa Bortolas, Alessandro Lupi, Massimo Dotti, and Sandra I. Raimundo. Dynamical friction-driven orbital circularization in rotating discs: a semi-analytical description. , 494(2):3053–3059, May 2020.

[257] Andrei Gruzinov, Yuri Levin, and Christopher D. Matzner. Negative dynamical friction on compact objects moving through dense gas. , 492(2):2755–2761, February 2020.

[258] Xinyu Li, Philip Chang, Yuri Levin, Christopher D. Matzner, and Philip J. Armitage. Simulation of a compact object with outflows moving through a gaseous background. , 494(2):2327–2336, May 2020.

[259] eLISA Consortium, P. Amaro Seoane, S. Aoudia, H. Audley, G. Auger, S. Babak, J. Baker, E. Barausse, S. Barke, M. Bassan, V. Beckmann, M. Benacquista, P. L. Bender, E. Berti, P. Binétruy, J. Bogenstahl, C. Bonvin, D. Bortoluzzi, N. C. Brause, J. Brossard, S. Buchman, I. Bykov, J. Camp, C. Caprini, A. Cavalleri, M. Cerdonio, G. Ciani, M. Colpi, G. Congedo, J. Conklin, N. Cornish, K. Danzmann, G. de Vine, D. DeBra, M. Dewi Freitag, L. Di Fiore, M. Diaz Aguilo, I. Diepholz, R. Dolesi, M. Dotti, G. Fernández Barranco, L. Ferraioli, V. Ferroni, N. Finetti, E. Fitzsimons, J. Gair, F. Galeazzi, A. Garcia, O. Gerberding, L. Gesa,

D. Giardini, F. Gibert, C. Grimani, P. Groot, F. Guzman Cervantes, Z. Haiman, H. Halloin, G. Heinzel, M. Hewitson, C. Hogan, D. Holz, A. Hornstrup, D. Hoyland, C. D. Hoyle, M. Hueller, S. Hughes, P. Jetzer, V. Kalogera, N. Karnesis, M. Kilic, C. Killow, W. Klipstein, E. Kochkina, N. Korsakova, A. Krolak, S. Larson, M. Lieser, T. Littenberg, J. Livas, I. Lloro, D. Mance, P. Madau, P. Maghami, C. Mahrdt, T. Marsh, I. Mateos, L. Mayer, D. McClelland, K. McKenzie, S. McWilliams, S. Merkowitz, C. Miller, S. Mitryk, J. Moerschell, S. Mohanty, A. Monsky, G. Mueller, V. Müller, G. Nelemans, D. Nicolodi, S. Nissanke, M. Nofrarias, K. Numata, F. Ohme, M. Otto, M. Perreur-Lloyd, A. Petiteau, E. S. Phinney, E. Plagnol, S. Pollack, E. Porter, P. Prat, A. Preston, T. Prince, J. Reiche, D. Richstone, D. Robertson, E. M. Rossi, S. Rosswog, L. Rubbo, A. Ruiter, J. Sanjuan, B. S. Sathyaprakash, S. Schlamminger, B. Schutz, D. Schütze, A. Sesana, D. Shaddock, S. Shah, B. Sheard, C. F. Sopuerta, A. Spector, R. Spero, R. Stanga, R. Stebbins, G. Stede, F. Steier, T. Sumner, K. X. Sun, A. Sutton, T. Tanaka, D. Tanner, I. Thorpe, M. Tröbs, M. Tinto, H. B. Tu, M. Vallisneri, D. Vetrugno, S. Vitale, M. Volonteri, V. Wand, Y. Wang, G. Wanner, H. Ward, B. Ware, P. Wass, W. J. Weber, Y. Yu, N. Yunes, and P. Zweifel. The Gravitational Universe. *arXiv e-prints*, page arXiv:1305.5720, May 2013.

[260] M. Colpi, M. Dotti, L. Mayer, and S. Kazantzidis. Birth of massive black hole binaries. *arXiv e-prints*, page arXiv:0710.5207, October 2007.

[261] D. Gerosa, B. Veronesi, G. Lodato, and G. Rosotti. Spin alignment and differential accretion in merging black hole binaries. , 451(4):3941–3954, August 2015.

[262] Davide Gerosa, Giovanni Rosotti, and Riccardo Barbieri. The Bardeen-Petterson effect in accreting supermassive black hole binaries: a systematic approach. , 496(3):3060–3075, August 2020.

[263] M. Coleman Miller and Julian H. Krolik. Alignment of Supermassive Black Hole Binary Orbits and Spins. , 774(1):43, September 2013.

[264] Federico Cattorini, Bruno Giacomazzo, Francesco Haardt, and Monica Colpi. Fully general relativistic magnetohydrodynamic simulations of accretion flows onto spinning massive black hole binary mergers. , 103(10):103022, May 2021.

[265] Philip F. Hopkins. Anisotropic diffusion in mesh-free numerical magnetohydrodynamics. , 466(3):3387–3405, April 2017.

[266] Carlos O. Lousto, Yosef Zlochower, Massimo Dotti, and Marta Volonteri. Gravitational recoil from accretion-aligned black-hole binaries. , 85(8):084015, April 2012.

[267] Feng Yuan and Ramesh Narayan. Hot Accretion Flows Around Black Holes. , 52:529–588, August 2014.

[268] J. Gofford, J. N. Reeves, D. E. McLaughlin, V. Braito, T. J. Turner, F. Tombesi, and M. Cappi. The Suzaku view of highly ionized outflows in AGN - II. Location, energetics and scalings with bolometric luminosity. , 451(4):4169–4182, August 2015.

[269] Sophie Koudmani, Rachel S. Somerville, Debora Sijacki, Martin A. Bourne, Yan-Fei Jiang, and Kasar Profit. A unified accretion disc model for supermassive black holes in galaxy formation simulations: method and implementation. *arXiv e-prints*, page arXiv:2312.08428, December 2023.

[270] Filip Huško, Cedric G. Lacey, Joop Schaye, Matthieu Schaller, and Folkert S. J. Nobels. Spin-driven jet feedback in idealized simulations of galaxy groups and clusters. , 516(3):3750–3772, November 2022.

[271] Rosie Y. Talbot, Martin A. Bourne, and Debora Sijacki. Blandford-Znajek jets in galaxy formation simulations: method and implementation. , 504(3):3619–3650, July 2021.

[272] Aleksander Sądowski. Slim Disks Around Kerr Black Holes Revisited. , 183(2):171–178, August 2009.

[273] Alessia Franchini, Giuseppe Lodato, and Stefano Facchini. Lense-Thirring precession around supermassive black holes during tidal disruption events. , 455(2):1946–1956, January 2016.

[274] Piero Madau, Francesco Haardt, and Massimo Dotti. Super-critical Growth of Massive Black Holes from Stellar-mass Seeds. , 784(2):L38, April 2014.

[275] Douglas Rennehan, Arif Babul, Belaid Moa, and Romeel Davé. Three regimes of black hole feedback. *arXiv e-prints*, page arXiv:2309.15898, September 2023.

[276] Aleksander Sądowski, Ramesh Narayan, Jonathan C. McKinney, and Alexander Tchekhovskoy. Numerical simulations of super-critical black hole accretion flows in general relativity. , 439(1):503–520, March 2014.

[277] Angelo Ricarte, Ramesh Narayan, and Brandon Curd. Recipes for Jet Feedback and Spin Evolution of Black Holes with Strongly Magnetized Super-Eddington Accretion Disks. , 954(1):L22, September 2023.

[278] Daniel J. D'Orazio and Paul C. Duffell. Orbital Evolution of Equal-mass Eccentric Binaries due to a Gas Disk: Eccentric Inspirals and Circular Outspirals. , 914(1):L21, June 2021.

[279] Magdalena Siwek, Rainer Weinberger, and Lars Hernquist. Orbital evolution of binaries in circumbinary discs. , 522(2):2707–2717, June 2023.

[280] Martin A. Bourne, Davide Fiacconi, Debora Sijacki, Joanna M. Piotrowska, and Sophie Koudmani. Dynamics and spin alignment in massive, gravito-turbulent circumbinary discs around supermassive black hole binaries. *arXiv e-prints*, page arXiv:2311.17144, November 2023.